



University of  
**Strathclyde**  
**Glasgow**

**Heterogeneous Integration of  
ZnCdSe/ZnCdMgSe Vertical-External-  
Cavity Surface-Emitting Laser  
Heterostructures**

PhD Thesis

**George Chappell**

Institute of Photonics  
Department of Physics  
University of Strathclyde

2023

This thesis is the result of the author's original research. It has been composed by the author and has not been previously submitted for examination which has led to the award of a degree.

The copyright of this thesis belongs to the author under the terms of the United Kingdom Copyright Acts as qualified by University of Strathclyde Regulation 3.50. Due acknowledgement must always be made of the use of any material contained in, or derived from, this thesis.

Signed:

Date:

*Solvitur ambulando*

# Acknowledgements

I would like to thank Dr Jennifer Hastie, my supervisor, for her guidance, mentorship and for giving me the opportunity to steer this PhD project in sometimes unexpected and interesting directions! It was a privilege to work in Dr Hastie's group, however particular thanks go to Dr Paulo Moriya and Martin Lee for their encouragement and interesting discussions.

The work of Professor Maria Tamargo's group at The City College of New York was essential for this project and I would like to thank them for hosting me, growing numerous samples and their helpful suggestions throughout the project. Many thanks go to Vasilios for his help in driving progress towards the end of the pandemic and to Marcel and Anita for their awesome hosting.

Thank you to my friends, from the Institute of Photonics and climbing, for the hilarious memories, epic adventures and listening to my grumbles about II-VI materials. Special thanks go to Grandma Chappell, for always having a keen interest in the progress of the project, and to my parents and sister for their support and taking me on Devon-based walking adventures. Finally, thank you to Holly for tolerating my thesis-related wobbles and complaints about VECSELs, but most importantly for your continuous support, encouragement and friendship, which I will always hold dear.



## Abstract

The wide bandgap ZnCdMgSe-on-InP material system offers the opportunity to develop vertical-external-cavity surface-emitting lasers (VECSELs) with a fundamental emission at typically hard to reach visible wavelengths (540 nm – 590 nm). This thesis reports the progress towards the development of this novel laser system.

The material parameters of the ZnCdMgSe-on-InP material system are less studied than their more mature III-V counterparts and so in this work a literature review is conducted and a list of all parameters necessary to design a ZnCdMgSe-based VECSEL are summarized. A simple model of the material gain of a ZnCdSe/ZnCdMgSe quantum well (QW) is assessed and used to inform an analysis, based on that proposed by Kuznetsov for infrared VECSELs [1], to calculate the optimum gain structure design for a 565 nm emitting ZnCdMgSe-based distributed-Bragg-reflector-free (DBR-free) VECSEL. The optimum structure consisted of 4 pairs of ZnCdSe/ZnCdMgSe QWs, spaced with a resonant periodic gain arrangement. The molecular beam epitaxial growth of this structure is completed and multiple growth campaigns are used to iteratively improve the material quality by varying the thicknesses of the II-VI and InGaAs buffer layers that are required for growth on InP substrates.

ZnCdMgSe DBR-free VECSEL structures need to undergo epitaxial lift off from their native (001) InP substrate, as it is opaque at visible wavelengths. The resulting ZnCdMgSe membranes need to be transferred onto single crystal, high thermal conductivity, intra-cavity, transparent heatspreaders such as diamond or silicon carbide (SiC) to achieve efficient thermal management. A full substrate removal method is developed to yield cm<sup>2</sup>-sized QW membranes, which are subsequently broken into pieces and bonded to diamond. The low quality membranes produced by the full substrate removal method did not reach the laser threshold. The low membrane quality is attributed to damage induced by the HCl-based wet etching of the InP substrate and the handling of membranes in liquid suspension.

Due to the poor results of the full substrate removal a suspension and transfer printing method was developed for the ZnCdMgSe-on-InP material system: 100- $\mu$ m-sided square membranes held by anchors to rails were patterned into a ZnCdMgSe layer, had sidewall protection applied and were under-etched using a three step wet etch to liberate them from the InP substrate and remove the InGaAs buffer layer. The resulting ZnCdMgSe membranes exhibit nm-scale root

mean square surface roughness and are transfer printed onto diamond, a result which highlights promise for the future heterogeneous integration of the ZnCdMgSe. The same suspension and transfer printing method is adapted to a GaInP/AlGaInP, DBR-free VECSEL structure and used to transfer print DBR-free VECSEL membranes onto diamond. The ZnCdMgSe and GaInP/AlGaInP membranes undergo surface roughness, photoluminescence and Raman spectroscopy characterization, which reveals that sidewall protection and under-etch chemistry improvements are required for transfer printed DBR-free VECSEL membranes to reach threshold.

## **References**

1. M. Kuznetsov, F. Hakimi, R. Sprague, and A. Mooradian, "Design and characteristics of high-power (>0.5-W CW) diode-pumped vertical-external-cavity surface-emitting semiconductor lasers with circular TEM<sub>00</sub> beams," *IEEE J. Sel. Top. Quantum Electron.* **5**(3), 561–573 (1999).

# Table of Contents

Acknowledgements .....	iii
Abstract .....	iv
References .....	v
Table of Contents .....	vi
<b>1. Introduction .....</b>	<b>1</b>
<b>1.1 Semiconductor basics .....</b>	<b>1</b>
<b>1.2 II-VI semiconductors and their growth.....</b>	<b>3</b>
1.2.1 The ZnCdMgSe material system .....	3
1.2.2 The growth process .....	5
<b>1.3 Fundamentals of the laser.....</b>	<b>6</b>
<b>1.4 Semiconductor lasers .....</b>	<b>10</b>
1.4.1 Semiconductors and lasers .....	10
1.4.2 Laser diodes (edge-emitters).....	11
1.4.3 Vertical-cavity surface-emitting lasers (VCSELs) .....	12
<b>1.5 Vertical-external-cavity surface-emitting lasers (VECSELs) .....</b>	<b>13</b>
1.5.1 Components and typical formats .....	13
1.5.2 Advantages of VECSELs.....	15
1.5.3 DBR-free operation.....	17
1.5.4 VECSEL thermal management.....	19
1.5.5 VECSEL spectral coverage to date.....	21
<b>1.6 ‘Green gap’ laser sources.....</b>	<b>22</b>
<b>1.7 Lasers from II-VI semiconductor structures.....</b>	<b>24</b>
1.7.1 II-VI DBRs.....	24
1.7.2 ‘Green gap’, quantum dot lasers .....	26
1.7.3 Electron-beam-pumped and optically-pumped II-VI lasers.....	26
<b>1.8 Potential applications of visible, II-VI VECSELs .....</b>	<b>28</b>
<b>1.9 Semiconductor processing for VECSEL technology.....</b>	<b>29</b>
<b>1.10 Thesis outline .....</b>	<b>31</b>
References .....	32
<b>2. ZnCdSe/ZnCdMgSe quantum well gain structure design .....</b>	<b>45</b>
Chapter overview .....	45
<b>2.1 The properties of II-VI semiconductors for QW modelling.....</b>	<b>45</b>
<b>2.2 QW design: quantum confinement, strain, temperature and bandgap engineering .....</b>	<b>49</b>
2.2.1 Schrödinger’s equation and solving for the finite potential QW .....	49
2.2.2 Designing a QW for a II-VI VECSEL .....	52
2.2.3 Thermal effects on the bandgap and lattice constant .....	52

2.2.4 Strain effects .....	53
<b>2.3 Calculating electric fields.....</b>	<b>61</b>
2.3.1 The optical transfer matrix .....	61
2.3.2 Angular dependent reflectivity from the optical transfer matrix .....	62
<b>2.4 Resonant periodic gain, resonant gain structures and calculating the optical confinement factor.....</b>	<b>63</b>
2.4.1 The longitudinal confinement factor and resonant periodic gain (RPG) .....	63
2.4.2 Resonant VECSEL structures and thermal rollover .....	65
2.4.3 Designing resonant VECSEL structures with RPG .....	67
<b>2.5 II-VI QWs and the minimum gain requirement .....</b>	<b>68</b>
2.5.1 The Kuznetsov analysis [1].....	68
2.5.2. Single quantum well gain modelling: an initial model .....	70
2.5.4 Calculating photoluminescence spectra .....	75
<b>2.6 Finalized design for the optimum II-VI DBR-free gain structure.....</b>	<b>83</b>
<b>2.7 Future perspectives .....</b>	<b>84</b>
<b>2.8 Conclusion .....</b>	<b>85</b>
<b>References .....</b>	<b>86</b>
<b>3. II-VI VECSEL development.....</b>	<b>90</b>
<b>Chapter overview .....</b>	<b>90</b>
<b>3.1 Context and goals .....</b>	<b>90</b>
<b>3.2 Pump optics and laser cavity design.....</b>	<b>92</b>
3.2.1 Barrier and in-well pumping capabilities.....	92
3.2.2 InGaN-diode-pumped red VECSEL development .....	93
3.2.3 DBR-free laser cavity designs and alignment.....	96
3.2.4 Mounting VECSEL samples.....	97
<b>3.3 Full substrate removal optimization.....</b>	<b>98</b>
3.3.1 Methodology and initial results .....	98
3.3.2 Effects of substrate grinding .....	99
3.3.3 Effects of mounting medium .....	99
3.3.4 Etching the InP substrate .....	101
3.3.5 Bonding II-VI DBR-free VECSELs to diamond.....	103
3.3.6 Optimized full substrate removal method.....	104
<b>3.4 Photoluminescence testing setup for unprocessed samples and membranes.....</b>	<b>106</b>
<b>3.5 The first and second growth campaigns: CDI 354, CDI 356, CDI 358, CDI 447, and CDI 517 .....</b>	<b>108</b>
3.5.1 Initial test growths CDI 354, CDI 356 and CDI 358 .....	108
3.5.2 Second growth campaign: CDI 447 growth and ELO .....	109
3.5.3 Second growth campaign: CDI 517 growth and ELO .....	113
3.5.4 Growth campaign 2 summary .....	114
<b>3.6 The third growth campaign: MgTe release layers .....</b>	<b>115</b>
<b>3.7 The fourth growth campaign: increased II-VI buffer layer and decreased III-V buffer layer thicknesses.....</b>	<b>116</b>
3.7.1 Adjusting the design .....	116
3.7.2 The “ten antinode structure” .....	117
3.7.3 ELO results of CDI 637, CDI 638 and CDI 640.....	121
<b>3.8 Laser testing.....</b>	<b>125</b>

3.8.1 Concentric resonator testing .....	125
3.8.2 Membrane-on-diamond bonded to HR mirror designs .....	126
<b>3.9 Future perspectives on II-VI VECSEL technology.....</b>	<b>128</b>
<b>3.10 Conclusion.....</b>	<b>129</b>
<b>References .....</b>	<b>129</b>
<b>4. Heterogeneous integration of DBR-free VECSEL structures .....</b>	<b>134</b>
<b>Chapter overview .....</b>	<b>134</b>
<b>4.1 Materials of interest .....</b>	<b>135</b>
4.1.1 Developing DBR-free VECSELS .....	135
4.1.2 ZnCdMgSe samples .....	135
4.1.3 GaInP/AlInGaP DBR-free VECSEL structure without strain balancing (MR3751).....	135
<b>4.2 Motivation for using microfabrication techniques to produce DBR-free VECSELS .....</b>	<b>137</b>
4.2.1 Previous II-VI processing work .....	137
4.2.2 Overview of the suspension and transfer printing method .....	138
4.2.3 Goals of this work .....	139
<b>4.3 Etching II-VI and III-V semiconductors.....</b>	<b>140</b>
4.3.1 Overview .....	140
4.3.2 Wet etching of semiconductors.....	141
4.3.3 Dry etch processes .....	143
<b>4.4 Suspension method for ZnCdMgSe-on-InP and GaInP/AlGaInP-on-GaAs: hardmask formation .....</b>	<b>144</b>
<b>4.5 Suspension method for ZnCdMgSe-on-InP and GaInP/AlGaInP-on-GaAs: ICP .....</b>	<b>146</b>
<b>4.6 Developing sidewall protection for ZnCdMgSe-on-InP.....</b>	<b>148</b>
4.6.1 The requirement for sidewall protection.....	148
4.6.2 The most successful strategy: dry etch anisotropy .....	150
<b>4.7 Suspension method for ZnCdMgSe-on-InP: wet under-etching and sidewall protection removal .....</b>	<b>152</b>
4.7.1 InP crystallography and under-etching .....	152
4.7.2 The optimized InP under-etch: methods and proposed mechanism .....	156
4.7.3 The InGaAs buffer layer etch.....	158
<b>4.8 Suspension method for GaInP/AlGaInP-on-GaAs: wet under-etching and silica removal.....</b>	<b>158</b>
4.8.1 GaAs under-etching .....	158
4.8.2 Wet etch contaminants and removing the protective SiO <sub>2</sub> layer .....	160
<b>4.9 ZnCdMgSe and GaInP/AlGaInP membrane detachment via transfer printing</b>	<b>162</b>
<b>4.10 Benefits of the suspension method over full substrate removal with ZnCdMgSe-on-InP .....</b>	<b>164</b>
<b>4.11 Future perspectives .....</b>	<b>166</b>
<b>4.12 Conclusion.....</b>	<b>168</b>
<b>References .....</b>	<b>169</b>
<b>5. Characterizing and testing DBR-free VECSEL membranes.....</b>	<b>175</b>
<b>Chapter overview .....</b>	<b>175</b>

<b>5.1 Surface roughness characterization.....</b>	<b>175</b>
5.1.1 Atomic force microscope measurements .....	175
5.1.2 ZnCdMgSe membrane surface roughness .....	176
5.1.3 Surface roughness of the GaInP/AlGaInP .....	177
<b>5.2 Photoluminescence characterization .....</b>	<b>178</b>
5.2.1 Photoluminescence characterization methods .....	178
5.2.2 ZnCdMgSe membranes on diamond .....	179
5.2.3 GaInP/AlGaInP DBR-free VECSEL membranes on diamond.....	181
<b>5.3 Processing induced damage and deformation .....</b>	<b>182</b>
<b>5.4 Raman spectroscopy for post-epitaxial lift-off assessment.....</b>	<b>184</b>
5.4.1 Raman spectroscopy overview .....	184
5.4.2 Raman spectra of transfer-printed ZnCdMgSe .....	188
5.4.3 Raman spectra of transfer-printed GaInP/AlGaInP .....	190
<b>5.5 Raman mapping of under-etched GaInP/AlGaInP membranes.....</b>	<b>193</b>
5.5.1 Mapping methodologies and motivation .....	193
5.5.2 Raman mapping of unprocessed and suspended GaInP/AlGaInP .....	194
<b>5.6 Charge carrier lifetime in II-VI VECSEL structures.....</b>	<b>197</b>
5.6.1 Motivation and background .....	197
5.6.2 Measurement setup and fitting.....	198
5.6.3 Time resolved PL measurements of CDI 447.....	200
<b>5.7 DBR-free VECSEL tests with transfer-printed membranes.....</b>	<b>202</b>
<b>5.8 Conclusions and future perspectives .....</b>	<b>205</b>
<b>References .....</b>	<b>207</b>
<b>6. Conclusion .....</b>	<b>212</b>
<b>6.1 II-VI gain structure design and membrane characterization .....</b>	<b>212</b>
<b>6.2 Material processing and VECSEL development.....</b>	<b>213</b>
<b>6.3 Physical limitations in II-VI DBR-free VECSEL development .....</b>	<b>215</b>
<b>6.4 Future vision .....</b>	<b>216</b>
<b>References .....</b>	<b>219</b>
<b>Research output .....</b>	<b>221</b>
<b>Appendix.....</b>	<b>222</b>

# 1. Introduction

Semiconductor lasers have proven themselves as an important enabling technology; advanced manufacturing, high power pumping, and even household consumer devices rely on the power and efficiency of semiconductor-based lasers. Highly directional, polarized, low divergence, high brightness and spectrally pure light from lasers of various wavelengths and classes underpin huge developments in modern life and industry, from manufacturing, to medical procedures, to enabling new science. The ability of the laser to enable progress is motivation enough for the further development of this technology. Vertical-external-cavity surface-emitting lasers (VECSELs) are a type of semiconductor laser of particular interest due to their combination of semiconductor gain spectral coverage and solid-state laser geometry.

In this thesis, work is presented towards the goal of further increasing the spectral coverage of VECSELs using the ZnCdMgSe-on-InP, II-VI semiconductor material system. In this first chapter, some key background information and concepts will be introduced. A brief overview of semiconductor material systems and II-VI semiconductors is given, followed by an outline of laser physics essentials and an introduction to laser diodes, vertical cavity surface-emitting lasers (VCSELs) and VECSELs. A summary of the current progress on II-VI semiconductor lasers and the key microfabrication techniques used in this project is presented. Finally, an outline of the thesis content is included.

## 1.1 Semiconductor basics

Semiconductors have electrical conductivity properties which are intermediate between conductors, such as metals, and insulators, such as plastics and glasses. Semiconductors are typically group IV semiconductors (such as Si, Ge), III-V compounds (such as GaAs and InP) or II-VI compounds (such as ZnSe and CdS), the constituent atoms of which bond by sharing valence electrons (electrons from the outermost atomic electron shell) [1]. The regular, periodic arrangement of the bonded atoms forms a periodic potential  $V(\mathbf{r}) = V(\mathbf{r} + \mathbf{R})$ , where  $\mathbf{r}$  is the direction vector of the atomic potential,  $V$  and  $\mathbf{R} = n_1\mathbf{a}_1 + n_2\mathbf{a}_2 + n_3\mathbf{a}_3$ , with  $n_i$  being integers and  $\mathbf{a}_i$  being the lattice vectors of the semiconductor [1]. From Schrodinger's equation and Bloch theorem a periodic wavefunction of the electrons is found, called a Bloch function, which forms  $n$  electron energy bands given by  $E = E_n(\mathbf{k})$ , with  $\mathbf{k}$  as the electron wavevector [1]. The primitive cell of a crystal lattice can be expressed in reciprocal,  $\mathbf{k}$ -space,

to define a region called the Brillouin zone, where the  $\mathbf{k} = 0$  point is the centre  $\Gamma$  point. The different energy bands,  $E_n(\mathbf{k})$ , exist within the conduction and valence bands and at 0 K all of the electrons within a semiconductor are located within the valence band. The minimum energy difference, in  $\mathbf{k}$ -space, between the conduction band and the valence bands is called the bandgap energy,  $E_g$ , see Fig. 1 a). When a photon of energy greater than  $E_g$  is incident on a semiconductor, it breaks a bond holding an electron within the valence band and promotes the electron to the higher energy conduction band. The remaining electron vacancy can be modelled as a quasi-particle called a hole, see Fig. 1 a).

The nature of the bandgap within semiconductors is either direct, with conduction and valence band minima aligned at the  $k = 0$  ( $\Gamma$  point) as in Fig 1 b), or indirect bandgap with the conduction and valence band minima separated in  $\mathbf{k}$ -space as in Fig. 1 c). Direct bandgap semiconductors are more suited to photonic devices as the generation of light is a two-body process, with an electron and hole recombining to emit a photon with energy equal to the recombination energy. Light generation within indirect semiconductors requires an electron-hole pair and a phonon to provide the additional momentum for the electron to move to the  $k = 0$  point, where recombination can occur. The three-body nature of photon generation in indirect semiconductors is a low probability event and therefore prevents these materials from being efficient photonic platforms.

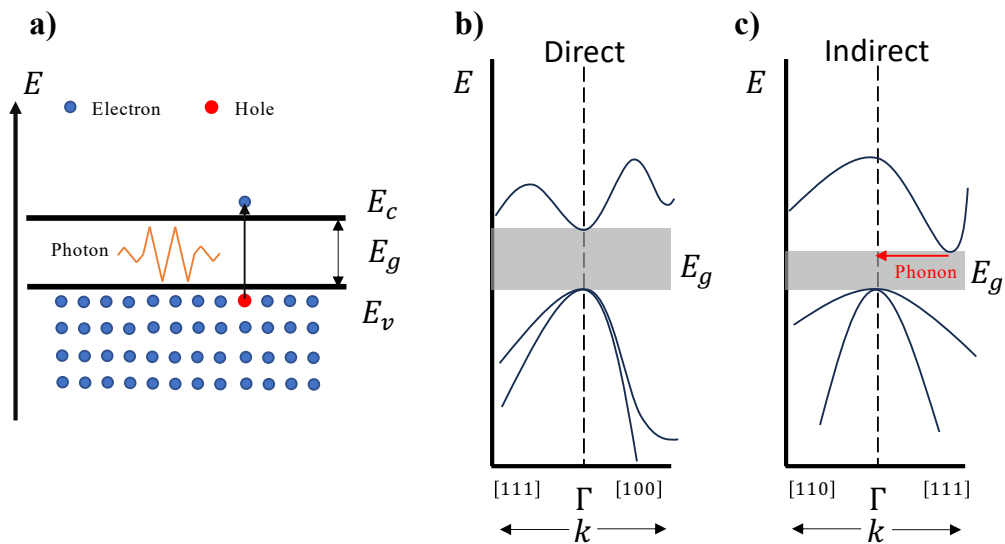


**Figure 1. a)** The absorption of a photon with an energy greater than  $E_g$  creating an electron-hole pair, based on a figure from [1]. The electron energy increases resulting in its promotion to the conduction band.  $E_{c/v}$  is the energy of the conduction/valence band edge.  $E_n(\mathbf{k})$  for **b)** direct bandgap, and **c)** indirect bandgap semiconductors [2]. In **c)** the red arrow represents the phonon required for optical recombination at the  $\Gamma$  point.



Alloying different semiconductors enables the engineering of ternary and quaternary semiconductors with designed, specific properties, such as bandgap, strain state and effective charge carrier masses. As an example, Fig. 2 shows the energy bandgaps and the lattice constants of some III-V and II-VI semiconductors, with lines showing the energy bandgap of a ternary compound formed by alloying two binary compounds [3]. The properties of alloyed semiconductors can be interpolated using Vegard's Law, discussed further in Chapter 2 [4].

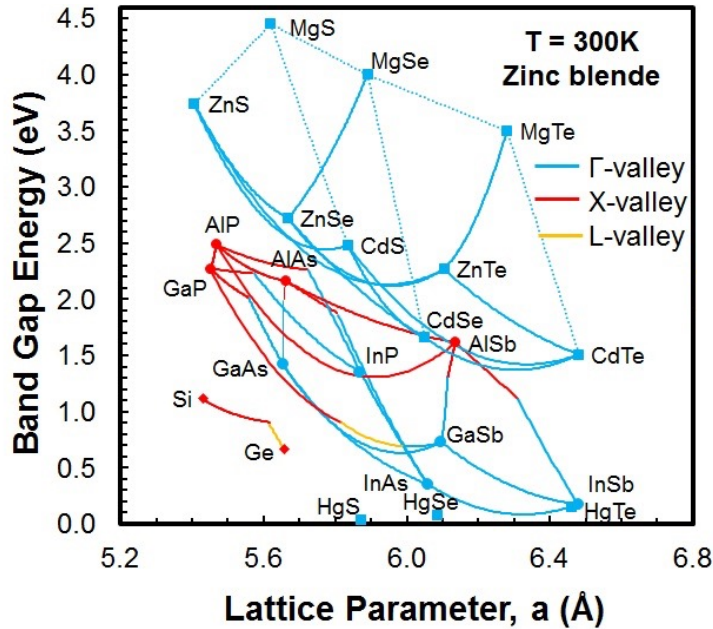


**Figure 2.** The energy bandgap at the  $\Gamma$ -valley point (direct bandgap) and X- and L- valley points (indirect bandgap) as a function of the lattice constant for a selection of zincblende (cubic) III-V and II-VI semiconductors at 300 K, where the dashed lines represent estimated bandgaps due to lack of experimental data. Taken from [3].

## 1.2 II-VI semiconductors and their growth

### 1.2.1 The ZnCdMgSe material system

Wide bandgap II-VI semiconductors can be engineered to target almost any wavelength across the entire visible spectrum, offering the opportunity to develop ‘green-gap’ (540-580 nm) photonic systems such as light-emitting diodes (LEDs) [5], lasers [6–8], and colour converters [9]; and their capacity for very large conduction band offsets is of interest for developing quantum cascade lasers and photodetectors in the infrared [7,10]. II-VI semiconductors are grown on GaAs, GaP, and InP substrates [11], with appropriate buffer layers. ZnCdSe/ZnCdMgSe-on-InP is the II-VI material system of interest in this project, which has a wide, direct bandgap, is lattice-matched to (0 0 1) InP, is zincblende (see Section 2.1) at the compositions of interest and is grown with an InGaAs buffer layer (see Section 1.2.2). P-

type doping, as required for electrical injection, is challenging within II-VI devices and so GaN-based devices have been the focus of greater research work, demonstrating long operation times at blue to green wavelengths [12]. There is renewed interest in using II-VI materials to target the green to yellow spectral regions (see Section 1.6.3) due to the difficulties of growing InGaN devices with the high indium contents necessary to target these longer wavelengths [12].

Fig. 3 a) and the table in Fig. 3 b) demonstrate that the composition of the quaternary ZnCdMgSe can be varied, through alloying, to give the material a bandgap with an energy value throughout the visible spectrum, whilst maintaining lattice-matching to (0 0 1) InP substrates. The ternary material  $\text{Zn}_{0.48}\text{Cd}_{0.52}\text{Se}$  is lattice-matched to (0 0 1) InP and by setting this as the quantum well (QW) material, the laser emission wavelength can be engineered by exploiting quantum confinement (see Chapter 2, which also includes material parameters).

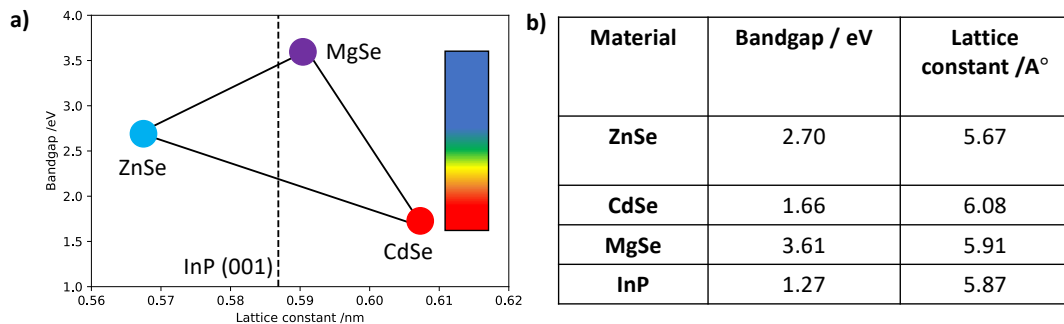


**Figure 3. a)** The range of ZnCdMgSe compounds possible within the triangle of binaries, where the compositions along the (0 0 1) InP line are lattice-matched to InP. **b)** The bandgap and lattice constant of the II-Se binaries and the InP substrate.

To fully incorporate these II-VI epitaxial layers into devices, epitaxial lift-off (ELO) is essential due to the poor thermal and optical properties (at visible wavelengths) of the InP substrate and the InGaAs buffer layer. A variety of methods have been devised to accomplish this, ranging from chemical or mechanical thinning of InP substrates and a subsequent selective wet etch of the InGaAs buffer layer [13,14], to making use of metastable, sacrificial layers for growths on GaAs [15,16]. The large bandgap range of II-VI semiconductors that may be grown lattice-matched to InP in particular enables the fabrication of unstrained QWs suitable for emission from blue to orange without the requirement for strain compensation [8]. InP is already a common substrate for the growth of infrared structures based on III-V semiconductors and so the optimization of ELO of epitaxial layers from these substrates is important for a broad range of novel devices beyond this project.

### *1.2.2 The growth process*

II-VI semiconductors can be grown by metal organic vapour phase epitaxy (MOVPE) [17] and by molecular beam epitaxy (MBE) [18,19]. MOVPE is the growth of semiconductor layers using chemical reactions on the deposition surface between organic molecules carrying the required group II, III, V or VI elements [20]. MBE uses vaporised and thermally-accelerated atoms of the constituent elements of a specific semiconductor layer to give a physical deposition onto a growth substrate [20]. MOVPE offers a high growth rate with high crystalline quality and MBE offers a fast switching, which is better suited for thin and alternating layers [20]. ZnCdSe has a crystalline structure that is composition dependent, with a cubic, zincblende structure (see Chapter 2, Fig. 1) at high zinc concentrations, and a wurtzite structure at low zinc concentrations [4]. When ZnCdSe is grown by MBE it exhibits a zincblende structure over its entire composition range [4].

For this project the zincblende ZnCdSe and ZnCdMgSe are grown using MBE by collaborators in the group of Professor Maria C. Tamargo at The City College of New York. The MBE is completed in a dual Riber 2300P chamber with ultra-high vacuum transfer modules, and is capable of growing III-V and II-VI semiconductors (see Fig. 4 [19]). Reflection high energy electron diffraction (RHEED) is used to give a continuous assessment of the crystal quality during the growth and the oscillatory amplitude of the RHEED signals gives an indication of the number of monolayers grown. The majority of the II-VI samples grown in this project are lattice-matched to the (0 0 1) face of an InP substrate with an  $\text{In}_{0.53}\text{Ga}_{0.47}\text{As}$  buffer layer to improve growth quality [19]. The growth of II-VI materials has now progressed towards complex device architectures such as quantum cascade laser structures and detectors [7,21].

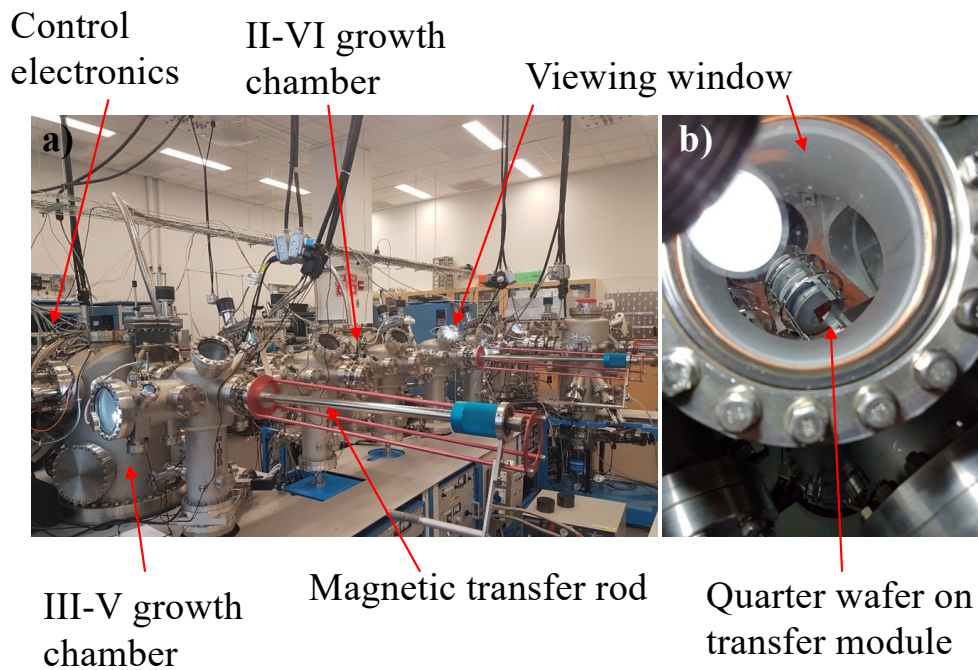


**Figure 4.** a) Image of the MBE and transfer chambers used to grow the samples studied in this work at The City College of New York; and b) a wafer being transferred inside the chamber.

### 1.3 Fundamentals of the laser

The goal of this work is to develop laser sources that use the wide bandgap ZnCdMgSe material system as a gain material. Chapter 2 will outline the design of quantum wells (QWs) and the laser heterostructure in this material, building upon the laser fundamentals discussed here.

The gain mechanism used in the majority of lasers is stimulated emission; the optical perturbation of the excited state of a gain medium, which leads to a quantum mechanical interaction in which an electron is reduced to a lower energy state and a photon with identical phase, polarization, frequency and direction as the perturbing photon is emitted. Stimulated emission amplifies the original input signal of photons, and is favoured when there is a higher concentration of electrons in the excited state than the ground state, known as a population inversion. The population inversion is maintained through an energy input into the gain medium known as pumping. A laser gain medium is situated within an optical resonator which cycles photons through the amplifying gain medium. If the amplification (gain) exceeds the loss for a cavity round trip then a stable laser mode can form. A laser mode is a self-consistent electric field distribution within the laser resonator [22]. The laser modes within a resonator can be described in terms of their longitudinal component, the electric field distribution along

the resonator axis, and their transverse component, the electric field distribution in the plane perpendicular to the resonator axis. The light emitted from a laser source is bright, has a low divergence and is coherent.

Semiconductor lasers exhibit threshold behaviour; increasing the pump power will result in steady-state laser oscillation once the gain and loss are balanced. This process is modelled by the coupled semiconductor laser rate equations, which for the case of electrically-pumped lasers are given by [1]:

$$\frac{dn(t)}{dt} = \eta_i \frac{J(t)}{qd} - \frac{n(t)}{\tau} - v_g g(n)S(t) \quad (1)$$

and,

$$\frac{dS(t)}{dt} = \Gamma v_g g(n)S(t) - \frac{S(t)}{\tau_p} + \beta R_{sp}(n), \quad (2)$$

where  $n(t)$  is the electron number density in the excited state within the active region as a function of time,  $\frac{dn(t)}{dt}$  is the rate of change of electrons in the excited state within the active region,  $S(t)$  is the photon density in the resonator as a function of time,  $\frac{dS(t)}{dt}$  is the rate of change of photon density in the resonator,  $\eta_i$  is the pump absorption efficiency,  $J(t)$  is the current density,  $q$  is the electron charge,  $d$  is the active region thickness,  $\tau$  is the electron lifetime in the excited state,  $v_g$  is the group velocity of light,  $g(n)$  is the gain coefficient (in units of  $s^{-1}$ ) as a function of charge carrier density,  $\Gamma$  is the optical confinement factor (a quantification of how much of the laser electric field is within the active region),  $\tau_p$  is the photon lifetime,  $\beta$  is the spontaneous emission factor and  $R_{sp}(n)$  is the rate of spontaneous emission as a function of charge carrier density [1]. The  $\eta_i \frac{J(t)}{qd}$  term in the equation for  $\frac{dn(t)}{dt}$  is the source term from the pump,  $\frac{n(t)}{\tau}$  quantifies the reduction in  $n(t)$  due to spontaneous emission and non-radiative processes and  $v_g g(n)S(t)$  gives the reduction in  $n(t)$  due to stimulated emission. The photon density is increased by the stimulated emission process,  $\Gamma v_g g(n)S(t)$ , and spontaneous emission,  $\beta R_{sp}(n)$ , but is decreased by output coupling and parasitic resonator losses,  $\frac{S(t)}{\tau_p}$ . For optical, rather than electrical, pumping  $\frac{P}{hv(L_A A_p)}$  can replace the  $\frac{J(t)}{qd}$  where  $P$  is the input optical pump power,  $h$  is the Planck constant,  $v$  is the frequency of the pump photons,  $L_A$  is the length of the active region and  $A_p$  is the pump spot area.

From these coupled equations a population inversion is achievable due to the quasi-three level behaviour of semiconductor lasers [23]. Fig. 5 shows an optically-pumped quasi-three level scheme. The quasi-three level behaviour arises as an electron population is present within the QW and barrier valence bands under normal operating temperatures [23].

Below the laser threshold, as pump power is increased,  $\frac{dn(t)}{dt}$  is increased and  $n(t)$  increases, simultaneously resulting in an increase in  $S(t)$ . At threshold the gain is equal to the resonator losses and the laser enters the steady-state,  $\frac{dn(t)}{dt} = 0$  and  $\frac{dS(t)}{dt} = 0$ . In the steady state  $n(t)$  is clamped at a specific value, and so the amplification of the gain medium is held at a fixed value, resulting in gain clamping. Increasing pump power beyond the threshold value increases  $S(t)$  and results in a higher laser output power.

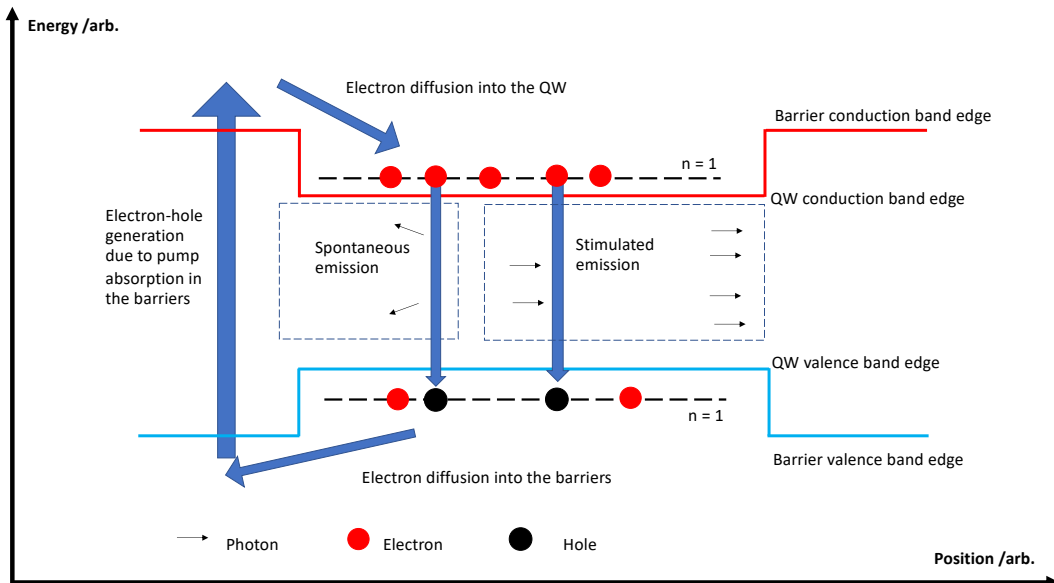


**Figure 5.** The quasi-three level system of an optically-pumped semiconductor QW laser [23]. Electron-hole pairs are generated by pumping, which excites electrons from the barrier valence band to the barrier conduction band. The electrons diffuse throughout the gain structure and relax into the potential well of the QW. Stimulated and spontaneous emission events trigger electron-hole recombination and the electron de-excites to the QW valence band. Within the QW valence band, at  $n = 1$  a population of electrons exists under thermal equilibrium resulting in the quasi-three level behaviour. From the QW valence band electrons diffuse into the barrier valence band. The blue arrows indicate the electron movements.

The basic structure of the majority of CW lasers is the same; a resonator contains an electric field mode and a gain material provides amplification of the intracavity electric field via

stimulated emission. In modern laser physics the resonator itself can take many forms, from waveguides, semiconductor heterostructures, colloids, optics in free space (including unstable resonators), to micro-ring resonators, but all work on the principle of forming a containment of an oscillating electric field and having a partial leakage of the contained electric field as an output. The threshold gain,  $g_{th}$ , required to achieve laser oscillation is given by:

$$R_1 R_2 T_{loss} \exp(2\Gamma g_{th} L) = 1, \quad (3)$$

where  $R_1$  and  $R_2$  are the reflectivity of the laser cavity mirrors,  $\Gamma$  is the longitudinal confinement factor,  $L$  is the length of the gain medium and  $T_{loss}$  is the laser cavity loss (1 – the transmission losses per cycle) [24,25].

Stability is a key parameter to consider when designing a laser resonator, and this can be assessed by using the ABCD matrix formalism to calculate the conditions for round trip stability [25]. A ray can be described in terms of a column vector, with one component describing its displacement from the propagation axis and another describing its angle of propagation. It follows that optical components acting on rays can be described as  $2 \times 2$  matrices (an ABCD matrix), and a propagation through multiple components is described by multiplication of these matrices. For a generic spherical resonator comprised of two mirrors with radii of curvature  $R_1$  and  $R_2$  respectively, a distance  $d$  apart, the matrices of these components can be multiplied together and rearranged to give the resonator stability condition [25,26]:

$$0 \leq \left(1 - \frac{d}{R_1}\right) \left(1 - \frac{d}{R_2}\right) \leq 1. \quad (4)$$

This condition can be expressed as a plot, to demonstrate the degrees of freedom and possible configurations of a stable resonator. If we let  $g_1 = \left(1 - \frac{d}{R_1}\right)$  and  $g_2 = \left(1 - \frac{d}{R_2}\right)$ , it can be seen that the maximum of the inequality is satisfied when  $g_1 g_2 = 1$ . If  $g_2 = 1/g_1$  is plotted, as in Fig. 6, the line is a graphical representation of the range of values for which  $g_1$  and  $g_2$  satisfy the maximum of the inequality. Likewise, the minimum of the equality is satisfied for  $g_1 = 0$  and/or  $g_2 = 0$ , which is the boundary represented by the  $g_1$  and  $g_2$  axes. Therefore, any resonator configuration under the curve and between the  $g_1$  and  $g_2$  axes is stable, represented by the blue shaded area in Fig. 6, as it satisfies the conditions of the inequality. Examples of different resonator classes are plotted as orange crosses and labelled in Fig. 6. These resonator

design principles are applied in Chapters 4 and 5 to determine the optimum resonator for testing the laser samples developed in this work.

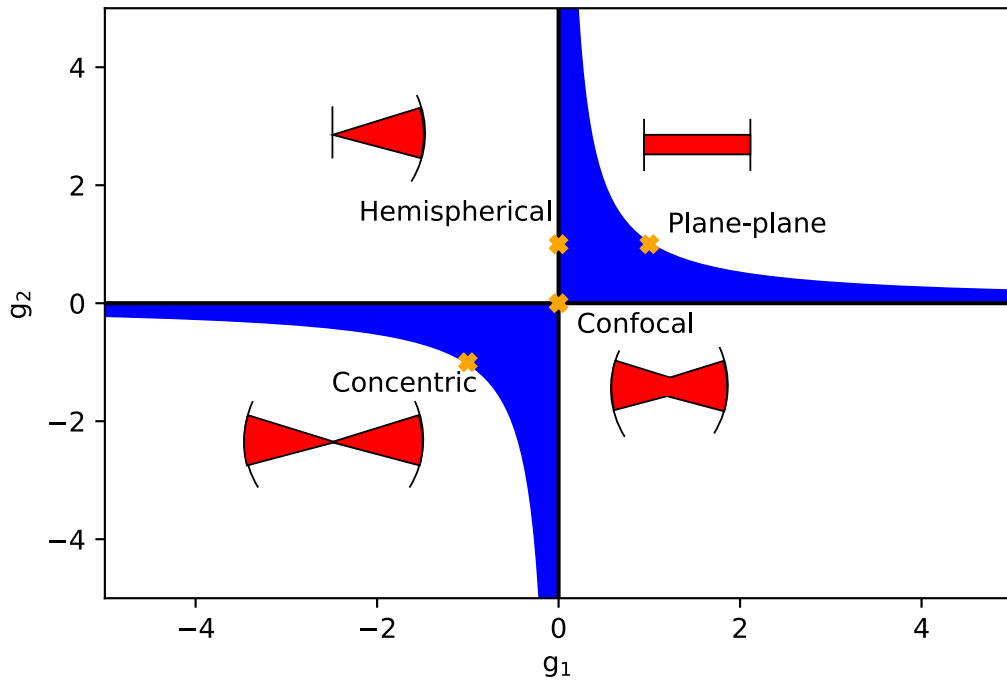


**Figure 6.** The stability plot of two-mirror laser resonators, with example two-mirror laser cavities plotted.

## 1.4 Semiconductor lasers

### 1.4.1 Semiconductors and lasers

Semiconductors can be used to form the resonator, as well as the gain medium, of a laser system. Numerous laser architectures have been developed, but semiconductor lasers in particular have enabled the integration of laser light sources with electronic components easily. The first semiconductor lasers operated through an electrically-pumped p-n junction and utilized electron-hole recombination to produce photons with an energy dictated by the bandgap of the materials at the junction. This relatively simple design was improved by using a QW to locally reduce the density of states (discussed further in Chapter 2) in the active region which allowed for a more efficient electron-hole recombination at states around the laser photon energy.

Semiconductors are useful gain materials as their solid-state physical properties are well understood, their properties can be engineered by alloying, and their compatibility with modern electronic foundry capabilities is high. The semiconductors used for lasers are



typically direct bandgap III-V semiconductor material systems such as InGaAsP, AlInGaP, GaAlAs, AlInGaN or AlInAs.

#### 1.4.2 Laser diodes (edge-emitters)

Edge-emitters use a semiconductor QW active region and the semiconductor heterostructure waveguide as the laser cavity. Cleaved, and sometimes high-reflectivity-coated, end facets form the cavity mirrors. As the laser cavity and the gain material are the same structure, the gain length is the round-trip length of the cavity which results in edge-emitters being very tolerant to losses due to their large round-trip gain. This allows one of the end cavity mirrors to have a high output coupling of up to 50 %, giving edge-emitters a high output power.

The edge-emitter laser mode oscillation is perpendicular to the growth direction and in the plane of QWs and waveguiding layers (see Fig. 7). The gain structure is a high aspect ratio cuboid, with the laser axis having a much greater length than the cavity width to suppress laser modes perpendicular to the intended laser axis. Edge-emitters are often multi-QW structures to encourage a greater spatial overlap between the QW gain sources and the refractive index guided laser mode. The rectangular output coupler yields a highly elliptical output profile, with a fast and slow axis that have different divergences and also a different beam waist position when focussed (astigmatism). The highly astigmatic and divergent edge-emitter output requires collimation and beam shaping, often using cylindrical optics, which increases the size and complexity of the optical systems required for many applications.

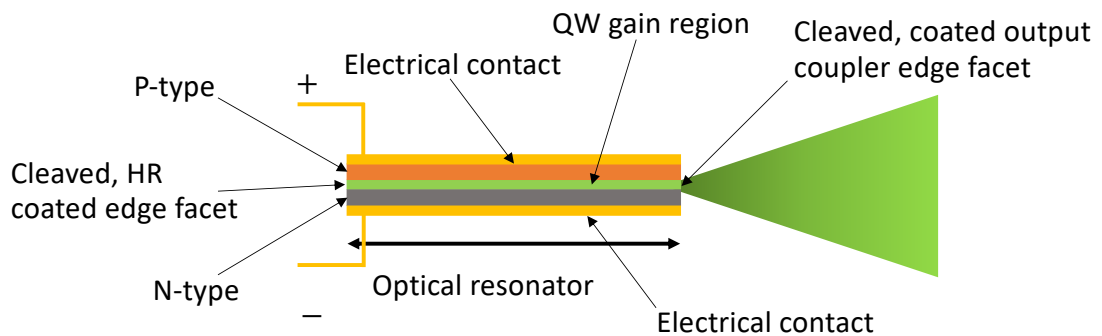


**Figure 7.** A laser diode structure comprised of p-type and n-type layers for electrical injection and a multi-QW active region. Adapted from Fig. 15.1 in ref [25].

Edge-emitters are electrically-pumped, which allows for their easy integration into household and industrial technology. High input currents cause Joule heating and so the input power to a

single edge-emitter is limited by the damage threshold of the device. Additionally, high laser output powers from edge-emitters can cause catastrophic optical damage (COD) to the semiconductor structure and the edge facets, which vastly reduces the efficiency or destroys the laser entirely. Joule heating and COD set a limit on the maximum output power achievable with an edge-emitter. To increase the available output power from a single device, edge-emitters can be stacked into large arrays of single emitters, or the beams of multiple diode lasers combined, to yield high power units with maximum output powers of the order of kW in CW operation.

#### 1.4.3 Vertical-cavity surface-emitting lasers (VCSELs)

The first vertically-emitting semiconductor laser, where coherent emission is parallel to the injection current and epitaxial growth directions and perpendicular to the QW plane, was developed in 1965 by I. Melngailis *et al* [27]. The first VCSEL was reported in 1979, with the important development of using Au-based contacts as the laser resonator mirrors [28]. The modern VCSEL is a monolithic vertically-emitting semiconductor laser, see Fig. 8, with an electrically-pumped QW gain region situated inside a semiconductor distributed Bragg reflector (DBR) mirror-based laser cavity, with a high reflectivity DBR on the substrate side of the QWs and an output-coupling DBR on the surface side of the QWs. The DBR is comprised of repeating pairs of high refractive index contrast layers, each a quarter wavelength thick. Reflections from the quarter wavelength layers constructively interfere to give a high reflectivity at a target wavelength.

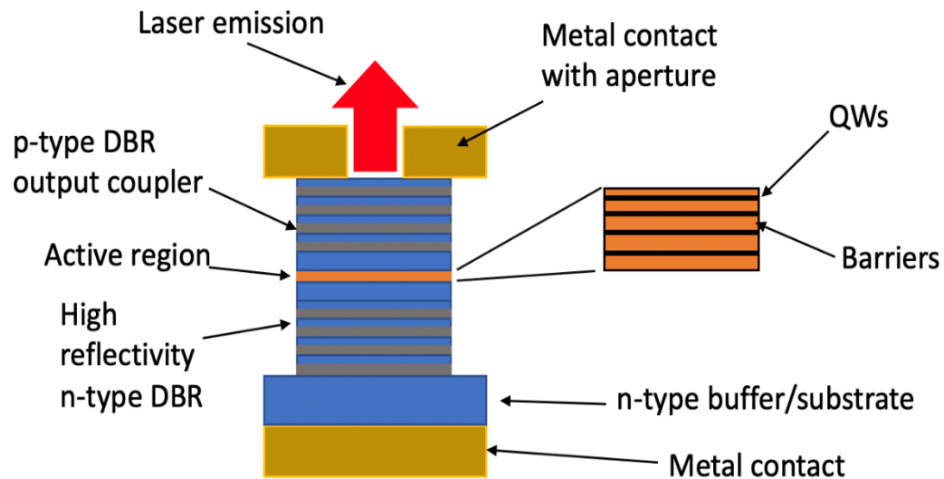


**Figure 8.** A generic vertical-cavity surface-emitting laser structure comprised of a multi-QW active region within a resonator formed by p-type and n-type DBRs. The doped DBRs allow current to spread from the metallic contacts to the active region. The topside metal contact has an aperture to allow for laser output coupling.

The larger, circular aperture of VCSELs gives higher beam quality than edge-emitters and the short resonator ensures single longitudinal and transverse mode operation. VCSELs have a reduced gain volume, in comparison to edge-emitters, which along with a higher finesse DBR based cavity results a much lower threshold current than an edge-emitter. VCSELs can be easily mass-produced, have a small footprint and their vertical emission enables simple testing during manufacture, which gives them great industrial appeal. VCSEL power can be increased by increasing the emission aperture size and pumping with greater current or by building large arrays of multiple VCSELs. A downside of power-scaling individual VCSELs is that radially scaling the emission aperture results in sub-optimal charge carrier distribution over the mode profile at large aperture sizes. Additionally, any heat generated in the gain region must travel through the multi-layered DBR structures before removal, resulting in high temperatures in the gain region that inhibit efficient high power operation. VCSELs are therefore best suited to lower power applications. The miniaturization of VCSEL technology has already led to its integration into communications, displays, computer mice and laser printers [29].

## **1.5 Vertical-external-cavity surface-emitting lasers (VECSELs)**

### *1.5.1 Components and typical formats*

The vertical-external-cavity surface-emitting laser (VECSEL) is a vertically-emitting QW laser, similar to a VCSEL but differing in two important ways: it is typically optically-pumped, and has an external laser resonator that is separate from the epitaxial structure. The epitaxial structure is a gain mirror comprised of resonantly spaced QWs as the gain medium, which are grown upon a high reflectivity (>99.9 %) DBR mirror which forms one of the cavity mirrors. QWs emitting in the vertical format give a low single pass gain and therefore VECSELs require a high finesse resonator in order to reach threshold. A high finesse laser resonator is formed using the VECSEL gain mirror and external free-space mirrors. Examples of a two mirror and a four mirror VECSEL resonator are shown in Fig. 9 a) and b) respectively, along with a schematic of a typical VECSEL gain structure showing the QW gain region and DBR layers within the gain mirror, in Fig. 9 c).

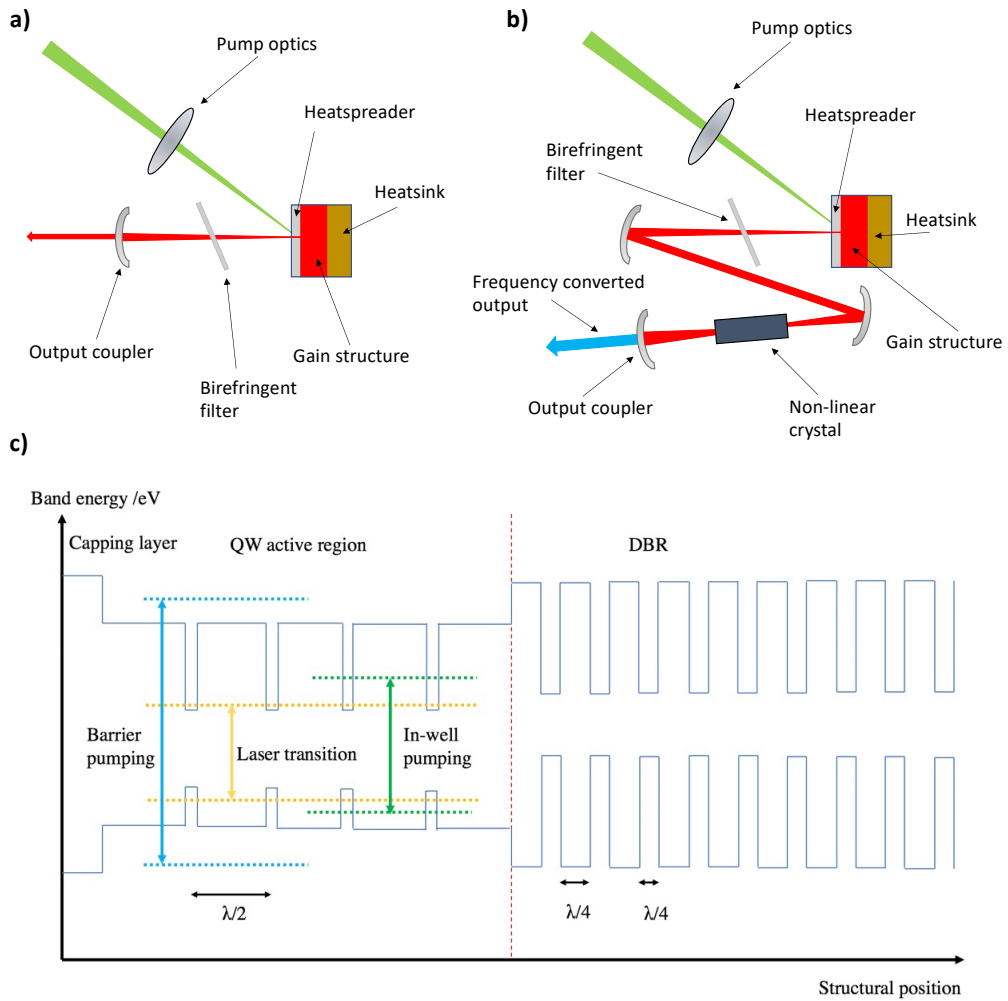


**Figure 9.** a) A two-mirror VECSEL and b) non-linear frequency conversion of the fundamental laser emission within the external cavity of a four-mirror VECSEL. Based on figures in references [30,31]. c) An example of a VECSEL gain structure, showing the active region left of the red dotted line and the DBR to the right.

The gain spectrum of QWs is broad and this means that multiple longitudinal spectral modes can exist within a VECSEL cavity; however, the free-space nature of the external cavity allows the insertion of etalons and birefringent filters (BRFs) to force single longitudinal mode operation and/or allow spectral tuning.

For VECSELs the QWs are usually optically-pumped into charge carrier population inversion by a diode or solid-state laser, however electrical injection is possible [31]. An interesting pump mechanism of a monolithically-integrated laser diode, coupled to a QW gain structure through evanescent coupling has also been reported as a pump source [32]. The pump light is typically absorbed within the barriers of the QWs. Electron-hole pairs are created in the

barriers during optical-pumping and these quickly diffuse through the VECSEL structure and into the potential wells of the QWs (see Fig. 5).

Optical in-well pumping is possible using a pump source with a photon energy below the barrier bandgap, which is directly absorbed within the QWs [30,31] (see Fig. 9 c)). The low absorption efficiency available with in-well pumping means that complex pump recycling optics are required. Quantum defect quantifies the amount of pump photon energy converted to heat (ratio between pump and laser wavelengths) and is discussed in Section 3.2. The advantage of in-well pumping is the reduced quantum defect, due to longer pump wavelengths used than in the barrier pumped case, which lowers the thermal load placed upon the laser.

VECSELs are capable of true power scaling [33], as the output power can be increased by radially scaling the optical pump spot, whilst maintaining diffraction limited beam quality as long as sufficient thermal management is achieved, resulting in one dimensional heat flow from the active region [30,33,34]. The thermal management of VECSELs is discussed further in Section 1.5.4. The optical pump spots can be scaled to much larger sizes than the electrically-pumped VCSEL apertures due to the Gaussian or top-hat spatial distribution of the optically-injected charge carriers.

#### *1.5.2 Advantages of VECSELs*

The external cavity and vertical, semiconductor-based, light generation gives VECSELs some of the important properties of both semiconductor and solid-state lasers; see a summary in Table 1. VECSELs encompass the spectral coverage and broad optical absorption afforded by bandgap-engineered semiconductors, but with the diffraction limited, TEM<sub>00</sub>, output beam quality given by external resonators [35]. The thermal management of VECSELs is similar to solid-state lasers, where the thin disk geometry offers a high surface area for heat flow.

The VECSEL QW barriers are bulk semiconductor absorbers which absorb light above their bandgap and place no strict criteria on the spectral width of the pump source. This suits pumping with cheap, efficient, compact, laser diodes. The opportunity for compact pumping, a small laser head and cm-scale resonator make VECSELs an appealing laser with a low size, weight, power consumption and cost.

The high reflectivity DBR and low transmission output coupler of the VECSEL external cavity enable a high intra-cavity power to be achieved. The external cavity allows non-linear

intracavity elements to be aligned within this high circulating power which enhances non-linear effects, allowing efficient non-linear frequency conversion (see Fig. 9 b)) [31,36,37].

**Table 1.** The typical properties of solid-state lasers, semiconductor lasers and VECSELs.

<b>Laser property</b>	<b>Solid-state laser</b>	<b>Semiconductor laser</b>	<b>VECSEL</b>
<b>Examples</b>	Ti:Sapphire, Nd:YAG	InGaN laser diode, AlGaAs VCSEL	AlInGaP- or AlGaAs-based VECSELs
<b>System size</b>	Several litres	cm <sup>3</sup> with electronics	< 0.5 litres
<b>CW output power</b>	W-scale	kW arrays possible, W-scale single units	Typically W-scale
<b>Tunability</b>	Dependent on material properties, birefringent filter tuning	Temperature tuned or via external grating	Temperature and birefringent filter tuning
<b>Charge carrier lifetime</b>	Long, up to $\mu$ s. Problematic for low noise CW	Short $\sim$ ns	Short $\sim$ ns. Not suitable for high energy pulses
<b>Resonator</b>	External cavity	Monolithic, short cavity	High finesse and external cavity
<b>Pumping</b>	Optically-pumped by laser diode or flash lamp, at specific pump wavelengths	Electrically-pumped (typically). Requires dopants and contacts	Optically-pumped by diode or solid-state laser. Broad optical absorption
<b>Thermal management</b>	Disk geometry and heatspreader	Joule heating limits output power	Disk geometry and heatspreader
<b>Fabrication difficulty</b>	Requires free space optical alignment	Monolithic semiconductor design	Gain mirror with free space optical alignment

The long (in comparison to VCSELs), high finesse external cavity yields a long photon lifetime which, in combination with the much shorter ns charge carrier lifetime, results in relaxation-oscillation-free performance and low intrinsic noise [30].

VECSELs can undergo frequency stabilization through Pound-Drever-Hall (PDH) and Hänsch-Couillaud (HC) locking techniques to achieve sub-kHz linewidths whilst maintaining output powers exceeding 100 mW [38–40]. Both of these locking techniques generate an error signal based on the frequency of the laser source with respect to a reference cavity, which is used within a feedback loop to apply a correction to the laser resonator via a piezoelectrically-driven cavity mirror. PDH applies a radiofrequency phase modulation to a sample of the laser output and assesses the reflection of the laser mode from the reference cavity mode to generate an error signal. HC reflects a sample beam, off-axis, from a confocal cavity containing a tilted linear polarizer, which gives the reflected output a frequency dependent elliptical polarization. Analysis of the orthogonal components of this polarization is used to generate the error signal. VECSELs also have an inherently low Schawlow–Townes linewidth limit (the quantum mechanically limited linewidth) on the order of 1 Hz, as shown in calculations in reference [41], which will likely be approached with future engineering of the VECSEL laser systems.

### *1.5.3 DBR-free operation*

DBR-free VECSELs, also sometimes called membrane external-cavity surface-emitting lasers (MECSELs), use an optically-pumped QW membrane as the laser gain medium within an external resonator, see Fig. 10. Omitting the DBR simplifies epitaxial growth and allows for an increase in the possible wavelength coverage of VECSELs as strain free, low absorption, high reflectivity, homoepitaxially grown DBRs are not possible for all wavelengths and material systems. Using this project as an example, ZnCdSe/ZnCdMgSe QWs can offer optical gain across the entire visible spectrum, however the varied compositions of ZnCdMgSe layers which are lattice-matched to InP do not offer the refractive index contrast necessary for a high reflectivity DBR, whilst maintaining a reasonable DBR length (see Section 1.7.1). Removing the DBR reduces the thermal barrier for heat flow from the QW active region and enables transparent crystalline heatspreaders to be bonded to each emission surface of the active region, further enhancing heat extraction and delaying the onset of thermal rollover [42]. The thermal management of VECSELs is discussed in more detail in Section 1.5.4.

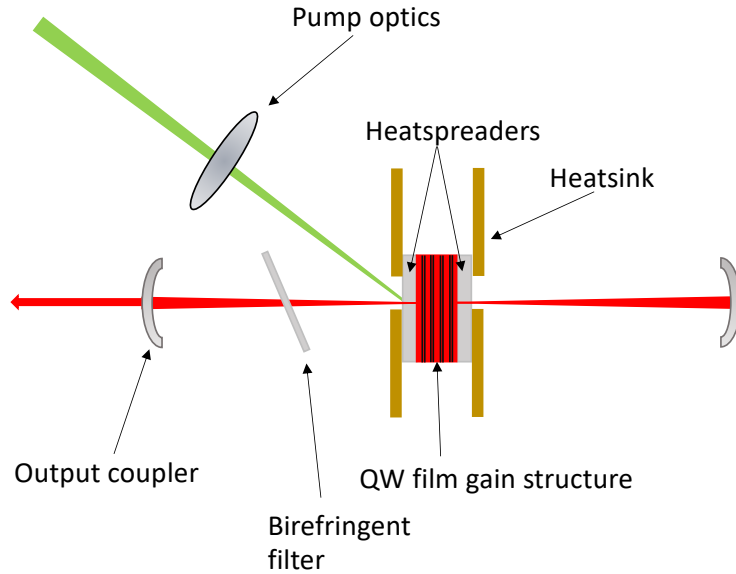


**Figure 10.** The typical DBR-free VECSEL geometry. Not to scale. A resonantly spaced multi-QW gain membrane has a diamond (or SiC) heatspreader bonded to each emission surface and is situated at the focal point of an external resonator. A birefringent filter is used for spectral tuning and the membrane is optically-pumped.

The first publications of DBR-free VECSEL operation were reports of theoretical calculations outlining the improved performance, in terms of output power and delayed thermal rollover onset of a QW gain membrane sandwiched between two diamonds, when compared to a standard VECSEL [43]. In this work high contrast gratings on diamond were proposed to enable pump recycling and to replace the DBR [43]. The first demonstrations of DBR-free VECSELs were at infra-red wavelengths, and used concentric and confocal resonators with optically-pumped QW gain membranes situated at the cavity focal point [42,44,45]. These lasers exhibited a tuning capability of up to 80 nm (centred at 1034 nm) and maximum CW output powers of 16 W at 1037 nm and 2.5 W at 1160 nm [42,44,45]. In 2016 the first visible DBR-free VECSEL was reported, with 595 mW maximum CW output power at 657 nm from an AlInGaP based DBR-free VECSEL [46].

Current work on DBR-free VECSELs is focussed on expanding the wavelength capability and output power of this platform (see Section 1.5.5). The intention of the development of the II-VI DBR-free VECSEL is to develop VECSEL technology which can be designed for fundamental emission at visible wavelengths from 500-600 nm, a challenging wavelength range for any semiconductor laser platform.



#### 1.5.4 VECSEL thermal management

As with all laser classes, the thermal management of VECSELs is essential for optimum performance. A temperature increase in the gain region increases the refractive index, decreases the bandgap of the gain structure layers, and reduces the magnitude of the material gain. Temperature increase red-shifts the sub-cavity resonance, resonant periodic gain (RPG) and material gain spectrum at different rates, reducing their spectral overlap (hence decreasing the modal gain) and causing thermal rollover, discussed further in Section 2.4.2 [47]. Maximum VECSEL output power is achieved when the sub-cavity resonance, material gain and RPG have an optimised spectral overlap. RPG and material gain are discussed further in Chapter 2. The goal of VECSEL thermal management is to ensure that pump-induced temperature rise is therefore minimized.

Full VECSEL structures can undergo substrate removal to form a “thin device”, see Fig. 11. left), resulting in a lower device thermal impedance. VECSELs can use high thermal conductivity ( $k$ ) heatspreaders such as diamond and silicon carbide to assist the removal of heat from the QW active region [34,47]. Highly transparent intracavity heatspreaders can be bonded onto the VECSEL surface, see Fig. 11, right), to give a low thermal impedance route for heat flow away from the pump spot. For thin device structures it is also common to bond a heatspreader between the gain structure and the heatsink to maximize heat flow through high  $k$  DBRs. Fig. 11 shows that in the thin device case the heat flows from the pumped active region and down through the DBR to the heatsink. With the intracavity heatspreader, the heat flows radially from the pumped active region and then either up through the brass/copper mount lid or back through the DBR and substrate.

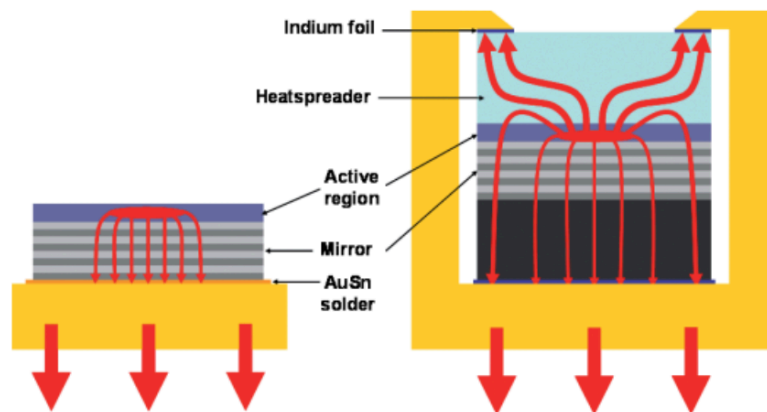


**Figure 11.** The heat flow is shown with red arrows for; **left**) a thin device without a heatspreader or substrate and **right**) an as-grown VECSEL with an intracavity heatspreader. Taken from [31].

DBR-free VECSELS undergo a full substrate removal to produce a gain membrane which is then bonded onto an optically transparent, high  $k$  intracavity heatspreader which acts as the new substrate. DBR-free VECSELS can operate in single or double sided heatspreader geometries, with the latter offering superior heat extraction [44]. Fig. 12 shows the active region temperature rises for single and dual heatspreader, thin device and DBR-free VECSELS [42]. DBR-free VECSELS with double heatspreaders offer the best thermal management and are therefore interesting lasers to investigate due to their potential for resistance to thermal rollover.

Assuming similar heat flow characteristics and thermal load to the III-V DBR-free VECSELS [42], either a single or double heatspreader geometry should be sufficient for II-VI DBR-free VECSEL operation demonstration. The II-VI materials may out-perform III-V equivalents in the single heatspreader geometry due to the slow change in bandgap with temperature of the ZnCdSe/ZnCdMgSe QWs [14]. The PL peak position of ZnCdSe/ZnCdMgSe QWs shifts at 0.11 nm/K, three to four times slower than near-infrared-emitting III-V materials [14,31]. It should be noted, however, that the  $C_{11}$  and  $C_{12}$  stiffness constants for ZnCdMgSe are smaller than typical III-V materials ( $C_{11} = 76.2$  GPa and  $C_{12} = 48.6$  GPa for  $Zn_{0.3}Cd_{0.28}Mg_{0.42}Se$ , in comparison to  $C_{11} = 390$  GPa and  $C_{12} = 145$  GPa for GaN [1,4]) and so clamping a double diamond bonded membrane under high stress to enforce thermal contact may damage the material or alter its strain state [1].

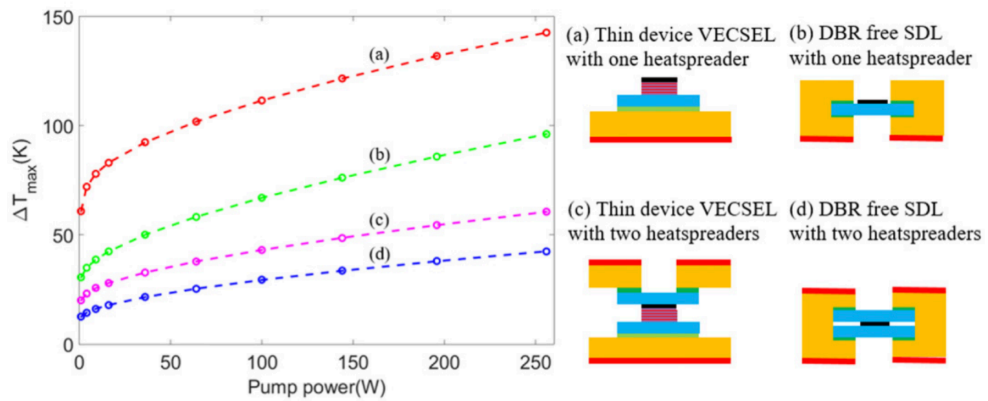


**Figure 12.** Temperature rise in the QW active region for increasing pump power and constant power intensity for four key VECSEL architectures: a) thin device with DBR heatspreader, b) DBR-free with single sided heatspreader, c) thin device with intracavity and DBR heatspreaders, and d) DBR-free with double sided heatspreaders. The QWs are InGaAs with GaAsP barriers with a GaAs/AlAs DBR. Taken from [42].

### *1.5.5 VECSEL spectral coverage to date*

Given the excellent thermal management possible with the DBR-free VECSEL, it is important to assess the spectral region in which a II-VI DBR-free VECSEL would operate, to further highlight its novelty. VECSEL technology spans a large section of the electromagnetic (EM) spectrum; from the deep UV at 224 nm via intracavity frequency tripling [48]; direct emission from the visible [49] to the far infrared at 5000 nm [50]; and even into the THz regime using intracavity difference frequency generation [51]. Fig. 13 shows continuous wave (CW) VECSEL spectral coverage up to 1800 nm, where maximum CW output powers range over seven orders of magnitude [37,42,55–64,44,65–74,45,75–81,46,48,49,52–54]. It should also be noted that GaSb-based VECSELs have high performance in the mid-infrared with in-well and barrier pumping [82,83].

Fig. 13 clearly demonstrates the lack of fundamental emission at shorter visible wavelengths below the red. The semiconductor ‘green gap’ spans from 540 nm to 580 nm and cannot be targeted with current III-V VECSEL technology, without using non-linear frequency conversion [84]. Although InGaN based devices can potentially demonstrate ‘green gap’ operation, the efficiency drop-off with increased QW size limits the progress of GaN based devices at longer visible wavelengths (green to red) [85]. In-well pumped InGaN-based VECSELs operating at 440 nm have been demonstrated using pulsed pumping at 384 nm from an N<sub>2</sub>-laser, however the output power is measured in arbitrary units and so its performance cannot be compared to the other VECSELs in Fig. 13 [86]. The wide bandgap of II-VI materials will allow for CW VECSEL fundamental emission in the visible spectrum and in the ‘green gap’.

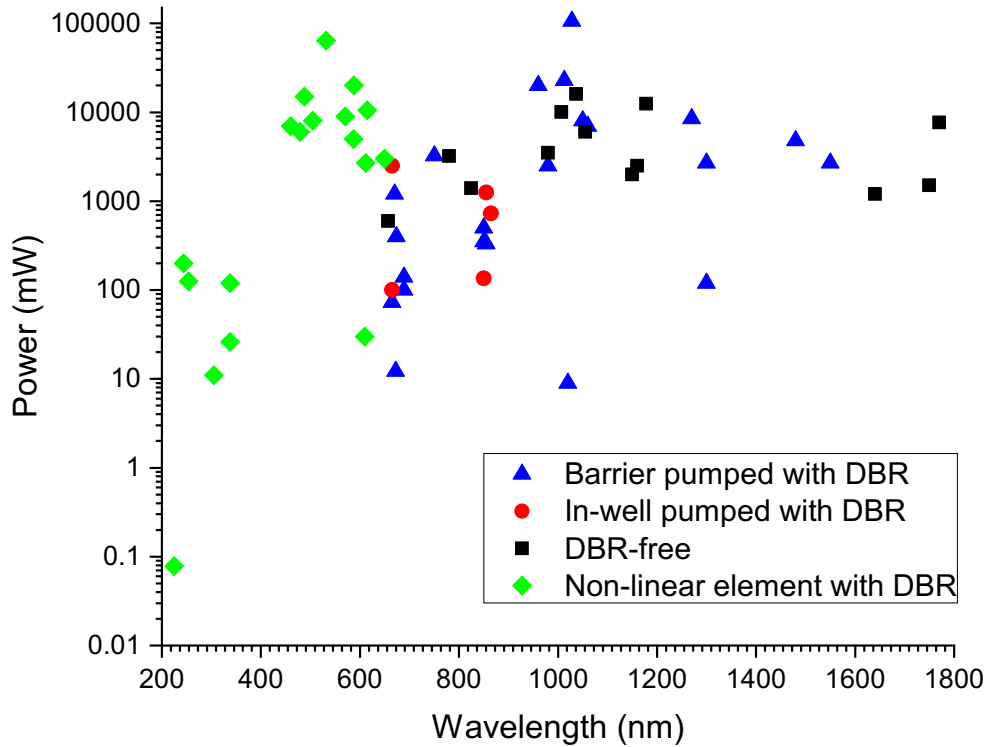


**Figure 13.** Maximum CW operating power against wavelength for a variety of III-V VECSEL subclasses found in literature. Blue triangles show barrier pumped VECSELs with a DBR (the typical design), red circles show in-well pumped VECSELs with a DBR, black squares show DBR-free VECSELs and green diamonds show VECSELs with intracavity nonlinear conversion. The references are: barrier pumped with DBR [40,49,61,63–65,87–91,53–60], in-well pumped [55,66–68], DBR-free [42,44,95–97,45,46,69–71,92–94] and non-linear frequency converted [48,72,81,98,99,73–80].

### 1.6 ‘Green gap’ laser sources

A variety of laser systems have been developed to attempt to bridge the gap between GaN-based technology on the blue side of visible and standard III-V materials on the red/IR side. Dye lasers offer high gain and tunable operation [100,101] and have been demonstrated to operate throughout the green gap [102]. Dye lasers are complex, often use toxic liquids and the gain media chemically degrades over short time periods [103]. Raman lasers have been reported to operate at 573 nm using diamond [104] and output at 560 nm has been achieved using frequency conversion of a Raman fibre amplifier [105]. These sources are not CW due to the high intensity pump pulses required for the Raman amplification. Perovskite based distributed feedback lasers have been reported which operate around 550 nm, however these are low power [106]. Fibre lasers based on Ho:Fluorozirconate have reported mW-level

emission at 549 nm however these lasers required 646.9 nm pumping from another ring dye laser [107].

Praseodymium lasers show promise for efficient laser emission across the visible spectrum due to the high cross-section laser transitions at 520 nm, 550 nm, 605 nm, 640 nm, 695 nm and 720 nm of the  $\text{Pr}^{3+}$  ion, see Fig. 14 [108,109].  $\text{Pr}^{3+}$  can be used to dope  $\text{YLiF}_4$  and  $\text{LiLuF}_4$  and is suited to visible optical pumping with absorptions lines at 444 nm, 469 nm and 479 nm [108,109]. Although initial GaN diode-pumped Pr lasers exhibited low power [110], these results were pump-power-limited and hundreds of mW of output power across the visible transitions is now possible with diode-pumping [108], and W-scale visible output power is achievable using frequency doubled optically-pumped semiconductor lasers (OPSL) as the pump source [109]. Other rare-earth ions, such as terbium,  $\text{Tb}^{3+}$  (see Fig. 14), show promise for use in green gap laser sources, with  $\text{Tb}^{3+}:\text{LiLuF}_4$  (Tb:LLF) and  $\text{Tb}^{3+}:\text{CaF}$  (Tb:CaF) lasers demonstrating green gap laser operation with up to a hundred mW of output power and several nm of tunability for the LLF case and up to 10 nm of tunability with a few mW of output power in the CaF case [111]. The material gain spectrum of II-VI QWs can be designed to cover many of the visible, discrete laser transitions discussed here and shows the potential for the II-VI VECSEL technology to simplify the design of CW, visible lasers.

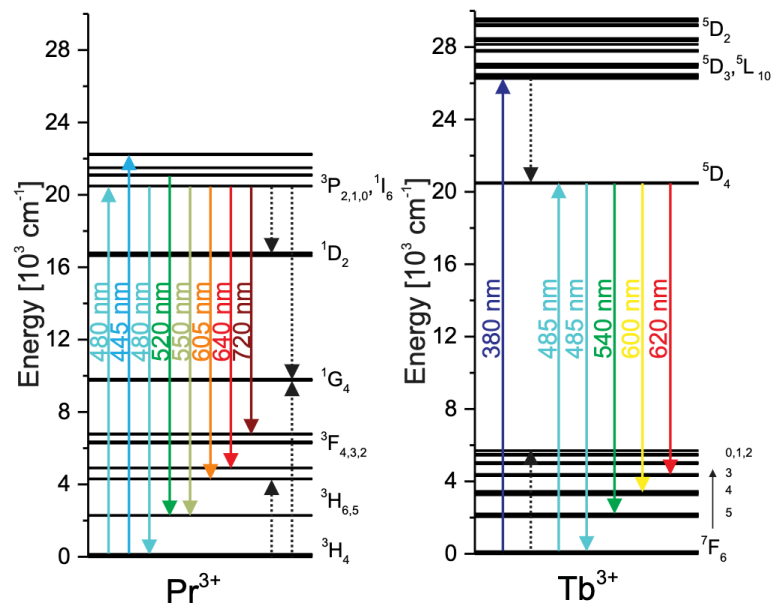


**Figure 14.** The visible energy level transitions within the  $\text{Pr}^{3+}$  and  $\text{Tb}^{3+}$  ions. Upward arrows show absorptions and downward arrows show emissions. Taken from [109].

## 1.7 Lasers from II-VI semiconductor structures

### 1.7.1 II-VI DBRs

A possible route to develop a II-VI VECSEL would be to construct a II-VI gain mirror comprised of a II-VI QW active region and a DBR. In this sub-section the previous work on the optimization of II-VI-based DBRs is summarized. Fig. 15 shows the refractive index as a function of composition for some common II-VI materials which are used within the DBRs discussed in this section.

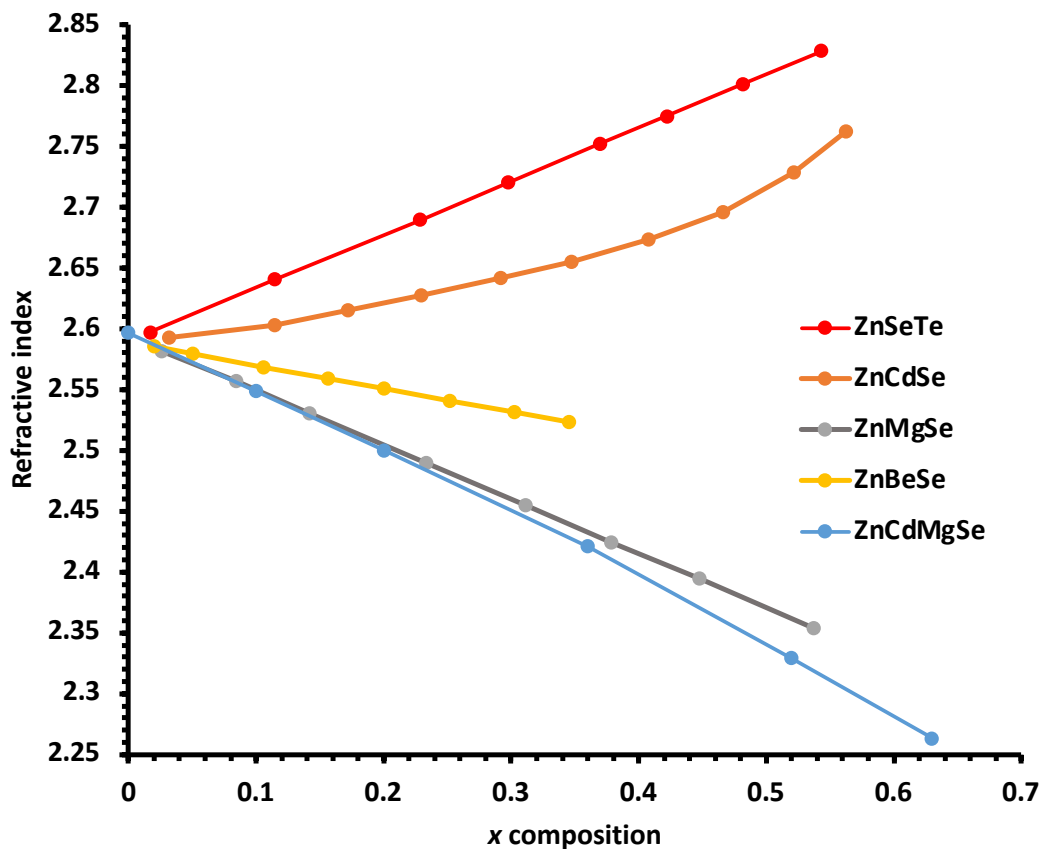


**Figure 15.** The refractive index of II-VI materials used in DBR development as a function of composition,  $x$ . The materials plotted are  $(\text{Zn}_{0.48}\text{Cd}_{0.52})_{1-x}\text{Mg}_x\text{Se}$ ,  $\text{ZnSe}_{1-x}\text{Te}_x$ ,  $\text{Zn}_{1-x}\text{Cd}_x\text{Se}$ ,  $\text{Zn}_{1-x}\text{Mg}_x\text{Se}$ , and  $\text{Zn}_{1-x}\text{Be}_x\text{Se}$  [112,113].

$\text{ZnMgSe}/\text{ZnSeTe}$  on GaAs has a refractive index contrast of  $\Delta n = 0.35$  [113], which should yield a high reflectivity DBR with a wide stop-band. The growth of  $\text{ZnMgSe}$  requires a high Se flux, whereas  $\text{ZnSeTe}$  requires a low Se flux, and this flux change gives a challenging growth which limits the structure to 10 periods [113]. A solution to the Se flux requirements for growing  $\text{ZnMgSe}$  and  $\text{ZnSeTe}$  together is to use two different Se sources in the MBE growth chamber [113]. The  $\text{ZnMgSe}/\text{ZnSeTe}$  DBR from reference [113] was reported to have a wide stop-band and a peak reflectivity of 85 % at 750 nm, which was shifted from the

designed centre of 633 nm due to Se flux changing difficulties during the growth [113]. ZnMgSe/ZnCdSe on GaAs DBRs have a lower refractive index contrast than ZnMgSe/ZnSeTe, with  $\Delta n = 0.20$ , however the growth is easier, allowing 20 periods to be grown and resulting in a DBR with up to 98 % reflectivity at 616 nm [113]. Using the ZnCdMgSe material system it is possible to obtain  $\Delta n = 0.285$  (not experimentally measured [114]) with different quaternary compositions, whilst being lattice-matched to InP substrates. ZnCdMgSe DBRs have been reported with 84.2 % reflectivity centred at 559 nm for a 20 period  $\text{Zn}_{0.42}\text{Cd}_{0.38}\text{Mg}_{0.2}\text{Se} / \text{Zn}_{0.24}\text{Cd}_{0.17}\text{Mg}_{0.59}\text{Se}$  structure and 98 % at 595 nm for a 30 period  $\text{Mg}_{0.1}(\text{Zn}_{0.48}\text{Cd}_{0.52})_{0.9}\text{Se} / \text{Mg}_{0.6}(\text{Zn}_{0.48}\text{Cd}_{0.52})_{0.4}\text{Se}$  structure [112,114]. It has been predicted that up to 40 periods would give the 99.9 % reflectivity required for a VECSEL gain mirror structure [112,114]. Growing a II-VI VECSEL structure with a 40 period DBR would be challenging as this would require the growth of QWs before or after the large DBR, which would likely generate stacking faults in such a large structure, introducing unwanted defects.

In order to avoid the use of hygroscopic Mg containing materials, II-VI DBRs have been developed using the binaries CdSe/ZnTe on GaAs:Si substrates and have a 95 % reflectance centred at 923 nm [115]. The development of II-VI microcavities for VCSELs and exciton-polariton experiments in II-VI materials has motivated further work on II-VI DBRs. CdZnMnTe/CdZnMgTe QWs have been grown within a 21 and 22 period  $\text{Cd}_{0.61}\text{Zn}_{0.06}\text{Mg}_{0.33}\text{Te} / \text{Cd}_{0.84}\text{Zn}_{0.08}\text{Mg}_{0.08}\text{Te}$  DBR microcavity [16]. In order to increase the refractive index contrast, whilst maintaining lattice-matching to GaAs, a DBR has been reported with a high refractive index layer of ZnMgSSe and a low refractive index layer comprised of a MgS/ZnCdSe superlattice [116]. The superlattice technique, see Fig. 16, enables a refractive index contrast of  $\Delta n = 0.43$  to be achieved, yielding 99 % reflectivity with a 40 nm stop-band for 21 period DBRs centred at 430 nm and 460 nm [116]. For longer wavelengths, a DBR grown on GaAs:Si substrates, using 20 periods of  $\text{Cd}_{0.86}\text{Zn}_{0.14}\text{Te}$  as a high refractive index layer and a superlattice of 20 layers of  $\text{Cd}_{0.86}\text{Zn}_{0.14}\text{Te}/\text{MgTe}$  as the low refractive index layer has demonstrated 95 % reflectivity centred at 900 nm, with a 70 nm stop-band and a calculated  $\Delta n = 0.34$  [117]. The high reflectivities and wide stop-bands achieved using the superlattice technique show great promise for use in II-VI microcavities and lasers, with the disadvantages that they are time consuming to grow and have poor thermal conductivity. The development of II-VI DBRs on GaAs and InP substrates is promising for the growing II-VI laser structures on both of these common substrates.

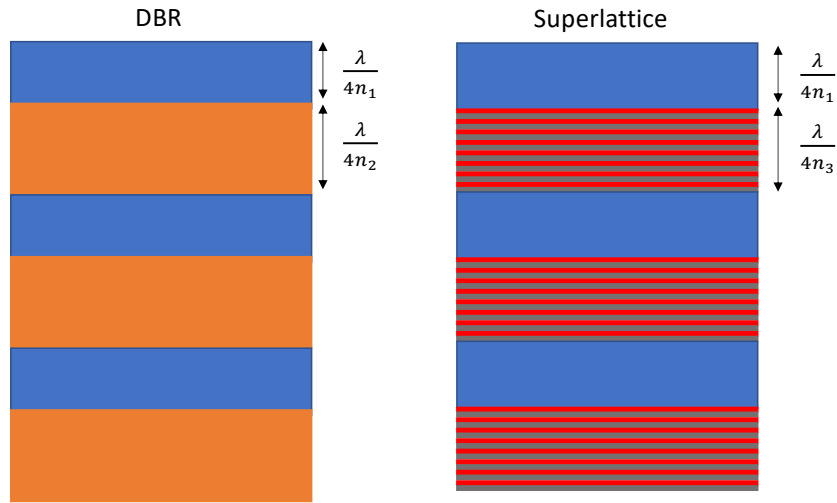


**Figure 16.** The DBR is typically of a stack of quarter-wavelength thick repeating units of refractive index  $n_1$  and  $n_2$ . For the superlattice DBR one (or both) of the quarter wavelength repeating units is a superlattice with a mean refractive index  $n_3$ , depending on its components. The superior performance of the II-VI superlattice arises as  $|n_1 - n_3| > |n_1 - n_2|$ .

### 1.7.2 'Green gap', quantum dot lasers

The II-VI material system has already been applied to build green gap devices based on quantum dots. CdZnSe/ZnS–CdSe/ZnS quantum dots (QDs) give 460 nm or 530 nm laser emission, depending on composition, with pulsed pumping [118,119]. Composition graded CdSe/Cd<sub>x</sub>Zn<sub>1-x</sub>Se QDs output 575 nm and 618 nm laser emission with pulsed pumping [119,120]. CdSe/ZnCdS QDs in a distributed feedback (DFB) cavity output 460 nm, 575nm and 610 nm laser emission with pulsed pumping [119,121]. These lasers have a low threshold of around tens to hundreds of  $\mu\text{Jcm}^{-2}$ , a high quantum confinement and a high quantum efficiency, but their small size reduces their directionality [119].

### 1.7.3 Electron-beam-pumped and optically-pumped II-VI lasers

The developments in the epitaxy of wide-bandgap II-VI materials has encouraged their development into novel laser sources, particularly to target wavelengths unobtainable to III-V technology. This sub-section discusses work on electron-beam-pumped and optically-pumped II-VI lasers, which are intended to tackle the challenge of the lack of effective and long-lasting p-type materials that has limited the optoelectronic development of II-VI semiconductors.

The very first optically-pumped, II-VI semiconductor laser was reported by G Stillman *et al*, and described multimode (690 nm to 700 nm) and single mode (689 nm) laser operation from a 2- $\mu\text{m}$ -thick, single crystal piece of CdSe, pumped from the edge facet of a GaAsP junction



laser [122]. Another method of injecting charge carriers into the QWs is to use electron beam pumping. Initial work on electron-beam-pumped, II-VI, graded-index separate-confinement heterostructures (GRINSCH) has reported multimode laser emission at 514 nm, 496/497 nm, 478.4 nm and 505.4 nm depending on the Cd concentration of the ZnCdSe QWs and at temperatures between 83 and 113 K [123,124]. A limitation of this work is the requirement for cryogenic temperatures and the high level of vacuum, which is not ideal for targeting compact, efficient, green gap laser operation.

Progress has been made on the development of II-VI VCSELs, starting with pulsed operation of ZnCdSe/ZnSe structures at 488 nm with temperatures of 30 K [125], and room temperature operation at 496 nm under pulsed optical-pumping [126]. Room temperature operation was shown from an all II-VI VCSEL consisting of a (MgS/ZnCdSe)/ZnSSe superlattice DBR, with spectral narrowing and threshold behaviour demonstrated, however this was still with pulsed optical-pumping [127]. These works were greatly improved upon with the reporting of high power electron-beam-pumped continuous wave (CW) VECSELs (called eVCSELs [128]) with Watt-level output powers at room temperature at 462 nm and 530 nm, again using the superlattice DBR [128].

Optically-pumped, room temperature laser operation has been reported of ZnSSe/ZnCdSe vertically-emitting lasers at around 505 nm with a threshold of 110 kW/cm<sup>2</sup> [129]. ZnSe/CdS type II QWs with ZnSSe barriers have been used to form optically-pumped microcavities, where HfO<sub>2</sub>/SiO<sub>2</sub> dielectric mirrors have been deposited onto the upper and lower faces of the II-VI gain structure to form a VCSEL resonator. When optically-pumped in a pulsed regime with 2 kW peak power, this II-VI structure has demonstrated pulsed, room temperature, laser operation with Watt-level output powers at 514 nm [17]. The low slope efficiency reported for the ZnSe/CdS/ZnSSe structure in a HfO<sub>2</sub>/SiO<sub>2</sub> resonator is attributed to parasitic amplified spontaneous emission [17]. ZnSe/CdS type II QWs with ZnSSe barriers have been used to construct a VECSEL with a HfO<sub>2</sub>/SiO<sub>2</sub> dielectric mirror deposited on one side of the gain structure and then an AR coating deposited on the other following substrate removal [130]. This structure was glued onto sapphire and combined with an external cavity to yield 750 mW pulsed output power at 496.5 nm, with around 60 W peak power pulsed pumping with a N<sub>2</sub> laser [130].

Edge-emitting laser oscillation at 497 nm, 540 nm and 604 nm has been demonstrated with the optical-pumping of ZnCdSe QWs with ZnCdMgSe barriers grown on InP substrates [8],

and amplified spontaneous emission has been observed with ZnCdSe/ZnCdMgSe MQWs grown on ZnCdMgSe DBRs [114]. Epitaxial lift off (ELO) techniques have also allowed II-VI MQW films to be used for colour conversion of 450 nm GaN micro-LEDs to 540 nm [9] and such films may be applied for usage in DBR-free SDLs, as has been demonstrated successfully with III-V semiconductors [42,44–46,69–71,83].

Fig. 17 summarizes the demonstrated II-VI laser systems discussed in this sub-section and further emphasizes the novelty in developing a CW, “green-gap” VECSEL. The II-VI material system has demonstrated that it can be applied to build various classes of visible semiconductor laser. By applying this material system in the VECSEL geometry, an extremely useful visible laser system could be developed.

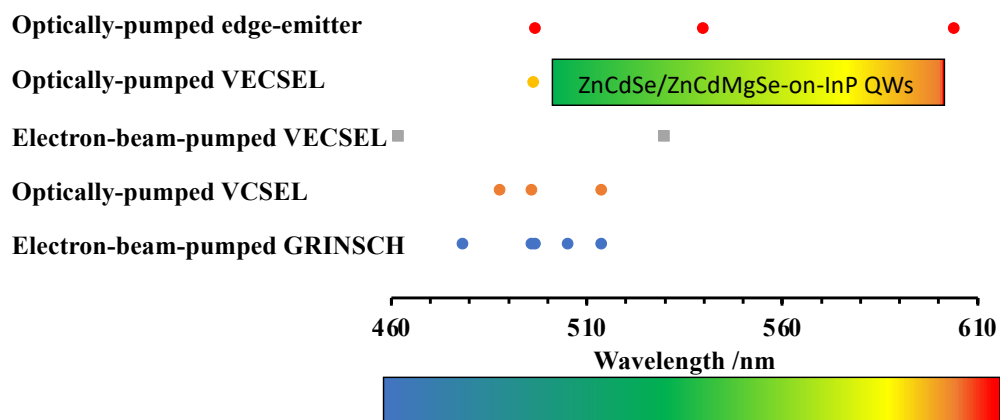


**Figure 17.** The spectral coverage of optical and electron-beam-pumped II-VI lasers in the GRINSCH, VCSEL, edge-emitter and VECSEL format. Circular and square markers represent pulsed and CW lasers respectively. The potential operating wavelength range of a ZnCdSe/ZnCdMgSe-on-InP-based VECSEL is shown.

### 1.8 Potential applications of visible, II-VI VECSELs

The power scaling, diffraction limited beam quality, narrow linewidth operation and wavelength versatility of the VECSEL platform suit it to a variety of applications. Quantum technology requires lasers with tunability and narrow linewidths for spectroscopic and atomic trapping/cooling applications [30,39,40]. Frequency-doubled VECSELs have been designed to target Na transitions for guide stars [72,131], and II-VI VECSELs could enable efficient targeting of atomic transitions of Na, Yb and Ba [30]. Visible wavelength organic dye lasers have a variety of medical applications [132], for which specifically designed II-VI VECSELs could be well-suited due to their reduced size, weight, input power and cost. An example of

this could be that a II-VI VECSEL could be used to produce a yellow laser for use in ophthalmology and treating vascular skin lesions [12].

VECSELs currently generate deep UV light through the conversion of infra-red wavelengths to visible wavelengths, and then to the deep UV via two frequency-doubling (second harmonic generation) steps or a less efficient frequency-tripling of visible light [48,133]. A single frequency-doubling step, of the green intracavity oscillating electric field in an InGaN-diode-pumped II-VI VECSEL, see Fig. 18, will allow for the efficient generation of coherent, tuneable, narrow linewidth, deep UV light.

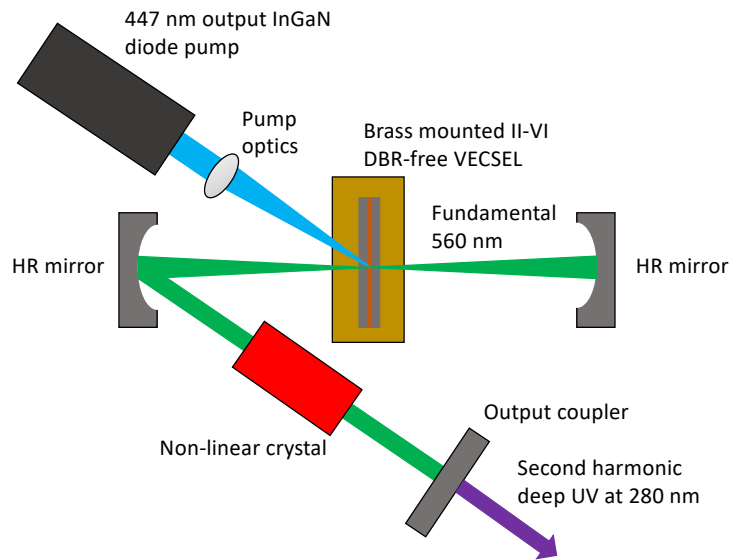


**Figure 18.** An example II-VI VECSEL application, in which the low noise, fundamental emission at 560 nm from an InGaN-diode-pumped, II-VI DBR-free VECSEL is efficiently frequency-doubled to the deep UV with an intracavity nonlinear crystal.

A ZnCdSSe monolithic nanosheet has previously been used to demonstrate simultaneous red, green and blue (RGB) laser emission, the so called “white lasing” [134]. Although operating through a different geometry, this raises the interesting idea of developing white VECSELs, which utilize RGB II-VI QWs in a single DBR-free structure. Such a VECSEL could easily find applications in colour displays/projectors, visible communication and sensing [134].

### 1.9 Semiconductor processing for VECSEL technology

Semiconductor processing and microfabrication are covered in detail in Chapter 4; here the themes of release layers and transfer printing are briefly introduced. The development of DBR-free VECSELs (Section 1.5.3) and thin device VECSELs (Section 1.5.4) has highlighted the

importance of epitaxial lift-off (ELO) for VECSEL progress. Removing the VECSEL device from its original growth substrate allows for a final device to be built without the thermal impedance of the substrate and to be integrated with other non-native materials and devices. The current strategies for VECSEL ELO are limited to full substrate removal [14,57,94] and AlAs release layers [42,46]. Although these methodologies are well understood and work well, the heterogeneous integration research community have moved onto higher precision methods such as membrane suspension and transfer printing [135,136].

Using transfer printing to integrate micron-scale photonic components with non-native substrates is a major theme of research as it enables the high precision construction of devices which cannot be grown homoepitaxially [137]. Transfer printing uses specifically shaped viscoelastic polydimethylsiloxane (PDMS) stamps to pick up and subsequently deposit devices. The viscoelasticity of PDMS enables a variable force of adhesion between the stamp and the device to be achieved. Once pressed onto a target device, a fast stamp retraction will give the PDMS a stiff, high viscosity nature, which maximizes adhesive forces causing device pick up. The chosen device can then be relocated and pressed onto a chosen deposition site. A slow retraction of the PDMS gives the stamp a low viscosity behaviour and minimizes the adhesive forces, allowing device deposition. A simple outline of the transfer printing mechanism is shown in Fig. 19. Chapter 4 will outline the use of transfer printing in this project and report the transfer printing of III-V DBR-free VECSEL structures and II-VI membranes.

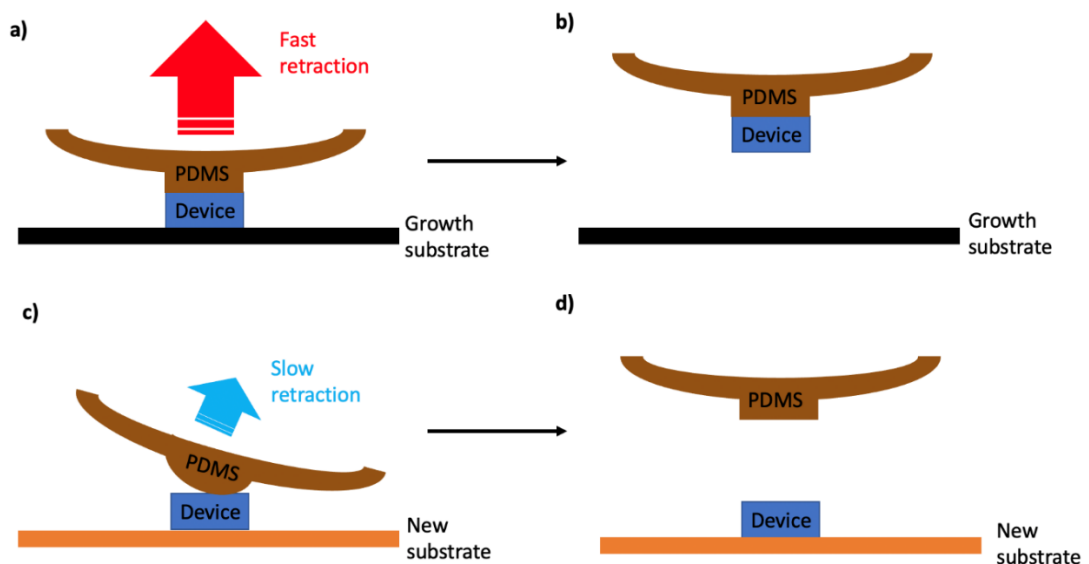


**Figure 19.** The PDMS transfer printing mechanism. Following contact and a fast retraction, **a)**, a device can be picked up, **b)** and held on the stamp. The device is pressed onto a new substrate and a slow retraction, **c)**, will lead to device deposition, **d)**.

## 1.10 Thesis outline

The overarching goal of this work is to use the novel ZnCdMgSe material system to increase VECSEL spectral coverage, whilst developing the techniques to enable the heterogeneous integration of VECSEL structures with non-native substrates.

The design of a VECSEL gain region from a novel material system requires accurate computational modelling, in order to determine the optimum structure for achieving the laser threshold. Chapter 2 outlines a series of numerical and analytical models which can be used to design a VECSEL structure, starting from the II-VI material parameters and the desired wavelength of operation. A simple model of QW gain is used to calculate the material gain parameter, which is used to inform a Kuznetsov analysis, which assists in the design of the II-VI VECSEL structures [138]. The methods presented in this chapter are useful for designing VECSELs of any material system. A design for a DBR-free II-VI VECSEL operating at 565 nm is presented.

The progress towards the II-VI DBR-free VECSEL is reported in Chapter 3, which will outline the development of the pump optics and resonator design for the II-VI VECSEL, along with the results of tests of II-VI QW gain films produced by the full substrate removal epitaxial lift-off method. The various generations of structures grown and tested will be presented and the future outlook of II-VI VECSELs is discussed.

Current, full substrate removal methods for the epitaxial lift-off of ZnCdMgSe-on-InP yield large but low-quality membranes. In Chapter 4 ambitious work is reported on developing the suspension method of under-etching the InP substrate from an array of pre-defined, 100  $\mu\text{m}$ -sided, square, ZnCdMgSe membranes and transfer-printing them onto a diamond heatspreader. Previous work on II-VI epitaxial lift-off is examined and is built upon in this work by using the substrate as an effective release layer for membranes. The transfer-printing of II-VI devices will enable their integration into novel photonic technologies. To assess whether this technique could be used for building a DBR-free VECSEL, the suspension and transfer printing method is also completed on GaInP/AlGaInP DBR-free VECSEL structures which have proven laser performance [139].

Chapter 5 focuses on the characterization and testing of ZnCdMgSe and GaInP/AlGaInP membranes on diamond, which were produced using the suspension and transfer printing methods developed and reported in Chapter 4. The characterization of the membranes focuses

on root-mean-square surface roughness, intensity-dependent photoluminescence, process-induced damage assessment and Raman spectroscopy. 100  $\mu\text{m}$ -square, GaInP/AlGaInP, DBR-free VECSEL membranes are tested in a VECSEL resonator however the laser threshold is not achieved. Initial work on using Raman mapping to characterize the GaInP/AlGaInP transfer-printed membranes is also presented as tool for assessing processing-induced strain changes.

Finally, Chapter 6 will present the conclusions from the project and discuss the future scope of this work and its potential future impact.

## References

1. S. L. Chuang, *Physics of Photonic Devices*, 2nd ed. (Wiley, 2009).
2. J. Singh, *Electronic and Optoelectronic Properties of Semiconductor Structures* (Cambridge University Press, 2003).
3. "Resources," <https://woodall.ece.ucdavis.edu/resources/>.
4. S. Adachi, *Properties of Semiconductor Alloys : Group-IV, III-V and II-VI Semiconductors* (Wiley, 2009).
5. W. Faschinger and J. Nürnberger, "Green II–VI light emitting diodes with long lifetime on InP substrate," *Appl. Phys. Lett.* **77**(2), 187–189 (2000).
6. T. Klein, S. Klembt, V. I. Kozlovsky, A. Zheng, M. D. Tiberi, and C. Kruse, "High-power green and blue electron-beam pumped surface-emitting lasers using dielectric and epitaxial distributed Bragg reflectors," *J. Appl. Phys.* **117**(11), (2015).
7. J. De Jesus, T. A. Garcia, S. Dhomkar, A. Ravikumar, C. Gmachl, G. Chen, A. Shen, D. Ferizovic, M. Muñoz, and M. C. Tamargo, "Characterization of the three-well active region of a quantum cascade laser using contactless electroreflectance," *J. Vac. Sci. Technol. B, Nanotechnol. Microelectron. Mater. Process. Meas. Phenom.* **31**(3), 03C134 (2013).
8. L. Zeng, B. X. Yang, A. Cavus, W. Lin, Y. Y. Luo, M. C. Tamargo, Y. Guo, and Y. C. Chen, "Red–green–blue photopumped lasing from ZnCdMgSe/ZnCdSe quantum well laser structures grown on InP," *Appl. Phys. Lett.* **72**(24), 3136 (1998).
9. J. M. M. Santos, B. E. Jones, P. J. Schlosser, S. Watson, J. Herrnsdorf, B. Guilhabert, J. J. D. McKendry, J. De Jesus, T. A. Garcia, M. C. Tamargo, A. E. Kelly, J. E. Hastie, N. Laurand, and M. D. Dawson, "Hybrid GaN LED with capillary-bonded II–VI MQW color-converting membrane for visible light communications," *Semicond. Sci. Technol.* **30**(3), 035012 (2015).

10. A. P. Ravikumar, A. Alfaro-Martinez, G. Chen, K. Zhao, M. C. Tamargo, C. F. Gmachl, and A. Shen, "ZnCdSe/ZnCdMgSe quantum well infrared photodetector," *Opt. Express* **20**(20), 22391 (2012).
11. A. Rajan, R. T. Moug, and K. A. Prior, "Growth and stability of zinc blende MgS on GaAs, GaP, and InP substrates," *Appl. Phys. Lett.* **102**(3), 032102 (2013).
12. S. V. Ivanov, S. V. Sorokin, and I. V. Sedova, "Molecular Beam Epitaxy of Wide Gap II–VI Laser Heterostructures," in *Molecular Beam Epitaxy* (Elsevier, 2018), pp. 571–595.
13. R. Moug, A. Alfaro-Martinez, L. Peng, T. Garcia, V. Deligiannakis, A. Shen, and M. Tamargo, "Selective etching of InGaAs/InP substrates from II-VI multilayer heterostructures," *Phys. status solidi* **9**(8–9), 1728–1731 (2012).
14. B. E. Jones, P. J. Schlosser, J. De Jesus, T. A. Garcia, M. C. Tamargo, and J. E. Hastie, "Processing and characterisation of II–VI ZnCdMgSe thin film gain structures," *Thin Solid Films* **590**, 84–89 (2015).
15. N. M. Eldose, J. Zhu, N. Mavridi, K. Prior, and R. T. Moug, "Stacking of ZnSe/ZnCdSe Multi-Quantum Wells on GaAs (100) by Epitaxial Lift-Off," *J. Electron. Mater.* **47**(8), 4366–4369 (2018).
16. B. Serebyński, M. Król, P. Starzyk, R. Mirek, M. Ściesiek, K. Sobczak, J. Borysiuk, D. Stephan, J.-G. Rousset, J. Szczytko, B. Piętka, and W. Pacuski, "(Cd,Zn,Mg)Te-based microcavity on MgTe sacrificial buffer: Growth, lift-off, and transmission studies of polaritons," *Phys. Rev. Mater.* **2**(4), 043406 (2018).
17. M.R. Butaev, V.I. Kozlovsky, and Ya.K. Skasyrsky, "Optically pumped semiconductor laser based on a type-II CdS/ZnSe heterostructure," *Quantum Electron.* **50**(7), 683–687 (2020).
18. S. V. Ivanov, S. V. Sorokin, and I. V. Sedova, "Molecular Beam Epitaxy of Wide Gap II–VI Laser Heterostructures," *Mol. Beam Ep.* 571–595 (2018).
19. E. Snoeks, L. Zhao, B. Yang, A. Cavus, L. Zeng, and M. C. Tamargo, "Structural quality of pseudomorphic Zn<sub>0.5</sub>Cd<sub>0.5</sub>Se layers grown on an InGaAs or InP buffer layer on (0 0 1)InP substrates," *J. Cryst. Growth* **179**(1–2), 83–92 (1997).
20. R. Pelzel, "A Comparison of MOVPE and MBE Growth Technologies for III-V Epitaxial Structures," in *CS MANTECH Conference* (2013), pp. 105–108.
21. A. P. Ravikumar, J. De Jesus, M. C. Tamargo, and C. F. Gmachl, "High performance, room temperature, broadband II-VI quantum cascade detector," *Appl. Phys. Lett.* **107**(14), 141105 (2015).
22. Paschotta R, "Modes, explained by RP Photonics Encyclopedia," <https://www.rp->

- photonics.com/modes.html.
23. Rüdiger Paschotta, "Four-level and Three-level Gain Media," [https://www.rp-photonics.com/four\\_level\\_and\\_three\\_level\\_gain\\_media.html](https://www.rp-photonics.com/four_level_and_three_level_gain_media.html).
  24. M. Kuznetsov, F. Hakimi, R. Sprague, and A. Mooradian, "Design and characteristics of high-power (>0.5-W CW) diode-pumped vertical-external-cavity surface-emitting semiconductor lasers with circular TEM<sub>00</sub> beams," *IEEE J. Sel. Top. Quantum Electron.* **5**(3), 561–573 (1999).
  25. P. W. Milonni and J. H. Eberly, *Laser Physics (2nd Edition)* (Wiley, 2010).
  26. K. Thyagarajan and Ajoy Ghatak, *Lasers*, 2nd edition (Springer, 2010).
  27. I. Melngailis, "Longitudinal injection-plasma laser of InSb," *Appl. Phys. Lett* **6**(3), (1965).
  28. H. Soda, K. Iga, C. Kitahara, and Y. Suematsu, "GaInAsP/InP Surface Emitting Injection Lasers," *Jpn. J. Appl. Phys.* **18**(12), 2329 (1979).
  29. R. Szweda, "VCSEL applications diversify as technology matures," *III-Vs Rev.* **19**(1), 34–38 (2006).
  30. M. Guina, A. Rantamäki, and A. Härkönen, "Optically pumped VECSELs: review of technology and progress," *J. Phys. D: Appl. Phys.* **50**(38), 383001 (2017).
  31. S. Calvez, J. E. Hastie, M. Guina, O. G. Okhotnikov, and M. D. Dawson, "Semiconductor disk lasers for the generation of visible and ultraviolet radiation," *Laser Photonics Rev.* **3**(5), 407–434 (2009).
  32. S. Illek, T. Albrecht, P. Brick, S. Lutgen, I. Pietzonka, M. Furitsch, W. Diehl, J. Luft, and K. Streubel, "Vertical-external-cavity surface-emitting laser with monolithically integrated pump lasers," *IEEE Photonics Technol. Lett.* **19**(24), 1952–1954 (2007).
  33. R. Paschotta, "Power scalability as a precise concept for the evaluation of laser architectures," arXiv:0711.3987 (2007).
  34. A. J. Kemp, G. J. Valentine, J.-M. Hopkins, J. E. Hastie, S. A. Smith, S. Calvez, M. D. Dawson, and D. Burns, "Thermal management in vertical-external-cavity surface-emitting lasers: finite-element analysis of a heatspreader approach," *IEEE J. Quantum Electron.* **41**(2), 148–155 (2005).
  35. R. Paschotta, "RP Photonics Encyclopedia - diffraction-limited beams, beam quality, Gaussian beams," [https://www.rp-photonics.com/diffraction\\_limited\\_beams.html](https://www.rp-photonics.com/diffraction_limited_beams.html).
  36. E. U. Rafailov, W. Sibbett, A. Mooradian, J. G. McInerney, H. Karlsson, S. Wang, and F. Laurell, "Efficient frequency doubling of a vertical-extended-cavity surface-emitting laser diode by use of a periodically poled KTP crystal," *Opt. Lett.* **28**(21), 2091 (2003).



37. J. E. Hastie, L. G. Morton, A. J. Kemp, M. D. Dawson, A. B. Krysa, and J. S. Roberts, "Tunable ultraviolet output from an intracavity frequency-doubled red vertical-external-cavity surface-emitting laser," *Appl. Phys. Lett.* **89**(6), 061114 (2006).
38. J. N. Tinsley, S. Bandarupally, J.-P. Penttinen, S. Manzoor, S. Ranta, L. Salvi, M. Guina, and N. Poli, "Watt-level blue light for precision spectroscopy, laser cooling and trapping of strontium and cadmium atoms," (2021).
39. P. H. Moriya, Y. Singh, K. Bongs, and J. E. Hastie, "Sub-kHz-linewidth VECSELs for cold atom experiments," *Opt. Express* **28**(11), 15943 (2020).
40. P. H. Moriya, R. Casula, G. A. Chappell, D. C. Parrotta, S. Ranta, H. Kahle, M. Guina, and J. E. Hastie, "InGaN-diode-pumped AlGaInP VECSEL with sub-kHz linewidth at 689 nm," *Opt. Express* **29**(3), (2021).
41. A. Garnache, A. Ouvrard, and D. Romanini, "Single-Frequency operation of External-Cavity VCSELs: Non-linear multimode temporal dynamics and quantum limit.," *Opt. Express* **15**(15), 9403 (2007).
42. Z. Yang, A. R. Albrecht, J. G. Cederberg, and M. Sheik-Bahae, "Optically pumped DBR-free semiconductor disk lasers," *Opt. Express* **23**(26), 33164 (2015).
43. V. Iakovlev, J. Walczak, M. Gębski, A. K. Sokół, M. Wasiak, P. Gallo, A. Sirbu, R. P. Sarzała, M. Dems, T. Czyszanowski, and E. Kapon, "Double-diamond high-contrast-gratings vertical external cavity surface emitting laser," *J. Phys. D: Appl. Phys.* **47**(6), 065104 (2014).
44. Z. Yang, A. R. Albrecht, J. G. Cederberg, and M. Sheik-Bahae, "DBR-free optically pumped semiconductor disk lasers," in *Vertical External Cavity Surface Emitting Lasers (VECSELs) V*, M. Guina, ed. (International Society for Optics and Photonics, 2015), **9349**, p. 934905.
45. Z. Yang, A. R. Albrecht, J. G. Cederberg, and M. Sheik-Bahae, "80 nm tunable DBR-free semiconductor disk laser," *Appl. Phys. Lett.* **109**(2), 022101 (2016).
46. H. Kahle, C. M. N. Mateo, U. Brauch, P. Tatar-Mathes, R. Bek, M. Jetter, T. Graf, and P. Michler, "Semiconductor membrane external-cavity surface-emitting laser (MECSEL)," *Optica* **3**(12), 1506 (2016).
47. O. G. Okhotnikov, *Semiconductor Disk Lasers: Physics and Technology* (Wiley-VCH, 2010).
48. J. M. Rodriguez-Garcia, D. Pabouf, and J. E. Hastie, "Tunable, CW Laser Emission at 225 nm via Intracavity Frequency Tripling in a Semiconductor Disk Laser," *IEEE J. Sel. Top. Quantum Electron.* **23**(6), 1–8 (2017).

49. J. E. Hastie, S. Calvez, M. D. Dawson, T. Leinonen, A. Laakso, J. Lyytikäinen, and M. Pessa, "High power CW red VECSEL with linearly polarized TEM<sub>00</sub> output beam," *Opt. Express* **13**(1), 77 (2005).
50. M. Rahim, F. Felder, M. Fill, D. Boye, and H. Zogg, "Lead chalcogenide VECSEL on Si emitting at 5 [micro sign]m," *Electron. Lett.* **44**(25), 1467 (2008).
51. M. Wichmann, M. Stein, A. Rahimi-Iman, S. W. Koch, and M. Koch, "Interferometric Characterization of a Semiconductor Disk Laser driven Terahertz Source," *J. Infrared, Millimeter, Terahertz Waves* **35**(6–7), 503–508 (2014).
52. A. Garnache, A. A. Kachanov, F. Stoeckel, and R. Houdré, "Diode-pumped broadband vertical-external-cavity surface-emitting semiconductor laser applied to high-sensitivity intracavity absorption spectroscopy," *J. Opt. Soc. Am. B* **17**(9), 1589 (2000).
53. A. J. Maclean, R. B. Birch, P. W. Roth, A. J. Kemp, and D. Burns, "Limits on efficiency and power scaling in semiconductor disk lasers with diamond heatspreaders," *J. Opt. Soc. Am. B* **26**(12), 2228 (2009).
54. T. Schwarzbäck, M. Eichfelder, W.-M. Schulz, R. Roßbach, M. Jetter, and P. Michler, "Short wavelength red-emitting AlGaInP-VECSEL exceeds 1.2 W continuous-wave output power," *Appl. Phys. B* **102**(4), 789–794 (2011).
55. C. M. N. Mateo, U. Brauch, T. Schwarzbäck, H. Kahle, M. Jetter, M. A. Ahmed, P. Michler, and T. Graf, "Enhanced efficiency of AlGaInP disk laser by in-well pumping," *Opt. Express* **23**(3), 2472 (2015).
56. E. J. Saarinen, A. Härkönen, S. Suomalainen, and O. G. Okhotnikov, "Power scalable semiconductor disk laser using multiple gain cavity," *Opt. Express* **14**(26), 12868 (2006).
57. B. Heinen, T.-L. Wang, M. Sparenberg, A. Weber, B. Kunert, J. Hader, S. W. Koch, J. V. Moloney, M. Koch, and W. Stolz, "106 W continuous-wave output power from vertical-external-cavity surface-emitting laser," *Electron. Lett.* **48**(9), 516 (2012).
58. S. T. Keller, A. Sirbu, V. Iakovlev, A. Caliman, A. Mereuta, and E. Kapon, "85 W VECSEL output at 1270 nm with conversion efficiency of 59 %," *Opt. Express* **23**(13), 17437 (2015).
59. J. E. Hastie, J.-M. Hopkins, S. Calvez, Chan Wook Jeon, D. Burns, R. Abram, E. Riis, A. I. Ferguson, and M. D. Dawson, "0.5-W single transverse-mode operation of an 850-nm diode-pumped surface-emitting semiconductor laser," *IEEE Photonics Technol. Lett.* **15**(7), 894–896 (2003).
60. J. E. Hastie, J.-M. Hopkins, C. W. Jeon, S. Calvez, D. Burns, M. D. Dawson, R.

- Abram, E. Riis, A. I. Ferguson, W. J. Alford, T. D. Raymond, and A. A. Allerman, "Microchip vertical external cavity surface emitting lasers," *Electron. Lett.* **39**(18), 1324 (2003).
61. S. A. Smith, J.-M. Hopkins, J. E. Hastie, D. Burns, S. Calvez, M. D. Dawson, T. Jouhti, J. Kontinnen, and M. Pessa, "Diamond-microchip GaInNAs vertical external-cavity surface-emitting laser operating CW at 1315 nm," *Electron. Lett.* **40**(15), 935 (2004).
  62. D. Pabœuf and J. E. Hastie, "Tunable narrow linewidth AlGaInP semiconductor disk laser for Sr atom cooling applications," *Appl. Opt.* **55**(19), 4980 (2016).
  63. B. Rudin, A. Rutz, M. Hoffmann, D. J. H. C. Maas, A.-R. Bellancourt, E. Gini, T. Südmeyer, and U. Keller, "Highly efficient optically pumped vertical-emitting semiconductor laser with more than 20 W average output power in a fundamental transverse mode," *Opt. Lett.* **33**(22), 2719 (2008).
  64. B. Cocquelin, D. Holleville, G. Lucas-Leclin, I. Sagnes, A. Garnache, M. Myara, and P. Georges, "Tunable single-frequency operation of a diode-pumped vertical external-cavity laser at the cesium D2 line," *Appl. Phys. B* **95**(2), 315–321 (2009).
  65. A. Smith, J. E. Hastie, A. J. Kemp, H. D. Foreman, M. D. Dawson, T. Leinonen, and M. Guina, "GaN diode-pumping of a red semiconductor disk laser," in *LEOS 2008 - 21st Annual Meeting of the IEEE Lasers and Electro-Optics Society* (IEEE, 2008), pp. 404–405.
  66. S.-S. Beyertt, U. Brauch, F. Demaria, N. Dhidah, A. Giesen, T. Kubler, S. Lorch, F. Rinaldi, and P. Unger, "Efficient Gallium–Arsenide Disk Laser," *IEEE J. Quantum Electron.* **43**(10), 869–875 (2007).
  67. C. M. N. Mateo, U. Brauch, H. Kahle, T. Schwarzbäck, M. Jetter, M. A. Ahmed, P. Michler, and T. Graf, "2.5 W continuous wave output at 665 nm from a multipass and quantum-well-pumped AlGaInP vertical-external-cavity surface-emitting laser," *Opt. Lett.* **41**(6), 1245 (2016).
  68. M. Schmid, S. Benchabane, F. Torabi-Goudarzi, R. Abram, A. I. Ferguson, and E. Riis, "Optical in-well pumping of a vertical-external-cavity surface-emitting laser," *Appl. Phys. Lett.* **84**(24), 4860–4862 (2004).
  69. Z. Yang, D. Follman, A. R. Albrecht, P. Heu, N. Giannini, G. D. Cole, and M. Sheik-Bahae, "16 W DBR-free membrane semiconductor disk laser with dual-SiC heatspreader," *Electron. Lett.* **54**(7), 430–432 (2018).
  70. A. Broda, A. Kuźmicz, G. Rychlik, K. Chmielewski, A. Wójcik-Jedlińska, I. Sankowska, K. Gołaszewska-Malec, K. Michalak, and J. Muszalski, "Highly efficient

- heat extraction by double diamond heat-spreaders applied to a vertical external cavity surface-emitting laser," *Opt. Quantum Electron.* **49**(9), 287 (2017).
71. S. Mirkhanov, A. H. Quarterman, H. Kahle, R. Bek, R. Pecoroni, C. J. C. Smyth, S. Vollmer, S. Swift, P. Michler, M. Jetter, and K. G. Wilcox, "DBR-free semiconductor disc laser on SiC heatspreader emitting 10.1 W at 1007 nm," *Electron. Lett.* **53**(23), 1537–1539 (2017).
  72. E. Kantola, T. Leinonen, S. Ranta, M. Tavast, and M. Guina, "High-efficiency 20 W yellow VECSEL," *Opt. Express* **22**(6), 6372 (2014).
  73. E. Kantola, T. Leinonen, J.-P. Penttinen, V.-M. Korpijärvi, and M. Guina, "615 nm GaInNAs VECSEL with output power above 10 W," *Opt. Express* **23**(16), 20280 (2015).
  74. D. Pabœuf, P. J. Schlosser, and J. E. Hastie, "Frequency stabilization of an ultraviolet semiconductor disk laser," *Opt. Lett.* **38**(10), 1736 (2013).
  75. Y. Kaneda, J. M. Yarborough, L. Li, N. Peyghambarian, L. Fan, C. Hessenius, M. Fallahi, J. Hader, J. V. Moloney, Y. Honda, M. Nishioka, Y. Shimizu, K. Miyazono, H. Shimatani, M. Yoshimura, Y. Mori, Y. Kitaoka, and T. Sasaki, "Continuous-wave all-solid-state 244 nm deep-ultraviolet laser source by fourth-harmonic generation of an optically pumped semiconductor laser using CsLiB<sub>6</sub>O<sub>10</sub> in an external resonator," *Opt. Lett.* **33**(15), 1705 (2008).
  76. J. Rautiainen, A. Härkönen, V.-M. Korpijärvi, J. Puustinen, L. Orsila, M. Guina, and O. Okhotnikov, "Red and UV Generation Using Frequency-Converted GaInNAs-Based Semiconductor Disk Laser," in *Conference on Lasers and Electro-Optics/International Quantum Electronics Conference* (OSA, 2009), p. CMRR7.
  77. A. Rantamäki, A. Sirbu, A. Mereuta, E. Kapon, and O. G. Okhotnikov, "3 W of 650 nm red emission by frequency doubling of wafer-fused semiconductor disk laser," *Opt. Express* **18**(21), 21645 (2010).
  78. M. Fallahi, Li Fan, Y. Kaneda, C. Hessenius, J. Hader, Hongbo Li, J. V. Moloney, B. Kunert, W. Stolz, S. W. Koch, J. Murray, and R. Bedford, "5-W Yellow Laser by Intracavity Frequency Doubling of High-Power Vertical-External-Cavity Surface-Emitting Laser," *IEEE Photonics Technol. Lett.* **20**(20), 1700–1702 (2008).
  79. J. Chilla, Q.-Z. Shu, H. Zhou, E. Weiss, M. Reed, and L. Spinelli, "Recent advances in optically pumped semiconductor lasers," in *Solid State Lasers XVI: Technology and Devices*, H. J. Hoffman, R. K. Shori, and N. Hodgson, eds. (International Society for Optics and Photonics, 2007), **6451**, p. 645109.
  80. E. Gerster, I. Ecker, S. Lorch, C. Hahn, S. Menzel, and P. Unger, "Orange-emitting

- frequency-doubled GaAsSb/GaAs semiconductor disk laser," *J. Appl. Phys.* **94**(12), 7397 (2003).
81. J. Rautiainen, A. Härkönen, V.-M. Korpijärvi, P. Tuomisto, M. Guina, and O. G. Okhotnikov, "2.7 W tunable orange-red GaInNAs semiconductor disk laser," *Opt. Express* **15**(26), 18345 (2007).
  82. N. Schulz, B. Rösener, R. Moser, M. Rattunde, C. Manz, K. Köhler, and J. Wagner, "An improved active region concept for highly efficient GaSb-based optically in-well pumped vertical-external-cavity surface-emitting lasers," *Appl. Phys. Lett.* **93**(18), 181113 (2008).
  83. J. Wagner, N. Schulz, M. Rattunde, C. Ritzenthaler, C. Manz, C. Wild, and K. Köhler, "Barrier- and in-well pumped GaSb-based 2.3  $\mu\text{m}$  VECSELs," *Phys. status solidi* **4**(5), 1597–1600 (2007).
  84. M. R. Krames, O. B. Shchekin, R. Mueller-Mach, G. O. Mueller, L. Zhou, G. Harbers, and M. G. Craford, "Status and Future of High-Power Light-Emitting Diodes for Solid-State Lighting," *J. Disp. Technol.* **3**(2), 160–175 (2007).
  85. S. V. Ivanov, S. V. Sorokin, and I. V. Sedova, "Molecular Beam Epitaxy of Wide Gap II–VI Laser Heterostructures," *Mol. Beam Ep.* 571–595 (2018).
  86. T. Wunderer, J. E. Northrup, Z. Yang, M. Teepe, A. Strittmatter, N. M. Johnson, P. Rotella, and M. Wraback, "In-well pumping of InGaN/GaN vertical-external-cavity surface-emitting lasers," *Appl. Phys. Lett.* **99**(20), 201109 (2011).
  87. A. Garnache, A. A. Kachanov, F. Stoeckel, and R. Houdré, "Diode-pumped broadband vertical-external-cavity surface-emitting semiconductor laser applied to high-sensitivity intracavity absorption spectroscopy," *J. Opt. Soc. Am. B* **17**(9), 1589 (2000).
  88. D. Pabœuf and J. E. Hastie, "Tunable narrow linewidth AlGaInP semiconductor disk laser for Sr atom cooling applications," *Appl. Opt.* **55**(19), 4980 (2016).
  89. F. Zhang, B. Heinen, M. Wichmann, C. Möller, B. Kunert, A. Rahimi-Iman, W. Stolz, and M. Koch, "A 23-watt single-frequency vertical-external-cavity surface-emitting laser," *Opt. Express* **22**(11), 12817 (2014).
  90. K. Nechay, H. Kahle, J. P. Penttinen, P. Rajala, A. Tukiainen, S. Ranta, and M. Guina, "AlGaAs/AlGaInP VECSELs with Direct Emission at 740-770 nm," *IEEE Photonics Technol. Lett.* **31**(15), 1245–1248 (2019).
  91. A. Sirbu, N. Volet, A. Mereuta, J. Lyytikäinen, J. Rautiainen, O. Okhotnikov, J. Walczak, M. Wasiak, T. Czystanowski, A. Caliman, Q. Zhu, V. Iakovlev, and E. Kapon, "Wafer-Fused Optically Pumped VECSELs Emitting in the 1310-nm and

- 1550-nm Wavebands," *Adv. Opt. Technol.* **2011**, (2011).
92. A. Broda, B. Jeżewski, I. Sankowska, M. Szymański, P. Hoser, and J. Muszalski, "Growth and characterization of InP-based 1750 nm emitting membrane external-cavity surface-emitting laser," *Appl. Phys. B Lasers Opt.* **126**(12), 192 (2020).
  93. A. Broda, B. Jeżewski, M. Szymanski, and J. Muszalski, "High-Power 1770 nm Emission of a Membrane External-Cavity Surface-Emitting Laser," *IEEE J. Quantum Electron.* **57**(1), 1–6 (2020).
  94. B. Jeżewski, A. Broda, I. Sankowska, A. Kuźmicz, K. Gołaszewska-Malec, K. Czuba, and J. Muszalski, "Membrane external-cavity surface-emitting laser emitting at 1640 nm," *Opt. Lett.* **45**(2), 539 (2020).
  95. H.-M. Phung, H. Kahle, J.-P. Penttinen, P. Rajala, S. Ranta, and M. Guina, "Power scaling and thermal lensing in 825 nm emitting membrane external-cavity surface-emitting lasers," *Opt. Lett.* **45**(2), 547 (2020).
  96. H. Kahle, J.-P. Penttinen, H.-M. Phung, P. Rajala, A. Tukiainen, S. Ranta, and M. Guina, "Comparison of single-side and double-side pumping of membrane external-cavity surface-emitting lasers," *Opt. Lett.* **44**(5), 1146 (2019).
  97. D. Priante, M. Zhang, A. R. Albrecht, R. Bek, M. Zimmer, C. Nguyen, D. Follman, G. D. Cole, and M. Sheik-Bahae, "Demonstration of a 20-W membrane-external-cavity surface-emitting laser for sodium guide star applications," *Electron. Lett.* **57**(8), 337–338 (2021).
  98. J. E. Hastie, L. G. Morton, A. J. Kemp, M. D. Dawson, A. B. Krysa, and J. S. Roberts, "Tunable ultraviolet output from an intracavity frequency-doubled red vertical-external-cavity surface-emitting laser," *Appl. Phys. Lett.* **89**(6), 61114 (2006).
  99. J. Paul, Y. Kaneda, T.-L. Wang, C. Lytle, J. V. Moloney, and R. J. Jones, "Doppler-free spectroscopy of mercury at 253.7 nm using a high-power, frequency-quadrupled, optically pumped external-cavity semiconductor laser," *Opt. Lett.* **36**(1), 61 (2011).
  100. T. W. Hänsch, *Repetitively Pulsed Tunable Dye Laser for High Resolution Spectroscopy* (n.d.).
  101. E. P. Ippen, C. V Shank, and A. Dienes, "Passive mode locking of the cw dye laser," *Appl. Phys. Lett* **21**, 348 (1972).
  102. L. E. Jusinski and C. A. Taatjes, "Efficient and stable operation of an Ar<sup>+</sup>-pumped continuous-wave ring laser from 505-560 nm using a coumarin laser dye," *Rev. Sci. Instrum.* **72**(6), 2837–2838 (2001).
  103. Rüdiger Paschotta, "RP Photonics Encyclopedia - dye lasers," <https://www.rp->

photonics.com/dye\_lasers.html.

104. R. P. Mildren and A. Sabella, "Highly efficient diamond Raman laser," *Opt. Lett.* **34**(18), 2811 (2009).
105. T. H. Runcorn, R. T. Murray, E. J. R. Kelleher, S. V. Popov, and J. R. Taylor, "Duration-tunable picosecond source at 560 nm with watt-level average power," *Opt. Lett.* **40**(13), 3085 (2015).
106. J. R. Harwell, G. L. Whitworth, G. A. Turnbull, and I. D. W. Samuel, "Green Perovskite Distributed Feedback Lasers," (n.d.).
107. D. S. Funk, S. B. Stevens, and J. G. Eden, "Excitation Spectra of the Green Ho: Fluorozirconate Glass Fiber Laser," *IEEE Photonics Technol. Lett.* **5**(2), 154–157 (1993).
108. A. Richter, E. Heumann, G. Huber, V. Ostroumov, W. Seelert, L. Esterowitz, R. Allen, M. Kruer, F. Bartoli, L. S. Goldberg, H. P. Jenssen, A. Linz, and V. O. Nicolai, "Power scaling of semiconductor laser pumped Praseodymium-lasers," *Opt. Express*, Vol. 15, Issue 8, pp. 5172-5178 **15**(8), 5172–5178 (2007).
109. C. Kränkel, D. T. Marzahl, F. Moglia, G. Huber, and P. W. Metz, "Out of the blue: semiconductor laser pumped visible rare-earth doped lasers," *Laser Photonics Rev.* **10**(4), 548–568 (2016).
110. A. Richter, E. Heumann, E. Osiac, G. Huber, W. Seelert, and A. Diening, "Diode pumping of a continuous-wave  $\text{Pr}^{3+}$ -doped  $\text{LiYF}_4$  laser," *Opt. Lett.* Vol. 29, Issue 22, pp. 2638-2640 **29**(22), 2638–2640 (2004).
111. C. Kränkel, D.-T. Marzahl, G. Huber, and P. W. Metz, "Performance and wavelength tuning of green emitting terbium lasers," *Opt. Express*, Vol. 25, Issue 5, pp. 5716-5724 **25**(5), 5716–5724 (2017).
112. T. Morita, H. Shinbo, T. Nagano, I. Nomura, A. Kikuchi, and K. Kishino, "Refractive index measurements of  $\text{MgZnCdSe}$  II–VI compound semiconductors grown on InP substrates and fabrications of 500–600 nm range  $\text{MgZnCdSe}$  distributed Bragg reflectors," *J. Appl. Phys.* **81**(11), 7575 (1998).
113. F. C. Peiris, S. Lee, U. Bindley, and J. K. Furdyna, " $\text{ZnMgSe}/\text{ZnCdSe}$  and  $\text{ZnMgSe}/\text{ZnSeTe}$  distributed Bragg reflectors grown by molecular beam epitaxy," *J. Appl. Phys.* **86**(2), 719–724 (1999).
114. J. De Jesus, T. A. Garcia, V. Kartazaev, B. E. Jones, P. J. Schlosser, S. K. Gayen, J. E. Hastie, and M. C. Tamargo, "Growth and characterization of  $\text{ZnCdMgSe}$ -based green light emitters and distributed Bragg reflectors towards II-VI based semiconductor disk lasers," *Phys. status solidi* **212**(2), 382–389 (2015).

115. K. E. Połczyńska, K. Sobczak, and W. Pacuski, "Distributed Bragg reflector made of CdSe and ZnTe," *Superlattices Microstruct.* **139**, 106422 (2020).
116. S. Klembt, H. Dartsch, M. Anastasescu, M. Gartner, and C. Kruse, "High-reflectivity II-VI-based distributed Bragg reflectors for the blue-violet spectral range," *Appl. Phys. Lett.* **99**(15), 151101 (2011).
117. J. G. Rousset, J. Kobak, T. Slupinski, T. Jakubczyk, P. Stawicki, E. Janik, M. Tokarczyk, G. Kowalski, M. Nawrocki, and W. Pacuski, "MBE growth and characterization of a II-VI distributed Bragg reflector and microcavity lattice-matched to MgTe," *J. Cryst. Growth* **378**, 266–269 (2013).
118. Y. Gao, G. Yu, Y. Wang, C. Dang, T. C. Sum, H. Sun, and H. V. Demir, "Green Stimulated Emission Boosted by Nonradiative Resonant Energy Transfer from Blue Quantum Dots," *J. Phys. Chem. Lett.* **7**(14), 2772–2778 (2016).
119. X. Zhuang, Y. Ouyang, X. Wang, and A. Pan, "Multicolor Semiconductor Lasers," *Adv. Opt. Mater.* **7**(17), 1900071 (2019).
120. J. Lim, Y. S. Park, and V. I. Klimov, "Optical gain in colloidal quantum dots achieved with direct-current electrical pumping," *Nat. Mater.* **17**(1), 42–49 (2017).
121. K. Roh, C. Dang, J. Lee, S. Chen, J. S. Steckel, S. Coe-Sullivan, A. Nurmikko, J. S. Steckel, J. Ho, C. Hamilton, C. Breen, W. Liu, P. Allen, J. Xi, S. Coe-Sullivan, K. S. Cho, E. K. Lee, W. J. Joo, E. Jang, T. H. Kim, S. J. Lee, S. J. Kwon, J. Y. Han, B. K. Kim, B. L. Choi, J. M. Kim, C. Dang, J. Lee, Y. Zhang, J. Han, A. Nurmikko, S. Mashford, M. Stevenson, Z. Popovic, Z. Q. Zhou, J. Steckel, V. Bulovic, M. Bawendi, and P. T. Kazlas, "Surface-emitting red, green, and blue colloidal quantum dot distributed feedback lasers," *Opt. Express*, Vol. 22, Issue 15, pp. 18800-18806 **22**(15), 18800–18806 (2014).
122. G. E. Stillman, M. D. Sirkis, J. A. Rossi, M. R. Johnson, and N. Holonyak, "Volume excitation of an ultrathin single-mode CdSe laser," *Appl. Phys. Lett.* **9**(7), 268 (1966).
123. D. Hervé, R. Accomo, E. Molva, L. Vanzetti, J. J. Paggel, L. Sorba, and A. Franciosi, "Microgun-pumped blue lasers," *Appl. Phys. Lett.* **67**, 2144 (1995).
124. D. Hervé, E. Molva, L. Vanzetti, L. Sorba, and A. Franciosi, "Microgun-pumped blue and blue-green lasers," *Electron. Lett.* **31**(6), 459–461 (1995).
125. P. D. Floyd, J. L. Merz, H. Luo, J. K. Furdyna, T. Yokogawa, and Y. Yamada, "Optically pumped CdZnSe/ZnSe blue-green vertical cavity surface emitting lasers," *Cite as Appl. Phys. Lett* **66**, 2929 (1995).
126. H. Jeon, V. Kozlov, P. Kelkar, A. V. Nurmikko, C. -C. Chu, D. C. Grillo, J. Han, G.



- C. Hua, and R. L. Gunshor, "Room-temperature optically pumped blue-green vertical cavity surface emitting laser," *Appl. Phys. Lett.* **67**(12), 1668–1670 (1995).
127. C. Kruse, S. M. Ulrich, G. Alexe, E. Roventa, R. Kröger, B. Brendemühl, P. Michler, J. Gutowski, and D. Hommel, "Green monolithic II–VI vertical-cavity surface-emitting laser operating at room temperature," *Phys. status solidi* **241**(3), 731–738 (2004).
128. T. Klein, S. Klembt, V. I. Kozlovsky, A. Zheng, M. D. Tiberi, and C. Kruse, "High-power green and blue electron-beam pumped surface-emitting lasers using dielectric and epitaxial distributed Bragg reflectors," *J. Appl. Phys.* **117**(11), 113106 (2015).
129. T. V. Shubina, S. V. Ivanov, A. A. Toropov, G. N. Aliev, M. G. Tkatchman, S. V. Sorokin, N. D. Il'inskaya, and P. S. Kop'ev, "Extremely thick ZnCdSe/ZnSSe multiple quantum-well heterostructures for optoelectronic applications," *J. Cryst. Growth* **184–185**, 596–600 (1998).
130. M. R. Butaev, V. I. Kozlovsky, and Y. K. Skasyrsky, "Nanosecond semiconductor disk laser emitting at 496.5 nm," *Quantum Electron.* **50**(10), 895–899 (2020).
131. D. Priante, M. Zhang, A. R. Albrecht, R. Bek, M. Zimmer, C. Nguyen, D. Follman, G. D. Cole, and M. Sheik-Bahae, "Demonstration of a 20-W membrane-external-cavity surface-emitting laser for sodium guide star applications," *Electron. Lett.* ell2.12008 (2021).
132. F J Duarte, "Tunable organic lasers and organic molecules for medicine," in *Organic Lasers and Organic Photonics* (2018).
133. M. Yakshin, C. Prasad, C. Hessenius, and M. Fallahi, *A Compact, Efficient, Optically Pumped Deep UV Laser* (2019).
134. F. Fan, S. Turkdogan, Z. Liu, D. Shelhammer, and C. Z. Ning, "A monolithic white laser," *Nat. Nanotechnol.* **10**(9), 796–803 (2015).
135. A. J. Trindade, B. Guilhabert, D. Massoubre, D. Zhu, N. Laurand, E. Gu, I. M. Watson, C. J. Humphreys, and M. D. Dawson, "Nanoscale-accuracy transfer printing of ultra-thin AlInGaN light-emitting diodes onto mechanically flexible substrates," *Appl. Phys. Lett.* **103**(25), 253302 (2013).
136. S. Park, Y. Xiong, R. Kim, P. Elvikis, M. Meitl, D. Kim, J. Wu, J. Yoon, C. Yu, Z. Liu, Y. Huang, K. Hwang, P. Ferreira, X. Li, K. Choquette, and J. A. Rogers, "Deformable, Printed Assemblies of Inorganic Light-emitting Diodes," *Science* (80-). **325**(August), 977–982 (2009).
137. B. Corbett, R. Loi, W. Zhou, D. Liu, and Z. Ma, "Transfer print techniques for heterogeneous integration of photonic components," *Prog. Quantum Electron.* **52**, 1–

17 (2017).

138. M. Kuznetsov, F. Hakimi, R. Sprague, and A. Mooradian, "Design and characteristics of high-power ( $>0.5$ -W CW) diode-pumped vertical-external-cavity surface-emitting semiconductor lasers with circular TEM<sub>00</sub> beams," *IEEE J. Sel. Top. Quantum Electron.* **5**(3), 561–573 (1999).
139. B. E. Jones, "ZnCdMgSe and AlGaInP multi-quantum well films for colour conversion and optically-pumped visible lasers," (2015).

## 2. ZnCdSe/ZnCdMgSe quantum well gain structure design

### Chapter overview

In this chapter the key design concepts for DBR-free VECSELS are introduced and applied to the ZnCdMgSe-on-InP material system. One of the difficulties in developing a ZnCdMgSe-based VECSEL is that useful material parameters are not well characterized in comparison to the III-V material systems usually applied in VECSELS. A thorough literature review and a simple Vegard interpolation scheme are used to determine the necessary physical parameters, which are tabulated in Section 2.1 for the ZnSe, CdSe and MgSe binaries along with  $\text{Zn}_{0.48}\text{Cd}_{0.52}\text{Se}$  and  $\text{Zn}_{0.3}\text{Cd}_{0.28}\text{Mg}_{0.42}\text{Se}$ . The II-VI quantum wells (QWs), for the gain medium, are designed by numerically solving the time-independent Schrödinger equation for a  $\text{Zn}_{0.48}\text{Cd}_{0.52}\text{Se}$  QW within a finite potential barrier of  $\text{Zn}_{0.3}\text{Cd}_{0.28}\text{Mg}_{0.42}\text{Se}$ , targeting an  $n = 1$  recombination with transition energy equivalent to a photon wavelength of 565 nm (see Section 2.2). The use of compressive strain in VECSEL threshold reduction is discussed (see Section 2.2.4) and the use of the optical transfer matrix to model the electric fields within VECSEL structures is introduced (Section 2.3). The key principles behind designing resonant VECSEL gain structures are reviewed (see Section 2.4). To determine the ideal number of QWs required for the II-VI DBR-free VECSEL, the material gain, accounting for transition broadening, is calculated and used to determine the material gain parameter,  $g_0$ , and the transparency carrier density,  $N_0$ , of a 4 nm  $\text{Zn}_{0.48}\text{Cd}_{0.52}\text{Se}/\text{Zn}_{0.3}\text{Cd}_{0.28}\text{Mg}_{0.42}\text{Se}$  QW unit, for use in a Kuznetsov analysis [1] (see Section 2.5). These were determined to be  $g_0 = 3428 \text{ cm}^{-1}$  and  $N_0 = 5.908 \times 10^{24} \text{ m}^{-3}$  at 565 nm, and  $g_0 = 8386 \text{ cm}^{-1}$  and  $N_0 = 5.864 \times 10^{24} \text{ m}^{-3}$  at the gain peak, at around 560 nm. The concepts and models introduced during the chapter are used to design a II-VI DBR-free VECSEL gain structure, presented in Section 2.6.

### 2.1 The properties of II-VI semiconductors for QW modelling

In this work  $\text{Zn}_x\text{Cd}_{1-x}\text{Se}$  and  $\text{Zn}_x\text{Cd}_y\text{Mg}_{1-x-y}\text{Se}$ , lattice-matched to (0 0 1) InP, are used to construct II-VI QWs, where  $x$  and  $y$  are the relative compositions of an element in the ternary or quaternary compound [2]. MBE-grown ZnCdSe and ZnCdMgSe possess a zincblende structure (see Fig. 1).

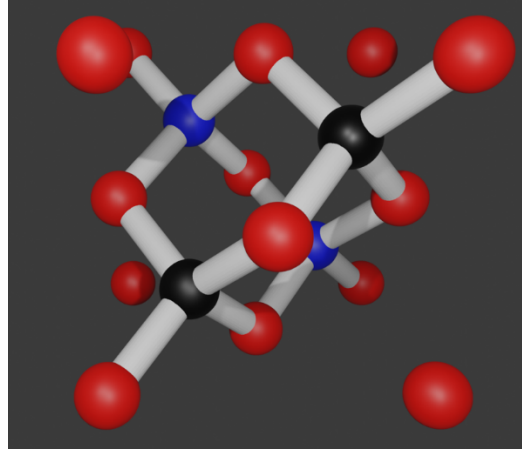


**Figure 1.** The structure of the unit cell of ZnCdSe, where Se atoms are red, Cd atoms are black, Zn atoms are blue, and the bonds are shown in white. Here it is assumed that the group II atoms are evenly distributed throughout the ZnCdSe layers.

The properties of the ternary and quaternary materials are deduced by composition weighted linear interpolation of the properties of the II-VI binaries, called Vegard's law. Most of the properties of the II-VI binaries are readily available and compiled into useful datasheets [3] and so other properties can be deduced using the interpolation scheme given by:

$$P(\text{Zn}_x\text{Cd}_{1-x}\text{Se}) = xP(\text{ZnSe}) + (1 - x)P(\text{CdSe}) \quad (1)$$

and

$$P(\text{Zn}_x\text{Cd}_y\text{Mg}_{1-x-y}\text{Se}) = xP(\text{ZnSe}) + yP(\text{CdSe}) + (1 - x - y)P(\text{MgSe}), \quad (2)$$

where  $P()$  denotes a property of the material given as an argument inside the parentheses. This linear interpolation scheme will yield properties with a small error, due to deviations from linearity which can be modelled with the addition of a composition dependent quadratic term, a "bowing parameter", into (1) and (2). The bowing parameters are not known for every physical property of the II-VI material system due to the lack of experimental measurements.

For the II-VI QW and VECSEL modelling, equations (1) and (2) are used to determine the properties of effective electron mass, effective hole mass, lattice constant, hydrostatic deformation potential, shear deformation potential and the  $C_{11}$  and  $C_{12}$  stiffness constants from the properties of the II-VI binaries (MgSe, CdSe and ZnSe). These important parameters, amongst others used in this work, are summarized for the binaries, along with the InP-lattice-matched  $\text{Zn}_{0.48}\text{Cd}_{0.52}\text{Se}$  and  $\text{Zn}_{0.3}\text{Cd}_{0.28}\text{Mg}_{0.42}\text{Se}$  in Table 1a and Table 1b.

**Table 1a.** Summary of the II-VI parameters used in the modelling of the QW gain structures in this thesis – Part 1.

Property	ZnSe	CdSe	MgSe	Zn <sub>0.48</sub> Cd <sub>0.52</sub> Se	Zn <sub>0.3</sub> Cd <sub>0.28</sub> Mg <sub>0.42</sub> Se	Comments	References
Conduction band offset ratio	N/A			ZnCdSe/ZnCdMgSe QW is 0.8		Very large and enables deep QWs to form.	[4–8]
Lattice constant /nm	0.56692	0.6077	0.591	0.588	0.588	Vergard interpolation for ZnCdSe and ZnCdMgSe.	[9]
Electron mass / m <sub>0</sub>	0.145	0.119	0.2	0.131	0.161	Vergard interpolation for ZnCdSe and ZnCdMgSe.	[3,10,11]
Hole mass / m <sub>0</sub>	0.52	0.45	0.78	0.484	0.61	Vergard interpolation for ZnCdSe and ZnCdMgSe.	[3,10,12]
Bandgap / eV (at room temperature)	2.7	1.658	3.61	2.089 2.091 (including strain)	2.790 2.792 (including strain)	Vergard interpolation for ZnCdSe and ZnCdMgSe. Shift due to strain from InP substrate calculated.	[3,9]
Temperature dependence of the bandgap	$\alpha = 0.73$ $meVK^{-1}$ $\beta = 295 K$	$\alpha = 0.696$ $meVK^{-1}$ $\beta = 281 K$	N/A	$-4.5 \cdot 10^{-4}$ eV/K	Not modelled	No data for MgSe.	[3,13]
Refractive index	Not used			2.72	2.39	From similar material compositions in ref [2].	[2]
Shear deformation potential /eV	-1.14	-0.8	-1.39	-0.96	-1.15	Vergard interpolation for ZnCdSe and ZnCdMgSe.	[3,10,11]

**Table 1b.** Summary of the II-VI parameters used in the modelling of the QW gain structures in this thesis – Part 2.

Property	ZnSe	CdSe	MgSe	Zn <sub>0.48</sub> Cd <sub>0.52</sub> Se	Zn <sub>0.3</sub> Cd <sub>0.28</sub> Mg <sub>0.42</sub> Se	Comments	References
Hydrostatic deformation potential /eV	-5.1	-3.664	-4.2	-4.35	-4.32	Vergard interpolation for ZnCdSe and ZnCdMgSe.	[3,10]
Elastic stiffness constant, C <sub>11</sub> /10 <sup>11</sup> dyn/cm <sup>2</sup>	8.57	6.67	7.58	7.58	7.62	Vergard interpolation for ZnCdSe and ZnCdMgSe.	[10]
Elastic stiffness constant, C <sub>12</sub> /10 <sup>11</sup> dyn/cm <sup>2</sup>	5.07	4.63	4.86	4.84	4.86	Vergard interpolation for ZnCdSe and ZnCdMgSe.	[10]
Monomolecular recombination coefficient, A /s <sup>-1</sup>	7.3 × 10 <sup>7</sup>			N/A		Dependent on material quality.	[14]
Bimolecular recombination coefficient, B /m <sup>3</sup> s <sup>-1</sup>	2.8 × 10 <sup>-16</sup>			N/A		Dependent on material quality. Converted from cm <sup>2</sup> s <sup>-1</sup> to m <sup>3</sup> s <sup>-1</sup> by multiplication of the QW thickness.	[14]
Auger recombination coefficient, C /m <sup>6</sup> s <sup>-1</sup>	6 × 10 <sup>-42</sup>					Dependent on material quality. Order of magnitude estimate from InGaAs/GaAsP VECSELs.	
E <sub>p</sub> /eV	19.5			N/A		Taken from literature.	[15,16]
γ /meV	10			N/A		Based on a similar model in literature for ZnCdSe QWs.	[13]

## 2.2 QW design: quantum confinement, strain, temperature and bandgap engineering

### 2.2.1 Schrödinger's equation and solving for the finite potential QW

In this section the design of the individual QWs for the II-VI VECSEL gain structure is discussed. VECSELs use optical pumping to reach a population inverted state. Pump light is absorbed by the gain structure QW barriers, generating electron-hole pairs which diffuse through the gain structure due to Brownian motion and Coulomb repulsion, and are captured by the QWs. The captured charge carriers lose energy non-radiatively through phonon scattering, relaxing to the ground,  $n = 1$ , state of the QW. The ground state recombination occurs between electrons and holes in the  $n = 1$  energy level through spontaneous emission or stimulated emission.

The time-independent Schrödinger equation (TISE) is used to calculate the energy levels of the finite potential QW [17], with the QW depths for electrons and holes given by the conduction and valence band offsets, respectively, of the bandgap difference of the QW and the barrier material. Only the  $n = 1$  and  $n = 2$  energy levels of the conduction and heavy hole valence bands are calculated in this work, as the majority of the electron/hole population will exist within the  $n = 1$  sub-band under the operating conditions of VECSELs, and TE gain and compressive strain are favoured for VECSEL operation [18] (discussed further in Section 2.2.4). Fig. 2 shows the basic energy band diagram of the QW model used within this project, with a ZnCdSe QW layer confined by ZnCdMgSe barriers.

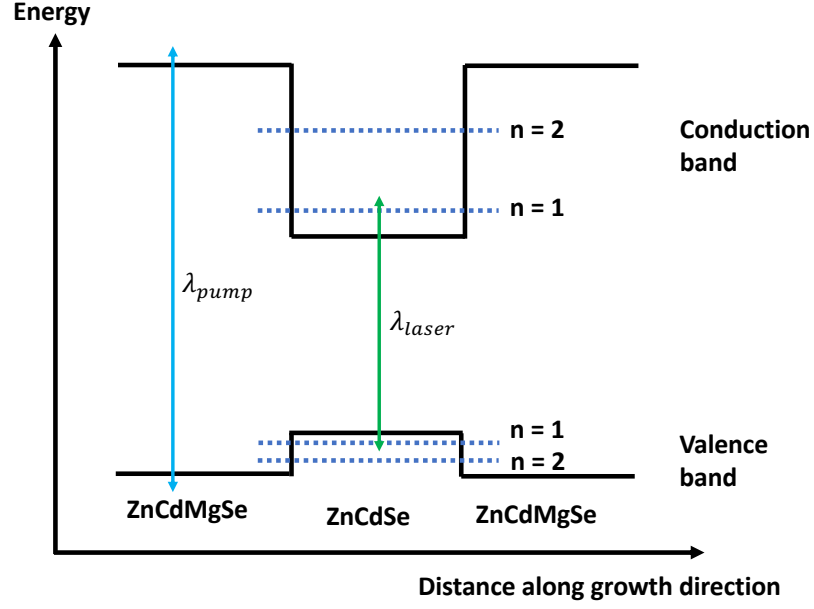


**Figure 2.** QW band structure model used for all calculations. A ZnCdSe QW is confined by ZnCdMgSe barriers. The  $n = 1$  and  $n = 2$  levels are marked on, not to scale, and the pump absorption and laser transitions are shown as the blue and green arrows, respectively.

The TISE for quantum confinement solely in the  $z$  Cartesian direction, assigned as the coordinate axis which is parallel to the semiconductor growth direction and perpendicular to the plane of the semiconductor layers ( $x, y$ ), is given by

$$-\frac{\hbar^2}{2m^*} \frac{d^2\psi(z)}{dz^2} + V(z)\psi(z) = \psi(z)E, \quad (3)$$

where  $m^*$  is the effective electron or hole mass,  $\hbar$  is the reduced Planck constant,  $\psi$  is the quantum mechanical wavefunction of a charge carrier,  $V$  is the potential energy applied to the charge carrier and  $E$  is the quantized energy of a discrete quantum well energy level [17]. Inside the QW  $V(z) = 0$ , so the solution to the TISE is given by a normalized, parity-dependent, sinusoidal function. Outside of the QW, within the larger bandgap barriers,  $V(z) \neq 0$  and the charge carrier wavefunction has an exponentially decaying nature. The solutions for odd and even parity can be summarized as follows for a QW of thickness,  $L$ , centred on  $z = 0$  [17]:



$$\psi(z) = \begin{cases} C_1 \exp\left(K\left(z + \frac{L}{2}\right)\right) & z < -\frac{L}{2} \text{ Even parity in barrier} \\ C_2 \cos(kz) & -\frac{L}{2} \leq z \leq \frac{L}{2} \text{ Even parity in QW} \\ C_1 \exp\left(-K\left(z - \frac{L}{2}\right)\right) & z > \frac{L}{2} \text{ Even parity in barrier} \end{cases}, \quad (4)$$

and

$$\psi(z) = \begin{cases} -D_1 \exp\left(K\left(z + \frac{L}{2}\right)\right) & z < -\frac{L}{2} \text{ Odd parity in barrier} \\ D_2 \sin(kz) & -\frac{L}{2} \leq z \leq \frac{L}{2} \text{ Odd parity in QW} \\ D_1 \exp\left(-K\left(z - \frac{L}{2}\right)\right) & z > \frac{L}{2} \text{ Odd parity in barrier} \end{cases}, \quad (5)$$

where  $k = \sqrt{\frac{2m^*E}{\hbar^2}}$ ,  $K = \sqrt{\frac{2m^*(V-E)}{\hbar^2}}$ , and  $C_1$  and  $C_2$ , and  $D_1$  and  $D_2$ , are normalizing constants for the even and odd parity cases respectively [17]. The boundary conditions of the continuity of  $\psi\left(z = \pm \frac{L}{2}\right)$  and  $\frac{1}{m^*} \frac{d\psi(z)}{dz}\left(z = \pm \frac{L}{2}\right)$  at the QW boundaries and substituting in the correct effective masses of the charge carriers can be applied to yield the odd and even parity eigenvalue equations

$$\frac{m_{well}}{m_{barrier}} \frac{K}{k} = \begin{cases} -\cot\left(\frac{kL}{2}\right) & \text{Odd parity} \\ \tan\left(\frac{kL}{2}\right) & \text{Even parity} \end{cases}, \quad (6)$$

where  $m_{well}$  is the effective mass of a charge carrier in a QW and  $m_{barrier}$  is the effective mass of a charge carrier in the barriers [17]. Equation (6) cannot be solved analytically and hence numerical methods must be recruited. For this (6) must be rearranged into a function given by (7),

$$0 = f(E) = \begin{cases} \left( \sqrt{\frac{(V-E)}{E}} + \left(\frac{m_{barrier}}{m_{well}}\right)^{\frac{1}{2}} \cot\left(\sqrt{\frac{2m_{well}EL}{\hbar^2}} \frac{L}{2}\right) \right) & \text{Odd parity} \\ \left( \sqrt{\frac{(V-E)}{E}} - \left(\frac{m_{barrier}}{m_{well}}\right)^{\frac{1}{2}} \tan\left(\sqrt{\frac{2m_{well}EL}{\hbar^2}} \frac{L}{2}\right) \right) & \text{Even parity} \end{cases}, \quad (7)$$

where  $f(E)$  denotes the function to be minimized. The minimization of (7) will yield the values of  $E$  for which  $f(E) = 0$ , which are the eigenenergies of the QW energy levels. This process can be completed for electrons and holes within the conduction and valence bands respectively.

### 2.2.2 Designing a QW for a II-VI VECSEL

There is no specific target wavelength for this project - the main goal is a first demonstration - and so  $\sim 565$  nm is chosen as it represents a challenging wavelength for current semiconductor devices, being in the middle of the ‘green gap’.  $\text{Zn}_{0.48}\text{Cd}_{0.52}\text{Se}$  and  $\text{Zn}_{0.3}\text{Cd}_{0.28}\text{Mg}_{0.42}\text{Se}$  are the QW and barrier compositions respectively, to maintain lattice-matching with InP throughout the structure to give unstrained material which is ideal for ELO. Fig. 3 shows the wavelength corresponding to the calculated  $n = 1$  electron-hole recombination energy as a function of QW thickness. Using the calculation shown in Fig. 3, a 4 nm QW thickness is chosen for targeting 565 nm.

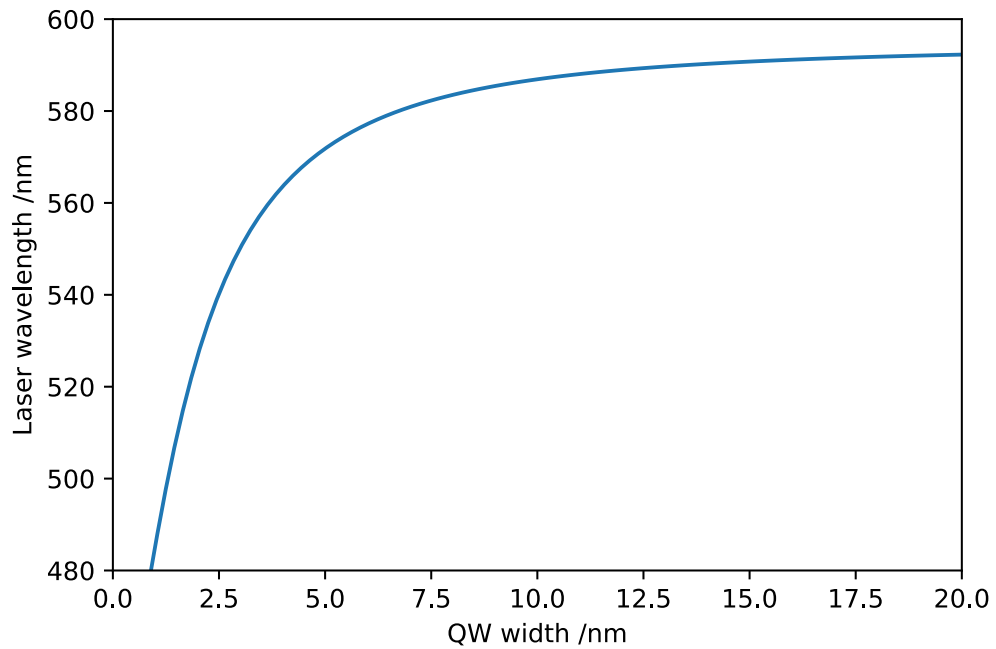


**Figure 3.** Wavelength of a photon emitted, at room temperature, due to an  $n = 1$  electron-hole recombination as a function of QW thickness for a  $\text{Zn}_{0.48}\text{Cd}_{0.52}\text{Se}$  QW with  $\text{Zn}_{0.3}\text{Cd}_{0.28}\text{Mg}_{0.42}\text{Se}$  barriers.

### 2.2.3 Thermal effects on the bandgap and lattice constant

The Varshni model [19] and empirically-derived relations can be used to quantify the bandgap energy shift with temperature. The Varshni model is given by [19]:

$$E_g(T) = E_g(0) - \frac{\alpha T^2}{\beta + T}, \quad (8)$$

where  $E_g(T)$  is the bandgap energy as a function of temperature,  $T$ ,  $E_g(0)$  is the bandgap at absolute zero, and  $\alpha$  and  $\beta$  are material specific constants. The Varshni model can give the temperature dependent bandgap of the II-VI binaries which, in conjunction with (1) or (2), can be linearly interpolated to give the  $Zn_xCd_{1-x}Se$  or  $Zn_xCd_yMg_{1-x-y}Se$  bandgap temperature dependence. Alternatively, empirically-derived laws can be used such as

$$E_g(x, T) = 2.7 - 1.31(1 - x) + 0.3(1 - x)^2 - 4.5 \cdot 10^{-4}(T - 300), \quad (9)$$

which gives the bandgap of  $Zn_xCd_{1-x}Se$  in eV as a function of temperature and ZnSe fraction [13]. From this empirical rule it can be found that  $\frac{dE_g}{dT} = -4.5 \cdot 10^{-4}$  eV/K.

Temperature impacts the optical length of VECSEL structures through direct changes in the lattice constant of semiconductor layers, quantified by the coefficient of thermal expansion,  $\alpha_{th} = \frac{1}{a} \left( \frac{\partial a}{\partial T} \right)$  where  $a$  is the lattice constant [10], and through changes in the refractive index, quantified by the thermo-optic coefficient  $\left( \frac{\partial n_r}{\partial T} \right)$ , where  $n_r$  is the refractive index), arising from material density changes with temperature.

## 2.2.4 Strain effects

### 2.2.4.1 Strain definition

Lattice constant differences in a layered semiconductor heterostructure result in the layers applying either compressive or tensile strain on each other. The strain of a material with a lattice constant  $a_L$ , on a substrate of lattice constant  $a_{sub}$ , is given by

$$\varepsilon = \frac{a_{sub} - a_L}{a_L}. \quad (10)$$

Compressive and tensile strain are defined by negative and positive  $\varepsilon$  respectively, see Fig. 4.

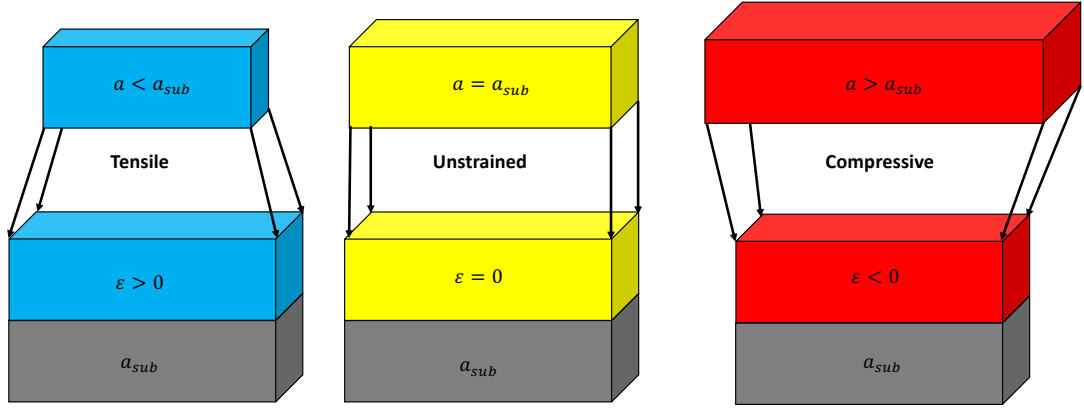


**Figure 4.** Schematic of tensile-strained, unstrained and compressively-strained layers on a substrate.

Small amounts of strain can be accommodated due to the elastic properties of a crystal structure, however once the thickness of the strained layer exceeds the Matthews-Blakeslee critical thickness it becomes energetically favourable for misfit defects to form [20]. In order to avoid this within multilayer heterostructures, the zero-stress method can be used to strain balance a structure. The zero stress condition between two layers is given by [21]:

$$0 = a_2 \epsilon_1 d_1 A_1 + a_1 \epsilon_2 d_2 A_2, \quad (11)$$

where  $d_n$  is the layer thickness, and  $A_n = \left( C_{11} + C_{12} - \frac{2C_{12}^2}{C_{11}} \right)$  where  $C_{11}$  and  $C_{12}$  are the stiffness constants of the layer denoted by  $n$ . For example, each compressively-strained QW can be paired with a carefully designed, tensile-strained, “strain compensation” layer resulting in zero in-plane stress for the overall structure [21].

Since the II-VI materials studied here have a cubic, zincblende structure the Cartesian coordinate system can be used to describe the strain directions, assigning the  $x$ ,  $y$ , and  $z$  directions as the  $[100]$ ,  $[010]$  and  $[001]$  directions respectively. The stress and strain of epitaxial layers can be related through the inverse of Hooke’s Law [22]

$$\epsilon_{ij} = S_{ijkl} \sigma_{kl}, \quad (12)$$

where  $\epsilon_{ij}$  and  $\sigma_{kl}$  are the strain and stress components respectively in the Cartesian coordinate system and  $S_{ijkl}$  is the compliance tensor. The II-VI and III-V binaries, of interest in this

project, have a zincblende structure with a cubic unit cell and biaxial strain ( $\sigma_{xx} = \sigma_{yy} = \sigma$ ,  $\sigma_{zz} = 0$  and  $\varepsilon_{xx} = \varepsilon_{yy} = \varepsilon$ ) and so we can simplify this to

$$\begin{pmatrix} \varepsilon \\ \varepsilon \\ \varepsilon_z \end{pmatrix} = \begin{pmatrix} S_{11} & S_{12} & S_{12} \\ S_{12} & S_{11} & S_{12} \\ S_{12} & S_{12} & S_{11} \end{pmatrix} \begin{pmatrix} \sigma \\ \sigma \\ 0 \end{pmatrix}. \quad (13)$$

From this the Poisson ratio, relating the change in the  $z$  strain from the biaxial strain can be found:

$$\frac{\varepsilon_z}{\varepsilon} = \frac{2S_{12}}{S_{11} + S_{12}}. \quad (14)$$

The  $S_{11}$  and  $S_{12}$  compliance components can be related to the stiffness constants via [22]:

$$S_{11} = \frac{C_{11} + C_{12}}{(C_{11} - C_{12})(C_{11} + 2C_{12})} \quad (15)$$

and

$$S_{12} = \frac{-C_{12}}{(C_{11} - C_{12})(C_{11} + 2C_{12})}. \quad (16)$$

Using (15) and (16), the strain in the  $z$ -direction from biaxial strain can be calculated as

$$\varepsilon_{zz} = -2 \frac{C_{12}}{C_{11}} \varepsilon. \quad (17)$$

#### 2.2.4.2 Strain effects on the bandgap, gain, laser threshold and the density of states of semiconductors

The shape of a semiconductor energy band in momentum space,  $E(\mathbf{k})$ , is given by

$$E(\mathbf{k}) = E_0 + \frac{\hbar^2 \mathbf{k}^2}{2m^*}, \quad (18)$$

where  $E_0$  is the band edge energy,  $\mathbf{k}$  is the electron wavevector and  $m^*$  is the effective mass of the charge carrier present in the band. Taking the second derivative of (18) with respect to  $\mathbf{k}$  shows the dependence of band curvature on the effective mass of charge carriers:

$$m^* = \frac{\hbar^2}{\left( \frac{d^2 E(\mathbf{k})}{d\mathbf{k}^2} \right)}. \quad (19)$$

The biaxial strain present in a semiconductor layer has three effects which are important for laser performance and these are shown schematically in Fig. 5, for the case of a QW. Quantum confinement removes the light and heavy hole degeneracy at  $k = 0$  [23], as can be seen for the unstrained case in Fig. 5. Increasing the compressive strain:

1. Lifts the conduction band to increase the bandgap energy
2. Increases the curvature of the heavy hole band, reducing the heavy hole mass
3. The light hole energy band sinks and has a decreased curvature

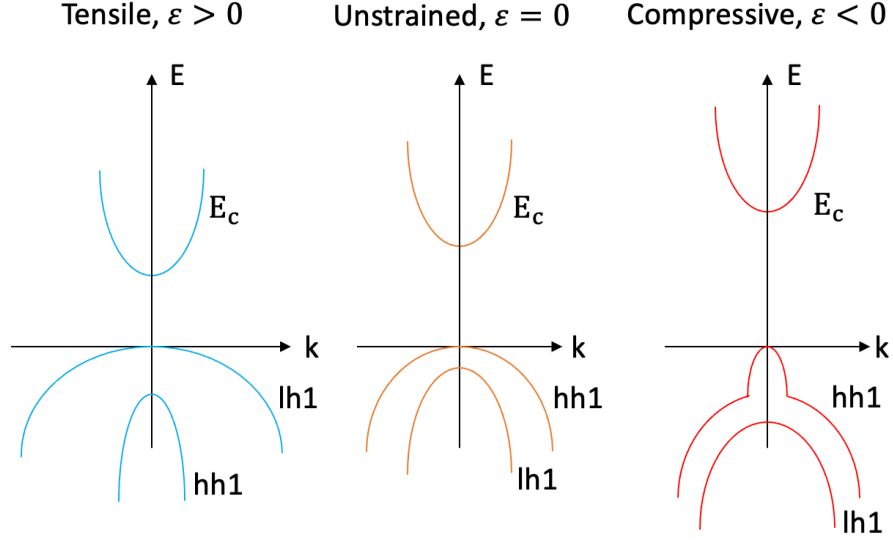


**Figure 5.** Qualitative diagram of the dependence of the valence band curvature in a QW with, from left to right, biaxial tensile strain, lattice-matching and biaxial compressive strain [23].

We can therefore use biaxial epitaxial strain to modify the structure of the QW sub-bands.

Strain can be hydrostatic, causing a change in the unit cell volume but not its shape (the ratio of a:b:c is constant), or shear, causing a change in angle of the unit cell. Strain adds a hydrostatic and shear energy shift, due to the conduction and valence band deformation, to the bandgap energy. The hydrostatic energy shift,  $P$ , is given by [17]:

$$P = -\alpha(2\varepsilon_{xx} + \varepsilon_{zz}), \quad (20)$$

where  $\alpha$  is the hydrostatic deformation potential. The Shear energy shift,  $Q$ , is given by [17]:

$$Q = -\frac{b}{2}(2\varepsilon_{xx} - 2\varepsilon_{zz}), \quad (21)$$

where  $b$  is the Shear deformation potential.  $\varepsilon_{xx} = \varepsilon_{yy}$  in the biaxial strain case and  $\varepsilon_{zz}$  is found using the Poisson ratio. The energy shifts given by (20) and (21) are added to the bandgaps of the QW and barriers before calculation of the electron and hole eigenenergies given by (7) [17].

A change in the strain state of the QW materials will shift their bandgap and therefore alter the operating wavelength of the VECSEL. Additionally, strain changes will alter the QW density of states and the polarization dependence of the QW gain [18], the consequences of which on the laser threshold are discussed in the next paragraphs.

The quasi-Fermi level is a function of temperature and sub-band energy and describes the energy state within the conduction or valence band with a probability of occupation of 0.5 (see Fig. 6 a) and b)). The Bernard-Duraffourg population inversion condition states that [17]:

$$F_C - F_v > E_C - E_v = \hbar\omega, \quad (22)$$

which means that the separation between the quasi-Fermi levels of the conduction and valence bands,  $F_C$  and  $F_v$  respectively, exceeds the difference in the energy difference between the conduction and valence band minima,  $E_C$  and  $E_v$  respectively, in order to achieve an electron population inversion.  $\hbar\omega$  is the photon energy (where  $\omega$  is the photon angular frequency) equivalent to  $E_C - E_v$ .

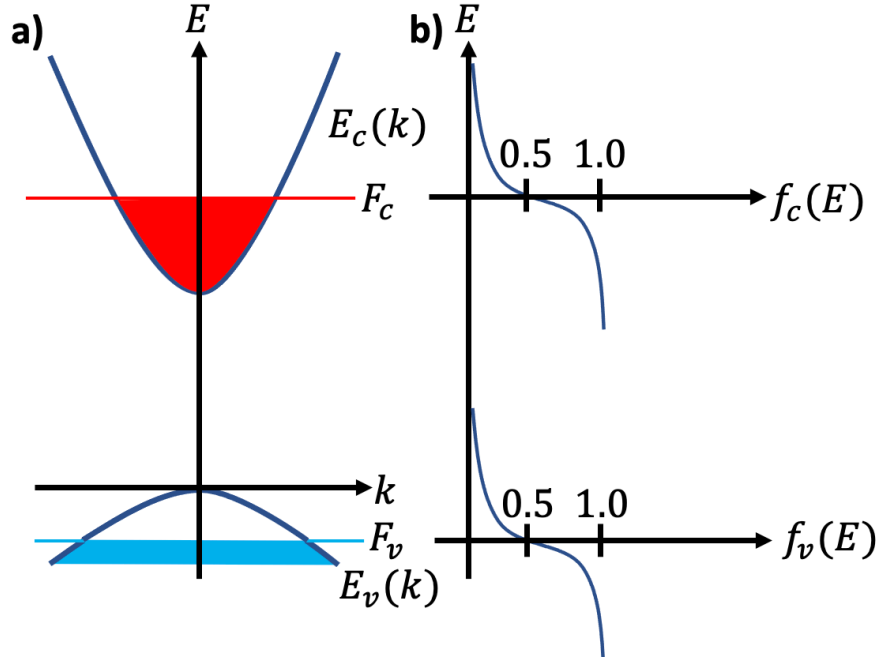


**Figure 6.** **a)** The electron occupancy within the conduction and valence bands, with the quasi-Fermi levels marked. **b)** The Fermi-Dirac functions of the conduction and valence bands on a common energy axis. The Fermi-Dirac function of the conduction/valence band has a value of 0.5 at the quasi-Fermi level of the respective conduction/valence band. Based on a figure in reference [17].

For the model used in this work the zero-point of the energy scale is set at the top of the valence band and the Fermi-Dirac functions, which give the occupancy probability of a state, for the conduction and valence bands respectively are defined as [17]:

$$f_c^n(E_t) = \frac{1}{1 + \exp\left(\frac{E_g + E_n + \frac{m_r^*}{m_e^*} E_t - F_c}{kT}\right)}, \quad (23)$$

and,

$$f_v^m(E_t) = \frac{1}{1 + \exp\left(\frac{E_m - \frac{m_r^*}{m_h^*} E_t - F_v}{kT}\right)}, \quad (24)$$

where  $n$  denotes the electron energy level,  $m$  denotes the hole energy level,  $m_e^*$  is the effective electron mass,  $m_h^*$  is the effective hole mass,  $m_r^*$  is the reduced mass given by  $\frac{1}{m_r^*} = \frac{1}{m_e^*} + \frac{1}{m_h^*}$ ,  $E_g$  is the bandgap energy,  $E_n$  is the quantized electron energy level,  $E_m$  is the quantized



hole energy level,  $k$  is the Boltzmann constant,  $T$  is temperature and  $E_t$  is an energy variable which accounts for the band structure curvature. In this work  $T$  is taken as 280 K to represent the operating temperature of a VECSEL.

For a QW the number density of charge carriers within the conduction or valence band,  $N$ , can be found by integrating the product of the density of states and the Fermi-Dirac function and summing the contributions from each sub-band [17]:

$$N = \sum_n \int_0^\infty \rho_{2D}(E) f_{c/v}^{n/m}(E) dE, \quad (25)$$

where  $E$  is the energy position in the band, there are  $N$  occupied sub-bands and

$$\rho_{2D}(E) = \frac{m^*}{\pi \hbar^2 L} \sum_{n/m} H(E - E_{n/m}). \quad (26)$$

is the 2D density of states of electrons or holes [17], where  $L$  is the QW thickness,  $m^*$  is the effective charge carrier mass (which for holes is a function of biaxial strain),  $E_N$  is the value of the  $N$  quantized energy levels and  $H(x)$  is the Heaviside step function, for which

$$H(x) = \begin{cases} 0 & x < 0 \\ 1 & x \geq 0 \end{cases}. \quad (27)$$

$L$  and  $m^*$  are the only parameters that can be used to modify the density of states and strain can adjust the  $m^*$  of the holes in the valence band. From (24) and (25) it can be noted that  $F_V$  can be kept constant for a reduced hole number density if  $\rho_{2D}(E)$  is reduced. Biaxial strain can be used to reduce  $\rho_{2D}(E)$  by increasing hole sub-band curvature and reducing  $m^*$ . Hence the Bernard-Duraffourg condition for population inversion is met for a lower carrier concentration, reducing the laser threshold.

Biaxial semiconductor strain gives a volumetric distortion to the unit cell which modifies the p-orbital shape of semiconductor compounds. In an unstrained cubic unit cell the charge carrier population exists in identical orbitals, arranged in paired lobes along the  $x$ ,  $y$ , and  $z$  Cartesian directions (see Fig. 7). Biaxial compressive strain along the  $x$ - $y$  plain increases charge carrier occupancy in the  $P_x$  and  $P_y$  orbitals and decreases the  $P_z$  population density [18].

The opposite is true for biaxial tensile strain. The changes in p-orbital shape due to  $x$ - $y$  biaxial strain are shown in Fig. 7.

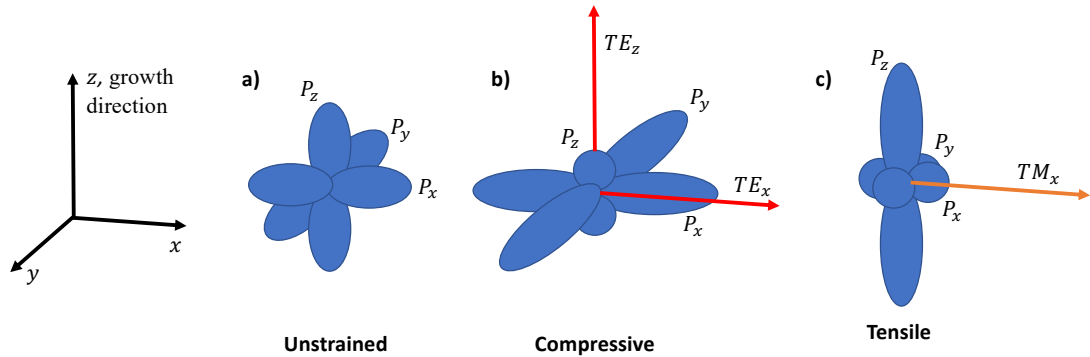


**Figure 7.**  $P_x$ ,  $P_y$  and  $P_z$  orbital shape for a) zero, b) compressive and c) tensile strain in the  $x$ - $y$  plain. Based on [18]. Compressive strain increases the TE gain in the growth direction, which is ideal for vertical emitters, such as VECSELS.

VECSEL laser oscillation is along the  $z$  direction, favouring linearly polarized transverse-electric (TE) modes originating from  $P_x$  and  $P_y$  orbitals. Heavy holes within a QW have a momentum matrix element which favours interaction with TE polarized light, propagating in the  $z$  direction. Compressive strain can therefore be used to enhance the TE gain through  $P_x$  and  $P_y$  orbital shaping (increasing the hole occupancy) and through raising the heavy hole sub-band towards the valence band edge, so that the Bernard-Duraffourg condition is satisfied for a lower quasi-Fermi level separation for the heavy hole sub-band. Additionally, the compressive strain reduces the  $m^*$  of the heavy holes, reducing the density of states of the heavy hole sub-band and therefore reducing the required charge carrier density to satisfy the Bernard-Duraffourg condition. The compressive strain can therefore reduce the laser threshold pump power of a VECSEL. Ideally the conduction and valence bands will have matching curvature at the  $\mathbf{k} = 0$  point so that  $F_C$  and  $F_V$  shift at equal rates with increased pump intensity.

The inclusion of compressively strained QWs within VECSEL structures increases the epitaxial growth challenges, hence impacting upon the material quality, however the effects of raising the heavy-hole sub-band, increasing the hole density in the plane perpendicular to the growth direction and the reduction in the valence band density of states collectively reduce the threshold charge carrier density.

In this project the QWs were designed to be lattice-matched to the InP substrate of the II-VI material, in order to maximize the material quality for the epitaxial lift-off steps used to produce the II-VI VECSEL membranes (see Chapter 3). For the work presented in Chapter 3

(on the full substrate removal) and in Chapters 4 and 5 (on the under-etching, transfer-printing and membrane characterization), it is important to understand how strain relaxation and material processing-induced changes alter strain-related properties of the II-VI and compressively-strained III-V materials.

## 2.3 Calculating electric fields

### 2.3.1 The optical transfer matrix

For the design of VECSELS it is important to be able to calculate the position and magnitude of electric field antinodes (see Section 2.4), along with the reflectivity of DBR mirrors to ensure the desired laser performance for a VECSEL heterostructure. The propagation of electric and magnetic fields through a material can be described using the optical transfer matrix [24,25]. The electric and magnetic fields at an arbitrary point A can be written vectorially as  $\begin{pmatrix} E_a \\ B_a \end{pmatrix}$ , and can be related to the electric and magnetic fields following propagation to an arbitrary point B,  $\begin{pmatrix} E_b \\ B_b \end{pmatrix}$ , using the optical transfer matrix [24,25]:

$$\begin{pmatrix} E_a \\ B_a \end{pmatrix} = \begin{pmatrix} \cos(\delta(n_r, \theta, t)) & \frac{i \sin(\delta(n_r, \theta, t))}{\gamma(n_r, \theta)} \\ i \gamma(n_r, \theta) \sin(\delta(n_r, \theta, t)) & \cos(\delta(n_r, \theta, t)) \end{pmatrix} \begin{pmatrix} E_b \\ B_b \end{pmatrix} = \mathbf{M}(n_r, \theta, t) \begin{pmatrix} E_b \\ B_b \end{pmatrix}, \quad (28)$$

where  $M$  is the optical transfer matrix.

$$\delta(n_r, \theta, t) = \frac{2\pi}{\lambda} n t \cos \theta, \quad (29)$$

is the phase shift acquired by an electromagnetic wave of wavelength  $\lambda$ , travelling through a material of thickness,  $t$ , refractive index  $n_r$  at an incident angle of  $\theta$ .  $\gamma(n_r, \theta)$  is a polarization-dependent property defined by [24,25]:

$$\gamma(n, \theta) = \begin{cases} n_r \sqrt{\epsilon_0 \mu_0} \cos(\theta), & \text{p polarization} \\ \frac{n_r \sqrt{\epsilon_0 \mu_0}}{\cos(\theta)}, & \text{s polarization} \end{cases} \quad (30)$$

where  $\epsilon_0$  is the permittivity of free space and  $\mu_0$  is the permeability of free space. The complex refractive index  $\underline{n} = n_r + ik$ , can be used to include gain and absorption,  $\alpha$ , into the optical transfer matrix via the inclusion of the imaginary component  $k = \frac{\alpha \lambda}{4\pi}$ .

For the purposes of these calculations it has been assumed that the thin film layers are non-magnetic [25], which for semiconductors is valid, and that the films are homogeneous and isotropic [24], which for the high quality growth targeted in these investigations is a valid assumption. For DBR-free gain structures, assuming symmetry of the refractive index profile along the growth axis of the gain region simplifies the calculations as the angle at which light enters the membrane is equal to the angle at which light will leave the membrane (see Appendix A2.1).

### 2.3.2 Angular dependent reflectivity from the optical transfer matrix

Each individual layer of a semiconductor heterostructure can be assigned a transfer matrix and the transfer matrices of the individual layers multiply in a non-commutative way to yield the overall transfer matrix for the heterostructure,  $\mathbf{M}_T(\lambda, \theta)$ ,

$$\begin{pmatrix} E_a \\ B_a \end{pmatrix} = \mathbf{M}_1 \mathbf{M}_2 \mathbf{M}_3 \dots \mathbf{M}_N \begin{pmatrix} E_b \\ B_b \end{pmatrix} = \mathbf{M}_T(\lambda, \theta) \begin{pmatrix} E_b \\ B_b \end{pmatrix}, \quad (31)$$

where the subscript number on the individual layer transfer matrices runs from 1 for the first layer encountered by the light to the N<sup>th</sup> layer encountered [24,25]. The four individual components of  $\mathbf{M}_T$ ,  $m_{11,12,21,22}$ , can be individually calculated and used to find the optical transmission and reflection coefficients [24,25],

$$t = \frac{2\gamma_0}{\gamma_0 m_{11} + \gamma_0 \gamma_s m_{12} + m_{21} + \gamma_s m_{22}} \quad (32)$$

and

$$r = \frac{\gamma_0 m_{11} + \gamma_0 \gamma_s m_{12} - m_{21} - \gamma_s m_{22}}{\gamma_0 m_{11} + \gamma_0 \gamma_s m_{12} + m_{21} + \gamma_s m_{22}} \quad (33)$$

respectively, where the “s” subscript denotes the substrate and the “0” subscript denotes the incident material. In (32) and (33) the  $(\lambda, \theta)$  arguments have been dropped for clarity. The reflectivity and transmission spectrum can then be found by  $R(\lambda, \theta) = |r(\lambda, \theta)|^2$  and  $T(\lambda, \theta) = |t(\lambda, \theta)|^2$  respectively [24,25]. Fig. 8 shows an example plot of the reflectivity of a DBR at normal incidence, comprised of 32.5 pairs of AlAs/AlGaAs with 56.3 nm and 45.6 nm layer thicknesses respectively.

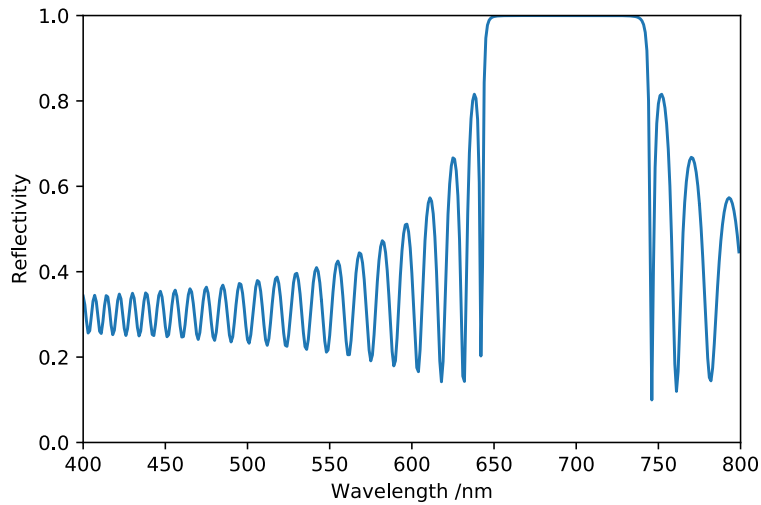


**Figure 8.** Reflectivity spectrum of an AlAs/AlGaAs DBR calculated using the optical transfer matrix.

## 2.4 Resonant periodic gain, resonant gain structures and calculating the optical confinement factor

### 2.4.1 The longitudinal confinement factor and resonant periodic gain (RPG)

The positioning of QWs within a VECSEL gain structure impacts the thermal and spectral performance during laser operation. In this section the key physical and design principles governing the positioning of QWs are discussed.

The optical confinement factor,  $\Gamma$ , quantifies the proportion of the laser electric field,  $E(x, y, z)$ , that exists in the gain region of a laser.  $\Gamma$  can be split into  $x$ ,  $y$  and  $z$  components [26]

$$\Gamma = \Gamma_x \Gamma_y \Gamma_z, \quad (34)$$

and for the VECSEL geometry  $\Gamma_x \Gamma_y = 1$ , as the transverse element of the mode has complete spatial overlap in the large lateral dimensions of the semiconductor structures, so  $\Gamma = \Gamma_z$ .  $\Gamma$  can therefore be calculated by integration and normalization of the electric field along the  $z$  axis

$$\Gamma_z = \frac{\int |E(z_{active})|^2 dz_{active}}{\int_0^L |E(z)|^2 dz}, \quad (35)$$

where  $L$  is the length of the gain structure along the  $z$  axis and the integral on the numerator is evaluated over the active region [26]. The solution from Corzine *et al* [26] states that

$$\Gamma_z = \frac{d}{L} \left( 1 + \frac{\sin\left(\pi \frac{t}{\left(\frac{\lambda}{2}\right)}\right)}{\pi \frac{t}{\left(\frac{\lambda}{2}\right)}} \right) = \frac{d}{L} \left( 1 + \frac{\sin\left(\pi \frac{d}{L}\right)}{\pi \frac{d}{L}} \right) = \frac{d}{L} \Gamma_{RPG} \quad (36)$$

where  $t$  is the QW thickness,  $L$  is the structure length,  $d$  is the total active region thickness (sum of QW thickness for VECSELS) and  $\lambda$  is the laser wavelength for which a structure is designed.  $\Gamma_{RPG}$  is the resonant periodic gain (RPG) factor and it quantifies the transition from a uniform gain material to one in which active regions are sited at anti-nodes of the electric field standing wave. This transition, along with a plot of  $\Gamma_z$  are shown in Fig. 9 below as a function of  $\frac{d}{L}$ .

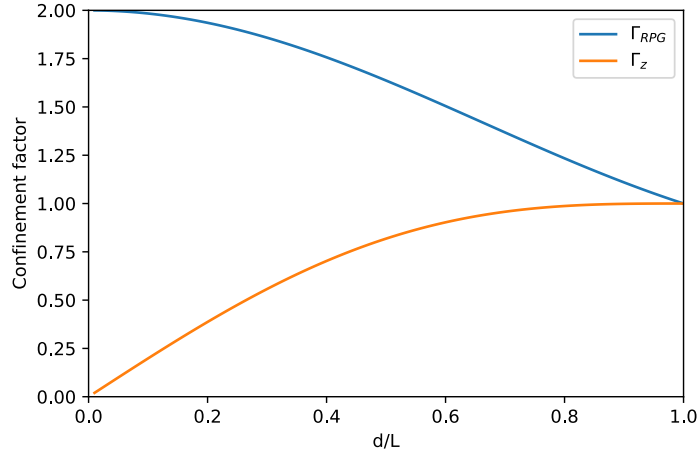


**Figure 9.**  $\Gamma_{RPG}$  and  $\Gamma_z$  as a function of  $\frac{d}{L}$ . Calculated from the Corzine model [26].

As the active region transitions from a single continuous block to discrete small segments (QWs),  $\frac{d}{L} \rightarrow 0$  results in a reduced proportion of the total electric field intensity being within the active region so  $\Gamma_z \rightarrow 0$ . As long as the active elements (QWs) are positioned at the antinodes of  $E(z)$  (RPG spaced) then as  $\frac{d}{L} \rightarrow 0$ ,  $\Gamma_{RPG} \rightarrow 2$ , as opposed to when  $\frac{d}{L} = 1$ ,  $\Gamma_{RPG} \rightarrow 1$ . Using QWs positioned at the electric field antinodes reduces the laser threshold power as there is no gain material positioned at the electric field nodes, which contribute very little to the modal gain and still require pumping.

The threshold gain,  $g_{th}$ , relates to  $\Gamma_{RPG}$  via

$$R_1 R_{OC} T_{loss} \exp(2\Gamma_{RPG} g_{th} N_w L_w) = 1, \quad (37)$$

where  $R_1$  is the reflectivity of the DBR, or an external cavity mirror for DBR-free VECSELs,  $R_{OC}$  is the output coupler reflectivity,  $N_w$  is the number of QWs in the gain structure,  $L_w$  is the QW thickness and  $T_{loss}$  is the laser cavity loss (1 – the transmission losses per cycle) [1]. A transition from uniform to resonant periodic gain ( $\Gamma_{RPG} \rightarrow 2$ ) reduces the necessary  $g_{th}$  required for laser oscillation by a factor of 2. Along with reducing the threshold gain requirement the RPG format suppresses spatial hole burning, as the majority of the gain structure is not active and wavelengths of modes with antinodes which do not overlap well with the RPG aligned QWs will have a reduced stimulated emission rate [27].

#### 2.4.2 Resonant VECSEL structures and thermal rollover

The VECSEL gain region forms a Fabry-Perot etalon due to the semiconductor/heatspreader interface, with a peak transmission referred to as the sub-cavity resonance. For a given laser target wavelength,  $\lambda$ , gain structures can be resonant, with the total gain region being an integer multiple of  $\frac{\lambda}{2}$  and with  $|E^2|$  antinodes coinciding with the gain structure surface (see Fig. 10 a)) [27]. Anti-resonant structures are odd, integer multiples of  $\frac{\lambda}{4}$  in length, resulting in  $|E^2|$  nodes aligned with the gain structure surface (see Fig. 10 b)) [27]. Resonant structures offer a reduced laser threshold, due to the enhancement of  $|E^2|$  at the designed wavelength,  $\lambda$ , in the active region, whereas anti-resonant structures offer a greater tunability as the overlap of  $|E^2|$  with the QWs varies slowly with  $\lambda$  [27].

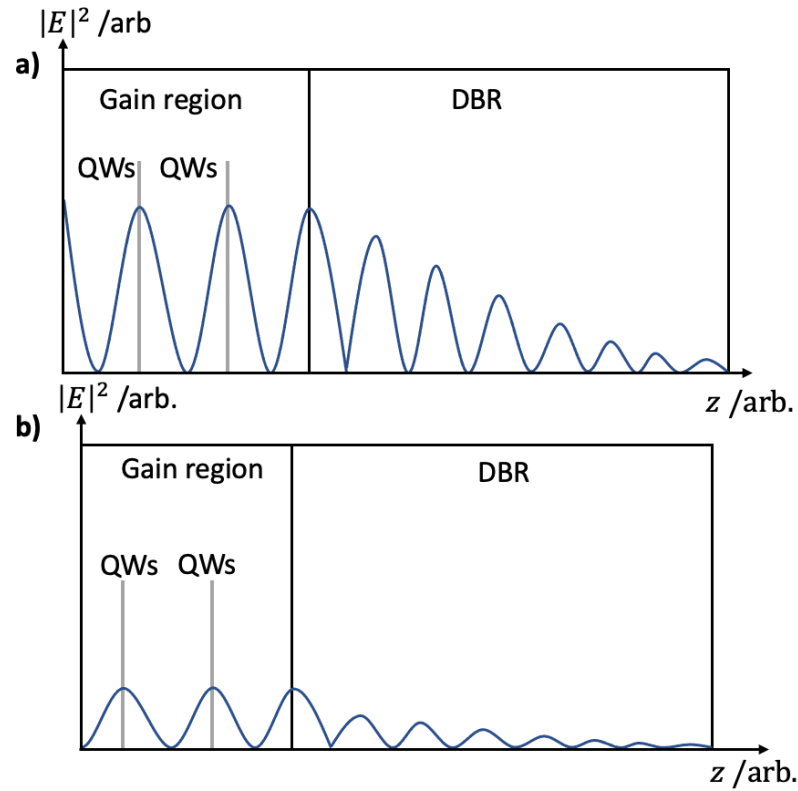


**Figure 10.** The  $|E|^2$  plotted throughout the VECSEL gain structure for **a)** the resonant and **b)** anti-resonant designs [27].

The sub-cavity resonance of the VECSEL gain structure redshifts with increased temperature due to the thermo-optic coefficient and the coefficient of thermal expansion of the semiconductor materials. As pump power is increased, pump-induced heating from the quantum defect increases the gain structure temperature, causing the material gain peak and the sub-cavity resonance of the VECSEL to redshift (see Fig. 11) [28]. Maximum VECSEL output power, for a given output coupler and input power, occurs when the material gain peak and the sub-cavity resonance align, however temperature-induced redshift reduces the overlap of the material gain peak and the sub-cavity resonance and causes a drop in output power called thermal rollover [28]. Additionally, as the temperature increases the material gain of the QWs decreases, further contributing to the thermal rollover.



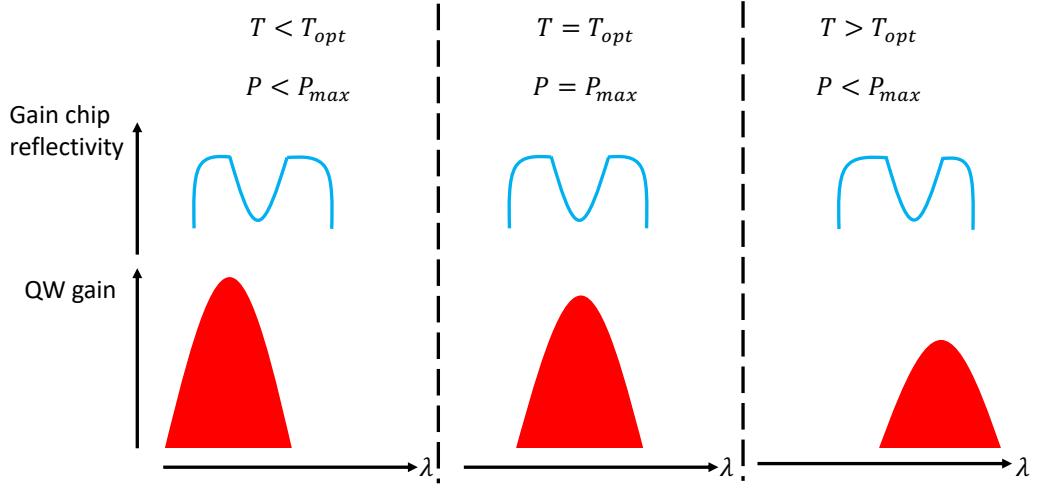


**Figure 11.** The thermal rollover process. As the temperature,  $T$ , of the VECSEL sample increases the QW gain spectrum and the VECSEL sub-cavity resonance (the gain mirror reflectivity profile) redshift at different rates, causing variation in the output power,  $P$ . There exists an optimum operation temperature,  $T_{opt}$ , at which the maximum output power,  $P_{max}$ , for a given output coupling and input power is achieved.

#### 2.4.3 Designing resonant VECSEL structures with RPG

The II-VI DBR-free VECSEL structures have QWs, barriers, QW spacing barriers and Mg-free capping layers to protect from oxidation. The QW spacing barriers physically separate the electron/hole wavefunctions within the individual QWs of a QW antinode pair, preventing the coupling of the wavefunctions which adjust the recombination energy. In this work the QW spacing barriers were set to 10 nm. The semiconductor layer thicknesses are designed so that the structures are resonant and have QWs positions to enforce RPG, and are calculated using

$$\frac{\lambda}{2} = L_{cap}n_{cap} + L_{end\_barrier}n_{barrier} + L_{QW}n_{QW} + \frac{1}{2}L_{QW\_barrier}n_{barrier} \quad (38)$$

and

$$\frac{\lambda}{2} = L_{barrier}n_{barrier} + 2L_{QW}n_{QW} + L_{QW\_barrier}n_{barrier} \quad (39)$$

where  $\lambda$  is the operating wavelength,  $L_{cap}$  is the cap thickness,  $n_{cap}$  is the refractive index of the capping layer,  $L_{end\_barrier}$  is the thickness of the first and final barriers of a DBR-free structure,  $n_{barrier}$  is the refractive index of the barriers,  $L_{QW}$  is the QW thickness,  $n_{QW}$  is the refractive index of the QWs and  $L_{QW\_barrier}$  is the thickness of the QW spacing barrier. See

Fig. 12 for clarification. Typically,  $L_{QW}$  is picked to achieve gain at the target oscillation wavelength,  $L_{cap}$  and  $L_{QW\_barrier}$  are set and then the barrier thicknesses are calculated from the target laser wavelength.

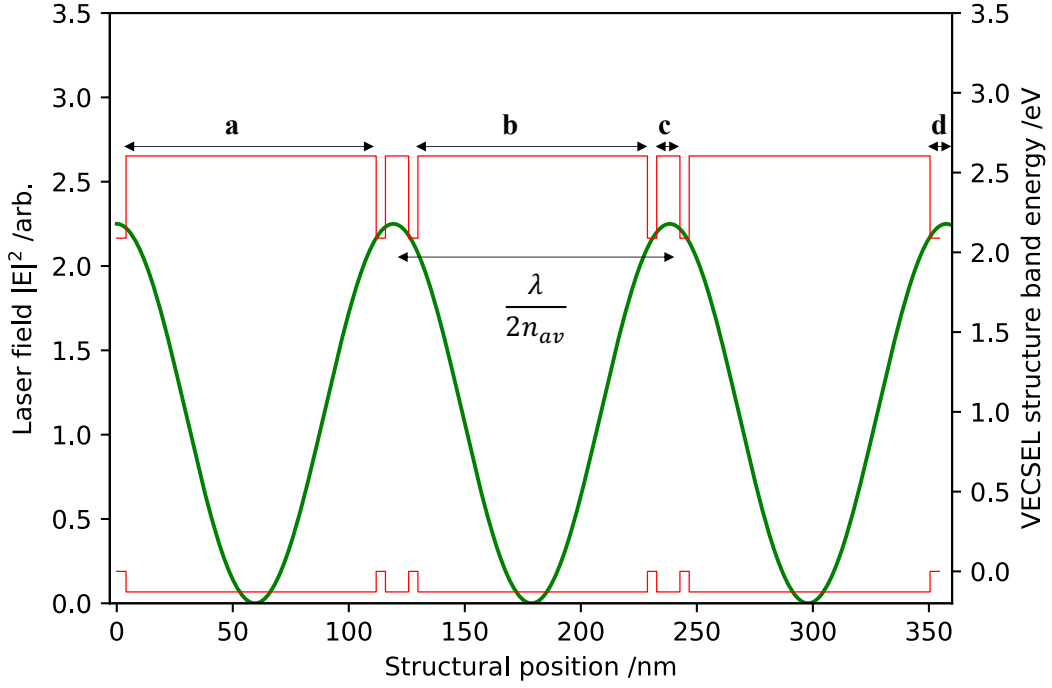


**Figure 12.** A simple DBR-free VECSEL gain structure design of 2 pairs of QWs for a laser wavelength,  $\lambda$ . The laser electric field is plotted as the  $|E|^2$  of the standing wave within the laser cavity. **a** is the end barrier thickness, **b** is a standard barrier thickness, **c** is the QW separation layer thickness and **d** is the cap layer thickness. The gain structure is symmetrical along the  $z$  axis with respect to the centre of the gain structure and has a mean refractive index,  $n_{av}$ .

## 2.5 II-VI QWs and the minimum gain requirement

### 2.5.1 The Kuznetsov analysis [1]

The number of QWs within a VECSEL gain structure can be optimized to minimize the laser threshold and maximize the output power for a given input pump power. The optimum number of QWs within a gain structure can be calculated using the Kuznetsov analysis [1]. The charge carrier density within a single QW,  $N$ , injected by optical pumping, is given by

$$N = \frac{\eta_{abs} P_p}{h\nu N_w L_w A_p} \tau(N), \quad (40)$$

where  $\eta_{abs}$  is the pump absorption efficiency,  $P_p$  is the input pump power,  $\tau(N)$  is the charge carrier lifetime as a function of charge carrier density,  $h\nu$  is the product of the Planck constant and the pump photon frequency,  $N_w$  is the number of QWs,  $L_w$  is the QW thickness and  $A_p$  is the pump spot area. The carrier lifetime can be modelled using the ‘‘ABC model’’ [1]:

$$\frac{1}{\tau(N)} = A + BN + CN^2, \quad (41)$$

where  $A$  is the monomolecular (non-radiative) recombination coefficient,  $B$  is the bimolecular (radiative) recombination coefficient and  $C$  is the Auger recombination coefficient [1]. The power of  $N$  dependence of each term indicates the relative probability of each event occurring; events involving  $x$  particles have an  $N^{x-1}$  relation. Fig. 13 shows the charge carrier lifetime plotted as a function of charge carrier density using the  $A$ ,  $B$  and  $C$  coefficients from Table 1b.

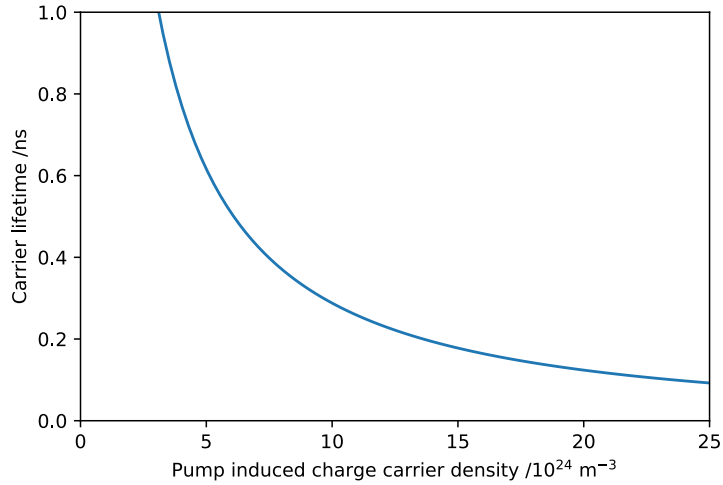


**Figure 13.** Charge carrier lifetime dependence on the charge carrier density for ZnCdSe using the estimated  $A$ ,  $B$  and  $C$  coefficients from Table 1b.

An approximation of the maximum semiconductor QW gain,  $g$ , is given by [29]:

$$g = g_0 \ln\left(\frac{N}{N_0}\right), \quad (42)$$

where  $g_0$  is the semiconductor material gain parameter and  $N_0$  is the transparency carrier density [1]. The threshold material gain,  $g_{th}$ , and the threshold carrier density,  $N_{th}$ , can also be related via (42), and along with (37) give [1]:

$$N_{th} = N_0 \left( \frac{1}{R_1 R_{OC} T_{loss}} \right)^{(2\Gamma_{RPG} g_0 N_w L_w)^{-1}}. \quad (43)$$

Equation (40) can then be rearranged to give an equation for the threshold input pump power,

$$P_{th} = N_{th} \frac{h\nu N_w L_w A_p}{\eta_{abs} \tau(N_{th})}. \quad (44)$$

The laser output power,  $P_{las}$ , can be calculated by subtracting the threshold power from the input pump power and multiplying by the laser process efficiencies [1],

$$P_{las} = (P_p - P_{th}) \eta_{out} \eta_{quantum} \eta_{abs} \eta_{rad} \quad (45)$$

where the output coupling efficiency is given by

$$\eta_{out} = \frac{\ln(R_{OC})}{\ln(R_1 R_{OC} T_{loss})}, \quad (46)$$

the quantum efficiency by

$$\eta_{quantum} = \frac{\lambda_{pump}}{\lambda_{laser}}, \quad (47)$$

the radiative efficiency, which dictates how many of the generated charge carriers undergo radiative recombination, is given by

$$\eta_{rad} = \frac{BN_{th}}{A + BN_{th} + CN_{th}^2} \quad (48)$$

and for the absorption efficiency  $\eta_{abs} = 1$  is assumed for short wavelength pump sources.

### 2.5.2. Single quantum well gain modelling: an initial model

Modelling the gain of QWs is important for VECSEL design as it allows for the number of QWs in a gain structure to be optimized in terms of the number required to minimize the threshold. The material gain as a function of photon energy,  $g(E)$ , of a QW is given by

$$g(E) = \alpha_0(E)(f_c - f_v), \quad (49)$$

where  $f_c$  is the Fermi-Dirac function of electrons,  $f_v$  is the Fermi-Dirac function of holes and

$$\alpha_0(E) = \frac{\pi e^2}{n_r c \epsilon_0 \omega m_0^2} |\hat{u} \cdot p_{cv}|^2 \frac{m^*}{\pi \hbar^2 L} \sum_n H(E - E_n), \quad (50)$$

is the material absorption coefficient as a function of photon energy at thermal equilibrium and with no carrier injection [17], where  $e$  is the electron charge,  $n_r$  is the real component of the QW refractive index,  $c$  is the speed of light in a vacuum,  $\omega$  is the frequency of the amplified/absorbed photon,  $m_0$  is the electron rest mass,  $|\hat{u} \cdot p_{cv}|^2$  is the momentum matrix element in the plane of the QW,  $m^*$  is the effective charge carrier mass,  $L$  is the QW thickness and the summation is over the  $n$  energy levels confined to the QW.

In order to evaluate the material gain the quasi-Fermi level for electrons (and holes) needs to be found from the injected charge carrier density,  $N$ . The integral in (25) can be evaluated to give [17]:

$$N = \frac{m^*}{\pi \hbar^2 L} k_B T \sum_n \ln \left( 1 + \exp \left( \frac{F_C - E_n}{k_B T} \right) \right). \quad (51)$$

An equivalent relation can be written for holes [17]. This relation can be used to find the quasi-Fermi level,  $F_C$ , for the II-VI QW from the carrier density using a minimization function given by:

$$Z(N, F_C) = \frac{m^*}{\pi \hbar^2 L} k_B T \sum_n \ln \left( 1 + \exp \left( \frac{F_C - E_n}{k_B T} \right) \right) - N = 0. \quad (52)$$

The minimization function can be defined for both electrons and holes and then solved numerically, for a given optically injected  $N$ , to give  $F_C$  and  $F_V$ .

### 2.5.3 QW gain model with linewidth broadening

In order to obtain a more realistic gain spectrum, delta function-like QW energy levels cannot be assumed and so the broadening of the energy levels can be incorporated using a Lorentzian function to account for electron-phonon scattering [17]. QW material gain with transition broadening is given by [17]:

$$g(\hbar\omega) = \frac{\pi e^2}{n_r c \epsilon_0 m_0^2 \omega} \sum_{m,n} |I_{hm}^{en}|^2 \int_0^\infty dE_t \rho_r^{2D} |\hat{e} \cdot \mathbf{p}_{cv}|^2 \left( \frac{\frac{\gamma}{\pi}}{(E_{hm}^{en} + E_t - \hbar\omega)^2 + \gamma^2} \right) \times (f_c^n(E_t) - f_v^m(E_t)). \quad (53)$$

$I_{hm}^{en}$  is the overlap integral of the electron and hole wavefunctions,  $I_{hm}^{en} = \int_{-\infty}^\infty \phi_n(z) g_m(z) dz$ , where  $\phi_n(z)$  and  $g_m(z)$  are the electron and hole wavefunctions, respectively, in the quantized axis,  $z$ , and  $n$  and  $m$  denote the electron and hole sub-band orders respectively [17].  $|I_{hm}^{en}|^2 \approx 1$  for  $m = n$  and  $|I_{hm}^{en}|^2 \approx 0$  for  $m \neq n$  [17]. The 2D density of states,  $\rho_r^{2D} = \frac{m^*}{\pi \hbar^2 L}$ , and  $|\hat{e} \cdot \mathbf{p}_{cv}|^2$  is the momentum matrix element of a given transition. For VECSELs the TE polarization is of interest and so the momentum matrix can be expressed as

$$|\hat{e} \cdot \mathbf{p}_{cv}|^2 = \frac{3}{4} (1 + \cos^2(\theta_{mn})) M_b^2, \quad (54)$$

with,

$$\cos^2(\theta_{mn}) = \frac{E_{en} + |E_{hm}|}{E_{en} + |E_{hm}| + \frac{\hbar^2 k_t^2}{2m_r^*}}, \quad (55)$$

where  $M_b^2$  is a material parameter which relates to the Kane momentum matrix energy parameter,  $E_p$ , via  $M_b^2 = \frac{m_0}{6} E_p$  [17]. Although the exact  $E_p$  will be specific to the strain and composition of the ZnCdSe used in the QW, in this calculation  $E_p = 19.5$  eV [15,16]. This  $E_p$  is taken from the calculations completed in references [15,16], where  $E_p$  is determined from reported values of the conduction band charge carrier masses of ZnSe and CdSe.

In (53) the integral is taken over  $k$ -space (as  $E_t = \frac{\hbar^2 k^2}{2m^*}$  and using  $E_t$  is a simpler variable for the integration) and is broadened by

$$L(E_t, \hbar\omega) = \left( \frac{\frac{\gamma}{\pi}}{(E_{hm}^{en} + E_t - \hbar\omega)^2 + \gamma^2} \right), \quad (56)$$

to show scattering processes contributing to sub-eigenenergy gain and photoluminescence and linewidth broadening [17]. The broadening is given by  $\gamma$  and  $\frac{1}{\pi}$  ensures normalization [17].

The summation in (53) accounts for the gain contribution from the different electron and hole sub-bands. For simplification only the  $n = 1$  and  $n = 2$  states are assumed to exist within the QW, only transitions with heavy-holes are included due to the TE-polarized operation of VECSELs and only transitions between energy levels of the same parity are permitted [18].

For evaluation of the model a 4 nm  $\text{Zn}_{0.48}\text{Cd}_{0.52}\text{Se}$  QW within  $\text{Zn}_{0.3}\text{Cd}_{0.28}\text{Mg}_{0.42}\text{Se}$  barriers, introduced in Section 2.2.2 to target the 565 nm wavelength, is modelled with the upper limit of the integral set as the conduction band depth of around 0.55 eV and the broadening is taken to be  $\gamma = 10$  meV [13]. Fig. 14 shows the calculated material gain spectrum of this  $\text{Zn}_{0.48}\text{Cd}_{0.52}\text{Se}/\text{Zn}_{0.3}\text{Cd}_{0.28}\text{Mg}_{0.42}\text{Se}$  QW for charge carrier densities ranging from  $1 \times 10^{24} \text{ m}^{-3}$  to  $1 \times 10^{25} \text{ m}^{-3}$  (typical of Watt-level, visible wavelength, optical pumping in VECSELs; see equation (40)), showing a peak material gain of  $5000 \text{ cm}^{-1}$  at around 560 nm.

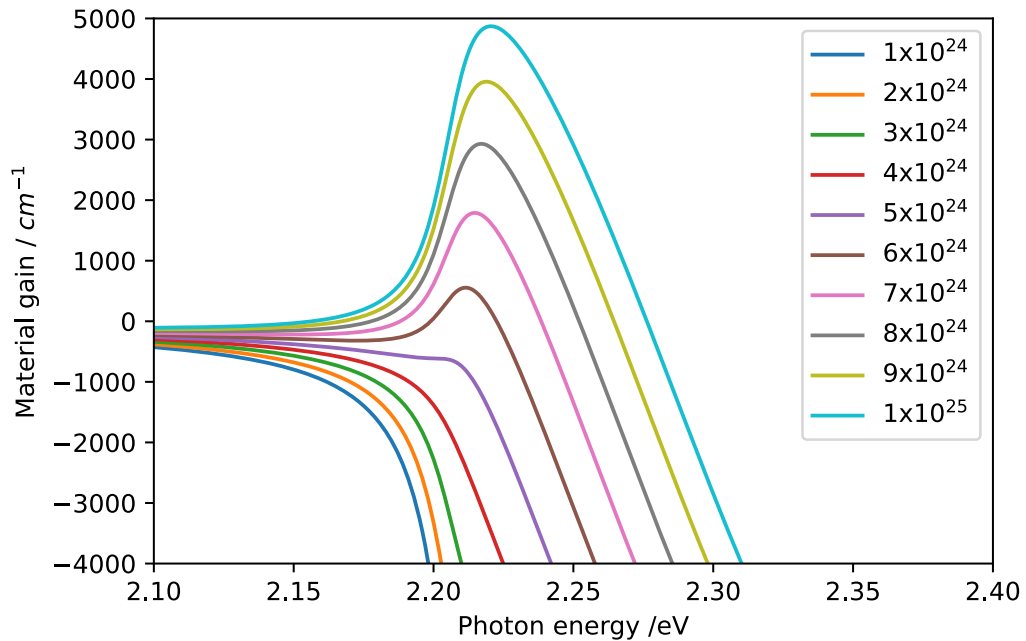


**Figure 14.** Calculated material gain spectrum of a  $\text{Zn}_{0.48}\text{Cd}_{0.52}\text{Se}/\text{Zn}_{0.3}\text{Cd}_{0.28}\text{Mg}_{0.42}\text{Se}$ , 4-nm-thick QW for charge carrier densities ranging from  $1 \times 10^{24} \text{ m}^{-3}$  to  $1 \times 10^{25} \text{ m}^{-3}$ , at room temperature. Here  $E_1 = 0.0908 \text{ eV}$ ,  $E_2 = 0.3473 \text{ eV}$ ,  $H_1 = -0.0239 \text{ eV}$ ,  $H_2 = -0.0912 \text{ eV}$  and for  $\text{Zn}_{0.48}\text{Cd}_{0.52}\text{Se}$   $E_g = 2.091 \text{ eV}$ .

By specifying the 565 nm wavelength of interest,  $N_0$ , the transparency carrier density, can be found by finding the carrier density for which  $g(\hbar\omega) = 0$  using a root finding function. From the model  $N_0 = 5.908 \times 10^{24} \text{ m}^{-3}$  is calculated at 565 nm.

From this model we can calculate a value for  $g_0$ , the semiconductor material gain parameter of the Kuznetsov model. The material gain at 565 nm as a function of charge carrier density is plotted in Fig. 15, and equation (42) is fitted to this, using the *curve\_fit* function of the Python *SciPy.optimize* library, for  $N_0 = 5.908 \times 10^{24} \text{ m}^{-3}$ . The fit has been completed from  $2 \times 10^{24} \text{ m}^{-3}$  to  $20 \times 10^{24} \text{ m}^{-3}$  charge carrier densities. From the fit it is found that  $g_0 = 3428 \text{ cm}^{-1}$  at 565 nm. The material gain for an 8 nm InGaAs/InGaAsP QW emitting at  $1.25 \mu\text{m}$ , where  $N_0 = 1.17 \times 10^{24} \text{ m}^{-3}$  and  $g_0 = 1575 \text{ cm}^{-1}$ , is also plotted as a function of charge carrier density, in Fig. 15, as a comparison [28]. Fig. 15 shows that the ZnCdSe/ZnCdMgSe QW emitting at 565 nm has a higher transparency carrier density, but achieves a similar peak material gain at the higher charge carrier densities. Now  $N_0$  and  $g_0$  have been calculated it can be used to design the II-VI VECSEL structure, using the Kuznetsov model, for this wavelength.

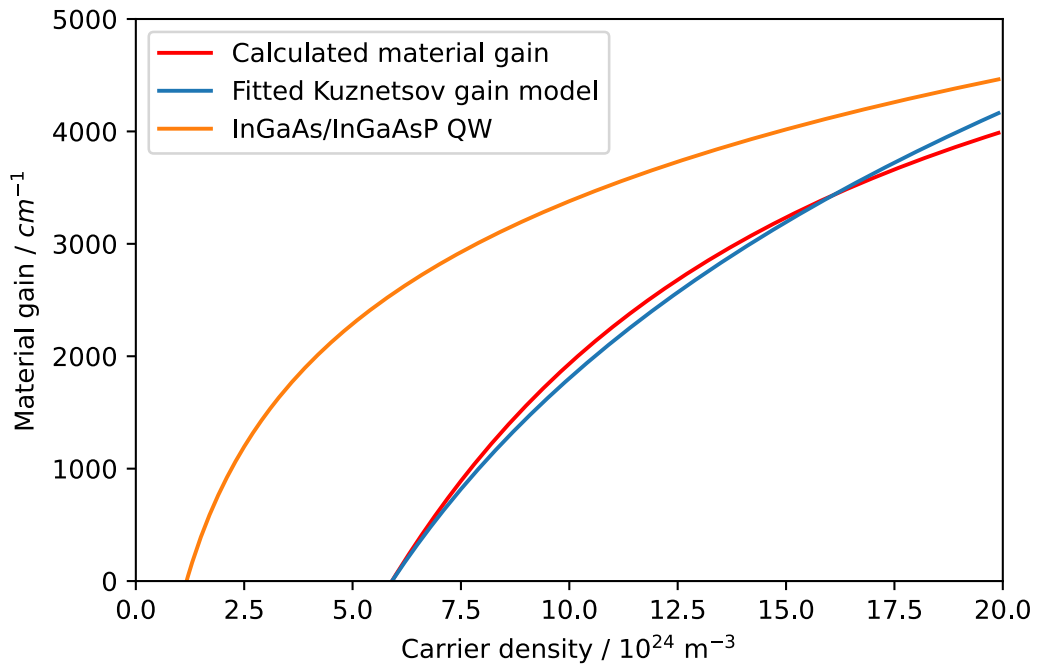


**Figure 15.** The calculated material gain of a  $\text{Zn}_{0.48}\text{Cd}_{0.52}\text{Se}/\text{Zn}_{0.3}\text{Cd}_{0.28}\text{Mg}_{0.42}\text{Se}$ , 4-nm-thick QW, at a 565 nm operating wavelength (red) as a function of charge carrier density and the fitted logarithmic dependence of the material gain (blue). Here  $g_0 = 3428 \text{ cm}^{-1}$  and  $N_0 = 5.908 \times 10^{24} \text{ m}^{-3}$ . The material gain for an 8 nm InGaAs/InGaAsP QW emitting at  $1.25 \mu\text{m}$  is also plotted as a function of charge carrier density [29]. Temperature change due to optical pumping is not included in this model.



If the above analysis is repeated, for the 4 nm  $\text{Zn}_{0.48}\text{Cd}_{0.52}\text{Se}$  QW within  $\text{Zn}_{0.3}\text{Cd}_{0.28}\text{Mg}_{0.42}\text{Se}$  barriers, introduced in Section 2.2.2 to target the 565 nm wavelength, but this time at the QW material gain peak at around 560 nm, then  $N_0 = 5.864 \times 10^{24} \text{ m}^{-3}$  and  $g_0 = 8386 \text{ cm}^{-1}$ , with a fit from  $2 \times 10^{24} \text{ m}^{-3}$  to  $20 \times 10^{24} \text{ m}^{-3}$  charge carrier densities. Fig. 16 shows the material gain at 560 nm as a function of charge carrier density, with a line fitted for the logarithmic gain dependence applied in the Kuznetsov model, equation (42). The material gain of an InGaAs/InGaAsP QWs is also plotted in Fig. 16 [29]. The model predicts that a laser based on ZnCdSe/ZnCdMgSe QWs and operating at the gain peak will have a higher threshold than an equivalent laser based on InGaAs/InGaAsP QWs, due to the much higher density of states within the II-VI sub-bands. The higher density of states of the ZnCdSe/ZnCdMgSe QWs gives a much higher material gain at higher pump intensities.

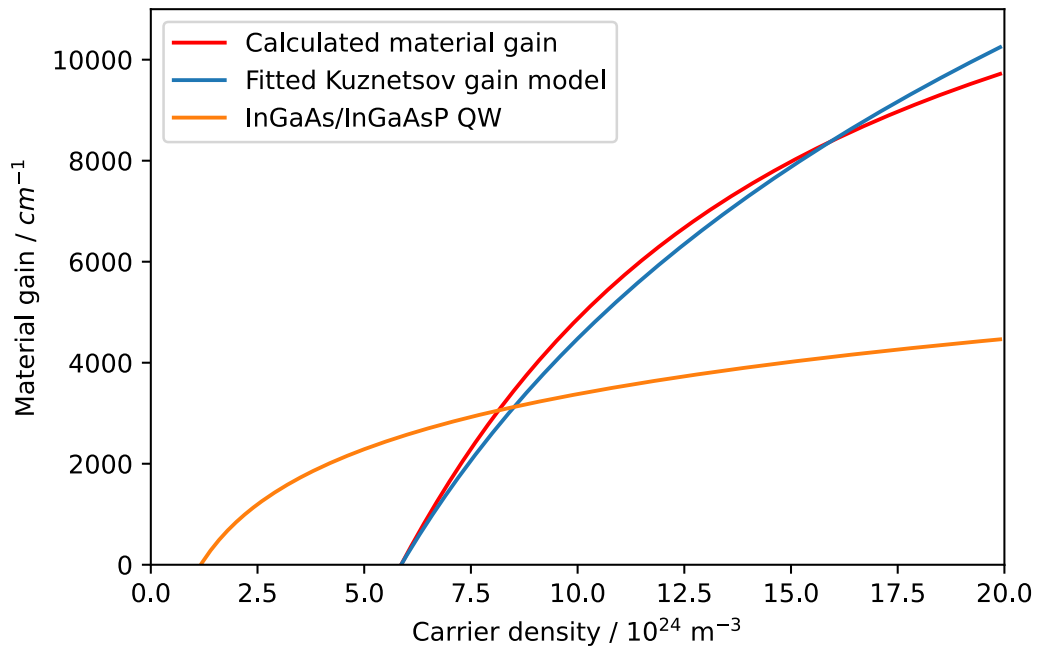


**Figure 16.** The calculated material gain of a  $\text{Zn}_{0.48}\text{Cd}_{0.52}\text{Se}/\text{Zn}_{0.3}\text{Cd}_{0.28}\text{Mg}_{0.42}\text{Se}$ , 4-nm-thick QW, at 560 nm (red) as a function of charge carrier density and the fitted logarithmic dependence of the material gain (blue) gives  $N_0 = 5.864 \times 10^{24} \text{ m}^{-3}$  and  $g_0 = 8386 \text{ cm}^{-1}$ . The material gain for an 8 nm InGaAs/InGaAsP QW emitting at 1.25  $\mu\text{m}$  is also plotted as a function of charge carrier density [29]. Temperature change due to optical pumping is not included in this model.

#### 2.5.4 Calculating photoluminescence spectra

The photoluminescence (spontaneous emission) spectrum output from a QW can be calculated by adjusting the inversion factor, to account for the occupancy probability of an electron being

in the conduction band and there being a vacancy in the valence band. The rate of spontaneous emission per unit volume per unit energy is given by [17]:

$$R(\hbar\omega) = \frac{\pi e^2}{n_r c \epsilon_0 m_0^2 \omega} \sum_{m,n} |I_{hm}^{en}|^2 \int_0^\infty dE_t \rho_r^{2D} |\hat{e} \cdot \mathbf{p}_{cv}|^2 \left( \frac{\frac{\gamma}{\pi}}{(E_{hm}^{en} + E_t - \hbar\omega)^2 + \gamma^2} \right) \times f_c^n(E_t)(1 - f_v^m(E_t)) \quad (57)$$

For a real VECSEL sample the photoluminescence spectrum output is modified by sub-cavity resonances which occur from the microcavity formed between the DBR and the air-semiconductor (or diamond-semiconductor when a heatspreader is used) interface. Here, for the DBR-free case, for simplification it is assumed that these sub-cavity effects are small as there is no high reflectivity DBR, simply the ZnCdMgSe/InGaAs boundary for the as-grown sample. In Fig. 17 The calculated material gain and spontaneous emission spectrum are plotted for a 4 nm  $\text{Zn}_{0.48}\text{Cd}_{0.52}\text{Se}$  QW with  $\text{Zn}_{0.3}\text{Cd}_{0.28}\text{Mg}_{0.42}\text{Se}$  barriers with a carrier density of  $8 \times 10^{24} \text{ m}^{-3}$ , along with a line showing the RPG designed for 565 nm and a PL spectrum measurement from a gain structure sample CDI 640 in its as-grown state (see Chapter 5 for experimental and sample details).  $8 \times 10^{24} \text{ m}^{-3}$  is chosen as it gives a match to the measured spectral profile.

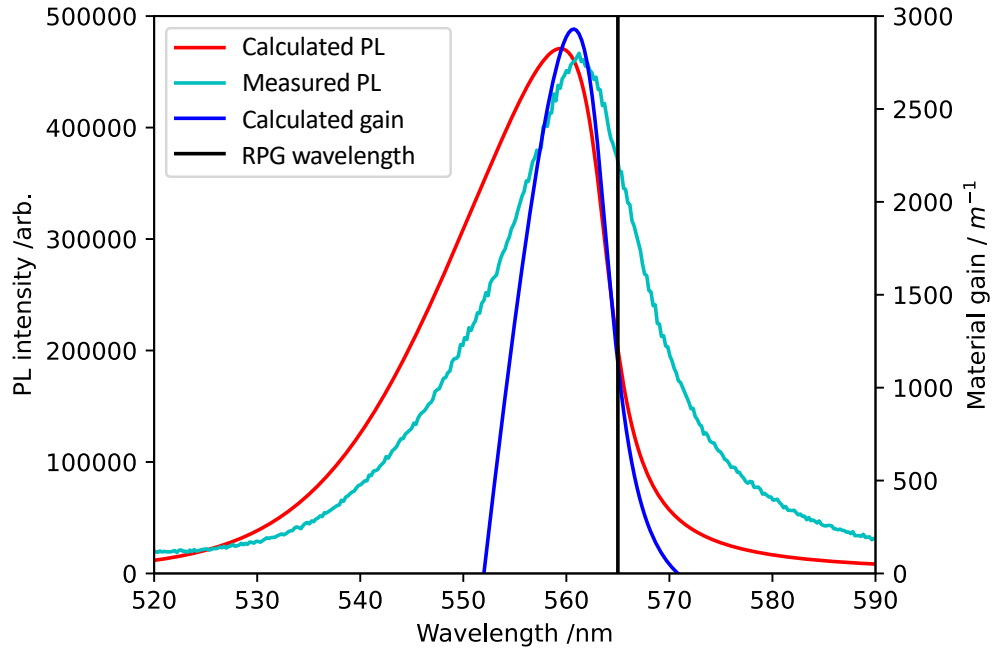


**Figure 17.** The calculated material gain (dark blue) and spontaneous emission spectrum (red) of a 4 nm  $\text{Zn}_{0.48}\text{Cd}_{0.52}\text{Se}$  QW with  $\text{Zn}_{0.3}\text{Cd}_{0.28}\text{Mg}_{0.42}\text{Se}$  barriers designed for 565 nm emission, at a charge carrier density of  $8 \times 10^{24} \text{ m}^{-3}$ . The measured PL spectrum (light blue) of an as-grown sample, CDI 640 is plotted for comparison. The PL spectrum of CDI 640 has been normalized to the same scale as the calculated PL spectrum.

The spontaneous emission spectrum serves as a useful characterization tool for seeing how closely MBE grown samples match with the intended gain structure design. The intensity of the calculated and measured PL spectra cannot be compared as the experimental setup does not capture all spontaneous emission from the pumped volume. Additionally, the charge carrier density is challenging to accurately characterize and so here, for PL spectra taken at low pump powers, only the spectral profile is compared. The experimental PL peak is red shifted in comparison to the calculated one due to sample heating, variation in the QW growth and its lower charge carrier density than the calculated QWs. The measured PL spectrum serves as a guide to confirm that the grown samples are close to the experimental design and that the QW gain peak will redshift towards the RPG wavelength. Given the redshift of the experimentally measured PL with respect to the calculated one, the gain peak will also exhibit a redshift in comparison to the calculated one.

Typically, the RPG wavelength is designed with a small red-shift from the PL and material gain peak to account for the redshift of the gain spectrum as the sample heats during optical pumping. For the ZnCdSe/ZnCdMgSe II-VI material system the shift of the PL spectrum is 0.13 nm/K, a reduction compared with typical III-V material systems [30]. The II-VI VECSEL has therefore been designed with a smaller RPG to material gain offset than the typical 10 nm of III-V VECSELs [31].

Ideally a measurement of the optical gain using pump-probe spectroscopy (as in reference [32]) could be used to confirm the gain calculations, however a suitable probe source in the 540 nm – 580 nm region was not available for this project. For a gain measurement to be completed a high-quality membrane would need to be achieved (see Chapter 5) and a transmission-based amplification measurement would need to be completed using a supercontinuum laser as a probe source.

#### 2.5.5 Kuznetsov analysis for the II-VI

Using the values in Table 1a and Table 1b the Kuznetsov model was evaluated to assess how the threshold absorbed input power and the maximum output power of a II-VI DBR-free VECSEL scale with the number of QWs in the gain structure for two cases: laser operation at 565 nm ( $N_0 = 5.908 \times 10^{24} \text{ m}^{-3}$  and  $g_0 = 3428 \text{ cm}^{-1}$ ) or at the gain peak ( $N_0 = 5.864 \times 10^{24} \text{ m}^{-3}$  and  $g_0 = 8386 \text{ cm}^{-1}$ ). This analysis can be completed to calculate some options for the optimum II-VI DBR-free VECSEL gain structure. For these calculations an

additional round trip loss term of 1 % was included to account for scattering and parasitic resonator losses [1], however for the novel ZnCd(Mg)Se material system in the DBR-free format this roundtrip loss could be higher due to membrane debonding, contaminants and growth defects. The reflectivity of the other external mirror of the cavity was taken as 99.9 %. The input absorbed pump power was set at a maximum of 5 W at 447 nm with an 80  $\mu\text{m}$  pump spot diameter.

Fig. 18 a) and b) show the absorbed input power at threshold as a function of output coupling (OC) and the number of QWs in the gain structure for 565 nm operation (assuming minimal sub-cavity resonance and material gain peak shift) and the peak material gain case (assuming that the sub-cavity resonance and material gain peak redshift into perfect alignment) respectively. In both cases as the OC is increased for a given number of QWs the threshold increases due to greater round-trip losses. As the number of QWs increases from one the threshold initially decreases due to the increased modal gain of the structure. At low numbers of QWs the gain structure has a very high threshold due to the logarithmic dependence of gain upon carrier density, see equation (42), so an extremely high carrier density is required to balance the system losses. Referring to equation (43), as  $N_w$  is increased  $N_{th}$  decreases however each QW must be pumped to a carrier density above  $N_0$ . From equation (43) as  $N_w$  increases  $N_{th} \rightarrow N_0$  and as a result  $\tau(N_{th}) \rightarrow \tau(N_0)$  (a constant value). Therefore as  $N_w$  increases, equation (44) shows that  $P_{th}$  develops a linear dependence on  $N_w$ . The logarithmic dependence of the material gain and the transition to a linear dependence on  $N_w$  of  $P_{th}$  results in there being a minimum threshold value for a specific number of QWs, for a given input pump spot size.

For a given OC and number of QWs the condition of the VECSEL operating exactly on the material gain peak, Fig. 18 b), results in a lower threshold due to the lower transparency carrier density in this regime and the significantly larger amplification possible in comparison to the operation at 565 nm gain values, in Fig. 18 a).

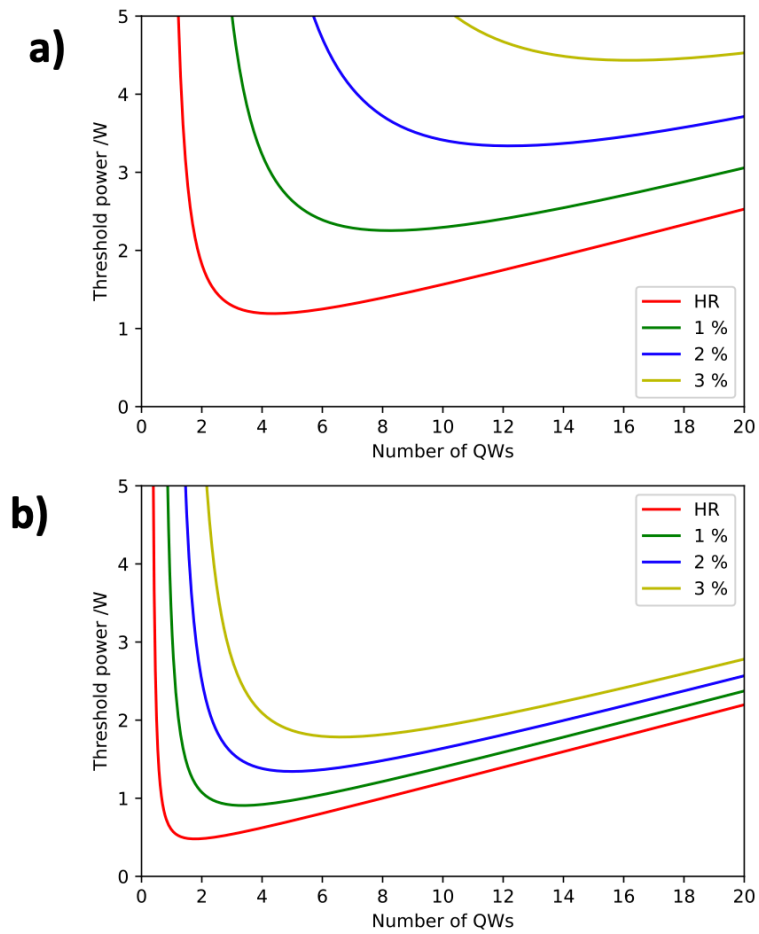


**Figure 18.** Threshold absorbed input power as a function of the number of QWs plotted for **a)** the 565 nm gain case ( $N_0 = 5.908 \times 10^{24} \text{ m}^{-3}$  and  $g_0 = 3428 \text{ cm}^{-1}$ ) and **b)** the gain peak case ( $N_0 = 5.864 \times 10^{24} \text{ m}^{-3}$  and  $g_0 = 8386 \text{ cm}^{-1}$ ). The output coupling is varied between high reflectivity (HR) and 3 %. The modelling is completed with an 80  $\mu\text{m}$  pump spot diameter and a maximum absorbed input power of 5 W.

The Kuznetsov analysis can also be used to determine the number of QWs required to reach a specified output power for a given maximum input pump power.

Fig. 19 a) and b) show output power as a function of output coupling (OC) and the number of QWs in the gain structure for the 565 nm and peak material gain case respectively, with a maximum absorbed pump power of 5 W.

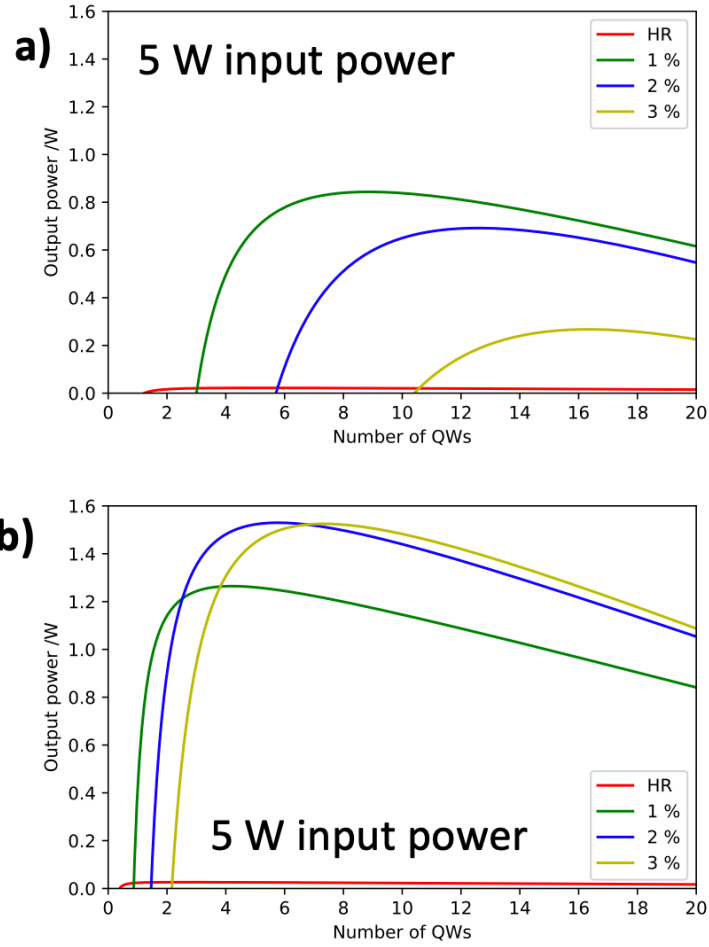


**Figure 19.** Output power as a function of the number of QWs plotted for **a)** the 565 nm gain case ( $N_0 = 5.908 \times 10^{24} \text{ m}^{-3}$  and  $g_0 = 3428 \text{ cm}^{-1}$ ) and **b)** the gain peak case ( $N_0 = 5.864 \times 10^{24} \text{ m}^{-3}$  and  $g_0 = 8386 \text{ cm}^{-1}$ ). The output coupling is varied between high reflectivity (HR) and 3 %. The modelling is completed with an 80  $\mu\text{m}$  pump spot diameter and a maximum absorbed input power of 5 W.

In both cases the HR output coupler has a very low output power due to the low  $\eta_{out}$  in this configuration. Irrespective of OC, as the number of QWs increases the output power increases to a maximum value, due to the reduction in threshold initially, with increasing the number of QWs beyond this adding QWs reduces the output power due to a reduced carrier density per well and a greater threshold requirement. For the 565 nm and peak material gain cases the maximum output power is achieved at 1 % and 3 % OC respectively. The higher gain of the peak material gain case gives this regime a greater resistance to optical losses and so can also tolerate a greater  $\eta_{out}$ , favouring higher OC for maximum output power. If the increase in OC

is too high, as in the 3 % OC for the 565 nm gain case, the maximum output power decreases due to the large increase in the threshold power.

Given that the II-VI VECSEL is an undemonstrated laser system loss tolerance has been selected as the priority design criterion, with the chosen structure determined from the lower gain scenario presented in Fig. 18 a) and Fig. 19 a). 8 QWs has been selected as the number of QWs as this format can resist total roundtrip losses (OC and resonator losses) of around 3 % and still provide a laser demonstration with 5 W of absorbed input power. Additionally, the 8 QW structure is calculated to have the highest output power at 1 % OC of 840 mW. Adding more QWs would further improve the loss tolerance but would raise the threshold and increase the growth complexity. For initial laser testing HR mirrors will be used to reduce roundtrip losses and this results in a predicted threshold of around 1.39 W with an 80  $\mu\text{m}$  pump spot, well within the available pump power.

The predicted power transfer for an 8 QW gain structure is plotted in Fig. 20 a) and b) for the 565 nm and peak material gain case respectively and the maximum output power and threshold absorbed input power as a function of OC are summarized in Table 2. It should be noted that the power transfer model used here has no sub-cavity effect modelling or thermal dependence and so the thermal rollover is not accounted for, which will decrease the output power in a real system. Additionally, the real performance of the II-VI DBR-free VECSEL depends on the material growth quality as the radiative efficiency and charge carrier lifetime are dependent on the  $A$ ,  $B$ , and  $C$  coefficients.

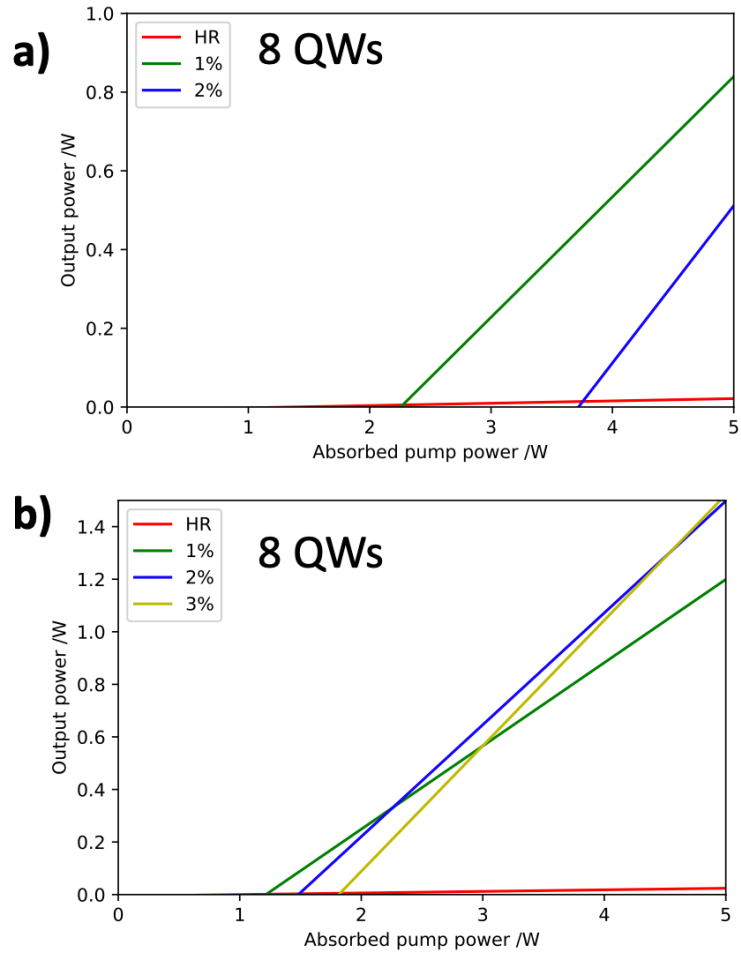


**Figure 20.** The predicted power transfers of an 8 QW ZnCdSe/ZnCdMgSe VECSEL structure plotted for **a)** the 565 nm gain case ( $N_0 = 5.908 \times 10^{24} \text{ m}^{-3}$  and  $g_0 = 3428 \text{ cm}^{-1}$ ) and **b)** the gain peak case ( $N_0 = 5.864 \times 10^{24} \text{ m}^{-3}$  and  $g_0 = 8386 \text{ cm}^{-1}$ ). The output coupling is varied between high reflectivity (HR) and 3 %. The modelling is completed with an 80  $\mu\text{m}$  pump spot diameter and a maximum absorbed input power of 5 W. The 565 nm gain case does not reach threshold with 3 % OC under these pumping conditions.

The predicted power transfers show similar performance to reported (Al)InGaP DBR-free VECSELs [33], with an important difference that the II-VI DBR-free VECSEL has 8 QWs and not 20 QWs as per the (Al)InGaP demonstration [33]. At 545.9 nm  $\text{Pr}^{3+}$  lasers have reported a slope efficiency,  $\eta_s = 52.1 \%$  in terms of absorbed pump power [34], and from the above analysis  $\eta_s = 40.0 \%$  in the 565 nm gain case with 2 % OC and 47.8 % in the peak material gain case with 3 % OC, showing potentially comparable performance. The main advantage of the proposed II-VI DBR-free VECSEL is the possibility to take advantage of the low noise and intrinsic narrow linewidth of VECSELs with the spectral coverage of the ZnCdMgSe-on-InP material system, which is not limited to discrete atomic transitions.



**Table 2.** Summary of the calculated threshold absorbed input power and the maximum output power with 5 W absorbed pump power of 447 nm optical pumping and an 80  $\mu\text{m}$  pump spot diameter for the 8 QW design.

Output coupler reflectivity /%	565 nm $N_0 = 5.908 \times 10^{24} \text{ m}^{-3}$ $g_0 = 3428 \text{ cm}^{-1}$		Material gain peak $N_0 = 5.864 \times 10^{24} \text{ m}^{-3}$ $g_0 = 8386 \text{ cm}^{-1}$	
	Threshold power /W	Maximum output power /W	Threshold power /W	Maximum output power /W
99.99 (HR)	1.39	0.02	1.00	0.02
99.0	2.25	0.84	1.21	1.20
98.0	3.72	0.51	1.48	1.50
97.0	6.23	N/A	1.81	1.52

## 2.6 Finalized design for the optimum II-VI DBR-free gain structure

Given the design criteria discussed in the previous sections and the results of the calculations in Section 2.5, a II-VI DBR-free VECSEL structure design is outlined in this section. The design of the II-VI gain structure must account for the short absorption length of the 447 nm pump wavelength, which limits the length of the active region of the structure to around 500 nm. The absorption of the pump light can be modelled by the Beer-Lambert law as

$$I(z) = I_0 \exp(-\alpha z) \quad (58)$$

where  $I(z)$  is the intensity of the light as a function of the propagation distance,  $z$ ,  $I_0$  is the input intensity (which is taken as unity for the purposes of this investigation) and  $\alpha$  is the absorption coefficient, which can be weighted by the geometry and composition of the structure. The pump intensity is proportional to  $|E|^2$  of the pump light electric field.

Given that  $\alpha \approx 2.5 \times 10^6 \text{ m}^{-1}$  at 447 nm for  $\text{Zn}_{0.3}\text{Cd}_{0.28}\text{Mg}_{0.42}\text{Se}$  [35], this limits the gain structure to around 5 antinodes at the laser wavelength and so the 8 QWs from the solution of the Kuznetsov analysis need to be arranged within an RPG format within this length. The optimum design therefore has the 8 QWs arranged as four pairs, one pair per antinode. In 532-nm-pumped AlInGaP VECSELs, where  $\alpha \approx 2.4 \times 10^6 \text{ m}^{-1}$  at 532 nm, QW pairs are commonly used [36,37] and so due to the absorption coefficient equivalence for the

ZnCdMgSe and AlGaInP material systems the QW pairs are likely the best arrangement for a II-VI DBR-free VECSEL. Mg-free capping layers are included in the growth to prevent the oxidation of the structure, which is mostly Mg-containing  $\text{Zn}_{0.3}\text{Cd}_{0.28}\text{Mg}_{0.42}\text{Se}$ . The exact structures that were designed, grown and tested are presented in Chapter 5.

The suggested optimum design is shown in Fig. 21, with the  $|E|^2$  of the resonant laser mode and the exponential decay of the 447 nm pump light due to optical absorption. Any transmitted pump light could be reimaged back onto the membrane.

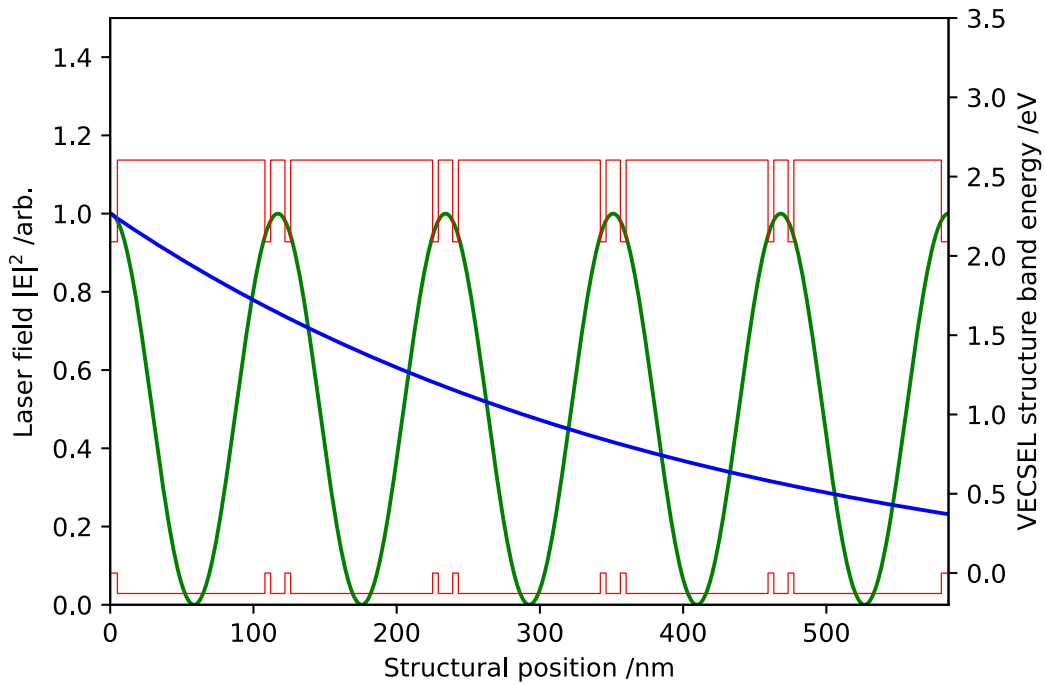


**Figure 21.** Conduction and valence band edge profiles of the suggested 8 QW II-VI DBR-free VECSEL structure with the  $|E|^2$  of the laser standing wave (green line and 565 nm) and the decay of the  $|E|^2$  of the pump (blue line and 447 nm). Note that the laser electric field is a cosine plot and not a finite element method calculation.  $\alpha \approx 2.5 \times 10^6 \text{ m}^{-1}$  has been used as an estimate for ZnCdMgSe at 447 nm based on reference [35].

## 2.7 Future perspectives

A main effort for future work should focus on experimental confirmation of the material parameters in Section 2.1 along with measurements of the TE material gain spectrum of the II-VI QWs to determine the accuracy of the simple modelling completed here. This could include the introduction of small amounts of compressive strain in both the model and future growths, as determined via X-ray diffraction measurements. The design and performance of the II-VI DBR-free VECSEL could be assisted greatly by precise determination of the

temperature dependence and dispersion relations of the refractive index, as a function of composition for the ternary and quaternary alloys. The under-etching and transfer printing methods of epitaxial lift-off developed in Chapter 4 will benefit efforts to determine the gain spectrum and optical properties of the II-VI materials as very high-quality membranes will be required so that processing-induced damage does not affect the results.

The gain model could be enhanced further by calculating more accurate band structures using the  $k \cdot p$  method and by accounting for more complicated many body and multiband effects using the semiconductor Bloch equations [31]. To further analyse the potential II-VI VECSEL performance the linewidth enhancement factor, which quantifies the coupling of intensity and phase noise in semiconductor lasers, could also be calculated to assess the linewidth limit of this laser system [38,39]. The Kuznetsov model assumes that the injected charge carrier distribution is uniform throughout the sample, which for 447 nm pumping is not the case and could be amended by including the charge carrier mobility of the gain structure material and by weighting the carrier concentrations of individual, successive QWs when the number of QWs is varied during the analysis.

## 2.8 Conclusion

Starting with the determination of the fundamental material parameters of the novel ZnCdMgSe-on-InP material system, the electronic transitions of a ZnCdSe QW with ZnCdMgSe barriers were calculated and used to design a QW unit with an  $n = 1$  recombination with transition energy equivalent to a photon wavelength of 565 nm. The material gain spectrum of the QW unit was calculated, accounting for transition broadening, allowing for the determination of the  $g_0$  and  $N_0$  parameters of the ZnCdSe/ZnCdMgSe QW which were used within the Kuznetsov modelling. The predicted PL spectrum of a sample was calculated and was blue-shifted in comparison to experimentally measured PL, likely due to QW variance and sample heating during PL measurements. The Kuznetsov analysis predicted a maximum output power of 840 mW, with 5 W absorbed pump power with 447 nm optical pumping, for the 565 nm gain case. The Kuznetsov analysis predicted a maximum output power of 1.52 W, with 5 W absorbed pump power with 447 nm optical pumping, for operation at the gain peak at around 560 nm. A candidate II-VI DBR-free VECSEL gain structure of eight QWs arranged into a resonant periodic gain format of four pairs of QWs, has been determined from a Kuznetsov analysis to be a promising gain structure design for demonstrating laser performance from a II-VI DBR-free VECSEL due to its resistance to optical losses. The focus

of future work should be on improving the model accuracy by adding microscopic effects and by confirming the model outputs with experimental verification of the TE gain spectrum.

## References

1. M. Kuznetsov, F. Hakimi, R. Sprague, and A. Mooradian, "Design and characteristics of high-power ( $>0.5$ -W CW) diode-pumped vertical-external-cavity surface-emitting semiconductor lasers with circular TEM<sub>00</sub> beams," *IEEE J. Sel. Top. Quantum Electron.* **5**(3), 561–573 (1999).
2. O. Maksimov, S. P. Guo, L. Zeng, M. C. Tamargo, F. C. Peiris, and J. K. Furdyna, "Distributed Bragg reflectors based on (Zn,Cd,Mg)Se for use in the visible spectral range," *J. Appl. Phys.* **89**(4), 2202–2207 (2001).
3. I. Hernández-Calderón, "Optical properties and electronic structure of wide band gap II-VI semiconductors," in *II-VI Semiconductor Materials and Their Applications*, M.O. Manasreh, ed., Volume 12 (n.d.).
4. M. Soheli, X. Zhou, H. Lu, M. N. Perez-Paz, M. Tamargo, and M. Muñoz, "Optical characterization and evaluation of the conduction band offset for ZnCdSe/ZnMgSe quantum wells grown on InP(001) by molecular-beam epitaxy," in *Journal of Vacuum Science and Technology B: Microelectronics and Nanometer Structures* (American Vacuum Society AVS, 2005), **23**(3), pp. 1209–1211.
5. M. Muñoz, H. Lu, X. Zhou, M. C. Tamargo, and F. H. Pollak, "Band offset determination of Zn<sub>0.53</sub>Cd<sub>0.47</sub>Se/Zn<sub>0.29</sub>Cd<sub>0.24</sub>Mg<sub>0.47</sub>Se," *Appl. Phys. Lett.* **83**(10), 1995–1997 (2003).
6. H. Lu, A. Shen, M. Muñoz, M. N. Perez-Paz, M. Soheli, S. K. Zhang, R. R. Alfano, and M. C. Tamargo, "Zn<sub>x</sub>Cd<sub>1-x</sub>Se/Zn<sub>x</sub>'Cdy'Mg<sub>1-x</sub>'-y' Se multi-quantum well structures for intersubband devices grown by MBE," *Phys. status solidi* **243**(4), 868–872 (2006).
7. J D Wu, J W Lin, Y S Huang, W O Charles, A Shen, Q Zhang, and M C Tamargo, "Characterization of a Zn<sub>x</sub>Cd<sub>1-x</sub>Se/Zn<sub>x</sub>'Cdy'Mg<sub>1-x</sub>'-y' Se multiple quantum well structure for mid-infrared device applications by contactless electroreflectance and Fourier transform infrared spectroscopy - IOPscience," <https://iopscience.iop.org/article/10.1088/0022-3727/42/16/165102>.
8. W. O. Charles, K. J. Franz, A. Shen, Q. Zhang, Y. Gong, B. Li, C. Gmachl, and M. C. Tamargo, "Molecular beam epitaxy growth of Zn<sub>x</sub>Cd<sub>(1-x)</sub>Se/Zn<sub>x</sub>'Cdy'Mg<sub>(1-x</sub>'-y')Se-InP quantum cascade structures," *J. Cryst. Growth* **310**(24), 5380–5384 (2008).
9. T. A. Garcia, *CCNY Empirical Data* (n.d.).

10. S. Adachi, *Properties of Semiconductor Alloys : Group-IV, III-V and II-VI Semiconductors* (Wiley, 2009).
11. H. Yıldırım, "Exciton binding energies in CdSe/MgSe quantum well structures," *Superlattices Microstruct.* **114**, 207–213 (2018).
12. K. L. Teo, Y. P. Feng, M. F. Li, T. C. Chong, and J. B. Xia, "Band structure of  $Mg_{1-x}Zn_xSySe_{1-y}$ ," *Semicond. Sci. Technol.* **9**(4), 349 (1994).
13. Y. H. Wu, "Structure-Dependent Threshold Current Density for CdZnSe-Based II - VI Semiconductor Lasers," *IEEE J. Quantum Electron.* **30**(7), 1562–1573 (1994).
14. C. Jordan, J. F. Donegan, J. Hegarty, B. J. Roycroft, S. Taniguchi, T. Hino, E. Kato, N. Noguchi, and A. Ishibashi, "Carrier-density dependence of the photoluminescence lifetimes in ZnCdSe/ZnSSe quantum wells at room temperature," *Appl. Phys. Lett.* **74**(22), 3359 (1999).
15. P. M. Young, E. Runge, M. Ziegler, and H. Ehrenreich, "Optical absorption and exciton linewidths of ZnCdSe quantum wells," *Phys. Rev. B* **49**, 15–1994 (1994).
16. G. Zi-zheng, L. Xi-xia, and B. Shi-liang, "Temperature dependence of excitonic transition in ZnSe/ZnCdSe quantum wells," *Optoelectron. Lett.* **1**(3), (2005).
17. S. L. Chuang, *Physics of Photonic Devices*, 2nd ed. (Wiley, 2009).
18. A. R. Adams, "Strained-layer quantum-well lasers," *IEEE J. Sel. Top. Quantum Electron.* **17**(5), 1364–1373 (2011).
19. Y. P. Varshni, "Temperature dependence of the elastic constants," *Phys. Rev. B* **2**(10), 3952–3958 (1970).
20. J.W. Matthews and A.E.Blakeslee, "Defects in epitaxial multilayers: I. Misfit dislocations," *J. Cryst. Growth* **27**, 118 (1974).
21. N. J. Ekins-Daukes, K. Kawaguchi, and J. Zhang, "Strain-Balanced Criteria for Multiple Quantum Well Structures and Its Signature in X-ray Rocking Curves †," *Cryst. Growth Des.* **2**(4), (2002).
22. L. . B. Freund and S. Suresh, *Thin Film Materials: Stress, Defect Formation and Surface Evolution* (Cambridge University Press, 2003).
23. D. P. Bour, R. S. Geels, D. W. Treat, T. L. Paoli, F. Ponce, R. L. Thornton, B. S. Krusor, R. D. Bringans, and D. F. Welch, "Strained Ga/sub x/In/sub 1-x/P/(AlGa)/sub 0.5/In/sub 0.5/P heterostructures and quantum-well laser diodes," *IEEE J. Quantum Electron.* **30**(2), 593–607 (1994).
24. E. Hecht, *Optics*, 4th ed. (2002).
25. F. L. Pedrotti and L. S. Pedrotti, *Introduction to Optics*, 2nd ed. (Englewood Cliffs, 1993).

26. S. W. Corzine, R. S. Geels, J. W. Scott, R. H. Yan, and L. A. Coldren, "Design of Fabry-Perot Surface-Emitting Lasers with a Periodic Gain Structure," *IEEE J. Quantum Electron.* **25**(6), 1513–1524 (1989).
27. A. Garnache, A. A. Kachanov, F. Stoeckel, and R. Houdré, "Diode-pumped broadband vertical-external-cavity surface-emitting semiconductor laser applied to high-sensitivity intracavity absorption spectroscopy," *J. Opt. Soc. Am. B* **17**(9), 1589 (2000).
28. A. J. Maclean, R. B. Birch, P. W. Roth, A. J. Kemp, and D. Burns, "Limits on efficiency and power scaling in semiconductor disk lasers with diamond heatspreaders," *J. Opt. Soc. Am. B* **26**(12), 2228 (2009).
29. T. Makino, "Analytical formulas for the optical gain of quantum wells," *IEEE J. Quantum Electron.* **32**(3), 493–501 (1996).
30. B. E. Jones, P. J. Schlosser, J. De Jesus, T. A. Garcia, M. C. Tamargo, and J. E. Hastie, "Processing and characterisation of II–VI ZnCdMgSe thin film gain structures," *Thin Solid Films* **590**, 84–89 (2015).
31. J. V. Moloney, J. Hader, and S. W. Koch, "Quantum design of semiconductor active materials: laser and amplifier applications," *Laser Photonics Rev.* **1**(1), 24–43 (2007).
32. M. Mangold, V. J. Wittwer, O. D. Sieber, M. Hoffmann, I. L. Krestnikov, D. A. Livshits, M. Golling, T. Südmeier, and U. Keller, "VECSEL gain characterization," *Opt. Express* **20**(4), 4136 (2012).
33. H. Kahle, C. M. N. Mateo, U. Brauch, P. Tatar-Mathes, R. Bek, M. Jetter, T. Graf, and P. Michler, "Semiconductor membrane external-cavity surface-emitting laser (MECSEL)," *Optica* **3**(12), 1506 (2016).
34. G. Huber, P. Metz, and T. Gün, "Power scaling of laser diode pumped  $\text{Pr}^{3+}:\text{LiYF}_4$  cw lasers: efficient laser operation at 522.6 nm, 545.9 nm, 607.2 nm, and 639.5 nm," *Opt. Lett.* Vol. 36, Issue 6, pp. 1002-1004 **36**(6), 1002–1004 (2011).
35. H. Hattori, I. Nomura, T. Nagano, H. Shimbo, M. Haraguchi, T. Morita, A. Kikuchi, and K. Kishino, "Absorption Coefficient Measurements of MgZnCdSe II-VI Compounds on InP Substrates and Quantum Confined Stark Effect in ZnCdSe/MgZnCdSe Multiple Quantum Wells," *Jp. Appl. Phys.* **37**, 1465–1469 (1998).
36. P. H. Moriya, Y. Singh, K. Bongs, and J. E. Hastie, "Sub-kHz-linewidth VECSELs for cold atom experiments," *Opt. Express* **28**(11), 15943 (2020).
37. P. H. Moriya, R. Casula, G. A. Chappell, D. C. Parrotta, S. Ranta, H. Kahle, M. Guina, and J. E. Hastie, "InGaN-diode-pumped AlGaInP VECSEL with sub-kHz

- linewidth at 689 nm," Opt. Express **29**(3), (2021).
38. W.-P. Hong and S.-H. Park, "Linewidth enhancement factor of hybrid green InGaN/MgZnO quantum well structures," Phys. E Low-dimensional Syst. Nanostructures 114678 (2021).
  39. R. Paschotta, "Linewidth enhancement factor," [https://www.rp-photonics.com/linewidth\\_enhancement\\_factor.html](https://www.rp-photonics.com/linewidth_enhancement_factor.html).

# 3. II-VI VECSEL development

## Chapter overview

In this chapter the progress towards building a II-VI VECSEL is reported. The II-VI VECSEL can be barrier-pumped at 447 nm, using InGaN laser diodes, or in-well-pumped at 532 nm using frequency-converted semiconductor lasers or solid-state lasers. A blue, InGaN diode-pumping system was developed and used to demonstrate a visible, diode-pumped III-V VECSEL (AlGaInP-based) to target emission at 689 nm (wavelength required in a parallel project for the cooling transition of neutral strontium atoms). Having developed and optimised the 447 nm pump and optics for a VECSEL gain structure with known laser performance, a two-mirror concentric laser resonator and a DBR-free sample mount were designed for the II-VI VECSEL. Full InP substrate removal from the ZnCdSe/ZnCdMgSe structures is optimized and used to process gain structures, eventually yielding  $\text{cm}^2$  membrane sizes. The gain structure design and growth is iteratively improved and the addition of a large II-VI buffer layer, with a 30 nm – 40 nm InGaAs buffer layer, offers improved II-VI material quality. The epitaxial lift-off (ELO) results of key structures are presented and photoluminescence is used to characterize the membranes. Membranes on diamond heatspreaders are tested within a resonator, however the laser threshold is not achieved with the II-VI device.

## 3.1 Context and goals

The first DBR-free VECSEL was demonstrated by Yang *et al* [1,2], and was based on InGaAs QWs with strain compensated GaAsP barriers and InGaP window layers. The gain structure was held in black wax and liberated from its GaAs substrate by laterally etching an AlAs release layer using diluted hydrofluoric acid [2]. Once the substrate was removed the gain structure was bonded onto a diamond or SiC optically transparent heatspreader [2]. This work, and subsequent work by Yang *et al* marked an important step in demonstrating the benefits of DBR-free VECSELs over standard DBR-based VECSELs: improved thermal management, high tunability, the potential for monolithic integration, simplified epitaxial growth and targeting hard-to-reach wavelengths where high reflectivity DBRs are not possible [2–4]. Additionally, these works showed that ELO and microfabrication techniques could be used to enhance the performance of VECSELs and also highlighted that high membrane and heatspreader bonding quality are essential to DBR-free VECSEL performance.



The first visible DBR-free VECSEL was reported by Kahle et al [5] and had an output power of 595 mW at a 657 nm wavelength. The gain structure used was GaInP/AlInGaP grown on GaAs and made use of an AlAs release layer. The majority of ELO with DBR-free VECSELs is centred on samples grown on GaAs and using AlAs release layers, selectively etched away with an HF-based etchant [2,4,5]. Recent progress on DBR-free VECSELs has seen the ELO of gain structures from InP substrates, using wet etchants to selectively remove the InP substrate from an InGaAs-capped structure [6,7].

Specific steps towards VECSEL-to-diamond heterogenous integration, without using release layers, have been reported and exploit Ag-based bonding of flip chip VECSEL structures to diamond and removing the entire substrate using mechanical polishing and selective wet etching [8,9]. The downside to this methodology is that the entire substrate is removed and so substrate recycling is impossible, and the integration possibilities of the VECSEL structure to substrates other than diamond is not necessarily feasible.

Testing of II-VI DBR-free VECSEL structures requires the removal of the opaque InP substrate. In this chapter, the full substrate removal technique utilized in references [10,11] is applied to produce membranes for laser testing. Full substrate removal is the most common ELO method for II-VI-on-InP. Previous demonstrations of full substrate removal have shown the construction of ZnCdMgSe colour converters [12–14] and high quality membranes of mm length scales [10,11].

Full substrate removal is fast and therefore allows for a greater testing throughput than the suspension method developed in Chapter 4. The full substrate removal method focusses on a multi-step strategy of substrate removal via mechanical polishing and wet etching, followed by buffer layer wet etching [10,11]. Often the II-VI structure is held in wax and released using solvents following the substrate removal. The goals for this section of work were to obtain a high quality, well bonded II-VI membrane on diamond, to optimize the II-VI gain structure and to develop the pump optics and resonator for a II-VI VECSEL. The next section details the design of a laser cavity and pump optics, which can be used to test II-VI VECSEL membranes.

## 3.2 Pump optics and laser cavity design

### 3.2.1 Barrier and in-well pumping capabilities

For VECSELs, the highest overall system efficiency and lowest pump complexity is achieved when using laser diodes to optically inject charge carriers into the barriers of the QWs of the gain structure. This is the result of the high wall-plug efficiency of laser diodes and the strong absorption of the shorter pump wavelengths (with a photon energy exceeding the barrier bandgap) within the gain structure. The wide bandgap, ZnCdMgSe material system suits barrier pumping with efficient, 447 nm, InGaN-based laser diode sources, and hence this is selected as the pump mechanism for the testing of the II-VI VECSEL gain structures.

The wide bandgap of the ZnCdSe QW layer enables the use of 532 nm laser sources for in-well pumping, injecting charge carriers directly into the QWs. The first demonstration of optically in-well pumped VECSELs is reported in reference [15], and developed further in reference [16], and used a fibre-coupled 808 nm laser diode to pump an 850-nm-emitting VECSEL. In-well pump schemes will sometimes require the use of non-diode pump sources, such as in reference [17] where a dye laser is used as the in-well pump, resulting in an improved slope efficiency (when comparing output power to absorbed pump power) and thermal management, in comparison to barrier pumping with 532 nm [17]. The use of the dye laser as pump source, however, reduces the overall system efficiency.

The longer pump wavelengths used within in-well pumping reduces the quantum defect,  $\eta$ , which is defined by

$$\eta = 1 - \frac{\lambda_p}{\lambda_L}, \quad (1)$$

where  $\lambda_p$  is the pump wavelength and  $\lambda_L$  is the laser wavelength (see Section 2.5.1 for additional details on VECSEL efficiency). Given the intended laser wavelength of 565 nm, in-well pumping offers a significant reduction in the quantum defect ( $\eta = 0.06$  at 532 nm, compared to  $\eta = 0.21$  at 447 nm) and therefore the heat load on the laser (see Section 2.4.2); however, the low single-pass absorption efficiency necessitates additional optics to re-image the transmitted and reflected pump light, which adds to the laser design complexity. High quality frequency-doubled solid-state laser sources operating at 532 nm are available and laser diodes operating at 532 nm are developing in their maturity, however the additional system complexity and reduced wall-plug efficiency, makes in-well pumping less desirable for the II-VI VECSEL, when compared to 447 nm barrier pumping with laser diodes. In the next sub-

section, a 447 nm InGaN-diode-based pump optics system is developed and tested on a working, well-understood III-V VECSEL sample.

### 3.2.2 InGaN-diode-pumped red VECSEL development

The improved output powers of commercially available InGaN-based laser diodes offer the opportunity to develop diode pump systems operating at 447 nm, which could be used to optically inject charge carriers into the barrier of a II-VI, ZnCdMgSe-based VECSEL. Given that the modelling completed in Chapter 2 assumed an 80- $\mu\text{m}$ -diameter pump spot, an initial test needed to be completed on a III-V VECSEL system, with well-understood material properties, to demonstrate that 447 nm diode pumping with an 80- $\mu\text{m}$ -diameter pump spot could be used to reach the laser threshold. In order to facilitate the development of the diode pump optics for the II-VI DBR-free VECSEL, a project to develop an InGaN-diode-pumped, GaInP/AlGaInP, VECSEL was decided as an appropriate test, given that this material system had been demonstrated in 447-nm-diode-pumped VECSELs with a much smaller pump spot and at low pump powers ( $< 500$  mW) [18]. An additional goal for this work was to tune the diode-pumped VECSEL to a wavelength of 689 nm for targeting the neutral Sr cooling transition line.

The output beam of a 447 nm Laserglow LRD-0447 InGaN-diode was comprised of multiple stripes due to the multiple emitters and was elliptical (4.0 mm  $\times$  3.1 mm). The output diameter was reduced using a Keplerian telescope ( $f = 250$  mm into  $f = 26$  mm) and then the sagittal and tangential components of the beam were shaped separately to reduce the ellipticity. The tangential component (perpendicular to table top) was focussed onto the sample using a 19 mm focusing lens and the sagittal component (in the plane of the table top) was passed through a slightly length offset Keplerian telescope comprised of a 200 mm cylindrical lens and the 19 mm focussing lens. These pump optics give a pump spot of 107  $\mu\text{m}$   $\times$  78  $\mu\text{m}$ , with at least the minor axis of the elliptical pump spot matching the 80- $\mu\text{m}$ -diameter pump spot modelled in Chapter 2.

The laser resonator, shown in Fig. 1 a), was designed using the Laser Canvas 5 software, an ABCD matrix model which calculates the beam waist of the sagittal and tangential components of a propagating beam. The VECSEL structure was modelled as a plane mirror and the resonator was comprised of an additional planoconcave mirror and a plane output coupler. The positions of the components and the angle between the two laser arms of the three-mirror resonator design were optimized to obtain a beam waist on the VECSEL sample

which was approximately mode-matched to the 80- $\mu\text{m}$ -diameter pump spot modelled in Chapter 2. The final resonator design was a three-mirror cavity comprised of the VECSEL gain mirror, an  $r = -100$  mm curved mirror 52 mm from the VECSEL gain structure and a plane-mirror 1 % output coupler 189 mm from the folding mirror, which yields a calculated  $72.8 \mu\text{m} \times 69.4 \mu\text{m}$  mode diameter on the VECSEL chip. The laser cavity is approximately mode matched to the minor axis of the elliptical pump spot.

Fig. 1 b) shows the power transfer of the diode-pumped VECSEL at a 10 °C heatsink temperature, without a birefringent filter (BRF) and with 1 % output coupling. The maximum output power is 105 mW, an order of magnitude improvement on published results at the time of the work [18], with a threshold of  $32.6 \text{ MWm}^{-2}$ . Table 1 shows a detailed examination of the heatsink temperature, maximum output power, threshold pump power and intensity, pump spot diameter, pump angle, slope efficiency and the calculated intra-cavity power of the diode-pumped VECSEL, and is compared to reference [18] (the only other reported diode-pumped red-emitting VECSEL at the time the work was completed). When compared to [18], these results show a 44 % reduction in pump intensity and a 38 % improvement in slope efficiency, both of which are likely due to the improved gain structure quality and larger pump spot, which improves thermal management [19].

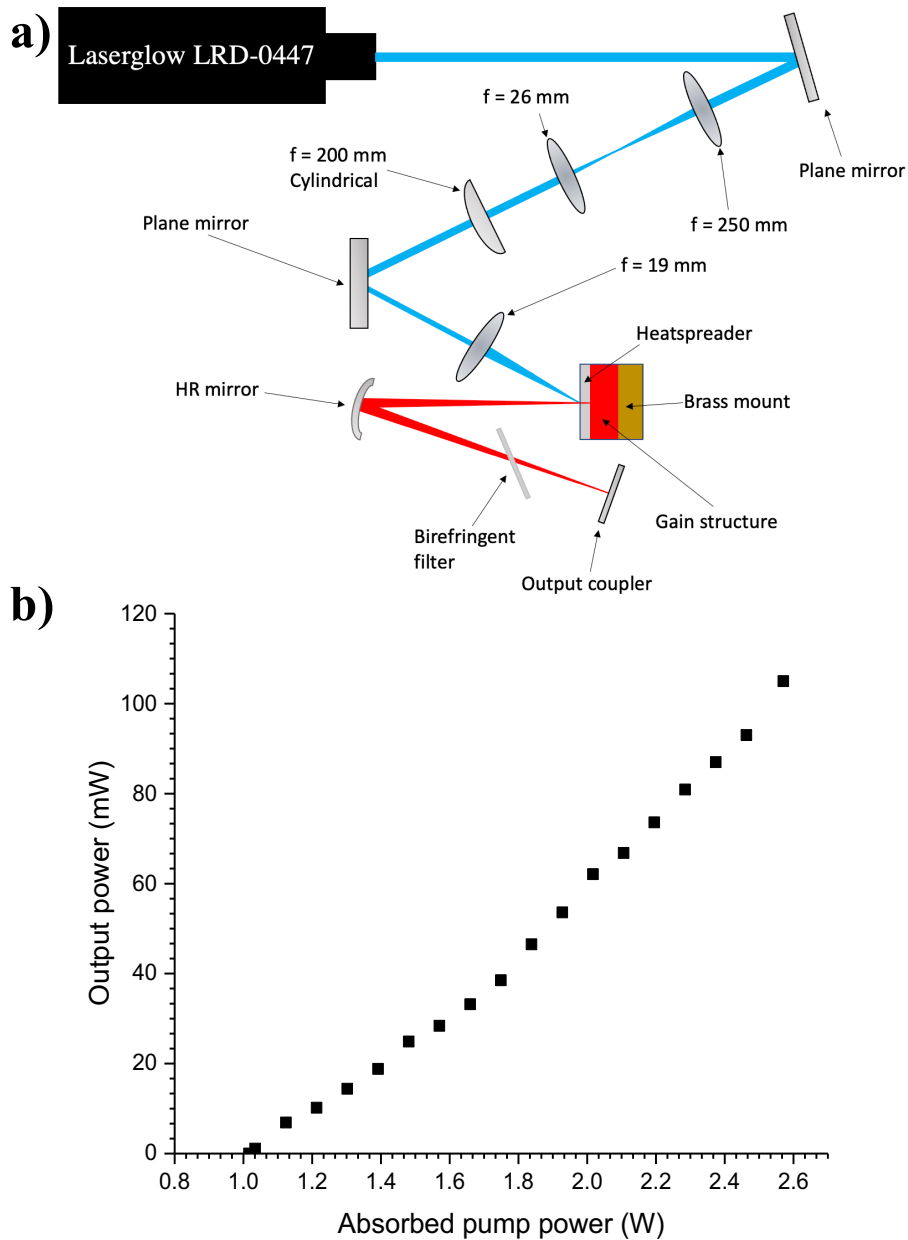


**Figure 1. a)** Schematic of the prototype InGaN diode-pumped VECSEL along with **b)** the VECSEL power transfer at  $10 \text{ }^\circ\text{C}$  heatsink temperature, no BRF and 1 % output coupling.

With the BRF added the VECSEL was tuned to give  $33 \text{ mW}$  at  $688.98 \text{ nm}$ , demonstrating the capability to tune the system to the correct wavelength range. This setup and these results were improved upon, by Dr P Moriya and Dr R Casula, with the development of a fibre-coupled  $447 \text{ nm}$  single emitter laser diode source, the output of which coupled be imaged onto the VECSEL sample using a fibre-coupled matched lens pair. We report the final system in reference [20], which also details the VECSEL gain structure design.

**Table 1.** Detailed power transfer measurements of the blue diode-pumped red SDL

	<b>Output coupler</b>					<b>Previously reported [18] (3% OC)</b>
	<b>T = 1 %</b>		<b>T = 2 %</b>	<b>T = 3 %</b>	<b>HR</b>	
<b>Heatsink temperature /°C</b>	5	10	5	5	5	5
<b>Maximum output power /mW</b>	73	105	74	64	26	17
<b>Threshold pump power /W</b>	1.28	1.03	1.45	1.84	0.92	0.34
<b>Pump spot diameter /<math>\mu\text{m}</math></b>	107 $\times$ 78					32 $\times$ 32
<b>Pump angle /°</b>	34					10
<b>Threshold pump power density /<math>\text{MWm}^{-2}</math></b>	40.5	32.6	45.8	58.2	29.1	104.1
<b>Slope efficiency /%</b>	5.7	6.8	6.6	8.8	1.6	6.4
<b>Calculated intra-cavity power /W</b>	7.2	10.4	3.6	2.1	52.0	0.55

Following on from the successful development of the pump optics system, the next sub-section details the design of the DBR-free resonator for a II-VI VECSEL.

### 3.2.3 DBR-free laser cavity designs and alignment

DBR-free VECSELs have been reported to operate with two-mirror concentric and confocal resonators (as discussed in Section 1.5.3) and three-mirror resonators [21]. The main criterion considered, when designing the resonator for this project, is mode matching with the pump. Following the modelling in Chapter 2, the pump spot size on the gain structure is set to around 80  $\mu\text{m}$  in diameter and so the resonator mode must be closely matched to this value at the DBR-free VECSEL surface. To achieve an 80  $\mu\text{m}$  mode diameter a concentric resonator is the most practical, with the gain structure located at the focal point. Two- and three-mirror resonators can be used, however in this work the majority of cavity designs tested were two-mirror, to minimize degrees of freedom and reduce round trip losses.

The laser cavity designs were completed in the Laser Canvas 5 software, which calculates a stable resonator design using ABCD-matrices. The gain structure and diamond were modelled

as a single 0.5 mm layer with  $n = 2.4$  (500- $\mu\text{m}$ -thick diamond and  $\sim 500\text{-nm}$ -thick II-VI layer modelled as a single layer as the II-VI is three orders of magnitude thinner than the diamond), due to the II-VI and diamond refractive index matching, with the laser wavelength set to 565 nm and the M-squared value taken to be 1.0. Using two planoconcave, 100 mm radius of curvature (ROC) mirrors it is possible to vary the beam waist of the laser mode, where the sample is located, between 53  $\mu\text{m}$  and 83  $\mu\text{m}$  in diameter by varying the spacing between the external mirrors and the total cavity length. An  $\sim 80 \mu\text{m}$  diameter cavity beam waist can be formed with a 198 mm cavity length and a 99 mm spacing ( $L_1$  and  $L_2$ ) between the 100 mm ROC mirrors and the centre of the resonator. The resonator design is shown in Fig. 2 and the design of the mount for the membrane samples is discussed in the next sub-section.

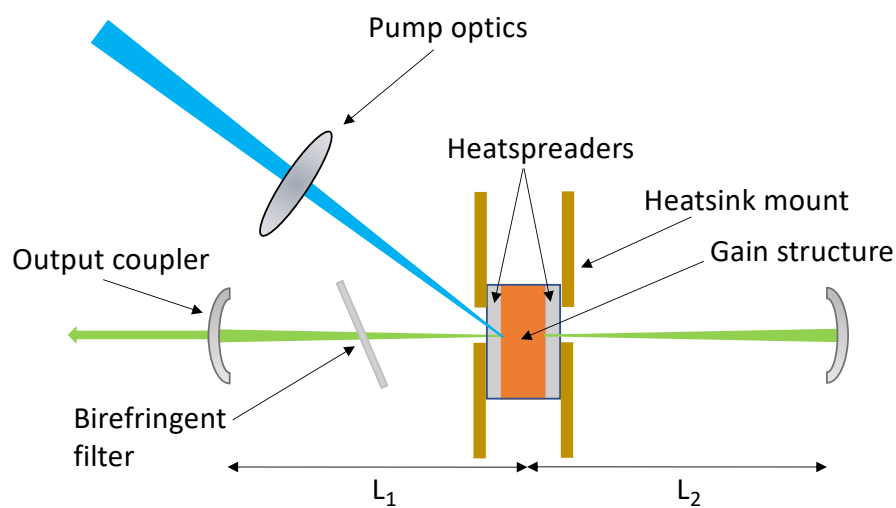


**Figure 2.** The II-VI DBR-free VECSEL design. 447 nm light from a laser diode is imaged onto the bonded II-VI membrane to give an 80  $\mu\text{m}$  pump spot diameter. The distances  $L_1$  and  $L_2$  of the 100 mm ROC concave mirrors from the membrane can be tuned to vary the cavity beam waist to optimise mode-matching. Not to scale.

### 3.2.4 Mounting VECSEL samples

The DBR-free VECSEL mount has been designed to ensure that heat flows from the diamond heatspreaders (by maximizing the diamond-metal surface contact) and that there is space for the short working distance pump optics used in diode-pumping. A new mount was designed with a hexagonally arranged screw system for the sample lid, a smaller profile and a wide opening on either side to allow for wide pump angles. The design for this mount is in the Appendix A3.1. Within the mount a thin layer of indium foil provides thermal contact between

the diamond, which holds the semiconductor gain membrane, and the brass mount (the heatsink).

The DBR-free II-VI QW gain structure at the centre of the concentric resonator in Fig. 2 needs to be a high-quality membrane with excellent thermal contact to an intracavity heatspreader. The following section outlines the full substrate removal epitaxial lift-off (ELO) method for removing the InP substrate from the MBE-grown, II-VI gain structures to produce QW gain membranes. Section 3.3 outlines the deposition of these membranes onto transparent, single crystal diamond heatspreaders and the optimization of the full substrate removal process for the II-VI-on-InP material system.

### **3.3 Full substrate removal optimization**

#### *3.3.1 Methodology and initial results*

A generic process flow for the full InP substrate removal method is shown in Table 2 and was the subject of optimization in order to improve the II-VI membrane quality [11]. Full substrate removal is fast and produces large membranes; however, it has a low yield of useable material, in the case of II-VI-on-InP, and it destroys the entire substrate. The general methodology involves: sample cleaning, mounting the sample to protect the II-VI epilayer, removal of the InP substrate, removal of the InGaAs buffer layer and membrane release.

Initial work following the methodology in Table 2 showed that releasing the membranes from the thick Apiezon black wax, which is typically used in full substrate removal, caused them to shatter due to the sudden strain changes on the sample and the turbulent wax removal. The HCl:H<sub>3</sub>PO<sub>4</sub> etchant often damaged the InGaAs buffer layer and the substrate grinding introduced a tilt to the InP etching surface each time. These steps were varied systematically and discussed below. The membranes produced by this initial method were extremely low quality and heavily contaminated by wax residues and so the full substrate removal process underwent optimization, discussed in the next sub-sections. The next sub-section specifically details the impacts of substrate grinding on the processing.



**Table 2.** Summary of the full substrate removal methodology

<b>Process step</b>	<b>Description</b>
1. Sample preparation	<ul style="list-style-type: none"> <li>• Sample cleaning: acetone, methanol, isopropanol and DI water rinsing</li> </ul>
2. Sample mounting	<ul style="list-style-type: none"> <li>• Bonding wax melted (or photoresist spin coated) onto a silicon carrier wafer</li> <li>• Sample mounted epi-side down onto carrier</li> </ul>
3. InP substrate removal	<ul style="list-style-type: none"> <li>• (Optional) Substrate undergoes mechanical polishing with SiC paper</li> <li>• InP substrate removed using HCl-based etchants to reveal the InGaAs buffer layer</li> </ul>
4. InGaAs buffer layer removal	<ul style="list-style-type: none"> <li>• InGaAs buffer layer removed with a short etch in <math>\text{H}_3\text{PO}_4:\text{H}_2\text{O}_2:\text{H}_2\text{O}</math> (1:1:6)</li> </ul>
5. Membrane release	<ul style="list-style-type: none"> <li>• Solvents used to release membrane from wax or photoresist</li> <li>• Membrane transferred from the solvent and onto a new substrate</li> <li>• Capillary action conforms the membrane to the new substrate surface and Van der Waals bonding holds the membrane in place</li> </ul>

### 3.3.2 Effects of substrate grinding

Substrate grinding is often used to thin substrates using mechanical polishing with an abrasive pad or slurry. Wafers are mounted in wax (the effects of the mounting medium are discussed in the next sub-section) and then ground down to the required thickness, however it is challenging to mount the wafer in the wax without any tilt. Substrate tilt introduced by substrate grinding results in the InGaAs buffer layer being reached at different times across the wafer during the InP wet etch. When the InGaAs buffer layer was exposed to the HCl-based etchants it caused degradation of the epilayer, likely due to defects within the InGaAs. Due to the difficulties with correcting the tilt introduced by the grinding, this was abandoned in favour of using wet etching for the whole substrate removal.

### 3.3.3 Effects of mounting medium

During the full substrate removal photoresist or wax are used as the mounting medium, which protects the epi-side and edges of the gain structure. Once the substrate is removed the

remaining membrane must be removed from the mounting medium for use in a device. The release of the membranes from the wax/photoresist can result in surface damage, contamination and fracturing of the membrane. The choice of mounting medium is essential to give full protection and stability during the substrate removal, whilst allowing easy membrane release afterwards. The mounting media tested and their effects are summarized in Table 3. Glycol phthalate and Microposit S1800-series photoresists were found to yield membranes which could be tested in a VECSEL resonator.

**Table 3.** Summary of the effects of different mounting media on the substrate removal success.

<b>Mounting medium</b>	<b>Removal methods</b>	<b>Effects</b>	<b>Testable membrane produced?</b>
Apiezon Black Wax	Dissolves in toluene.	<ul style="list-style-type: none"> <li>• Difficult to apply precisely</li> <li>• Hard to remove</li> <li>• Causes membrane fracturing during release</li> <li>• Poor adhesion to membrane edges</li> </ul>	No
Crystalbond 555 HMP wax	Dissolves in water.	<ul style="list-style-type: none"> <li>• Easily removed</li> <li>• Poor resistance to acids</li> <li>• Sample compromised during etching</li> </ul>	No
Microposit S1805/S1810 photoresist	Dissolves in solvents. Removal in Matrix asher.	<ul style="list-style-type: none"> <li>• Can be mounted onto carrier wafer or Kapton tape after spin coating</li> <li>• Kapton tape gives better results</li> <li>• Contamination highly likely</li> </ul>	Yes
Logitech glycol phthalate wax	Dissolves in acetone. Removal in Matrix asher.	<ul style="list-style-type: none"> <li>• Very good adhesion to membrane edges</li> <li>• Consistent release in acetone</li> <li>• Can form bubbles in the membranes</li> </ul>	Yes

The wet-etching of the InP substrate was developed alongside the investigations into the impact of substrate grinding and the effects of mounting medium. Section 3.3.4 details the chemistry behind the InP etching with HCl-based etchants and summarizes how etch variants impact the membrane quality produced during the full substrate ELO.

### 3.3.4 Etching the InP substrate

#### 3.3.4.1 Overview

InP has highly direction-dependent wet etch rates for the different faces of its zincblende crystal structure, shown in Fig. 3, and for different etchants [22–25]. Different faces of the InP crystal have different densities of atoms and surface terminations which influence their etch rate.

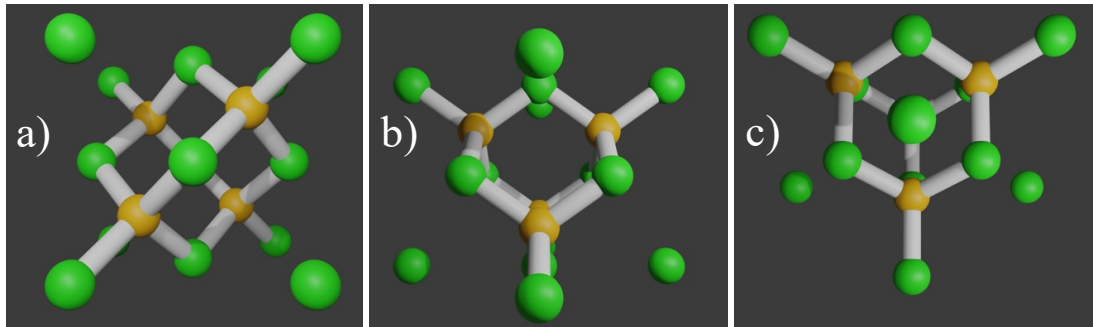


**Figure 3.** The zincblende structure of InP as viewed from **a)** [1 0 0], **b)** [1 1 0] and **c)** [1 1 1]. Green spheres are In atoms and yellow spheres are P atoms.

The etch rate anisotropy in InP arises from the different atomic number densities of the crystallographic faces,  $\frac{2}{a^2}$ ,  $\frac{4}{\sqrt{2}a^2}$  and  $\frac{4}{\sqrt{3}a^2}$  for the (1 0 0), (1 1 0) and (1 1 1) faces respectively, and their surface terminations, see Fig. 4. The (1 1 1) face can have two different surface terminations; a slow etching In-rich face, (1 1 1)A, and a highly reactive P-rich face, (1 1 1)B.

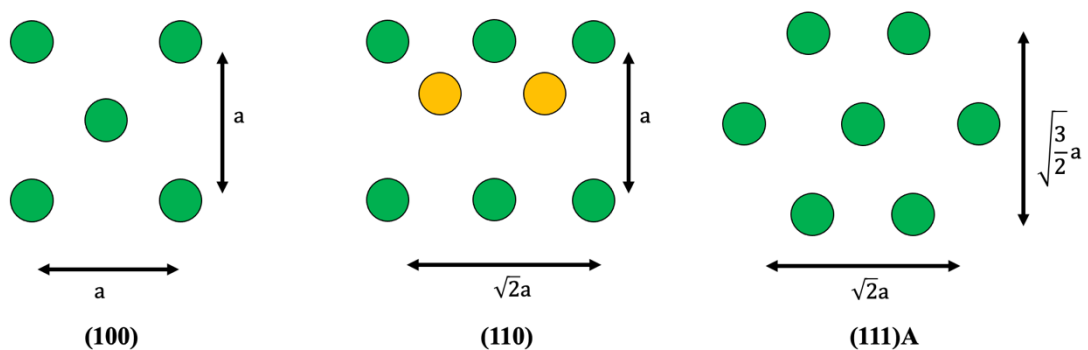
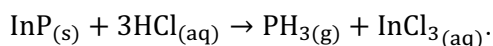


**Figure 4.** The crystalline faces of the three principal orientations of InP; (1 0 0), (1 1 0) and (1 1 1)A. Dimensions are shown in terms of the lattice constant,  $a = 0.587$  nm. Green circles are In atoms and yellow circles are P atoms. The varied atomic densities and surface terminations are the origin of the etch anisotropy.

The wet etching of InP is well-studied, particularly with HCl-based etchants [22,26]. The overall etch reaction of InP with HCl is



The etch rate is controlled by the concentration of HCl, temperature and the availability of In and P (determined by the crystallography) to react with the acid [22]. In the case of removing an InP substrate, phosphoric acid ( $\text{H}_3\text{PO}_4$ ) can be added to the HCl to reduce the aggression of the etch [10].

#### 3.3.4.2 Varied HCl-based etchants

The InP substrate was etched in different HCl-based solutions to assess the effects on the etch rates and the crystalline planes which form during the etch. Only HCl-based etchants were tested as they give high selectivity etching of InP over InGaAs [26]. Dilution of HCl with water has been reported to allow continuous variation of the InP etch rate from 15  $\mu\text{m}/\text{min}$  with HCl:H<sub>2</sub>O (5:1) to 10 nm/min with HCl:H<sub>2</sub>O (1:1) and so different HCl concentrations were tested [27].

HCl:H<sub>2</sub>O (1:1) was tested on an unetched substrate, with the intention of testing a very slow InP removal to avoid defect introduction. The etch progress was assessed by comparing etch progress images at regular intervals, however this etchant, as expected, was extremely slow. Increased HCl concentrations (HCl:H<sub>2</sub>O (2:1) and HCl:H<sub>2</sub>O (3:1)) increased the etch rate, with HCl:H<sub>2</sub>O (3:1) giving a much faster etch rate which quickly revealed the InGaAs layers below the substrate and resulted smooth InP etch faces (giving a more uniform etch of the substrate). The HCl:H<sub>2</sub>O (3:1) appeared to not etch the InGaAs, however etch damage and cracks were apparent within the InGaAs buffer layer, following full InP substrate removal with this etchant.

InP substrate removal using HCl:H<sub>3</sub>PO<sub>4</sub> (3:1) as used in reference [11], resulted in the penetration of the InGaAs buffer layer at the edges of the mounted samples. HCl:H<sub>2</sub>O (3:1) was determined to be best for InP substrate removal due to its fast etch rate and ability to leave sheet-like InGaAs following substrate removal. Collaborators at City College of New York reported clean substrate removals with HCl:H<sub>3</sub>PO<sub>4</sub>:H<sub>2</sub>O (1:1:6) with agitation by magnetic stirrer, however this could not be replicated in this work as the etch rate is extremely slow. Given the difficulties in mounting membranes in wax and the releasing of membranes from

these holding layers with solvents, Section 3.3.5 discusses the pre-bonding of II-VI VECSELS onto diamond heatspreaders prior to substrate removal, to simplify the ELO process.

### *3.3.5 Bonding II-VI DBR-free VECSELS to diamond*

DBR-free VECSELS, grown on InP substrates, use pre-bonding of the gain structure to the intracavity diamond heatspreader before full substrate removal [6,28,29] or bonding of the released membranes to heatspreaders [7]. The former uses capillary bonding to achieve optical and thermal contact between the III-V DBR-free structures and diamond, before manual polishing and wet etching of the InP substrate [6,28,29]. Direct capillary bonding using de-ionized (DI) water is applied in VECSEL construction; the diamond is cleaned, a drop of DI water is placed onto the VECSEL chip and then the diamond is manually pressed onto the semiconductor to initiate the bonding [30]. Obtaining a capillary bond with sufficient strength requires excellent surface flatness and roughness. The pre-bonding method facilitates manipulation of the thin membrane structures and likely gives enhanced structural stability to the gain structure as the substrate is removed [29]. Bonding the membranes to a rigid material, like diamond, likely prevents cracks forming from membrane flexing during substrate removal, and the avoidance of bonding wax removes defect-causing air bubbles from the processing and removes a source of organic contaminants.

During this project all attempts to capillary-bond the ZnCdMgSe gain structure to diamonds have failed. Atomic force microscope measurements reveal nm-scale surface roughness of the epi-side of ZnCdMgSe samples (presented in Chapter 5), and so it is likely that the surface flatness, rather than the roughness, of the II-VI materials is insufficient for direct capillary-bonding to diamond. Further work on this could focus on using novel bonding techniques to bond the II-VI to diamond or SiC such as: argon atom treatment and room temperature pressure bonding which is used to bond diamond to Nd:YAG laser structures [31], sodium silicate bonding which can form a silica bond between semiconductor saturable absorbers and sapphire [32], or low temperature plasma-assisted bonding which has been successfully demonstrated in bonding DBR-free VECSEL structures to diamond [3,33].

Having discussed the individual elements of the full substrate removal ELO process, the next sub-section summarizes an optimized methodology.

### 3.3.6 Optimized full substrate removal method.

The optimized method used glycol phthalate wax to mount the samples onto a silicon carrier wafer, and the substrate was removed without mechanical polishing, instead using a single long etch of HCl:H<sub>2</sub>O (3:1). Fig. 5 a)-c) shows the progression of the InP etch with HCl:H<sub>2</sub>O (3:1) of sample CDI 447 (sample details in Section 3.5.2) at 50, 85 and finally 125 minutes, at which point a large, undamaged sheet of InGaAs remains.

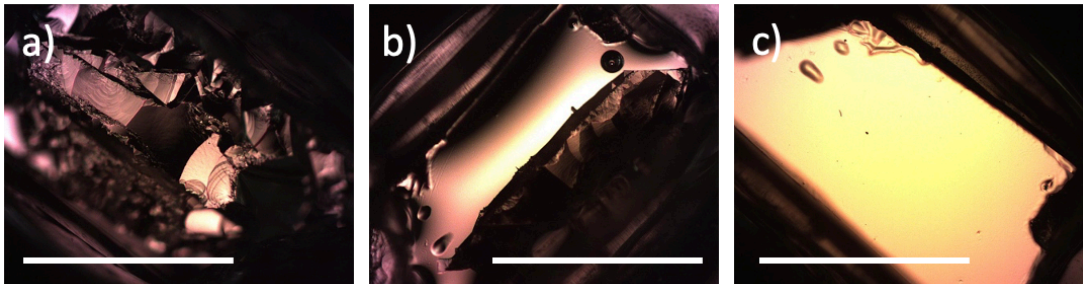


**Figure 5.** HCl:H<sub>2</sub>O (3:1) etching of CDI 447 (see Section 3.5.2 for structure details) at **a)** 50, **b)** 85 and **c)** 125 minutes. All images are at 5 × magnification and the white scale bar represents 1 mm.

The full substrate can be removed using this methodology to reveal cm<sup>2</sup>-sized InGaAs sheets. The InGaAs can then be removed by a short etch in H<sub>3</sub>PO<sub>4</sub>:H<sub>2</sub>O<sub>2</sub>:H<sub>2</sub>O (1:1:6) which has a reported etch rate of around 22.5 nm/s [10,11]. Fig. 6 a) shows the sample from Fig. 5 after an InGaAs etch. The H<sub>3</sub>PO<sub>4</sub>:H<sub>2</sub>O<sub>2</sub>:H<sub>2</sub>O (1:1:6) slowly etches the ZnCdMgSe and causes damage that can be seen in Fig. 6 b). Precise etch timing and having an accurate measurement of the InGaAs thickness is the only way to minimize this damage. Ripples visible on the over-etched sample in Fig. 6 b) signal a compressive strain relaxation process [10].

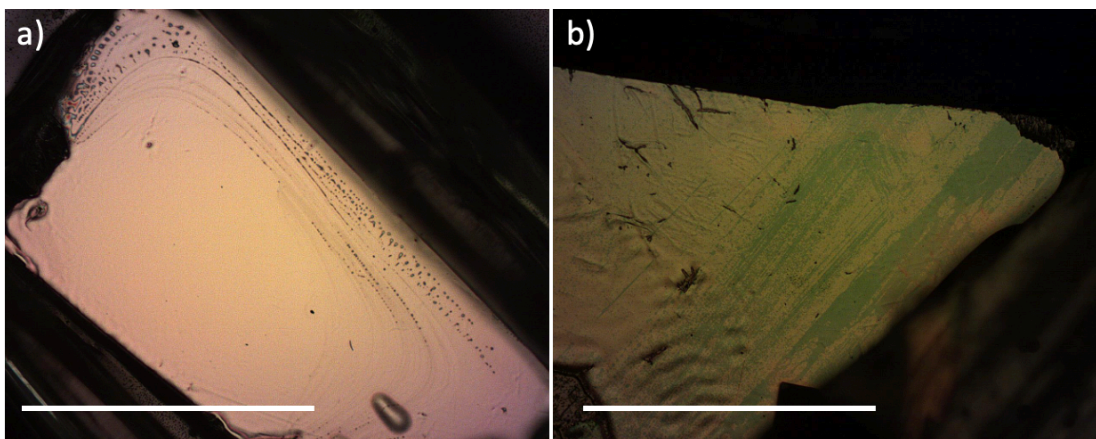


**Figure 6.** Post InGaAs removal of **a)** the sample from Fig. 5 and **b)** an over-etched sample. Both images are at 5 × magnification and the white scale bar represents 1 mm.

Following the InGaAs removal the remaining II-VI gain structure can be released by dissolving the glycol phthalate by pipetting acetone onto the sample drop at a time to give the slowest, and least turbulent, release. Following release into acetone the membranes initially rise and then sink over time, eventually bonding onto the glass container. The sinking can be avoided by displacing the acetone with water, however the membranes flex continuously in the liquid due to Brownian motion and convection, which causes damage. The released pieces of membrane can be picked up from the holding liquid using the diamond heatspreader, to which clean and smooth regions of the membrane spontaneously bond. It should be noted that with the substrate removed, the membranes bond well to diamond due to the strong Van der Waals forces that can be formed by a thin, flexible membrane.

Membranes which are strongly bonded to diamond can undergo further cleaning processes to remove organic contaminants from their surface. Weakly bonded membranes detach during additional cleaning steps. When membranes are picked up from the holding liquid (acetone or water), following substrate removal, numerous membranes are simultaneously captured and the cleaning process has a second use of removing membranes with poor bonding and hence quality. Repeated cleaning processes in a Matrix plasma asher, the conditions of which are described in greater detail in Chapter 4, followed by a solvent clean without agitation or ultrasonic aid can be used to remove surface contaminants. Fig. 7 shows a contaminated membrane before, Fig. 7 a), and after, Fig. 7 b), cleaning.

Contaminants in the membrane-diamond interface prevent effective bonding over the entire membrane surface, as shown in Fig. 7 c), where the light and fringed areas on the membrane contain contaminants. There is no way to clean these contaminants once the membrane is bonded. Local unbonded areas can cause thermal hotspots on the membranes during optical pumping and this heat can diffuse through the membrane and cause damage, delamination and debonding. A possible solution is to selectively remove the unbonded and contaminated areas, as completed with III-V materials in reference [34], which could be considered as future work.

The optical quality of the II-VI VECSEL samples was assessed using photoluminescence (PL) and the experimental setup used for this is explained in the next section.

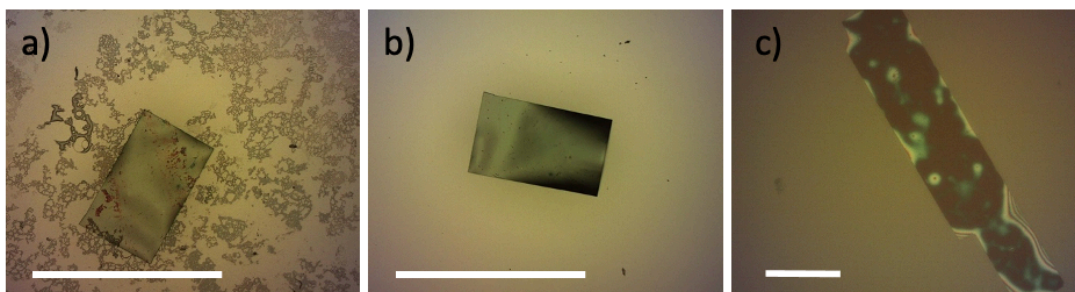


**Figure 7.** A membrane of CDI 447 **a)** following release from the wax and subsequent capture onto diamond at 10× magnification and **b)** after cleaning with a Matrix plasma asher and solvents, at 10× magnification. **c)** A bonded membrane imaged at 20× magnification through a diamond where dark areas are bonded and light areas contain contaminants. The white scalebar represents 500 μm in **a)** and **b)** and 100 μm in **c)**.

### 3.4 Photoluminescence testing setup for unprocessed samples and membranes

A photoluminescence test set up was used to assess the optical emission quality of unprocessed II-VI VECSEL samples and processed II-VI membranes on diamond. The initial PL test set up used a 4 W Laserglow LRD-0447 laser diode focussed onto the sample using a 15 mm lens, however this was improved upon by using the pump source reported in reference [20], a Nichia NUBM44 447 nm laser diode coupled to a 105 μm, multimode fibre and focussed using a matched aspheric lens pair (25 mm and 19 mm focal lengths). PL from the samples was collected and focussed onto the spectrometer optical fibre (600-μm-core, multimode) input using a 25 mm lens, with a filter to remove the pump signal (where possible). The majority of the PL tests were performed with 447 nm optical excitation, however a CNI MLL-W532, 1 W diode-pumped solid-state laser, focussed using a 250 mm lens was also used for 532 nm in-well optical excitation. An Ocean Optics USB 4000 (resolution ~ 0.2 nm) spectrometer was used during the PL measurements due to its sub-nm resolution, ease of use, ms integration times and wide spectral coverage which fully covers visible wavelengths. Fig. 8 a) summarizes the PL test set up used in this section of the project.

An important note is that during the membrane release the orientation of the membrane cannot be tracked, due to the rapid, random motion (membrane flipping and twisting) and splitting of the membrane in the release medium. Some of the II-VI VECSEL structures grown in this work contain thick II-VI buffer layers and so when membranes of these structures are tested on diamond the buffer layer orientation is unknown. Optical pumping of the structures through the thick II-VI buffer layers results in a different charge carrier profile to pumping through the QWs first. To investigate this the PL of membranes was collected in two different geometries;



upright, where the pump light is incident on the membrane first, and upside-down, where the pump light is incident on the diamond first. The combination of the unknown membrane orientation and diamond reflection losses results in PL differences between the upright and upside-down configurations. Fig. 8 b) shows the mounting arrangements for the PL testing of unprocessed samples and membranes in the upright and upside-down orientations.

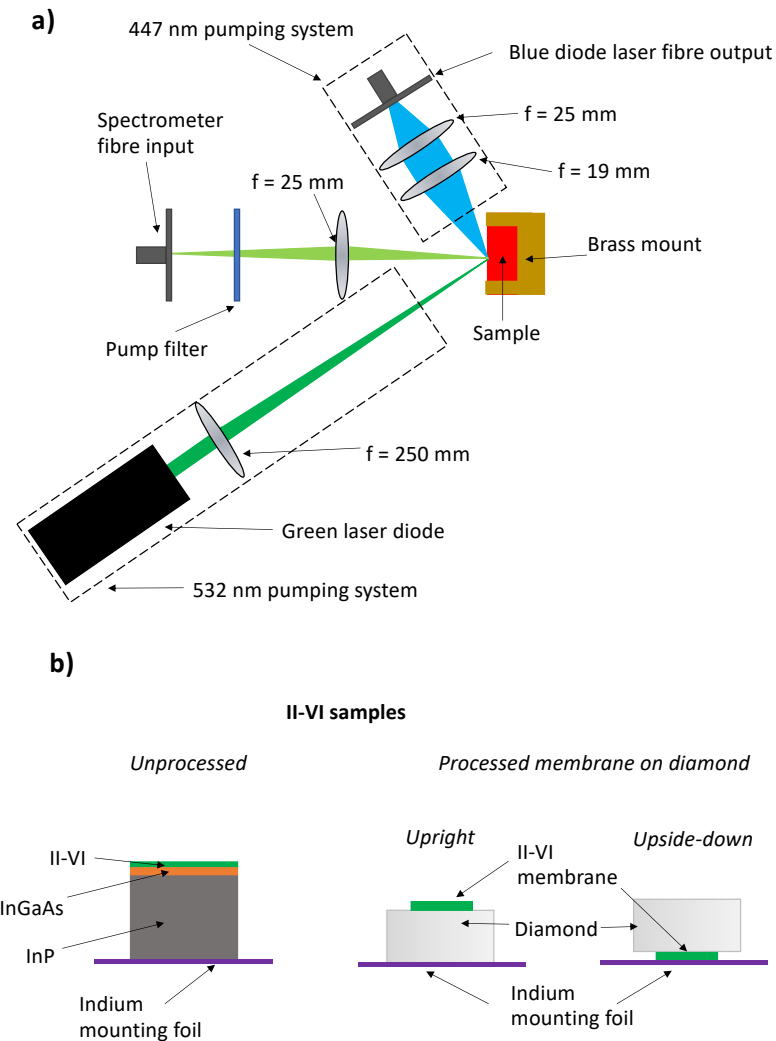


**Fig 8.** a) Schematic of the PL testing set up. The optical excitation source was interchangeable, with the 447 nm and 532 nm diode-pumping set ups shown in the dashed boxes. Only one excitation wavelength was used at any given time. The PL output was coupled into a 600- $\mu$ m-core multimode optical fibre which was connected to an Ocean Optics USB 4000 spectrometer. A brass mount was used to hold the samples. b) Both unprocessed II-VI VECSEL structures and II-VI VECSEL membranes on diamond were tested. The samples were mounted onto a 100- $\mu$ m-thick layer of indium foil to aid heat flow into the brass mount from the sample. The two geometries of II-VI membrane testing, upright and upside down are shown.

### **3.5 The first and second growth campaigns: CDI 354, CDI 356, CDI 358, CDI 447, and CDI 517**

#### *3.5.1 Initial test growths CDI 354, CDI 356 and CDI 358*

Section 3.3 described the development of the full substrate removal techniques for this work and Section 3.4 outlined the PL setup used to characterize the optical properties of the II-VI VECSEL structures before and after processing. This section outlines the structures which were grown within the first two growth campaigns and summarizes the processing and optical results which were obtained.

An initial growth campaign was completed to assess the II-VI growth quality, calibrate the numerical models to the experimental outputs and produce samples for trial substrate removals. Three samples were grown with different designs, however the QWs in each sample were spatially distributed to give resonant periodic gain, as described in Section 2.4. Adding compressive strain enhances TE gain (see Section 2.2.4.2) and so one sample, CDI 354, included 4 compressively-strained QWs (0.5 % compressive strain) positioned individually at antinodes of the standing wave of the laser mode electric field. To focus on enhanced structural quality the other two samples, CDI 356 and CDI 358, were comprised of four and eight unstrained QW pairs, respectively, with the QW pairs located at antinodes of the standing wave of the laser mode electric field.

All three structures were designed with resonant sub-cavities. Each structure was capped with a 1 nm layer of  $\text{Zn}_{0.52}\text{Cd}_{0.48}\text{Se}$  to prevent Mg-based oxidation. 447 nm pump light has a short absorption length within the  $\text{ZnCdMgSe}$  structures (see Section 2.6) and the short length of the CDI 354 and CDI 356 structures allows all of the QWs within the structure to be pumped at a high intensity. The longer length of CDI 358 is well-suited to in-well pumping at 532 nm, which is weakly absorbed, possibly with optical pumping of the membrane from both directions (perpendicular to the front and rear membrane surfaces). CDI 354 had a visibly poor surface quality and a very broad and weak PL, indicating a lower growth quality from the inclusion of a small compressive strain which likely introduces non-radiative defects. CDI 356 and CDI 358 gave stronger PL signals, indicating the superior growth quality of the unstrained II-VI material. The full substrate removal of CDI 354 was attempted, however the sample disintegrated once it was released from the holding wax adding further evidence of the poor growth quality.

### 3.5.2 Second growth campaign: CDI 447 growth and ELO

An improved gain structure design, CDI 447, was grown with a 360 nm InGaAs buffer layer (a thickness typically used by collaborators at CCNY) and a thicker 5 nm ZnCdSe capping layer on each surface of the DBR-free structure, to increase the structural oxidation resistance. The CDI 447 design was comprised of four pairs of QWs, designed to be lattice-matched to the (001) InP substrate, and spatially distributed to give resonant periodic gain at a target wavelength of 565 nm. The design is shown in Table 4 and Fig. 9 shows the conduction and valence band edge profile of the structure, along with the electric field magnitude of the standing wave of a 565 nm laser mode and the exponential decay of the electric field magnitude of the 447 nm pump light. CDI 447 exhibited a high brightness which was attributed to a very high growth quality, rather than the being design related.

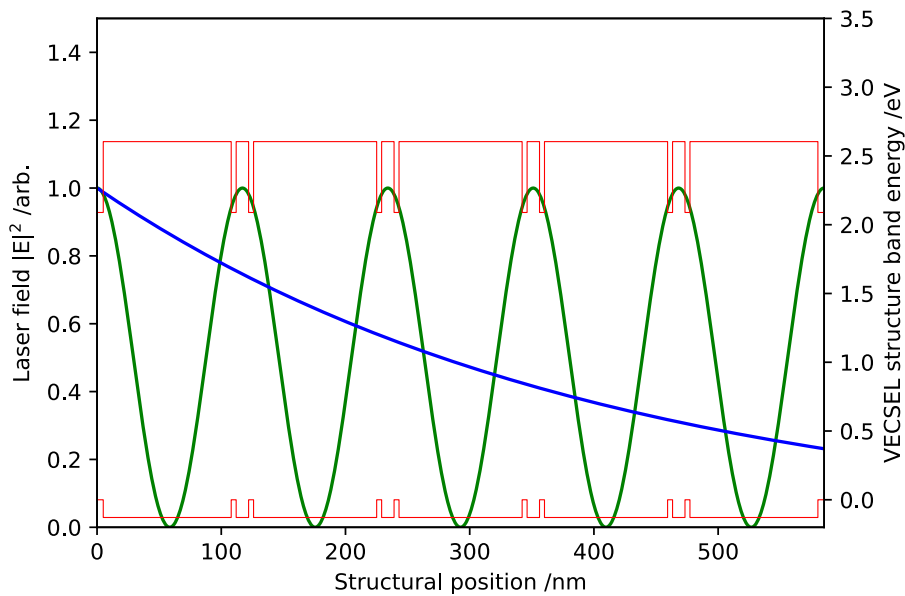


**Figure 9.** Schematic of the conduction and valence band edges of the CDI 447 structure, showing four pairs of QWs spaced in a resonant periodic gain format. The absorption profile of the 447 nm pump electric field (plotted as  $|E|^2$ ), along with the position of the antinodes (plotted as  $|E|^2$ ) of the standing wave of the 565 nm laser mode, which are aligned with the QW pairs of the gain structure are shown.

**Table 4.** The gain structure design of the second growth campaign.

Layer	Composition				Thickness /nm	Bandgap /eV	Refractive Index
	Zn	Cd	Mg	Se			
Cap	0.48	0.52	0	1	5	2.089	2.72
Barrier	0.3	0.28	0.42	1	103	2.733	2.39
QW	0.48	0.52	0	1	4	2.089	2.72
Barrier	0.3	0.28	0.42	1	10	2.733	2.39
QW	0.48	0.52	0	1	4	2.089	2.72
Barrier	0.3	0.28	0.42	1	99.1	2.733	2.39
QW	0.48	0.52	0	1	4	2.089	2.72
Barrier	0.3	0.28	0.42	1	10	2.733	2.39
QW	0.48	0.52	0	1	4	2.089	2.72
Barrier	0.3	0.28	0.42	1	99.1	2.733	2.39
QW	0.48	0.52	0	1	4	2.089	2.72
Barrier	0.3	0.28	0.42	1	10	2.733	2.39
QW	0.48	0.52	0	1	4	2.089	2.72
Barrier	0.3	0.28	0.42	1	99.1	2.733	2.39
QW	0.48	0.52	0	1	4	2.089	2.72
Barrier	0.3	0.28	0.42	1	10	2.733	2.39
QW	0.48	0.52	0	1	4	2.089	2.72
Barrier	0.3	0.28	0.42	1	103	2.733	2.39
Cap	0.48	0.52	0	1	5	2.089	2.72

During this project numerous membranes of CDI 447 were released and tested for laser operation. Fig. 10 shows an example of the PL characterization of a membrane of CDI 447 on diamond. Fig. 10 a) compares the PL of an unprocessed chip of CDI 447, without any heatspreader, and a membrane on diamond in the upright and upside-down configurations. It should be noted that the PL intensities of the upright and upside-down membranes cannot be compared due to the additional diamond reflections in the upside-down case. Although these measurements were completed with the same PL setup and the same integration time (4 ms), direct comparison of the PL intensities should be taken with caution as the optical excitation for the PL was targeted at different locations on the II-VI sample before and after processing. It is challenging to locate the same area of the membrane before and after processing due to the change in membrane appearance following the substrate removal, and the random movement of the membrane following release into the wax-dissolving medium. Therefore, the great difference in intensities between the upright and upside-down membrane could be due to localized variation of the membrane. The upright membrane has a PL red-shift, in comparison to the unprocessed sample, which likely arises from pump-induced heating [35]. The upside-down membrane has a blue-shifted PL peak in comparison to the unprocessed sample, and this is likely due to the point of highest pump intensity being closer to the diamond in this geometry, permitting greater heat flow from the active region than the unprocessed

sample which has no heatspreader. The shoulder in the PL is more apparent in the upside-down membrane and could originate from a QW with an incorrect thickness being cooled and pumped more effectively.

Fig. 10 b) shows the intensity-dependent PL (IDPL) of the upside-down (pumped through the diamond) membrane along with an inset image of the membrane. The vertical line at 561 nm helps to visualize the very small red-shift occurring as the pump power is increased, evidencing the strong thermal contact between the membrane and the diamond.

The high resolution x-ray diffraction (HR-XRD) measurements of CDI 447 are shown in Fig. 10 c). The position of the main superlattice (SL) peak of the HR-XRD, SL(0) can be used to infer the lattice mismatch of the II-VI heterostructure, where a positive shift in the Bragg angle position of the SL(0) peak with respect to the InP peak equates to a negative % mismatch along the growth direction, which indicates tensile strain. Likewise negative Bragg angle shifts indicate compressive strain. The long and short periods of the HR-XRD spectra give information on the structural layers, where the short period represents the sum of the first QW and the QW spacer thicknesses and the long period represents the sum of the second QW and the pump-absorbing barrier thicknesses. From Fig. 10 c) it is apparent that the CDI 447 structure has compressively strained components. The very high levels of periodicity in the HR-XRD indicate that the structure has an excellent growth quality, which results in the high PL brightness observed from the sample.

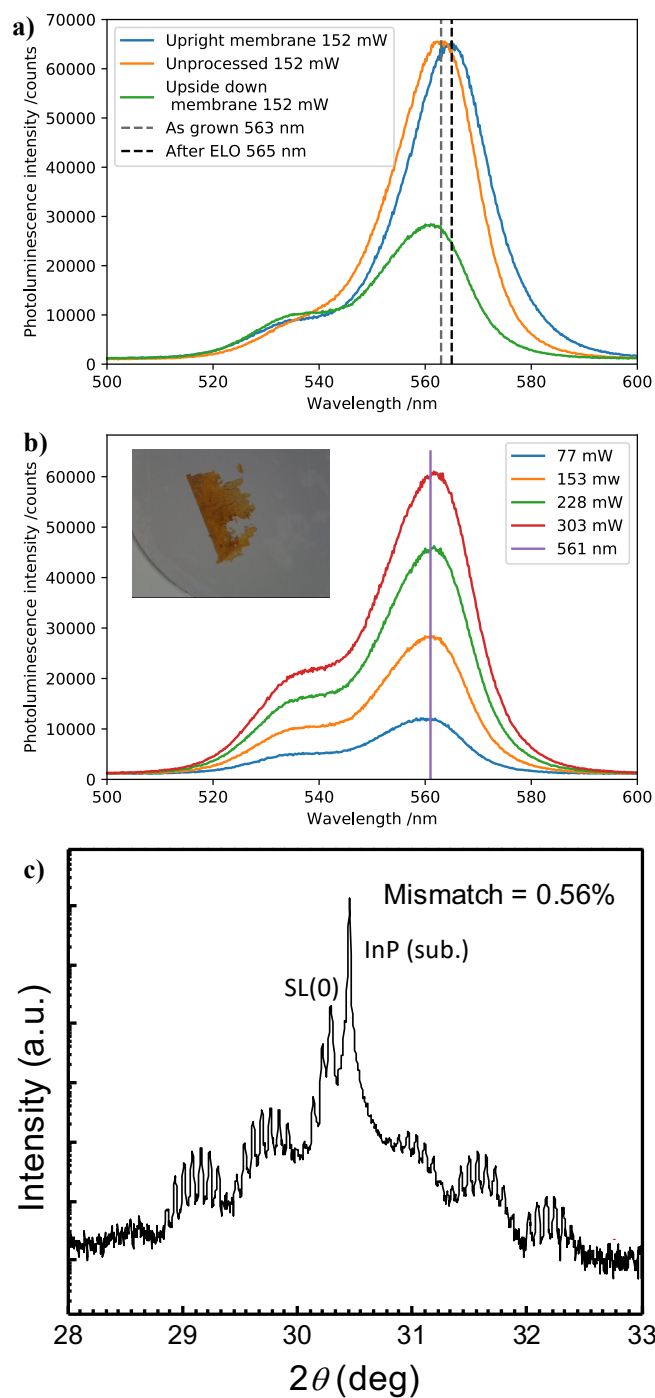


**Figure 10.** **a)** Comparison of the PL of an unprocessed CDI 447 chip along with a membrane of CDI 447 orientated with the membrane upright and upside-down with respect to the diamond (upright; the pump light is incident on the membrane first. Upside-down; the pump light is incident on the diamond first.). **b)** IDPL of the upside-down CDI 447 membrane with an inset image of the membrane seen through the diamond in this orientation. **c)** HR-XRD of CDI 447, showing the SL(0) and InP substrate peaks. The mismatch has been calculated by Dr Kuaile Zhao.

### 3.5.3 Second growth campaign: CDI 517 growth and ELO

Given the high brightness of CDI 447, CDI 517 was grown with the same design but with a 500-nm-thick InGaAs buffer layer to begin an investigation into how the buffer layer thickness affects the II-VI growth. The HR-XRD of CDI 517 is shown in Fig. 11 a).

The CDI 517 structural periodicity has been annotated on the HR-XRD graph by Dr Kuaile Zhao (CCNY) to correspond to two periods; one of 15 nm (first QW and QW spacer) and one of 117 nm (second QW and barrier). The weak interference fringes evidence a poor periodicity and quality within the structure. From the main SL(0) peak, CDI 517 has a 0.25 % compressive mismatch with the (001) InP substrate, which has likely introduced defects into the CDI 517 structure, giving it a weaker PL signal than CDI 447.

Membranes of CDI 517 on diamond, produced by full substrate removal, were tested using IDPL, see Fig. 11 b). IDPL measurements were taken at a heatsink temperature of 5 °C, with a longer integration time of 5 ms and higher pump powers than used with other samples in order to extract a stronger PL signal. The PL peak stays at 547 nm throughout 152 mW to 1209 mW of optical pumping at 447 nm, indicating a strong heat flow from the membrane to the diamond. Fig. 11 c) shows an example of a large membrane of CDI 517 where there are large bonded areas but many defects, cracks and delaminated regions.

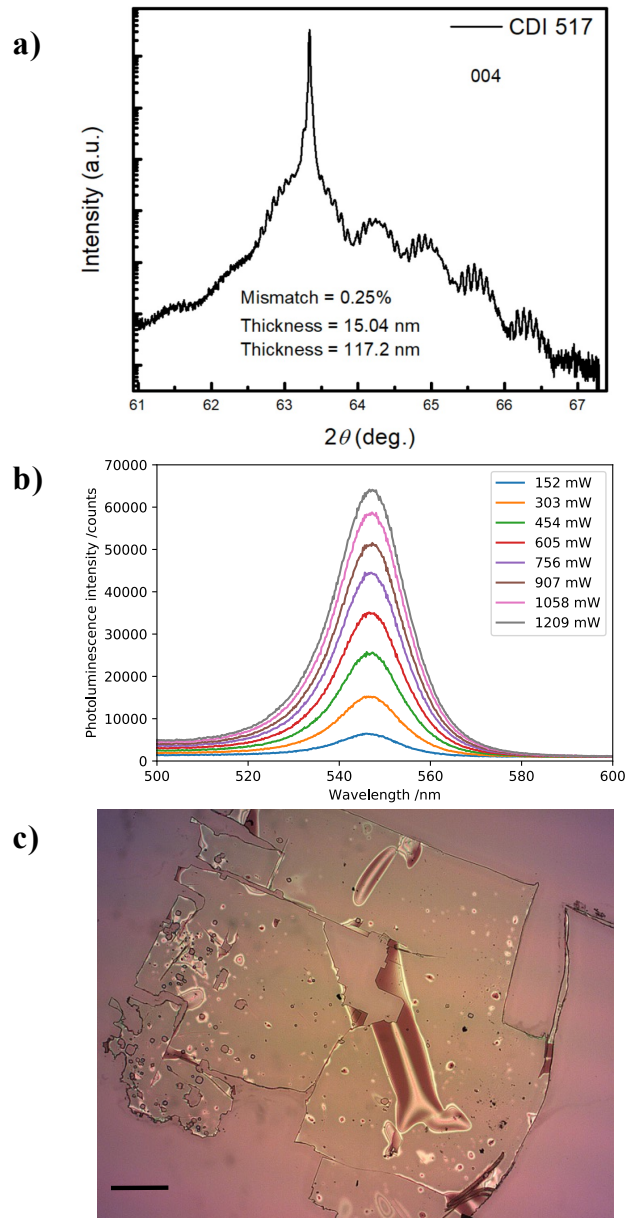


**Figure 11.** **a)** HR-XRD measurements of CDI 517 with the structural periodicity measured by Dr Kuaile Zhao. **b)** IDPL of a CDI 517 membrane on diamond and **c)** a 5x image of a CDI 517 membrane on diamond, with a black scale bar representing 200  $\mu\text{m}$ .

#### 3.5.4 Growth campaign 2 summary

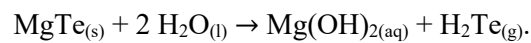
From this growth campaign, high brightness gain structures were realized, however errors with the growth rate resulted in poor structural periodicity and the defects within the samples result in a large number of cracks within the resulting membranes. The IDPL measurements of the II-VI membranes on diamond show that the membranes conform to the diamond surface and form strong, low-thermal-impedance bonds. The difficulties of the full substrate removal ELO



method could be avoided if a release layer with a high etch selectivity to the ZnCdMgSe-based gain structures, such as MgTe, could be developed for the II-VI VECSELs. This was investigated in the third growth campaign and is summarized in the next section.

### 3.6 The third growth campaign: MgTe release layers

Selective etching of a specifically-grown release layer gives the opportunity for the ELO of a membrane without the associated difficulties of removing the entire substrate. For the II-VI materials, metastable sacrificial layers (MgTe or MgS) for growths on GaAs substrates have been reported as useful release layers [36,37]. MgTe is hygroscopic and in the presence of water it dissociates into Mg(OH)<sub>2</sub> and H<sub>2</sub>Te, allowing epilayer release [37], via:



HCl etches MgS from other II-VI materials with a selectivity of 10,000:1, allowing a fast release of the epilayer from MgS, however etch damage to ZnCdMgSe is likely [36].

The Te-based release layer ELO scheme is highly advantageous for the II-VI materials as it does not require etching with HCl- or H<sub>2</sub>O<sub>2</sub>-based etchants, which damage ZnCdMgSe [38]. A 1000-nm-thick MgTe release layer has been demonstrated with II-VI on GaAs:Si (100) substrates by Seredynski *et al* [37], however Campbell *et al* report that thinner 20 nm MgTe release layers are required for the full ELO of II-VI from InSb substrates [38].

A third growth campaign was designed to focus on the feasibility of growing a DBR-free VECSEL structure on a layer of metastable MgTe on an InP substrate, unlike in previous work where the release layer of MgTe was grown on InSb or GaAs substrates [37,38]. A MgTe layer could be grown upon In<sub>0.53</sub>Ga<sub>0.47</sub>As lattice-matched to (001) InP, and its breakdown in water would release the II-VI gain structure.

MgTe has a reported lattice constant of 0.642 nm [39], and when grown on an InP substrate with a lattice constant of 0.587 nm, will be under a compressive strain of 8.6 %. On GaAs (0.565 nm lattice constant) and InSb (0.648 nm lattice constant) this strain is 12.0 % compressive and 0.9 % tensile respectively. Given that the strain case of the of MgTe-on-InP is similar in magnitude to MgTe-on-GaAs:Si, the goal structure for this campaign is identical to CDI 447 (four pairs of resonantly spaced QWs) and grown on 1000 nm of MgTe, as in reference [37].

The growth of MgS and Te-binaries on InP with Se-quaternaries is challenging and was not possible in this work. MgTe and MgS have a large lattice mismatch with InP, leading to a high level of defects in the target epitaxial layers [39]. For the ZnCdMgSe-on-InP material system this high strain at the structural base prevented the growth of the DBR-free VECSEL structure due to significant defect formation arising from the lattice mismatch. The interface between the selenium- and tellurium-based II-VI materials introduced defects to such an extent that this scheme of work was abandoned. Although ELO using water is ideal for minimizing structural damage, this is only useful if the QW has a high pre-processing quality. Given that release layer development was not possible at this stage in the II-VI VECSEL development, the fourth growth campaign, discussed in the next section, focussed on whether the optimization of the II-VI and III-V buffer layers used in the MBE growth could further improve the optical and post-ELO quality of the II-VI VECSEL membranes.

### **3.7 The fourth growth campaign: increased II-VI buffer layer and decreased III-V buffer layer thicknesses**

#### *3.7.1 Adjusting the design*

Growing and performing ELO on trial structures revealed that the II-VI/III-V interface may be a cause of defect generation within the II-VI gain structure and so a fourth growth campaign focussed on including a large ZnCdMgSe, two-wavelength buffer layer. Reference [40] shows that the inclusion of an InGaAs and a II-VI buffer layer can reduce the defect density of a ZnCdSe layer. The large II-VI buffer layer increases the physical distance between the active region and the II-VI/III-V interface, reducing the effects of the mismatch between the active region and the InP substrate, hence the defect density. The active region was the same structure as in CDI 447, with small adjustments to the barrier thickness and grown upon the ZnCdMgSe  $2\lambda$  layer.

Although the III-V InGaAs buffer layer is useful as an etch stop layer, collaborators at CCNY suspected that thicker InGaAs buffer layers have a larger number of defects due to Ga and In pooling, which generates stacking faults within the InGaAs. It has been reported that bonds between materials at II-VI/III-V epitaxial growth boundaries and roughness between II-VI and III-V boundaries cause stacking faults, which propagate through II-VI epitaxial structures [41]. This campaign focussed on using short growth times for the InGaAs buffer layers, with the intention of growing 30-40 nm of very high quality InGaAs buffer layer. By growing the II-VI epitaxial structure, with the additional II-VI buffer layers, on higher quality InGaAs,

superior material quality should be achievable. The next sub-section details the improved gain structure design and presents the characterization of the growths of this structure.

### 3.7.2 The “ten antinode structure”

Along with the defect-minimizing growth strategy, the growth parameters were tuned by our collaborators to encourage the highest level of lattice-matching to InP. The barrier composition was carefully determined to give lattice-matching and the lower capping layer was positioned to be grown before the  $2\lambda$  layer ZnCdMgSe buffer layer. The capping layer was designed to be 4 nm of ZnCdSe, and was grown as a low temperature II-VI buffer to further seed a high quality ZnCdMgSe growth. The layer composition of the adapted structure is shown in Table 5. Fig. 12 shows the conduction and valence band edges of the “ten antinode” gain structure design and the absorption profile of the 447 nm pump electric field (plotted as  $|E|^2$ ), along with the position of the antinodes (plotted as  $|E|^2$ ) of the standing wave of the 565 nm laser mode, which are aligned with the QW pairs of the gain structure. Although the ZnCdMgSe buffer and the first barrier grown in the structure are shown as separate layers, they have identical composition. From the design in Table 5, the short period should be 14 nm and the long period should be 102.9 nm.

**Table 5.** Adjusted gain structure to target the highest level of lattice-matching and material quality. A II-VI buffer is still present but the cap layer now serves as a low temperature buffer layer. These structures were grown on the reduced-thickness InGaAs III-V buffer layer.

Layer	Composition				Thickness /nm	Bandgap / eV	Refractive index
	Zn	Cd	Mg	Se			
Cap	0.48	0.52	0	1	4.0	2.089	2.72
Barrier	0.36	0.26	0.38	1	103.8	2.775	2.39
QW	0.48	0.52	0	1	4.0	2.089	2.72
Barrier	0.36	0.26	0.38	1	10.0	2.775	2.39
QW	0.48	0.52	0	1	4.0	2.089	2.72
Barrier	0.36	0.26	0.38	1	98.9	2.775	2.39
QW	0.48	0.52	0	1	4.0	2.089	2.72
Barrier	0.36	0.26	0.38	1	10.0	2.775	2.39
QW	0.48	0.52	0	1	4.0	2.089	2.72
Barrier	0.36	0.26	0.38	1	98.9	2.775	2.39
QW	0.48	0.52	0	1	4.0	2.089	2.72
Barrier	0.36	0.26	0.38	1	10.0	2.775	2.39
QW	0.48	0.52	0	1	4.0	2.089	2.72
Barrier	0.36	0.26	0.38	1	98.9	2.775	2.39
QW	0.48	0.52	0	1	4.0	2.089	2.72
Barrier	0.36	0.26	0.38	1	108.4	2.775	2.39
II-VI buffer	0.36	0.26	0.38	1	467.2	2.775	2.39
Cap	0.48	0.52	0	1	4.0	2.089	2.72

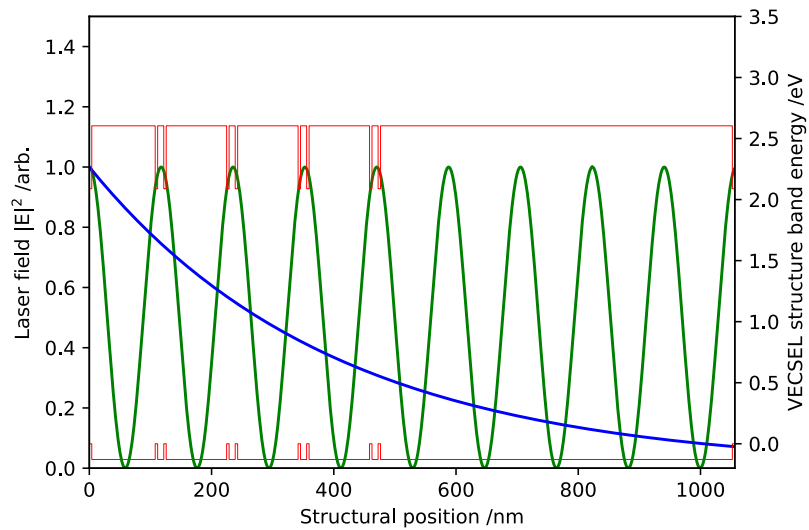


**Figure 12.** Schematic of the conduction and valence band edges of the “ten antinode” gain structure, with a  $2\lambda$  ZnCdMgSe buffer layer and ZnCdSe end capping layers. The absorption profile of the 447 nm pump electric field (plotted as  $|E|^2$ ), along with the position of the antinodes (plotted as  $|E|^2$ ) of the standing wave of the 565 nm laser mode, which are aligned with the QW pairs of the gain structure are shown.

Four samples of the ten-antinode structure were grown (CDI 637, CDI 638, CDI 639 and CDI 640) and their high-resolution x-ray diffraction (HR-XRD) and PL measurements are shown in Fig. 13. Analysis of the growth, completed by CCNY collaborators, is summarized in Table 6.

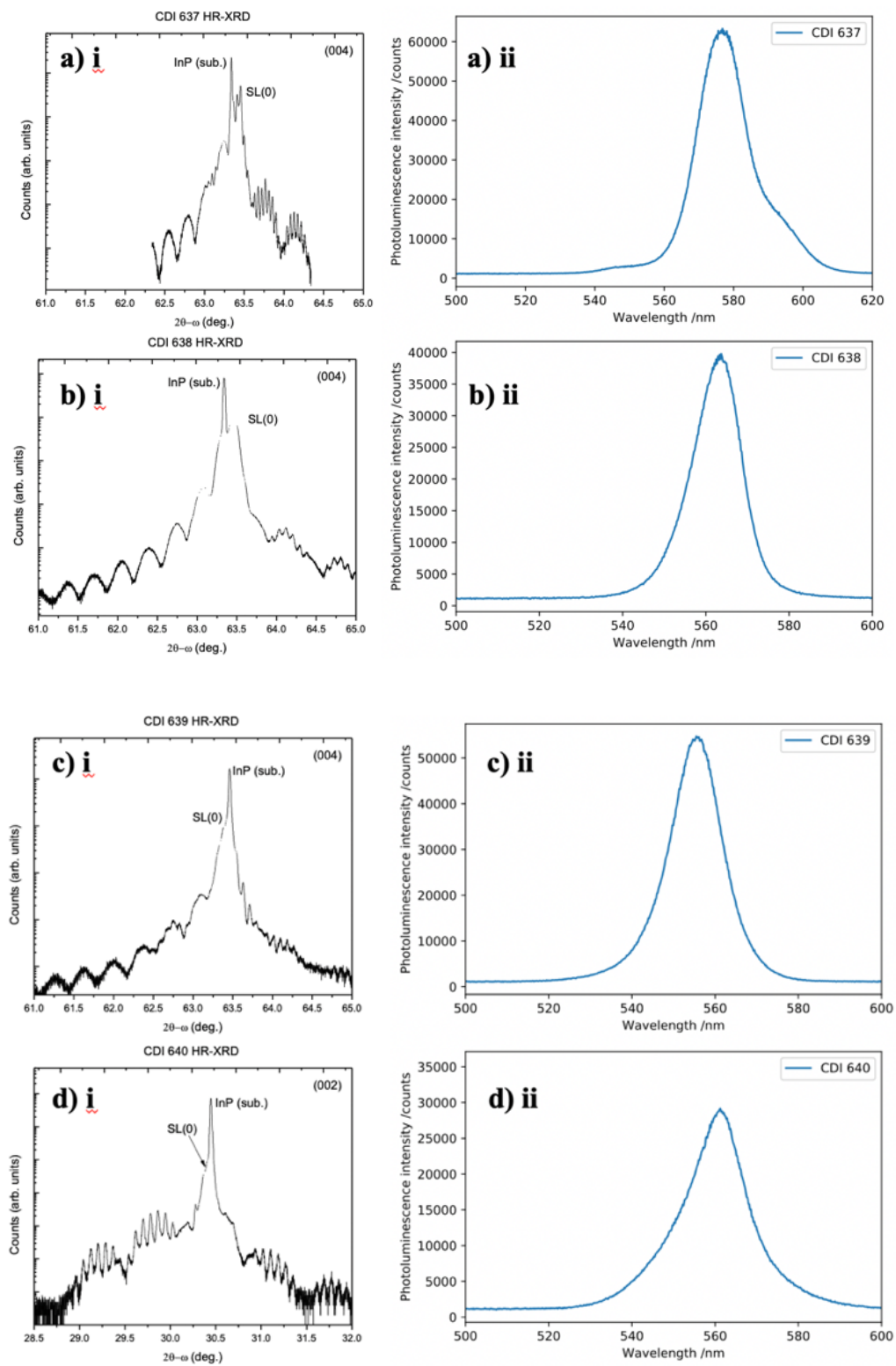


**Figure 13.** i) high resolution x-ray diffraction spectra and ii) PL spectra of a) CDI 637, b) CDI 638, c) CDI 639 and d) CDI 640. HR-XRD courtesy of V. Deligiannakis.

**Table 6.** Summary of the ten antinode structure samples grown. HR-XRD data and analysis courtesy of V. Deligiannakis.

Sample	InGaAs buffer layer thickness /nm	SL(0) lattice mismatch /%	Short period /nm	Long period /nm	PL peak /nm (in eV)
CDI 637	40	0.16	26	204	577±1 (2.15)
CDI 638	40	0.13	15	128	563±1 (2.20)
CDI 639	30	~0.0*	14.24	123	556±1 (2.23)
CDI 640	30	~0.0*	14.45	114	561±1 (2.21)

\*SL(0) and InP peak difference is unresolvable

The HR-XRD show that CDI 637 and CDI 638 are under small tensile strains, whereas CDI 639 and CDI 640 are very well lattice-matched to the InP substrate. The PL measurements of CDI 637 show a red-shift in the PL peak position from the designed wavelength of 565 nm which, in combination with the short period of the HR-XRD and calculations of the  $n = 1$  transition, show that the QW width is  $\sim 6$  nm and the QW spacer layer is  $\sim 20$  nm. From examining the long period of CDI 637 the barrier width is therefore 198 nm. The discrepancy from the intended design is the result of the iterative process of tuning the growth parameters. This can be seen in the next growth, CDI 638, where the HR-XRD show a long and short period which are much closer to the predicted values, although the structure maintains an overall tensile strain. Subsequent improvements in the material composition give CDI 639 and CDI 640 a high degree of lattice-matching with a short period which agrees well with the predicted value. The long period for CDI 639 and CDI 640 is still longer than the design, however not to an extent that laser performance should be inhibited. From Table 6, CDI 640 can be seen to have the closest match to the intended design.

Thinning the InGaAs buffer layer to 30 nm - 40 nm resulted in significant improvements to both the PL brightness and the surface quality. Fig. 14 a) and b) show example surfaces from samples with a 360 nm and a 30 nm InGaAs buffer layer respectively, with insets of the dark field microscope images of the surfaces. The improvement in the surface quality of the samples by thinning the InGaAs buffer layer is easily visible, by eye, and the dark field microscopy images show a reduction in the number density of scattering centres on the sample surface. Improvements in the surface quality are essential for the bonding performance of the samples.

The ELO of the structures CDI 637, CDI 638 and CDI 640 are discussed in the next subsection.

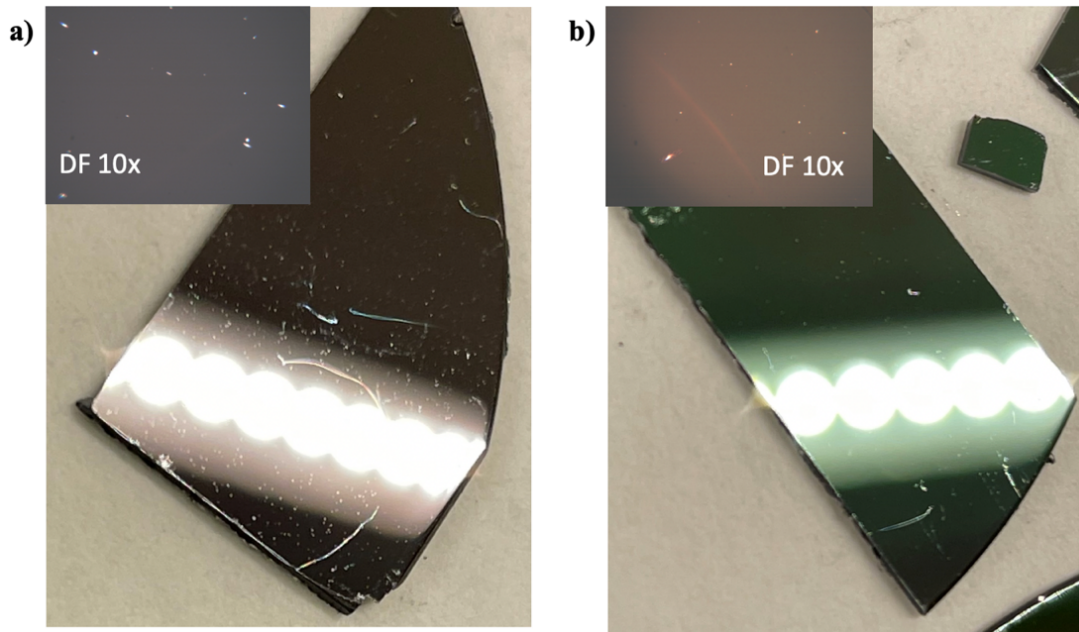


**Figure 14.** Images of the surface immediately after MBE growth, with inset dark field (DF) microscopy images of sample **a)** CDI 525 with a 360 nm InGaAs buffer layer and **b)** CDI 638 with a 40 nm InGaAs buffer layer. Images courtesy of V. Deligiannakis. The white circles in the images are the reflections of the room lights.

### 3.7.3 ELO results of CDI 637, CDI 638 and CDI 640

Membranes of CDI 637 were produced using the method in Section 3.3.6 however the membrane and optical quality of the samples following the ELO was poor. The ELO processing of CDI 638 used a modified version of the method presented in Section 3.3.6, with an additional S1805 spin-coated protective layer applied to the epi-side and the sample was mounted on Kapton tape (a chemically resistant tape) for handling. The substrate was etched off using HCl:H<sub>2</sub>O (3:1) and the InGaAs buffer layer was removed using a 3 s etch in H<sub>3</sub>PO<sub>4</sub>:H<sub>2</sub>O<sub>2</sub>:H<sub>2</sub>O (1:1:6). The resulting membrane was released in a beaker of acetone with a diamond positioned under the sample so that released segments would sink onto the diamond. This method yielded testable, but contaminated, membranes. The membranes were cleaned with a Matrix asher and solvent rinsing in a sonic bath.

The PL and IDPL measurements of a membrane of CDI 638 are compiled in Fig. 15, where, as in Fig. 8 b), the upright direction is assigned when the pump light is incident on the membrane first, and the upside-down direction is the case of the pump light incident on the

diamond first. Fig. 15 a) shows the IDPL of a membrane pumped through a diamond (upside-down), showing a 3 nm red-shift from the as-grown structure. The red-shift of the IDPL is minimal with increasing pump power, evidencing good thermal transport.

Fig. 15 b) shows a comparison of the PL of the membrane pumped through the diamond (upside-down) to the membrane pumped on top of the diamond (upright) with an inset image of the poor-quality membranes. In comparison to pumping the membrane first, pumping the membrane through the diamond yields less red-shift, as the pump induced heating is maximum closer to the heatspreader, and the PL intensity is lower (PL of both samples was measured with the same set up), due to pump reflection from the diamond, pump scattering from the diamond-membrane interface and the unknown orientation of the II-VI buffer layer.

Fig. 15 c) shows the PL measurements when the pump is incident on the membrane first (upright). There is a 4 nm red-shift from the as-grown structure, which is larger than the PL taken when the membrane is pumped through the diamond due to the pump induced heating maximum point being further from the diamond. In-well pumping, with 1 W of 532 nm optical excitation of the membrane gives a PL signal with an almost identical peak position to the 447 nm pumping, but with a significantly lower signal than the barrier pumped case due to the short absorption length of the QWs giving a low pump absorption.



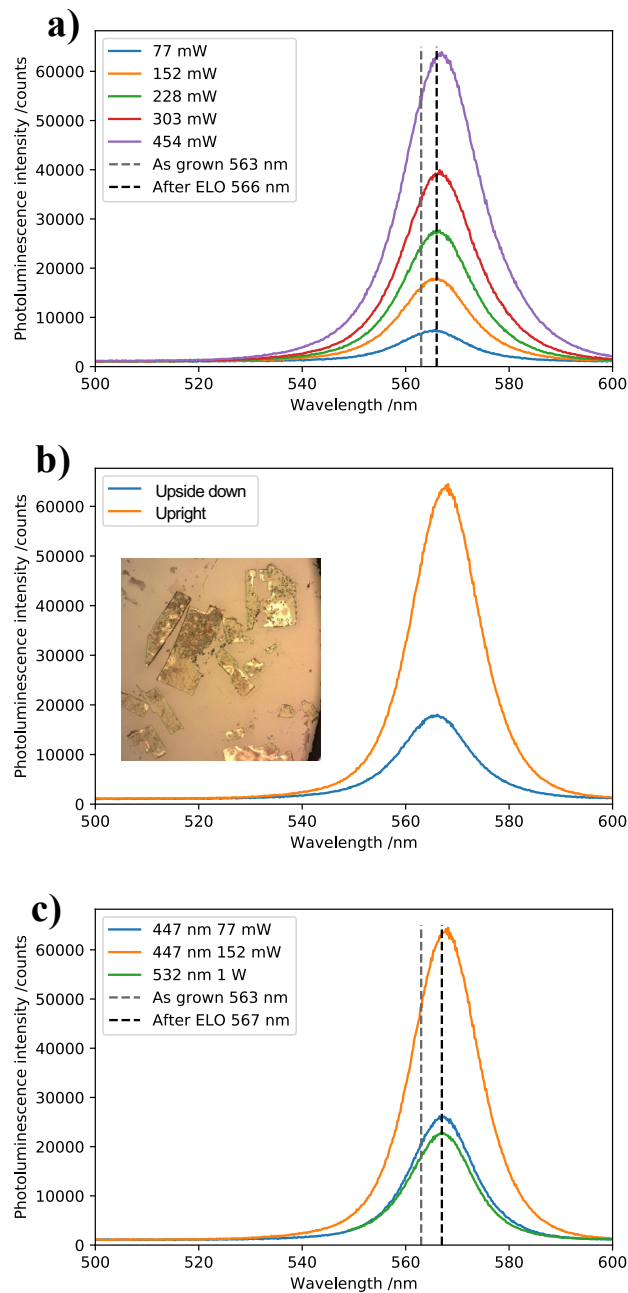


**Figure 15.** PL measurements of CDI 638 membranes on diamond. **a)** IDPL of a membrane pumped through the diamond and **b)** a comparison of the PL of a membrane pumped through the diamond (upside-down) and the membrane pumped on top of the diamond (upright) at 152 mW with 447 nm optical pumping, with an inset of an example membrane on top of the diamond. **c)** PL measurements of a CDI 638 membrane on top of a diamond with 447 nm and 532 nm optical excitation.

Following substrate removal, CDI 640 released as a cm-scale membrane, the first sample tested in this project in which the whole sample was successfully released without fracturing. Depositing cm-scale membranes onto 5-mm-diameter diamonds leads to the membrane

folding onto itself or folding around the diamond, which would prevent sufficient optical pumping of the gain structure. Due to the lack of deposition control of the large membrane, it was broken apart and a pipette was used to extract the smaller membranes and deposit them onto new substrates. Membranes were deposited onto diamond and sapphire heatspreaders.

CDI 640 membrane PL is red-shifted 1 nm from the unprocessed wafer peak position of 561 nm, with both 447 nm (barrier) and 532 nm (in-well) pumping, see Fig. 16 a). 532 nm pumping gives a lower PL brightness due to the short absorption length of the QWs. Fig. 16 b) shows the great variation in PL brightness across the sample (with 447 nm pumping), which is due to membrane quality and bonding strength variations over the membrane area. The inset in Fig. 16 b) shows a large membrane of CDI 640 on a 4 mm diameter diamond, with large dark areas signifying areas of membrane bonding. The membrane has a high density of etch pits and regions of localized debonding which will degrade the thermal transport and prevent any laser oscillation.

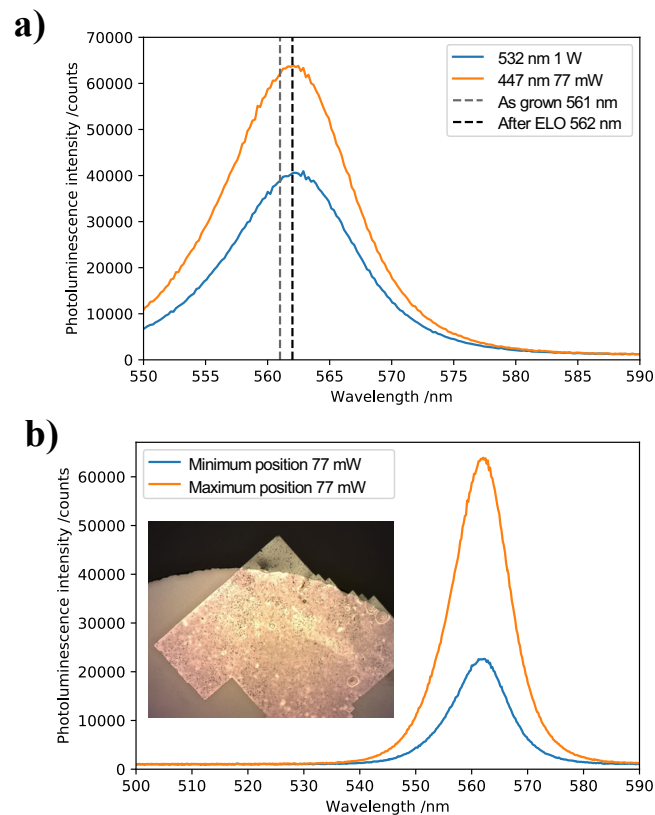


**Figure CDI 16.** CDI 640 membrane on diamond. **a)** Comparison of barrier (orange line) and in-well (blue line) pumped membrane showing the 1 nm post-processing red-shift, and **b)** a comparison of the maximum and minimum intensity of the PL, under 447 nm optical pumping, at different positions on the membrane. Inset is an image of the membrane on a 4 mm diameter diamond at  $5 \times$  magnification.

Every membrane that was successfully transferred onto diamond was tested for laser oscillation. The next section details this testing process.

### **3.8 Laser testing**

#### *3.8.1 Concentric resonator testing*

II-VI gain structure membranes on diamond were tested for laser oscillation in a two-mirror concentric resonator, as shown and discussed in Fig. 2 and Section 3.2.3, respectively. The laser threshold was not reached using any of the membranes tested. This is most likely due to the poor membrane surface quality and localized regions of de-bonding over the membrane surfaces. Fig. 17 shows an image, taken through a longpass filter to remove the pump scatter, of a membrane of CDI 637 during testing in a two-mirror concentric resonator. As can be seen in Fig. 17, the working distance of the matched lens pair of the diode-pump (used in reference [20]) is very short and has a very small depth of focus, which further adds to the challenging alignment of the II-VI VECSEL. However, the matched lens pair pump scheme has been demonstrated to give excellent results with the diode-pumping of AlInGaP red-emitting VECSELs and so is an optimal pump source for the II-VI DBR-free testing [20].

Verification of the alignment of the DBR-free VECSEL resonators was completed by coupling the output from a 633 nm helium-neon laser (HeNe) into these test resonators. The mirrors on the II-VI DBR-free VECSEL test resonator were coated for high reflectivity from 490 nm to 610 nm, but gave a sufficient reflection at 633 nm to form a Fabry-Perot resonator. The 633 nm light was focussed onto the DBR-free membrane in the geometric centre of the resonator using a lens and the mirrors of the resonator were adjusted until interference fringes, with a bright central Airy-disc, formed. The fringes and Airy-disc were viewed with a CMOS camera and the resonator mirrors were adjusted to give the maximum fringe visibility. Verification of the alignment of the resonator provides evidence that the failure to reach laser threshold is due to insufficient optical gain / excessive optical loss in the II-VI membranes. The next subsection gives an overview of the gain mirrors which were constructed, to simplify the alignment.

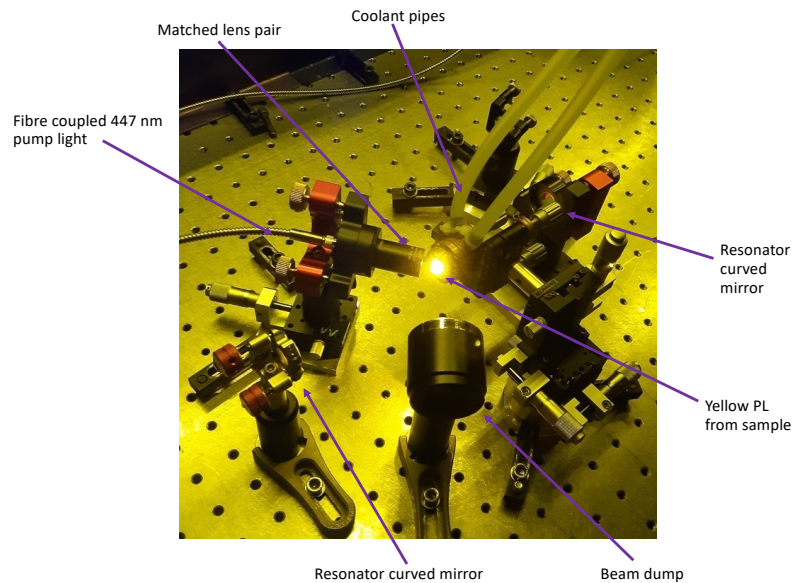


**Figure 17.** A CDI 637 membrane, optically-pumped at 447 nm during threshold tests inside a two-mirror concentric resonator. A longpass filter in front of the camera removes the blue pump scatter from the image. Note that the third mirror, behind the water pipes, is from a three-mirror resonator test.

### 3.8.2 Membrane-on-diamond bonded to HR mirror designs

In order to simplify the alignment of the II-VI DBR-free VECSEL a gain mirror geometry was constructed, in which the membrane-on-diamond was bonded onto a plane HR mirror and held by a brass mount, as shown in Fig. 18. A concern with this geometry is that the heat flow must be through the lid of the mount as the mirror acts as an insulator.

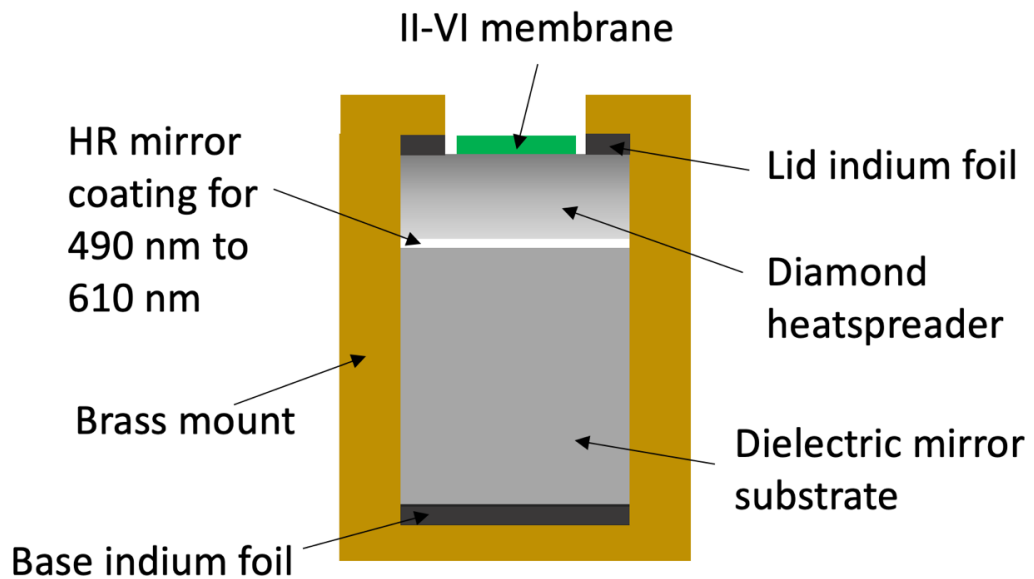


**Figure. 18.** Schematic of a constructed gain mirror. Membrane on diamond is bonded onto a HR mirror and clamped in a brass mount.

IDPL measurements of CDI 517 were taken in this geometry, shown in Fig. 19, and show a very small red-shift in the PL peak up to 1.4 W input pump power and shows a PL peak position at 547 nm, which is identical to the membrane mounted in the usual DBR-free geometry (see Section 3.5.3). This confirms that there is a comparable heat flow between the constructed gain mirror and the DBR-free mount geometries. After testing at maximum pump power the PL of the sample began to fade, due to pump induced damage. The laser threshold was not reached in this geometry, however it could prove to be a useful method of constructing DBR-free VECSELS, but with a reduced size resonator. The next section discusses the future of work on the development of the II-VI VECSEL using full substrate removal.

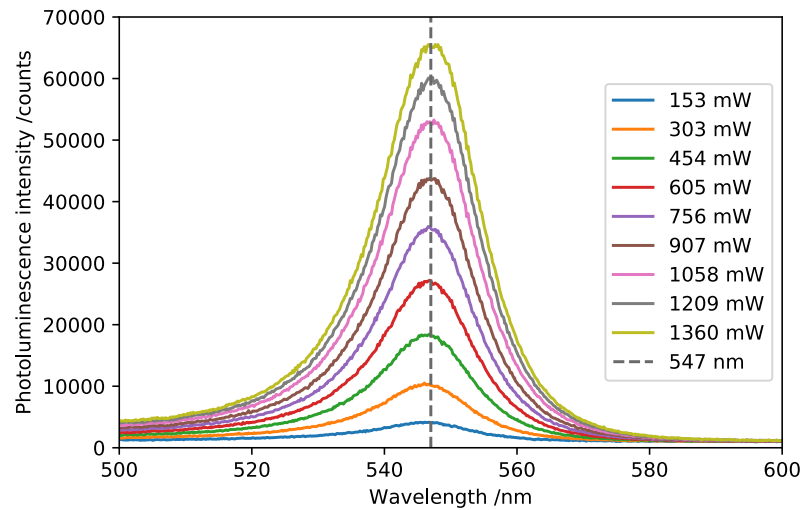


**Figure 19.** IDPL of a membrane of CDI 517 on diamond, bonded to a plane HR mirror to form a gain mirror.

### 3.9 Future perspectives on II-VI VECSEL technology

The future development of the II-VI VECSEL should focus on the material processing and quality issues raised within the previous sections. The HR-XRD and PL of CDI 447 (Fig. 10) demonstrated that it is possible to grow ZnCdSe/ZnCdMgSe-on-InP gain structures with high structural and optical quality, and through further optimization of the InGaAs and II-VI buffer layers it should be possible to grow II-VI VECSELs with a low defect density which are less susceptible to processing-induced damage.

For the full substrate removal methodology, pre-bonding the II-VI materials onto a diamond or SiC heatspreader before the substrate removal could eliminate the difficulties involved in releasing fragile membranes from wax. Future investigations into the plasma bonding of II-VI materials would facilitate this and offer a route to a full substrate removal method which does not damage or contaminate the II-VI VECSEL membranes.

Chapter 4 details the application of heterogeneous integration methods in a novel under-etching and transfer printing methodology for producing high quality ZnCdMgSe membranes. The methods presented in Chapter 4 eliminate the need to remove the entire substrate to obtain a II-VI membrane and the releasing of membranes from wax holding layers is no longer required.

### 3.10 Conclusion

In this chapter the progress towards the first demonstration of an optically-pumped II-VI, DBR-free VECSEL has been reported. An InGaN-diode-pumped VECSEL was demonstrated, as progress towards developing the pump optics for the II-VI, DBR-free VECSEL, and a resonator has been designed and tested. The full substrate removal methodology was improved to raise the membrane quality, with the best results arising from mounting samples in glycol phthalate or Microposit S1805 and etching the bulk of the InP substrate with HCl:H<sub>2</sub>O (3:1), without any mechanical polishing.

An iterative, multi-staged growth campaign was completed, starting from model calibration samples and finishing with high brightness, highly lattice-matched samples with improved surface quality. II-VI gain membranes were obtained by full substrate removal, bonded onto diamonds and tested for laser oscillation. The laser threshold was not reached on any sample. The lack of laser demonstration is likely due to the poor membrane bonding, etch pits in the sample and defects introduced during the substrate removal. Improvements in the II-VI material flatness should enable the as-grown sample to be capillary bonded onto diamond, which will offer greater support during the substrate removal. The main focus of future work on the II-VI, DBR-free VECSEL should be to obtain a high-quality membrane, bonded to an intracavity diamond heatspreader. Improving the quality of II-VI membranes motivates the development of the novel suspension method, presented in Chapter 4, which uses heterogeneous integration techniques such as under-etching and transfer printing to produce high quality ZnCdMgSe membranes.

### References

1. Z. Yang, A. R. Albrecht, J. G. Cederberg, and M. Sheik-Bahae, "DBR-free optically pumped semiconductor disk lasers," in *Vertical External Cavity Surface Emitting Lasers (VECSELs) V*, M. Guina, ed. (International Society for Optics and Photonics, 2015), **9349**, p. 934905.
2. Z. Yang, A. R. Albrecht, J. G. Cederberg, and M. Sheik-Bahae, "Optically pumped DBR-free semiconductor disk lasers," *Opt. Express* **23**(26), 33164 (2015).
3. Z. Yang, D. Follman, A. R. Albrecht, P. Heu, N. Giannini, G. D. Cole, and M. Sheik-Bahae, "16 W DBR-free membrane semiconductor disk laser with dual-SiC heatspreader," *Electron. Lett.* **54**(7), 430–432 (2018).
4. Z. Yang, A. R. Albrecht, J. G. Cederberg, and M. Sheik-Bahae, "80 nm tunable DBR-

- free semiconductor disk laser," *Appl. Phys. Lett.* **109**(2), 022101 (2016).
5. H. Kahle, C. M. N. Mateo, U. Brauch, P. Tatar-Mathes, R. Bek, M. Jetter, T. Graf, and P. Michler, "Semiconductor membrane external-cavity surface-emitting laser (MECSEL)," *Optica* **3**(12), 1506 (2016).
  6. A. Broda, B. Jeżewski, I. Sankowska, M. Szymański, P. Hoser, and J. Muszalski, "Growth and characterization of InP-based 1750 nm emitting membrane external-cavity surface-emitting laser," *Appl. Phys. B Lasers Opt.* **126**(12), 192 (2020).
  7. H. M. Phung, P. Tatar-Mathes, C. Paranthoën, C. Levallois, N. Chevalier, M. Perrin, A. Kerchaoui, H. Kahle, M. Alouini, and M. Guina, "Quantum dot membrane external-cavity surface-emitting laser at 1.5  $\mu\text{m}$ ," *Appl. Phys. Lett.* **118**(23), 231101 (2021).
  8. R. Sheikhi, Y. Huo, F. G. Shi, and C. C. Lee, "Low Temperature VECSEL-to-Diamond Heterogeneous Integration with Ag-In Spinodal Nanostructured Layer," *Scr. Mater.* **194**, 113628 (2021).
  9. B. Heinen, T.-L. Wang, M. Sparenberg, A. Weber, B. Kunert, J. Hader, S. W. Koch, J. V. Moloney, M. Koch, and W. Stolz, "106 W continuous-wave output power from vertical-external-cavity surface-emitting laser," *Electron. Lett.* **48**(9), 516 (2012).
  10. R. Moug, A. Alfaro-Martinez, L. Peng, T. Garcia, V. Deligiannakis, A. Shen, and M. Tamargo, "Selective etching of InGaAs/InP substrates from II-VI multilayer heterostructures," *Phys. status solidi* **9**(8–9), 1728–1731 (2012).
  11. B. E. Jones, P. J. Schlosser, J. De Jesus, T. A. Garcia, M. C. Tamargo, and J. E. Hastie, "Processing and characterisation of II–VI ZnCdMgSe thin film gain structures," *Thin Solid Films* **590**, 84–89 (2015).
  12. T. J. Miller, M. A. Haase, X. Sun, B. Hao, J. Zhang, T. L. Smith, T. Ballen, J. Xie, A. S. Barnes, F. Kecman, J. Yang, J. Thielen, C. A. Leatherdale, R. Wirth, A. Biebersdorf, K. Engl, and S. Groetsch, "High efficiency green LEDs using II-VI color converters," in *Proc. SPIE 7617, Light-Emitting Diodes: Materials, Devices, and Applications for Solid State Lighting XIV*, K. P. Streubel, H. Jeon, L.-W. Tu, and N. Linder, eds. (International Society for Optics and Photonics, 2010), **7617**, p. 76171A.
  13. M. A. Haase, J. Xie, T. A. Ballen, J. Zhang, B. Hao, Z. H. Yang, T. J. Miller, X. Sun, T. L. Smith, and C. A. Leatherdale, "II–VI semiconductor color converters for efficient green, yellow, and red light emitting diodes," *Appl. Phys. Lett.* **96**(23), 231116 (2010).
  14. J. M. M. Santos, B. E. Jones, P. J. Schlosser, S. Watson, J. Herrnsdorf, B. Guilhabert, J. J. D. McKendry, J. De Jesus, T. A. Garcia, M. C. Tamargo, A. E. Kelly, J. E.



- Hastie, N. Laurand, and M. D. Dawson, "Hybrid GaN LED with capillary-bonded II–VI MQW color-converting membrane for visible light communications," *Semicond. Sci. Technol.* **30**(3), 035012 (2015).
15. M. Schmid, S. Benchabane, F. Torabi-Goudarzi, R. Abram, A. I. Ferguson, and E. Riis, "Optical in-well pumping of a vertical-external-cavity surface-emitting laser," *Appl. Phys. Lett.* **84**(24), 4860–4862 (2004).
  16. W. Zhang, T. Ackemann, S. McGinily, M. Schmid, E. Riis, and A. I. Ferguson, "Operation of an optical in-well-pumped vertical-external-cavity surface-emitting laser," *Appl. Opt.* Vol. 45, Issue 29, pp. 7729–7735 **45**(29), 7729–7735 (2006).
  17. C. M. N. Mateo, U. Brauch, T. Schwarzbäck, H. Kahle, M. Jetter, M. A. Ahmed, P. Michler, and T. Graf, "Enhanced efficiency of AlGaInP disk laser by in-well pumping," *Opt. Express* **23**(3), 2472 (2015).
  18. A. Smith, J. E. Hastie, A. J. Kemp, H. D. Foreman, M. D. Dawson, T. Leinonen, and M. Guina, "GaN diode-pumping of a red semiconductor disk laser," in *LEOS 2008 - 21st Annual Meeting of the IEEE Lasers and Electro-Optics Society* (IEEE, 2008), pp. 404–405.
  19. A. J. Kemp, A. J. Maclean, J. E. Hastie, S. A. Smith, J.-M. Hopkins, S. Calvez, G. J. Valentine, M. D. Dawson, and D. Burns, "Thermal lensing, thermal management and transverse mode control in microchip VECSELs," *Appl. Phys. B* **83**(2), 189–194 (2006).
  20. P. H. Moriya, R. Casula, G. A. Chappell, D. C. Parrotta, S. Ranta, H. Kahle, M. Guina, and J. E. Hastie, "InGaN-diode-pumped AlGaInP VECSEL with sub-kHz linewidth at 689 nm," *Opt. Express* **29**(3), (2021).
  21. H.-M. Phung, H. Kahle, J.-P. Penttinen, P. Rajala, S. Ranta, and M. Guina, "Power scaling and thermal lensing in 825 nm emitting membrane external-cavity surface-emitting lasers," *Opt. Lett.* **45**(2), 547 (2020).
  22. P. Eliáš, I. Kosti, J. Šoltýs, and S. Hasenöhrl, "Wet-etch bulk micromachining of (100) InP substrates," *J. Micromechanics Microengineering* **14**(8), 1205–1214 (2004).
  23. P. Eliáš, J. Martaus, J. Šoltýs, and I. Kostič, "Micromachining of mesa and pyramidal-shaped objects in (1 0 0) InP substrates," *J. Micromechanics Microengineering* **15**(5), 1007–1014 (2005).
  24. S. Adachi, H. Kawaguchi, and G. Iwane, "InGaAsP/InP Planar-Stripe Lasers with Chemically Etched Mirrors," *J. Electrochem. Soc.* **129**(4), 883 (1982).
  25. B. Tuck and A. J. Baker, "Chemical etching of {1 1 1} and {1 0 0} surfaces of InP,"

- J. Mater. Sci. **8**(11), 1559–1566 (1973).
26. A. R. Clawson, *Guide to References on III-V Semiconductor Chemical Etching* (n.d.).
  27. P. Mounaix, P. Delobelle, X. Mélique, L. Bornier, and D. Lippens, "Micromachining and mechanical properties of GaInAs/InP microcantilevers," *Mater. Sci. Eng. B* **51**(1–3), 258–262 (1998).
  28. A. Broda, B. Jezewski, M. Szymanski, and J. Muszalski, "High-Power 1770 nm Emission of a Membrane External-Cavity Surface-Emitting Laser," *IEEE J. Quantum Electron.* **57**(1), 1–6 (2020).
  29. B. Jezewski, A. Broda, I. Sankowska, A. Kuźmich, K. Gołaszewska-Malec, K. Czuba, and J. Muszalski, "Membrane external-cavity surface-emitting laser emitting at 1640 nm," *Opt. Lett.* **45**(2), 539 (2020).
  30. Z. L. Liao, "Semiconductor wafer bonding via liquid capillarity," *Appl. Phys. Lett.* **77**(5), 651–653 (2000).
  31. H. Ichikawa, K. Yamaguchi, T. Katsumata, and I. Shoji, "High-power and highly efficient composite laser with an anti-reflection coated layer between a laser crystal and a diamond heat spreader fabricated by room-temperature bonding," *Opt. Express* **25**(19), 22797 (2017).
  32. L. Lang, F. Saltarelli, G. Lacaillle, S. Rowan, J. Hough, I. J. Graumann, C. R. Phillips, and U. Keller, "Silicate bonding of sapphire to SESAMs: adjustable thermal lensing for high-power lasers," *Opt. Express* **29**(12), 18059 (2021).
  33. D. Priante, M. Zhang, A. R. Albrecht, R. Bek, M. Zimmer, C. Nguyen, D. Follman, G. D. Cole, and M. Sheik-Bahae, "Demonstration of a 20-W membrane-external-cavity surface-emitting laser for sodium guide star applications," *Electron. Lett.* **57**(8), 337–338 (2021).
  34. J. H. Bahk, G. Zeng, J. M. O. Zide, H. Lu, R. Singh, D. Liang, A. T. Ramu, P. Burke, Z. Bian, A. C. Gossard, A. Shakouri, and J. E. Bowers, "High-temperature thermoelectric characterization of III-V semiconductor thin films by oxide bonding," *J. Electron. Mater.* **39**(8), 1125–1132 (2010).
  35. G. A. Chappell, B. Guilhabert, T. Garcia, K. Zhao, I. M. Watson, M. D. Dawson, M. C. Tamargo, and J. E. Hastie, "Suspension and transfer printing of ZnCdMgSe membranes from an InP substrate," *Opt. Mater. Express* **10**(12), (2020).
  36. N. M. Eldose, J. Zhu, N. Mavridi, K. Prior, and R. T. Moug, "Stacking of ZnSe/ZnCdSe Multi-Quantum Wells on GaAs (100) by Epitaxial Lift-Off," *J. Electron. Mater.* **47**(8), 4366–4369 (2018).
  37. B. Seredyński, M. Król, P. Starzyk, R. Mirek, M. Ściesiek, K. Sobczak, J. Borysiuk,

- D. Stephan, J.-G. Rousset, J. Szczytko, B. Piętka, and W. Pacuski, "(Cd,Zn,Mg)Te-based microcavity on MgTe sacrificial buffer: Growth, lift-off, and transmission studies of polaritons," *Phys. Rev. Mater.* **2**(4), 043406 (2018).
38. C. M. Campbell, C.-Y. Tsai, J. Ding, and Y.-H. Zhang, "Epitaxial Lift Off of II-VI Thin Films Using Water-Soluble MgTe," *IEEE J. Photovoltaics* 1–5 (2019).
39. J. M. Hartmann, J. Cibert, F. Kany, H. Mariette, M. Charleux, P. Alleysson, R. Langer, and G. Feuillet, "CdTe/MgTe heterostructures: Growth by atomic layer epitaxy and determination of MgTe parameters," *J. Appl. Phys.* **80**(11), 6257–6265 (1996).
40. E. Snoeks, L. Zhao, B. Yang, A. Cavus, L. Zeng, and M. C. Tamargo, "Structural quality of pseudomorphic Zn<sub>0.5</sub>Cd<sub>0.5</sub>Se layers grown on an InGaAs or InP buffer layer on (0 0 1)InP substrates," *J. Cryst. Growth* **179**(1–2), 83–92 (1997).
41. K. Fukada, I. Nomura, S. -B. Che, E. Ogiwara, A. Kikuchi, and K. Kishino, "Reduction of Defect Density of ZnCdSe on InP Substrates by Introducing BeZnTe Buffer Layers," *Phys. status solidi* **229**(1), 107–110 (2002).

## 4. Heterogeneous integration of DBR-free VECSEL structures

### Chapter overview

Optimum DBR-free VECSEL performance requires extremely high-quality membranes to be produced by liberating semiconductor gain structures from their growth substrates. In this chapter heterogeneous integration methodologies are developed with the goal of enabling the construction of high quality, transfer-printed DBR-free VECSELs. The suspension method, see Fig. 1, builds on previous techniques that were developed in-house for GaN-based LEDs [1,2], and in this work is adapted and developed for the under-etching and transfer printing of II-VI and III-V DBR-free VECSEL structures. The under-etching of II-VI-on-InP in particular required careful consideration of InP crystallographic directions, and the results are of wider interest beyond the current work, given the broad range of InP-based devices under development for heterogeneous integration.

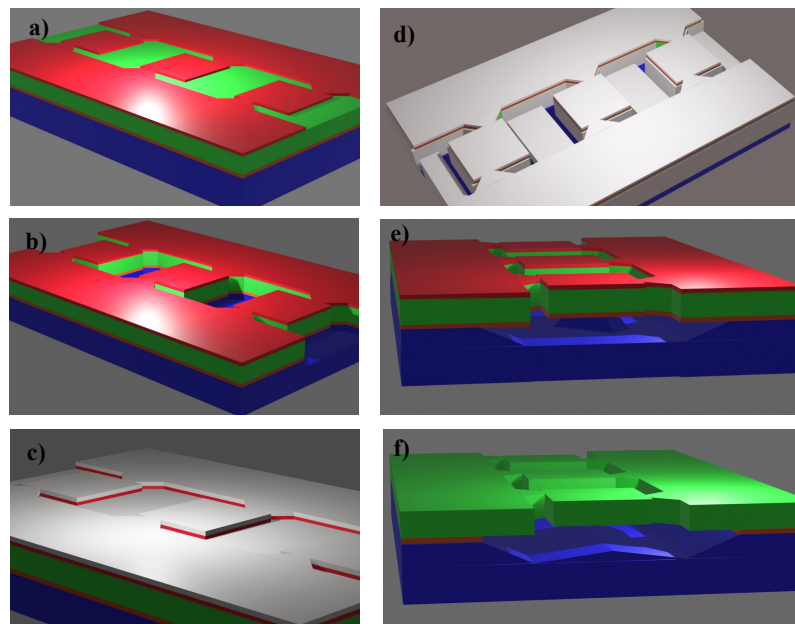


**Figure 1.** The six key microfabrication steps of the suspension method, presented in this chapter, for producing VECSEL membranes for transfer printing: **a)** device patterning using a hardmask, **b)** inductively coupled plasma (ICP) etching to define the hardmask profile into the VECSEL structure, **c)** depositing a protective silica layer, **d)** shaping the protective layer to allow the wet under-etching of the patterned devices, **e)** under-etching the membranes (sidewall protection not shown for clarity) and **f)** etching the buffer layer and removing the protective layers. The layer colours signify: red for the silica hardmask, green for the device layer, orange for the InGaAs buffer layer (not present in III-V structures tested here), white for the silica sidewall protection and blue is the substrate.

The development and optimization of the key steps of the suspension method are shown, which include: hardmask formation and device patterning (Fig. 1 a) and Fig. 1 b)), sidewall protection formation (Fig. 1 c) and Fig. 1 d)) and the under-etching of the individual DBR-free VECSEL membranes (Fig. 1 e) and Fig. 1 f)). The methodology presented is applied to the ZnCdMgSe-on-InP and GaInP/AlGaInP-on-GaAs material systems to produce 100- $\mu\text{m}$ -square membranes, which are transfer-printed onto optically transparent diamond heatspreaders.

## 4.1 Materials of interest

### 4.1.1 Developing DBR-free VECSELS

Following the difficulties with obtaining high quality membranes using full substrate removal in Chapter 3, this chapter investigates the development of both II-VI (ZnCdMgSe-on-InP) and III-V (GaInP/AlGaInP-on-GaAs) DBR-free VECSELS using the suspension method. As outlined in the Introduction, the ZnCdMgSe-on-InP material system is promising for “green gap” semiconductor laser sources, however the InGaAs buffer layer and InP substrate are opaque at visible wavelengths making epitaxial lift-off (ELO) essential for producing a DBR-free VECSEL. The GaInP/AlGaInP material system has been demonstrated as a visible, DBR-free VECSEL [3], however no DBR-free VECSEL has ever been built by transfer printing and so this material system is processed, using the methods developed in this chapter, to assess this. The II-VI and III-V structures used for testing the methods developed in this work are described below.

### 4.1.2 ZnCdMgSe samples

For the development of the suspension method of ZnCdMgSe-on-InP, simple sample architectures are used so that the sample was a control variable. The test samples are single layers of ZnCdMgSe, grown on InGaAs buffer layers on InP, where quantum wells (QWs) have not yet been implemented due to the strain and possible defects which can be introduced during their growth. For the successful demonstration of the suspension and transfer printing method of ZnCdMgSe, reported in reference [4], the sample (named CDI 340) was a 500-nm-thick, MBE grown,  $\text{Zn}_{0.37}\text{Cd}_{0.49}\text{Mg}_{0.14}\text{Se}$  layer with a 110 nm-thick  $\text{In}_{0.53}\text{Ga}_{0.47}\text{As}$  buffer layer.

### 4.1.3 GaInP/AlInGaP DBR-free VECSEL structure without strain balancing (MR3751)

For the development of the suspension method of GaInP/AlGaInP-on-GaAs, we used material from wafer MR3751, which was designed for previous VECSEL work by Dr Brynmor Jones. This structure was chosen as it had previously been successfully processed by full substrate removal and used in a working DBR-free VECSEL [5]. The structure was grown by

metalorganic chemical vapour deposition (MOCVD) at the EPSRC National Centre for III-V Technologies, and is comprised of ten pairs of resonantly spaced, compressively strained, GaInP QWs with AlGaInP barriers and a GaInP capping layer. It should be noted that the MR3751 structure, summarized in Table 1, did not include any strain compensating layers.

**Table 1.** The structure of MR3751, a 20 QW GaInP/AlGaInP DBR-free structure with demonstrated laser operation. There is no strain balancing within this structure.

Layer purpose		Material	Thickness /nm
Cap		$\text{Ga}_{0.515}\text{In}_{0.485}\text{P}$	10.0
Barrier		$(\text{Al}_{0.6}\text{Ga}_{0.4})_{0.525}\text{In}_{0.475}\text{P}$	82.6
QW repeating unit $\times$ 10	QW	$\text{Ga}_{0.44}\text{In}_{0.56}\text{P}$	8.2
	Barrier	$(\text{Al}_{0.6}\text{Ga}_{0.4})_{0.525}\text{In}_{0.475}\text{P}$	7.0
	QW	$\text{Ga}_{0.44}\text{In}_{0.56}\text{P}$	8.2
	Barrier	$(\text{Al}_{0.6}\text{Ga}_{0.4})_{0.525}\text{In}_{0.475}\text{P}$	80.5
Barrier		$(\text{Al}_{0.6}\text{Ga}_{0.4})_{0.525}\text{In}_{0.475}\text{P}$	103.0
Cap		$\text{Ga}_{0.515}\text{In}_{0.485}\text{P}$	10.0
Substrate		GaAs	N/A

MR3751 was designed to operate at  $\sim 689$  nm, with GaInP QWs designed for room temperature emission at  $\sim 674$  nm, and a resonant periodic gain and sub-cavity resonance set for 689 nm. Fig. 2 shows the refractive index profile of the structural layers of MR3751, with the standing wave electric field (the  $|E|^2$ ) of the laser mode showing the alignment of the QW pairs with the electric field antinodes [5]. During a previous laser demonstration a DBR-free VECSEL using MR3751 and high reflectivity cavity mirrors reached threshold at 0.4 W absorbed pump power [5]. With output coupling of 2%, output power of up to 21 mW was achieved at 682.4 nm for absorbed input power of 0.9 W.

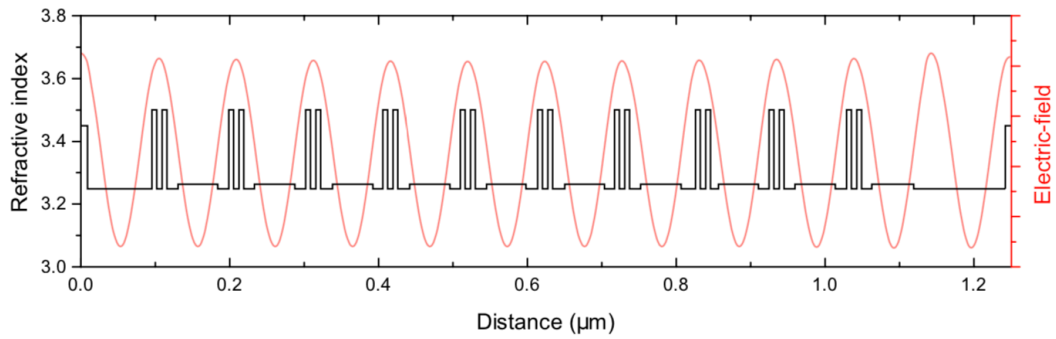


**Figure 2.** The MR3751 chip design. This was a GaInP/AlGaInP structure designed for previous work by Dr Brynmor Jones. The refractive index profile of the sample is plotted along with  $|E|^2$  of the standing wave electric field of the laser mode, showing the alignment of the QW pairs with the electric field antinodes. Figure taken from [5].

## 4.2 Motivation for using microfabrication techniques to produce DBR-free VECSELs

### 4.2.1 Previous II-VI processing work

There is limited work on developing ELO strategies specifically for the ZnCdMgSe-on-InP material system. II-VI semiconductors are grown on GaAs, GaP, and InP substrates [6], with appropriate buffer layers, and therefore, to fully incorporate these II-VI epitaxial layers into devices, ELO is essential due to the poor thermal and optical properties (at visible wavelengths) of the substrates. A variety of methods have been devised to accomplish this, ranging from chemical or mechanical thinning of InP substrates and a subsequent selective wet etch of the InGaAs buffer layer (as demonstrated in Chapter 3) [7,8], to making use of metastable sacrificial layers (MgTe or MgS) for growths on GaAs [9,10].

During the initial stages of this project, mechanically polishing InP substrates and wet etching any remaining InP with HCl-based etchants introduced significant defects into the epitaxial layer, particularly with strained structures. The usage of the InGaAs buffer layer as an etch stop proved ineffective over large scale substrate wet etching. The InP forms very deep etch pits, when bulk etched, which results in a non-uniform removal of the InP. The InP remnants micromask the InGaAs during the InGaAs buffer layer wet etch and this roughens the II-VI epitaxial layer underside. Additionally, handling epitaxial membranes in liquid suspension (as reported in reference [8] and completed in Chapter 3) is challenging, non-deterministic and impractical for the commercial scaling of ELO technologies. The damage to the II-VI VECSEL structures was deemed more than sufficient to prevent laser demonstration and this motivated using the suspension method to process the ZnCdMgSe-on-InP structures.

#### 4.2.2 Overview of the suspension and transfer printing method

Transfer printing for device construction has been a major topic of work within the heterogeneous integration community and this has enabled advancements in ELO, especially the under-etching of individual devices to release them from their native substrates [11]. The suspension method involves the formation of a device within an epitaxial structure and the subsequent under-etching, with wet etchants, of this patterned layer to liberate it from the growth substrate [12]. The device is held in place during the under-etch by anchors which can be photoresist- [12,13], polymer- [14,15] or semiconductor-based [1,16] and permit membrane release during transfer printing, see Fig. 3. This method has been successfully demonstrated in the production of InGaN micro-LEDs on diamond, AlInGaN LEDs on flexible substrates, InP-based etched facet lasers on Si substrates, VCSELs on Si substrates, III-V optical amplifiers on  $\text{Si}_3\text{N}_4$  and AlGaInP LEDs on thin, flexible plastic sheets [1,12,13,15–17]. These demonstrations have shown the possibility of using under-etching and transfer printing for high spatial precision heterogeneous integration of III-V epitaxial layers.

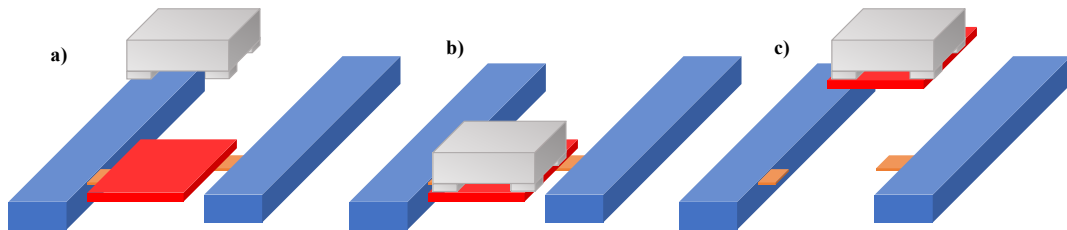


**Figure 3.** A micro-moulded PDMS stamp, grey, is used to detach a device, red, from the anchors, orange, which hold it onto the original epitaxial growth, blue. **a)** An under-etched device is held by anchors, **b)** the PDMS stamp is pressed onto the device, liberating it from the anchors. The device adheres to the PDMS stamp. **c)** The PDMS stamp can now be used to translate the device to a new substrate.

There has been no previous work on applying the suspension and transfer method to II-VI semiconductors, and for InP substrates the current suspension and transfer methods use release layers [13], which is currently not feasible for ZnCdMgSe-on-InP. The reported release layers for InP-based devices are InGaAs and InAlAs etched in  $\text{FeCl}_3\cdot\text{H}_2\text{O}$  [15,18], and in the case of GaN-based devices, the Si device substrate has been used as an effective release layer [1]. For the suspension and transfer printing method to be successful with II-VI semiconductors on InP, and indeed any material grown on InP, the key challenge is the difficulty of wet-etching



InP to a specifically masked shape during the under-etch. The other difficulty is the lack of any known selective etchant between ZnCdMgSe and InP.

Micro-moulding PDMS stamps enables their optimization for the transfer of discrete objects with specific geometries, including the detachment of suspended membranes from anchors. There have been no demonstrations of using transfer printing to construct a VECSEL, however membranes on PDMS can be transferred onto any suitable substrate and, in the case of many devices with strict thermal management requirements, this is ideally a transparent single crystal diamond or silicon carbide heatspreader, which is used to extract heat from an active region. For a membrane on diamond the continuity of contact, and hence the heat flow, between the membrane and the heatspreader depend strongly on their surface roughness. Transfer-printed membranes with a nm-scale surface roughness can Van-der-Waals bond onto the acceptor substrate, negating the use of adhesion layers, which add thermal impedance [16].

In this work, an array of 100- $\mu\text{m}$ -square ZnCdMgSe and GaInP/AlGaInP membranes are under-etched, using their substrates as effective release layers. These membranes are transfer-printed onto a diamond or SiC heatspreader. The methodology presented will enable the heterogeneous integration and miniaturization of II-VI membrane devices and will demonstrate the progress towards constructing a transfer-printed VECSEL.

#### *4.2.3 Goals of this work*

ZnCdMgSe is one of numerous semiconductor materials grown on InP which, along with GaAs, is a ubiquitous substrate within semiconductor device fabrication and heteroepitaxial growth, due to its low cost and lattice matching to useful III-V and II-VI materials. Whilst the novelty of the wide bandgap ZnCdMgSe motivates developing an ELO process for this material, developing an ELO system for semiconductors grown on InP, where highly-selective wet etching chemistry or release layers may not have been developed is an important step in expanding heterogeneous integration techniques to novel semiconductors. ELO of ZnCdMgSe from InP using full substrate removal yields inconsistent results, as demonstrated in Chapter 3, whereas as microfabrication techniques are consistent, highly precise and scalable with industrial techniques. In this chapter the development of a novel suspension and transfer printing method for ZnCdMgSe is presented. For optimum II-VI, DBR-free VECSEL performance the goals of this new ELO process for ZnCdMgSe-on-InP are to minimize the inclusion of defects and membrane strain changes during the processing, whilst achieving sub-nm-scale root mean square (RMS) surface roughness, ideally with no etch damage.

Transfer printing could be used to advance progress in the development of monolithic VECSELs, where the gain chip, resonator medium and external cavity mirror are bonded together to form a rigid laser cavity [19,20]. The thermal management of monolithic VECSELs can likely be improved by removing the substrate from the gain chip and by ensuring a high-quality diamond to semiconductor bond is achieved. In a monolithic VECSEL the gain chip must be bonded in a precise location, with a high quality, on the optical axis of the cavity, and transfer printing of small VECSEL membranes lends itself well to this application due to the nm-scale precision of deposition which is possible with transfer printing [21,22]. The suspension and transfer printing of GaInP/AlGaInP structures is investigated in this work to test whether a DBR-free VECSEL can be constructed by transfer printing, given the strict thermal transport requirements and necessity for high quality diamond-semiconductor bonds, which if possible opens up the possibility of constructing a chip-scale monolithic VECSEL using transfer printing. Using transfer printing and under-etching for the heterogeneous integration of VECSELs could allow for substrate recycling and the production of hundreds of individual VECSELs from a single epitaxial growth.

### **4.3 Etching II-VI and III-V semiconductors**

#### *4.3.1 Overview*

The purpose of semiconductor etching is to introduce specific geometries into semiconductor layers to form components of a device architecture or to prepare for subsequent deposition or etching processes. Etching can be completed by wet or dry processes. Wet processes use reactants in liquid solution to remove, or add, material by chemical reactions and are often isotropic and material selective processes. Dry processes use gases, often in plasma form, to etch through highly anisotropic physical sputtering or through isotropic chemical etching.

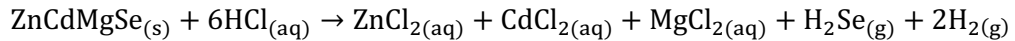
For the III-V material system there is a huge background of work on wet and dry etching [23], however for the II-VI material system this is not the case, adding to the challenge of developing a microfabrication process with these materials. Microfabrication of the II-VI-on-InP material system requires methods of etching the II-VI material itself and the unrequired InGaAs and InP layers.

### 4.3.2 Wet etching of semiconductors

#### 4.3.2.1 Wet etch of InP

The wet etching of InP has been introduced in Section 3.3.4. Here, the etching of InP is applied to under-etch II-VI membranes. Previous work has shown how InP etches when it is masked by square and rectangular masks tilted to align with specific crystallographic orientations and has highlighted the dominance of  $\langle 1\ 0\ 0 \rangle$  directions in the under-etch of masks on InP [24,25], which dictates the alignment of device masks for successful, efficient fabrication. Microfabrication on InP has been successful over multiple geometries, from microscale wedges and stripes to the under-etching of photonic crystal lasing membranes [26–28].

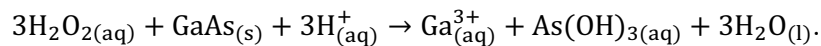
The HCl-based etchants applied in Chapter 3 are used for the under-etching presented here, however these etchants etch ZnCdSe and ZnCdMgSe, adding to the ELO difficulty. The etching of ZnCdMgSe via HCl can be simplified to:



where the overall ratio of  $\text{H}_2\text{Se}$  to  $\text{H}_2$  will depend on the pH of the etching solution as  $\text{H}_2\text{Se}$  can be quickly oxidized to  $\text{H}_2$  and elemental Se [29]. In this work all wet etch processes are completed at a room temperature of 21 °C and at standard atmospheric pressure.

#### 4.3.2.2 Wet etch of GaAs and InGaAs with $\text{H}_3\text{PO}_4:\text{H}_2\text{O}_2:\text{H}_2\text{O}$

$\text{H}_2\text{O}_2$  based etchants can be used to oxidize GaAs and InGaAs, which generates soluble etch products which are dissolved by an acid, in this case  $\text{H}_3\text{PO}_4$  [30]. Water is often added to  $\text{H}_2\text{O}_2$  based etchants to modify the etch rate and the etch selectivity between different materials. The etch proceeds as a cycle of generating surface oxides and then dissolving them.  $\text{H}_3\text{PO}_4:\text{H}_2\text{O}_2:\text{H}_2\text{O}$  mixtures have been reported to provide selective etching of GaAs over InGaP however there is very little information on the effects of this etchant on AlGaInP [23,31]. AlInGaP has been reported to be etched by  $\text{H}_2\text{SO}_4$ -based and HCl-based etchants and AlInP etchants are typically HCl-based so it can be assumed that  $\text{H}_3\text{PO}_4:\text{H}_2\text{O}_2:\text{H}_2\text{O}$  should not etch AlInGaP [23]. The etching of the GaAs proceeds as [30]:



In the case of InGaAs the Ga phase is etched as above and then etching of the In phase is assumed to proceed via a similar mechanism:

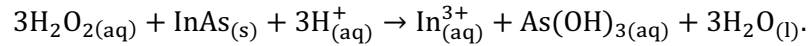


**Table 2.** Literature review of II-VI and InP wet etching

Reference	Materials	Etchants	Observations
[7]	ZnCdSe, MgSe, ZnCdMgSe, InGaAs	H <sub>3</sub> PO <sub>4</sub> :H <sub>2</sub> O <sub>2</sub> :H <sub>2</sub> O (1:1:6).	Selectivity of 70 between the mean etch rate of II-VI semiconductors and InGaAs.
[32]	ZnSSe, ZnMgSSe	Br <sub>2</sub> :CH <sub>3</sub> OH (0.4 % Br <sub>2</sub> )	Etch pits observed in ZnSSe but no effect on ZnMgSSe.
[33]	ZnSe, ZnCdSe, ZnCdMgSe	Br <sub>2</sub> :CH <sub>3</sub> OH (0.05 %, 0.10 % and 0.25 % Br <sub>2</sub> )	Good etchant of ZnSe.
		Br <sub>2</sub> : CH <sub>3</sub> OH (1.0 %, 1.5 %, 2.0 %, 2.5 %, 3.0 % and 3.5 % Br <sub>2</sub> )	“Reasonable etching” on ZnCdSe but “little effect on ZnCdMgSe”.
		HCl	Etches ZnCdSe and ZnCdMgSe
[26]	InP	Br <sub>2</sub> : CH <sub>3</sub> OH	Approximate etch rates of (001) InP from a log-log plot: 2 μm/min (0.1 % Br <sub>2</sub> ) 4 μm/min (0.2 % Br <sub>2</sub> ) 6 μm/min (0.3 % Br <sub>2</sub> ) 10 μm/min (1.0 % Br <sub>2</sub> )
[34]	InP	HCl:H <sub>3</sub> PO <sub>4</sub> (3:1)	Etches InP.
[35]	(Zn,Cd)Se, Zn(S,Se), GaAs, AlGaAs	Etchant not reported	Selective wet etch to form the ring shape of a micro-resonator disk. The etchant removes the III-V material without damaging the II-VI.
[36]	ZnSe, ZnCdSe, GaAs	NaOH:H <sub>2</sub> O <sub>2</sub> 42 ml NaOH (5 %) and 8 ml of H <sub>2</sub> O <sub>2</sub> (30 %)	Etch rate of 50 μm/hr for GaAs (likely to etch InGaAs) and 200 nm/hr ZnSe-based materials giving a selectivity of 250.
[37]	ZnSe, ZnCdSe, GaAs	NaOH:H <sub>2</sub> O <sub>2</sub> 42 ml NaOH (5 %) and 8 ml of H <sub>2</sub> O <sub>2</sub> (30 %)	Etch rate of 100 μm/hr for GaAs (likely to etch InGaAs) and 200 nm/hr for ZnSe-based structures, giving a selectivity of 500.

#### 4.3.2.3 Review of selective etchants for InP from ZnCdMgSe

There is very little work on examining the wet etching of II-VI materials (other than ZnSe) and no work on developing a selective etchant between ZnCdMgSe and InP, which would heavily reduce the risk of damage during the substrate removal. Table 2 summarizes the literature which relates to possible selective etchants of InGaAs and InP from ZnCdMgSe. Table 2 shows that Br<sub>2</sub>:CH<sub>3</sub>OH could be used to selectively etch InP from ZnCdMgSe and NaOH:H<sub>2</sub>O<sub>2</sub> or H<sub>3</sub>PO<sub>4</sub>:H<sub>2</sub>O<sub>2</sub>:H<sub>2</sub>O could be used to selectively etch InGaAs from ZnCdMgSe. It should be noted that H<sub>3</sub>PO<sub>4</sub>:H<sub>2</sub>O<sub>2</sub>:H<sub>2</sub>O does not etch InP and therefore is not a candidate for a II-VI/InP selective etch [23]. This is discussed further in Appendix A4.1.

#### 4.3.3 Dry etch processes

Dry processes utilize plasmas to generate ions, radicals and reactive molecules for the controlled etching and/or deposition of materials. For the II-VI and III-V microfabrication presented in this chapter the three key dry processes needed were reactive ion etching (RIE), plasma enhanced chemical vapour deposition (PECVD) and inductively coupled plasma etching (ICP). RIE uses a single radio frequency (RF) electrical source to control the plasma density and ion acceleration. A plasma is generated between an anode and a cathode, with the sample held to a platen which acts as the cathode. ICP uses two separate RF power sources; one for a plasma generating coil which is inductively coupled to a toroidal plasma and the second for creating a bias on the platen. ICP allows control of the plasma density and ion energy separately, allowing for greater control over plasma etching properties. RIE and ICP can utilize chemical etching and physical sputtering. PECVD uses high pressure plasma to give a controlled deposition of thin films and operates in a capacitive way similar to RIE. An ashers is a dry process tool which uses plasma to generate highly reactive oxygen radicals which selectively etch organic molecules from inorganic semiconductors and metals. The principle usage of ashers is to remove photoresist (PR) and organic contaminants from samples. The etch recipes for the RIE, ICP, ashers and PECVD processes used in the II-VI and III-V microfabrication processes are detailed in Table 3. ICP etch 2 was used to replace the ICP etch 1 processes due to problems with BCl<sub>3</sub> gas supply lines during the project.

**Table 3.** Summary of the dry process conditions used for the suspension of II-VI and III-V membranes. Adapted from published version [4].

Process	Device	Process gases (flow rate [sccm])	Substrate temperature [°C]	Pressure [mTorr]	Input power [W]	Total input power density [ $\text{kWm}^{-2}$ ]
PECVD	Oxford Instruments Plasmalab 80 Plus	SiH <sub>4</sub> 5% v/v in N <sub>2</sub> carrier gas (170), N <sub>2</sub> O (710)	300	1000	70	2.23
RIE		Ar (15), CHF <sub>3</sub> (5)	20	30	120	3.82
ICP etch 1	SPTS Multiplex	Ar (4), BCl <sub>3</sub> (16)	20	6	200 (platen), 500 (coil)	89.1
ICP etch 2		Ar (10), Cl <sub>2</sub> (30)	20	20	200 (platen), 400 (coil)	76.4
Asher	Matrix 105	Oxygen radical	250	3750	500	28.3

#### 4.4 Suspension method for ZnCdMgSe-on-InP and GaInP/AlGaInP-on-GaAs: hardmask formation

For the development of the suspension method for DBR-free VECSELs a microLED mask was chosen due to its successful use in the development of III-V, InGaN-based microLEDs at the Institute of Photonics [2]. The mask consisted of an array of 100- $\mu\text{m}$ -sided square membranes held by a pair of offset anchors to rails, see Fig. 4 a) and b). This mask allows the formation of channels for the wet under-etching of the membranes and the anchors hold the membrane in place during the suspension, maintaining the strain state of the sample during substrate removal.

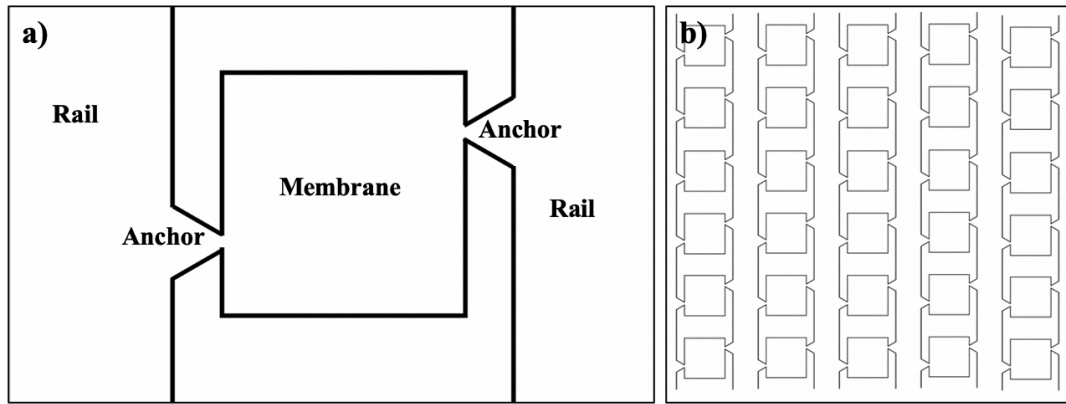


**Figure 4.** a) A single 100-µm-sided membrane held by anchors to rails and b) a highly scalable array of membranes.

Before processing the samples were cleaned using a three-step rinse in acetone, methanol and isopropanol, within a sonic bath (5 to 10 minutes for each solvent). The samples were then rinsed in deionized (DI) water to remove any trace organic contaminants and dried by a continuous flow of nitrogen gas.

Following solvent cleaning a 1.2 µm layer of SiO<sub>2</sub> is deposited by PECVD onto the sample surface (see Table 3 for conditions). SiO<sub>2</sub> is used as a hardmask material as it can be easily deposited using PECVD, easily etched using RIE and is inert with the reagents used in the wet etching of Ga(Al)InP, ZnCdMgSe, GaAs, InGaAs and InP. The PECVD growth of SiO<sub>2</sub> requires temperatures of 250 °C, however previous work has demonstrated dielectric thin film deposition on II-VI materials and so it is assumed that the NO<sub>x</sub> presence and the high temperatures of the growth introduce no additional defects or oxidation [38]. The deposition thickness of SiO<sub>2</sub> is chosen based on the ICP time required in the later steps (see Section 4.5).

A 0.5-µm-thick film of Microposit S1805 photoresist (PR) is spin-coated at 3800 rpm for 60 s onto the sample and soft-baked on a hotplate at 115 °C for 1 minute prior to masking. For the ZnCdMgSe the rails of the mask were aligned to run parallel to the  $[\bar{1} \bar{1} 0]$  direction to prevent the under-etch of the rails (see Section 4.7). The chromium mask is brought into hard contact (30 µm gap) with the sample in a Karl Suss MA6 Mask Aligner. The masked resist undergoes an exposure of 2.8 s with a UV lamp calibrated to 16 mW output power (365 - 435 nm, but optimized for 405 nm). The UV exposure chemically alters the PR so that when the exposed PR is placed into the alkaline development solution of Microposit Developer and DI water (1:1) for 30 seconds it is dissolved, and the unexposed PR remains and holds the device pattern [4].

RIE of 1.2  $\mu\text{m}$  of  $\text{SiO}_2$  is performed (see Table 3 for conditions) to transfer the PR pattern into the silica hard mask. The RIE etch recipe selectively etches silica over the organic resist. The remaining PR is then removed in a Matrix plasma asher with a 5-minute oxygen radical etch (see Table 3 for conditions). Then the samples are solvent cleaned again, as previously described but without the sonic bath. The  $\text{SiO}_2$  protects the membrane surface throughout all of these processes. A schematic and images of the completed hardmask for the ZnCdMgSe-on-InP and GaInP/AlGaInP-on-GaAs are shown in Fig. 5 a), b) and c) respectively.

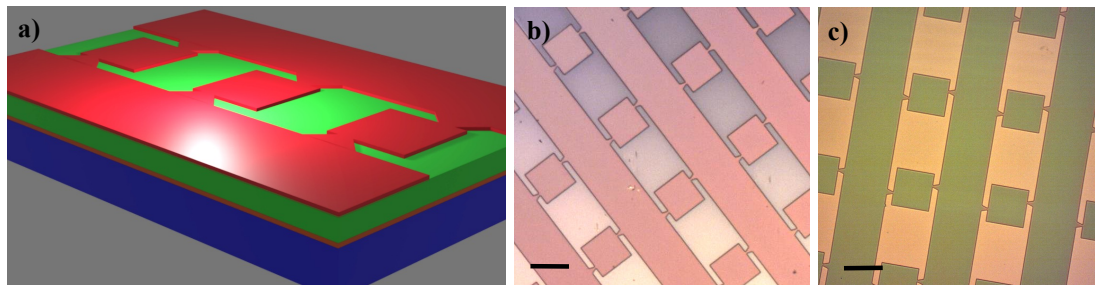


**Figure 5.** a) Schematic of the sample following the hardmask formation. The layer colours have the same meanings as in Fig.1. Images of b) ZnCdMgSe-on-InP and c) GaInP/AlGaInP-on-GaAs sample following the hardmask formation. The black scale bar represents 100  $\mu\text{m}$ .

#### 4.5 Suspension method for ZnCdMgSe-on-InP and GaInP/AlGaInP-on-GaAs: ICP

ICP etching has been used to etch CdTe, ZnCdTe and HgCdTe with Ar/ $\text{H}_2$  plasma [39], and ZnMgBeSe and ZnO with Ar/ $\text{Cl}_2/\text{BCl}_3$  plasma [40,41]. The Ar and  $\text{Cl}_2$  based ICP etch has been reported to be a universal III-V semiconductor etchant as the high ion flux possible with ICP ensures that all of the Cl-based etch products are volatile [42]. Given that the ICP recipe for the ZnCdMgSe-on-InP ideally needs to etch ZnCdMgSe, InGaAs and InP, recipes based on Ar/ $\text{Cl}_2/\text{BCl}_3$  were tested. The Ar ion is a heavy, high momentum etch component which gives an anisotropic physical sputtering of the sample surface and clears surface reaction products. The Cl-based components are highly chemically reactive and give an isotropic chemical etching component to exposed surfaces. The  $\text{BCl}_3$  ion gives a chemical etching component and has an additional physical sputtering effect due to its large mass. ICP etch 1 and ICP etch 2 (see Table 3), are based on in-house ICP recipes which were used to etch AlInGaP and GaN. Both recipes were used to successfully etch the ZnCdMgSe-on-InP and the GaInP/AlGaInP-on-GaAs samples and ICP etch 1 was used in the successful demonstration of the II-VI suspension and transfer printing method [4].



The ICP etches through the exposed material, which is not protected by the hardmask, to a depth of around 3  $\mu\text{m}$ , hence into the InP or GaAs substrate [4]. ICP etches the  $\text{SiO}_2$  mask at 80 nm/min and so the initial  $\text{SiO}_2$  deposition must be sufficiently thick to ensure that some remains to protect the membrane during the wet under-etch step. The mask geometry has a very high aspect ratio between the feature distances and the trench depths etched during the ICP stage (around 100:3) and this ensures that the ICP etched sidewalls are near-vertical [4]. A DEKTAK profilometer can be used to measure the depth profile of the trenches following the ICP and Fig. 6 shows an example from a total of 12 minutes of etching a ZnCdMgSe-on-InP sample with ICP etch 1.

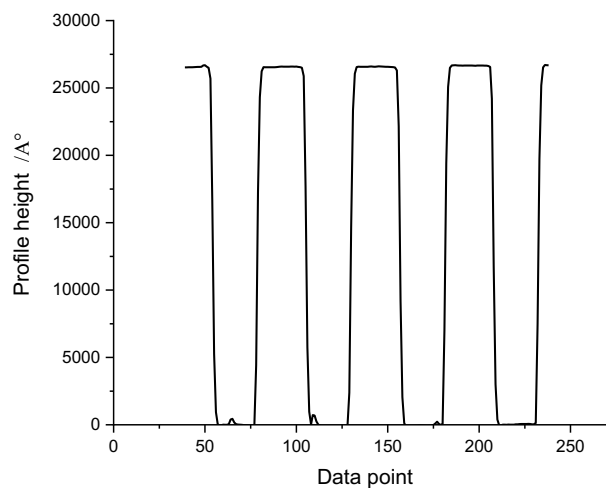


**Figure 6.** The profile of the trenches etched around the 100-micron membranes, measured using a DEKTAK profilometer, following ICP etch 1 testing on a ZnCdMgSe-on-InP sample. The maximum depth etched into the InP is estimated to be around 2  $\mu\text{m}$ .

The ICP etching of the silica hardmask can be monitored by etching a reference sample of  $\text{SiO}_2$  on Si alongside the masked II-VI samples. White light interference (Filmetrics) can be used to measure the  $\text{SiO}_2$  film thickness before and after the ICP etch. From the trench profile, such as in Fig. 6, and the  $\text{SiO}_2$  thickness etched, the depth into the substrate can be found. In Fig. 6, the 12-minute total ICP etch time depleted the  $\text{SiO}_2$  mask from 1080 nm to 120 nm, assuming an 80 nm/min etch rate of  $\text{SiO}_2$  in this ICP etch run. The trench depth measured in the DEKTAK was around 2600 nm and this includes the  $\text{SiO}_2$  top layer. This means that 2480 nm was etched through the quaternary and into the InP substrate. Given that the thickness of the ZnCdMgSe layer and the buffer layer is around 600 nm, the depth etched into the InP substrate is around 2  $\mu\text{m}$ .

Following the ICP etch the samples were inspected with an optical microscope, where a trench colour change to white can confirm that the substrate has been reached; see Fig. 7 for a schematic and examples of ICP-etched ZnCdMgSe-on-InP and GaInP/AlGaInP-on-GaAs samples, respectively. The thickness of the silica can vary over the sample surface, which causes a colour variation over the surface due to white light interference. The ICP can increase this variation further due to local etch rate variance over the sample surface.

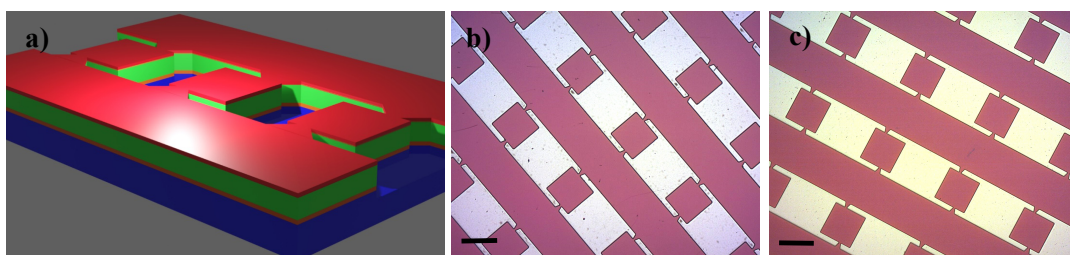


**Figure 7.** a) Schematic of the sample following the ICP etching through the II-VI, InGaAs and into the substrate. The layer colours have the same meanings as in Fig.1. Images of b) ZnCdMgSe-on-InP and c) GaInP/AlGaInP-on-GaAs sample following the ICP. The black scale bar represents 100  $\mu\text{m}$ .

## 4.6 Developing sidewall protection for ZnCdMgSe-on-InP

### 4.6.1 The requirement for sidewall protection

During initial trials of the under-etch for the ZnCdMgSe-on-InP, HCl-based etchants quickly damaged the ZnCdMgSe membranes (see Appendix A4.2). For the under-etch of GaInP/AlGaInP-on-GaAs this is not a problem as  $\text{H}_3\text{PO}_4\text{:H}_2\text{O}_2\text{:H}_2\text{O}$  selectively etches GaAs from GaInP/AlGaInP. The II-VI under-etch therefore required sidewall protection of the membranes to protect them during the wet under-etch, especially given the lack of selective etchants. Selective etchants, sidewall passivating etches, multi-step etches and varied etch concentrations were assessed to determine whether the optimization of the under-etching chemistry could yield improved membrane quality and this is summarized in Appendix A4.1. Developing sidewall protection is perhaps the most important, and the most difficult, problem to solve for the transfer print process.

The main goal for the development of the sidewall protection was to develop a protective layer for the membrane, which would still permit the wet under-etching to take place. For the formation of the sidewall protection silica was chosen due to its high growth quality by PECVD, easy dry etching, and chemical resistance to the wet etchants used in the under-

etching step. The II-VI material system contains magnesium which, when in high concentrations in the quaternary, can yield a very slow yet total oxidation of the device in atmospheric conditions. Silica sidewall protection can, however, be removed using oxygen-free plasmas, unlike thick PR which is often used for sidewall passivation [13]. PR stripping requires oxygen-based plasmas that could quickly oxidize the II-VI, and even a thorough solvent-based removal may leave residues or cause premature and unintended device release (following suspension by under-etching). Removing the SiO<sub>2</sub> using Ar:CHF<sub>3</sub> plasma avoids any oxidation risk at the expense of a small risk of physical sputtering damage to the surface of the epitaxial layers. The risk of sputtering damage can be negated by using a SiO<sub>2</sub>-on-Si reference sample and white light reflectance spectroscopy to carefully monitor the progress of the silica removal. PECVD and RIE were used to form the sidewall protection and the methods which were tested to obtain the optimum protection are summarized in Table 4. The most successful method, dry etch anisotropy, is discussed further below.

**Table 4.** Summary of the three key methods of forming SiO<sub>2</sub> based sidewall protection tested in this work.

<b>Strategy</b>	<b>Method</b>	<b>Failure mechanisms</b>	<b>Successful</b>
Dry etch anisotropy	Conformal PECVD deposition of 800 nm of SiO <sub>2</sub> into the trenches. Single RIE step to etch most of the SiO <sub>2</sub> creates etch holes at the base of the SiO <sub>2</sub> .	PH <sub>3</sub> damage, etch holes not being opened during the RIE resulting in no etching in some places, membrane damage due to defects in SiO <sub>2</sub> .	Yes
RIE and wet etch cycling	Conformal PECVD deposition of 800 nm of SiO <sub>2</sub> into the trenches. Then repeat the cycle of a short RIE followed by a wet under-etch. If insufficient RIE has been completed then the under-etch will not initiate and so another incremental RIE is completed.	PH <sub>3</sub> damage, etch holes not being opened during the RIE resulting in no etching in some places, membrane damage due to defects in SiO <sub>2</sub> .	No
Optical lithography	Conformal PECVD deposition of 800 nm of SiO <sub>2</sub> into the trenches, coating all of the sidewalls. S1805 PR is spin coated onto the samples and the pattern of the sidewall protection is masked into the PR. RIE then etches the exposed SiO <sub>2</sub> to form the sidewall protection.	Thick sidewall protection increases under-etch time by blocking access to InP next to the membrane, PH <sub>3</sub> damage, hard to track etch progress.	No

#### 4.6.2 The most successful strategy: dry etch anisotropy

Following the conformal SiO<sub>2</sub> deposition, RIE was used to preferentially etch the SiO<sub>2</sub> at the base of the trench to form holes for wet-etchant access to the InP. Scanning electron microscope (SEM) images were taken, using a Hitachi S-3000N SEM, of the conformal SiO<sub>2</sub> deposition (Fig. 8 a-c)) and the RIE step (Fig. 8 d) and e)) on test samples.

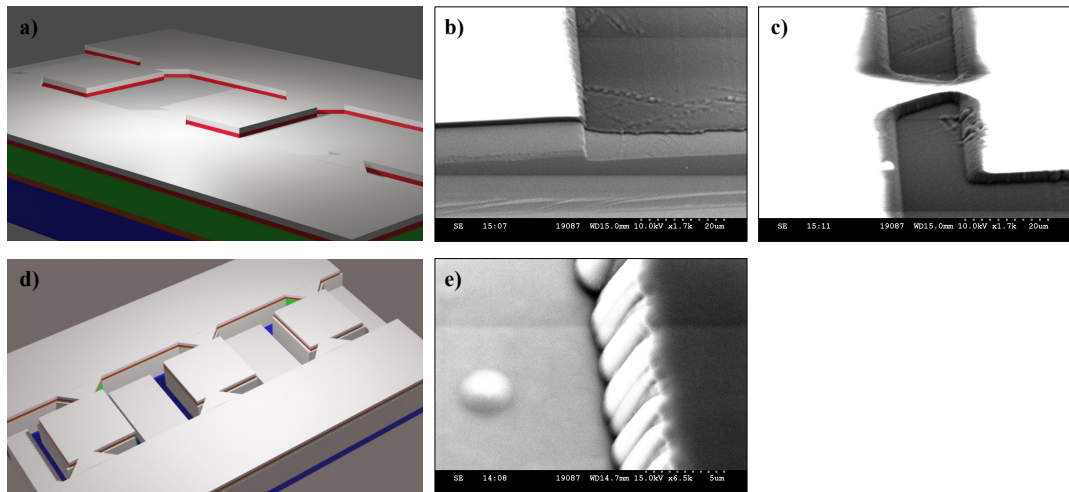


**Figure 8.** The key steps of the dry etch anisotropy method for sidewall protection. The conformal deposition of 800 nm of SiO<sub>2</sub> following the ICP shown in **a)** the schematic from Fig. 1, **b)** by SEM at a cleaved edge of a trench and **c)** by SEM over the anchor, rail and membrane. The RIE to open up etch holes shown in **d)** the schematic from Fig. 1 and **e)** as an SEM of the edge of a membrane following the RIE. The layer colours in **a)** and **d)** have the same meanings as in Fig.1.

Etch holes are formed by the etch anisotropy of the RIE step due to ion deflection from the sidewalls, see Fig. 9 a), which results in microtrenching at the corners of the trench base and the strained SiO<sub>2</sub> at the trench edges is etched [43]. The strained SiO<sub>2</sub> is susceptible to fractures that expose the InP, allowing the wet etchants to under-etch below the epitaxial layer of interest, see Fig. 9 b).

The principle failure mechanism for the SiO<sub>2</sub> sidewall protection was damage from PH<sub>3</sub> generation during the under-etch step. The dry etch anisotropy method, see Table 4, was the only method of forming the SiO<sub>2</sub> sidewall protection which was successfully demonstrated. The sidewall protection formation is challenging as the SiO<sub>2</sub> profile is highly dependent on the geometry of the ICP-etched trench, operating etch/deposition rates of the RIE and PECVD and local temperature variations due to sample mounting. Following hardmask development, four ZnCdMgSe-on-InP samples were ICP-etched to different trench depths by varying the etch length in 5-minute intervals from 10 minutes to 25 minutes and a sidewall protection developed by the dry etch anisotropy method. During the wet etch the sidewall protection on all four samples was compromised, suggesting that the trench depth tolerance for successful sidewall protection formation is very narrow (less than the difference in the 5-minute etch intervals) or that the deposition thickness of SiO<sub>2</sub> is the dominant variable in determining

sidewall protection success. It is possible that using a harder material, such as  $\text{Si}_3\text{N}_4$ , to form the sidewall protection may reduce the sidewall protection failure due to  $\text{PH}_3$  damage.

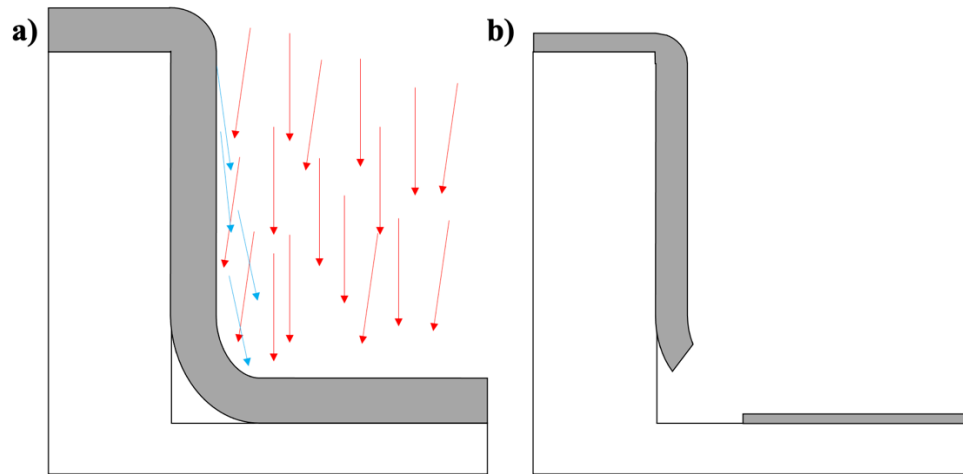


**Figure 9.** Side view schematic of the proposed sidewall protection formation mechanism. **a)** Reactive ions (red arrows) are reflected from the vertical sidewall protection edges, concentrating the ions towards the corner (reflected ions shown in blue). **b)** Etched corner of the sidewall protection, giving access to the underside of the membrane for the wet etchants. Figure based on supplementary material of reference [4].  $\text{SiO}_2$  is shown in grey.

#### 4.7 Suspension method for ZnCdMgSe-on-InP: wet under-etching and sidewall protection removal

##### 4.7.1 InP crystallography and under-etching

The under-etch of the ZnCdMgSe membranes proceeds via HCl-based etches to remove the InP substrate from beneath the membrane, see Fig. 10 a) and b), which is followed by a  $\text{H}_3\text{PO}_4:\text{H}_2\text{O}_2:\text{H}_2\text{O}$  etch to remove the InGaAs buffer layer. Once the under-etching is complete the protective  $\text{SiO}_2$  layers are removed using RIE to leave a suspended membrane, see Fig. 10 c) and d). The wet etch anisotropy of the InP-substrate results in the under-etch profile and etch rate being highly dependent on the hardmask orientation.

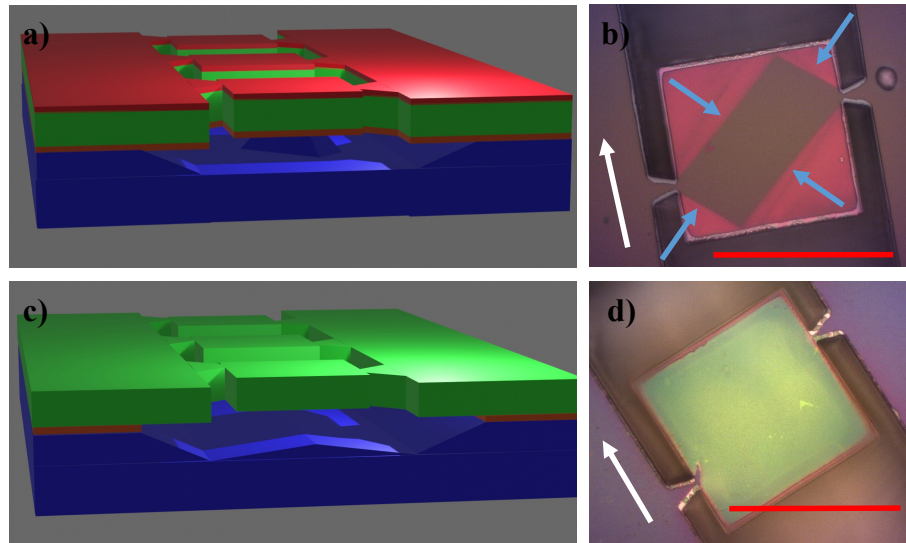


**Figure 10.** The ZnCdMgSe under-etch. **a)** Schematic of the InP substrate receding during the under-etch. The sidewall protection layer has been omitted from the schematic for clarity. **b)** Image of a ZnCdMgSe membrane during the HCl-based under-etching step, showing the InP receding. The blue arrows show the  $\langle 1\ 0\ 0 \rangle$ -like under-etch directions. **c)** Schematic of the suspended ZnCdMgSe membranes with all SiO<sub>2</sub> protective layers removed. **d)** Image of a suspended ZnCdMgSe membrane. The white arrows mark the  $[\bar{1}\ \bar{1}\ 0]$  direction of the InP and the red scale bar represents 100  $\mu\text{m}$ . The layer colours in **a)** and **c)** have the same meanings as in Fig.1.

The effects of the highly anisotropic etch properties of InP on the under-etching were examined by setting the rail alignment through  $30 \pm 1^\circ$ ,  $45 \pm 1^\circ$ ,  $60 \pm 1^\circ$  and  $90 \pm 1^\circ$  from the  $[\bar{1}\ 1\ 0]$  direction towards  $[\bar{1}\ \bar{1}\ 0]$  for different samples and examining the evolution of the resulting etch planes, see Fig. 11. The InP is masked by the membranes, rails and anchors, but the crystallographic alignment needs to be optimized to preferentially under-etch the membranes and not the rails. Fig. 11 shows the under-etch planes are pinned at the sites where the anchors mask the membrane edges, effectively preventing inward etching planes forming [4].

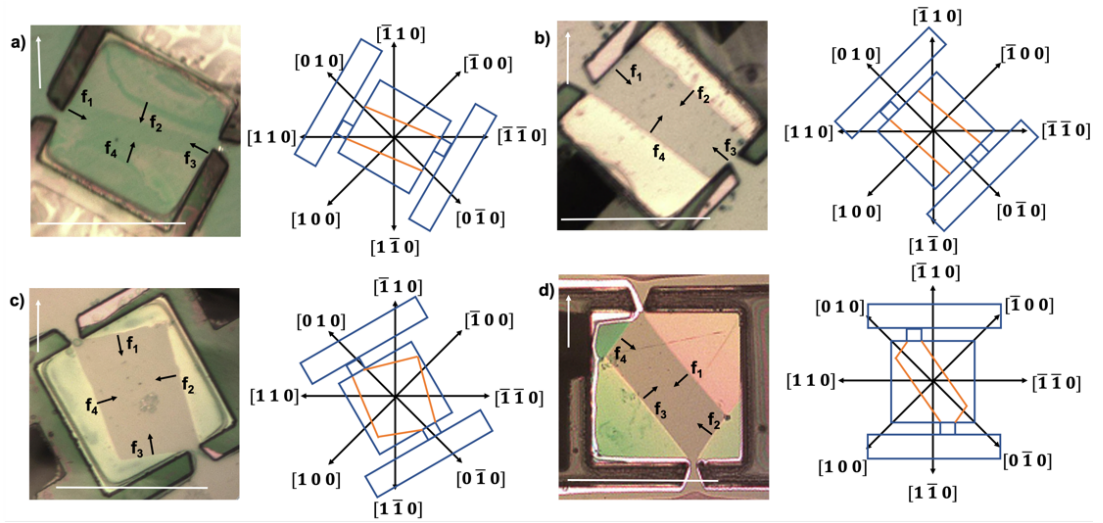


**Figure 11.** The response of the InP under-etch as a function of mask orientation. The orientation angles from  $[\bar{1} 1 0]$  towards  $[\bar{1} \bar{1} 0]$  and processing stages shown are **a)**  $30 \pm 1^\circ$  during InP etching, **b)**  $45 \pm 1^\circ$  during InP etching, **c)**  $60 \pm 1^\circ$  during InP etching, and **d)**  $90 \pm 1^\circ$  after an InGaAs etch. The process stages in the images were chosen for each angle according to their clarity. (Note that **a)** and **b)** were taken with slightly lower image quality.) The white arrow shows the  $[\bar{1} 1 0]$  direction and the white scale bar represents  $100 \mu\text{m}$ . To the right of each image is a schematic clarifying the crystallographic evolution of the angular dependent wet etch progress. The blue and orange lines represent the mask outline and the InP recession faces respectively. The recession face directions,  $f_n$ , are marked on each image. Figure and caption taken from reference [4].

$\langle 1 0 0 \rangle$  etch faces are most likely to result in a complete under-etch of a membrane [24,44], and optimization of the mask alignment direction is required to ensure this. Table 5 summarizes the crystallographic behaviour in Fig. 11. InP under-etch recession faces,  $f_n$ , are shown in Fig. 11 with an angle from  $[\bar{1} 1 0]$  shown in Table 5. The angle between  $f_n$  from  $[\bar{1} 1 0]$  can be used to calculate the crystallographic direction of the under-etch faces using

$$\cos(\theta) = \frac{u_1 u_2 + v_1 v_2 + w_1 w_2}{\sqrt{(u_1^2 + v_1^2 + w_1^2)(u_2^2 + v_2^2 + w_2^2)}}, \quad (1)$$

where 1 and 2 index different crystallographic vectors and  $u$ ,  $v$  and  $w$  represent the  $x$ ,  $y$  and  $z$  cartesian components of the different crystallographic vectors [45].



For a perfect  $\langle 1\ 0\ 0 \rangle$  under-etch, all recession faces should have a recession angle magnitude of  $45 \pm 1^\circ$  from  $[\bar{1}\ 1\ 0]$ . Previous work has shown that the ideal alignment for the under-etch of the square membranes alone would be to set the square edges perpendicular to the  $\langle 1\ 0\ 0 \rangle$  directions [24], however the inclusion of anchors and rails complicates this by adding extra mask features. From Table 5 the  $30^\circ$  (Fig. 11 a)) and  $60^\circ$  (Fig. 11 c)) alignments from  $[\bar{1}\ 1\ 0]$  towards  $[\bar{1}\ \bar{1}\ 0]$  only etch along high-order crystallographic directions and the  $30^\circ$  alignment also exhibits very little etch activity along the  $f_1$  and  $f_3$  etch directions due to the sidewall protection silica blocking the relatively small gap between the membrane and the rails in the mask design.

**Table 5.** Directions of the recession faces of InP during the wet under-etch of the square membranes with varied mask orientation. Directions are given as an angular magnitude from  $[\bar{1}\ 1\ 0]$  and a corresponding crystallographic direction. Table and caption taken from reference [4].

Rail orientation from $[\bar{1}\ 1\ 0]$ to $[\bar{1}\ \bar{1}\ 0]$ [ $^\circ$ ]	Magnitude of the recession face angles from $[\bar{1}\ 1\ 0]$ and recession direction <sup>b</sup> , $f_n$ [ $^\circ$ ]			
	$f_1$	$f_2$	$f_3$	$f_4$
30	60 <sup>a</sup> N/A	18 $[2\ \bar{1}\ 0]$	60 <sup>a</sup> N/A	18 $[\bar{2}\ 1\ 0]$
45	45 <sup>a</sup> N/A	41 $[1\ 0\ 0]$ -like	45 <sup>a</sup> N/A	37 $[\bar{1}\ 0\ 0]$ -like
60	13 $[2\ \bar{3}\ 0]$	77 $[3\ 2\ 0]$	9 $[\bar{3}\ 4\ 0]$	69 $[\bar{7}\ \bar{3}\ 0]$
90	47 $[1\ 0\ 0]$ -like	53 $[0\ 1\ 0]$ -like	52 $[\bar{1}\ 0\ 0]$ -like	54 $[0\ \bar{1}\ 0]$ -like

<sup>a</sup>Denotes a static (non-etching) direction.

<sup>b</sup>The crystallographic directions given take into account a  $\pm 1^\circ$  uncertainty in the mask orientation.

The alignments of  $45^\circ$  (Fig. 11 b)) and  $90^\circ$  (Fig. 11 d)) from  $[\bar{1} 1 0]$  towards  $[\bar{1} \bar{1} 0]$  allow InP etching along wholly  $\langle 1 0 0 \rangle$  (or  $\langle 1 0 0 \rangle$ -like) directions, but with important differences:  $45^\circ$  alignment positions the rails for under-etching along the  $[0 1 0]$  and  $[0 \bar{1} 0]$  directions, which would be highly disadvantageous for strain maintenance on the membrane as we require the anchors and rails to be as robust as possible. In contrast,  $90^\circ$  alignment (Fig. 11 d)) sets the rails perpendicular to the slow etching  $[\bar{1} 1 0]$  and  $[1 \bar{1} 0]$  directions, which greatly slows any under-etching. Interestingly,  $45^\circ$  (Fig. 11 b)) alignment prevents any under-etching along the  $[0 1 0]$  and  $[0 \bar{1} 0]$  directions, which is due to the sidewall protection silica blocking the etch gap, as described for the  $30^\circ$  orientation (Fig. 11 a)). This etching along only two directions of the possible  $\langle 1 0 0 \rangle$  set is disadvantageous for reducing etch time. It would be possible to increase the anchor length in the mask design to allow the full RIE etching of the sidewall protection between the membrane and the rails, however this would increase the mechanical moment on the anchor, which could compromise its strength during the under-etch or could allow for unwanted membrane bowing which would encourage strain changes. The  $90^\circ$  alignment (Fig. 11 d)) has no blocked etch directions, but it exhibits under-etching along faces which are not purely  $\langle 1 0 0 \rangle$ . The small angular difference (taking into account the uncertainty) between these  $\langle 1 0 0 \rangle$ -like and a pure  $\langle 1 0 0 \rangle$  face means that these higher order faces are comprised mostly of  $\langle 1 0 0 \rangle$ , which gives them similar under-etch properties to  $\langle 1 0 0 \rangle$ . The  $90^\circ$  alignment (Fig. 11 d)) provides the closest results to the ideal case and is selected for the under-etch process. We note that previous work by Cich *et al.* found that for InGaP etched in HCl the maximum under-etch rate has a twofold symmetry about  $[1 0 0]$  along  $55^\circ$  and  $125^\circ$  from  $[0 1 1]$  towards  $[0 \bar{1} 1]$ , only  $10^\circ$  off  $\langle 1 0 0 \rangle$  directions [46], similar to our observations for the binary InP. The InP recedes along the directions of maximum undercut when the rail orientation is set to  $90^\circ$  and we observe the  $f_4$  and  $f_3$  face angles at  $55 \pm 1^\circ$  and  $128 \pm 1^\circ$  degrees from  $[\bar{1} 1 0]$  to  $[1 1 0]$  respectively, and similarly for  $f_1$  and  $f_2$  face angles at  $54 \pm 1^\circ$  and  $124 \pm 1^\circ$  degrees from  $[\bar{1} 1 0]$  to  $[\bar{1} \bar{1} 0]$  respectively.

#### 4.7.2 The optimized InP under-etch: methods and proposed mechanism

Optimum under-etch results were obtained using a three step process; a two-step InP under-etch and a single step InGaAs etch, all completed at a room temperature of  $21.0 \pm 0.5^\circ \text{C}$ . HCl:H<sub>3</sub>PO<sub>4</sub> (3:1 by volume, HCl is 36% concentration by weight and H<sub>3</sub>PO<sub>4</sub> is 85% concentration by weight) is used to selectively etch InP over InGaAs to begin the under-etch [7,8]. The under-etch (see Fig. 10 b)) is allowed to progress for 20 minutes; Fig. 10 b) shows the recession of InP after 15 minutes of etching. During the wet etch bubbles of PH<sub>3</sub> are produced on the sample surface and float to the reactant surface. It should be noted that

agitation of the etch was not completed to minimize the risk of membrane detachment. For the purposes of monitoring the etch progress, the etch could be halted by removing the sample and submerging it in DI water, drying the sample and viewing it under an optical microscope.

The ZnCdMgSe is grown on the (0 0 1) face of InP, which is rapidly etched. The under-etch of the effective mask of SiO<sub>2</sub>/ZnCdMgSe can be seen as a recession of a dark shaded parallelogram, as the anchors impose a two-fold rotational symmetry masking on the InP under-etch directional progress. The rails are not under-etched due to their alignment with the  $[\bar{1} \bar{1} 0]$  crystallographic direction (see Section 4.7.1), which instead etches to sloped sidewalls, of the very slow etching, (1 1 1) A faces [25]. The SiO<sub>2</sub> sidewall protection prevents the etchants from attacking the ZnCdMgSe, but also covers some InP under the membrane, preventing initial etching directly in the [1 1 0],  $[\bar{1} 1 0]$ ,  $[1 \bar{1} 0]$  and  $[\bar{1} \bar{1} 0]$  directions. The etch of the membranes proceeds via etching down into the substrate along the  $[0 0 \bar{1}]$  direction through the microtrenches, whilst simultaneously etching the InP under the membranes in the [1 0 0],  $[\bar{1} 0 0]$ , [0 1 0] and  $[0 \bar{1} 0]$  directions and upwards from the underside of the membranes towards the InGaAs etch-stop in the [0 0 1] direction (once the sidewall protection is under-etched). Underneath the membranes, etching proceeds along the [1 1 0],  $[\bar{1} 1 0]$ ,  $[1 \bar{1} 0]$  and  $[\bar{1} \bar{1} 0]$  directions at a rate much slower than the [1 0 0]-like directions, which results in the dark parallelogram shape of the under-etch seen in Fig. 10 b), which has faces aligned to the [1 0 0],  $[\bar{1} 0 0]$ , [0 1 0] and  $[0 \bar{1} 0]$  like directions [4]. Here we assume that the InP etch planes are near parallel with respect to [0 0 1] as sloped facets such as {2 1 1}, which can arise at mask edges perpendicular to  $\langle 1 1 0 \rangle$ , have been reported to be eliminated by faster etch planes [24].

After the first etch the membrane is still held by a slow-etching InP pillar, which likely arises due to the formation of other, slower etching, crystallographic faces seeded by the anchors during the under-etch [24]. A second under-etching step is completed with undiluted HCl (36% concentration by weight), which has been reported to aggressively etch {1 0 0} faces of InP [47], for 1 minute. The InP pillar is etched by the HCl whilst the InGaAs buffer layer acts as an etch stop, to prevent further vertical etching, which protects the II-VI material. Following this etch a wide v-groove can be seen in the substrate, formed by {1 1 1} faces, which completes the suspension of the membranes [28]. The added aggression of the HCl results in some damage to the II-VI at the edge of the membrane, which can be seen by the recession, in Fig. 10 b), of the ZnCdMgSe (pink in this image) and the appearance of the InGaAs (white due to light scattering).

It should be noted that the colours in the images of the processing arises from interference effects of the white light source and will depend on the illumination source used, as well as the thickness and refractive index of the layers grown.

#### *4.7.3 The InGaAs buffer layer etch*

The third step is the careful removal of the InGaAs buffer layer with minimal damage to the ZnCdMgSe. The reported etch rate of InGaAs at the InGaAs/II-VI boundary with  $\text{H}_3\text{PO}_4:\text{H}_2\text{O}_2:\text{H}_2\text{O}$  (1:1:6 by volume) is reported at around 20 nm/s, with a claimed selectivity ratio of 70 between InGaAs and ZnCdSe [7].  $\text{H}_3\text{PO}_4:\text{H}_2\text{O}_2:\text{H}_2\text{O}$  is prepared by first mixing the  $\text{H}_3\text{PO}_4$  and the  $\text{H}_2\text{O}_2$ , then leaving the mixture to stand for 30 minutes to allow for etch-rate equilibration before adding the  $\text{H}_2\text{O}$ . The 110 nm-thick  $\text{In}_{0.53}\text{Ga}_{0.47}\text{As}$  buffer layer (of CDI 340) is removed using a 10 s etch of  $\text{H}_3\text{PO}_4:\text{H}_2\text{O}_2:\text{H}_2\text{O}$  (1:1:6 by volume) [7], which, when complete, results in the membranes changing colour to green. The colour change is the indicator of etch completion and timing error is a cause of membrane damage.

At the end of the three-step under-etch process, the membranes are now composed of ZnCdMgSe with a protective silica layer, suspended on anchors of the original growth structure. The final step is to remove the protective silica using RIE to reveal the epitaxial growth side of the membrane. This is clarified in Fig. 10 c) and an image of a fully suspended membrane is shown in Fig. 10 d). The time of the final RIE is determined from the quantity of  $\text{SiO}_2$  left on a reference sample. This successful under-etch was demonstrated on chips of the quaternary material CDI 340, and was unsuccessful when applied to other samples. As discussed in previous sections, this is due to the narrow tolerance on the conditions of the sidewall protection formation.

## **4.8 Suspension method for GaInP/AlGaInP-on-GaAs: wet under-etching and silica removal**

### *4.8.1 GaAs under-etching*

In this section the final steps of producing the GaInP/AlGaInP membranes is described. With reference to Fig. 1, following the ICP the GaInP/AlGaInP-on-GaAs membranes undergo an under-etching step to liberate them from the substrate (see Fig. 12 a) and b)). Following the under-etch, membrane cleaning and  $\text{SiO}_2$  protective layer removal, suspended membranes of GaInP/AlGaInP remain (see Fig. 12 c) and d)). In this section the under-etching crystallography of the GaAs is not analysed as it is less novel than the II-VI-on-InP case.

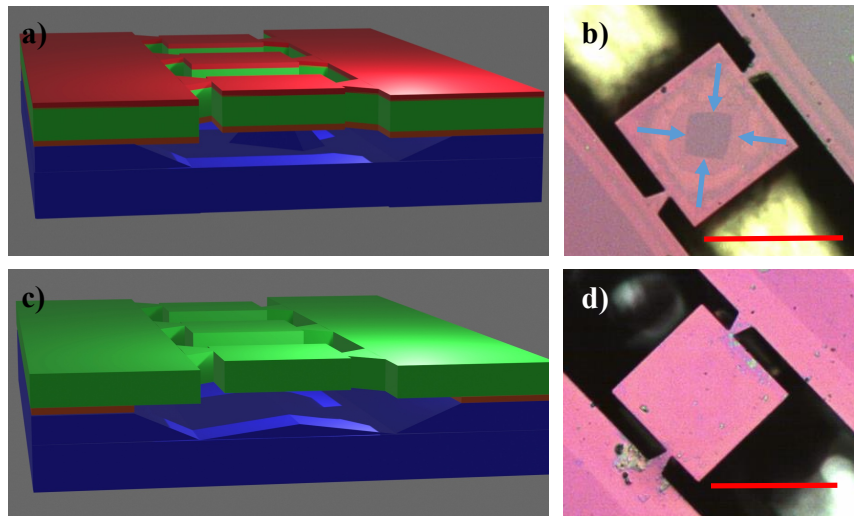


**Figure 12.** The under-etch of GaInP/AlGaInP membranes. The under-etch progress is shown **a)** as a schematic and **b)** as an image of a membrane. Following cleaning and the removal of the SiO<sub>2</sub> protective layer suspended membranes remain. **c)** Shows a schematic and **d)** shows an image, of a suspended membrane. The blue arrows show the under-etch direction and the red scale bar represents 100 μm. The layer colours in **a)** and **c)** have the same meanings as in Fig.1, however it should be noted that the orange layer, the buffer, is not present for this GaInP/AlGaInP-on-GaAs sample.

The under etch of the GaInP/AlGaInP membrane is completed in a single etch step using H<sub>3</sub>PO<sub>4</sub>:H<sub>2</sub>O<sub>2</sub>:H<sub>2</sub>O (3:4:3) [5], which is prepared using the same method as the InGaAs etch in Section 4.7.3. Unlike the ZnCdMgSe-on-InP samples, there is no buffer layer used in the GaInP/AlGaInP-on-GaAs growth and the underside protection of the GaInP/AlGaInP membrane during the under-etch relies on the AlGaInP barriers of the DBR-free VECSEL structure serving as an etch-stop layer. The etch was completed at a room temperature of 21.0 ± 0.5 °C and Fig. 13 shows the progress of the under-etch at 5, 15, 22 and 25 minutes, after which the GaInP/AlGaInP membranes are suspended. The receding purple in the centre of the membranes is the GaAs substrate and this allows for the under-etch progress to be easily monitored. The dark areas around the membranes are etch pits which descend into the substrate.

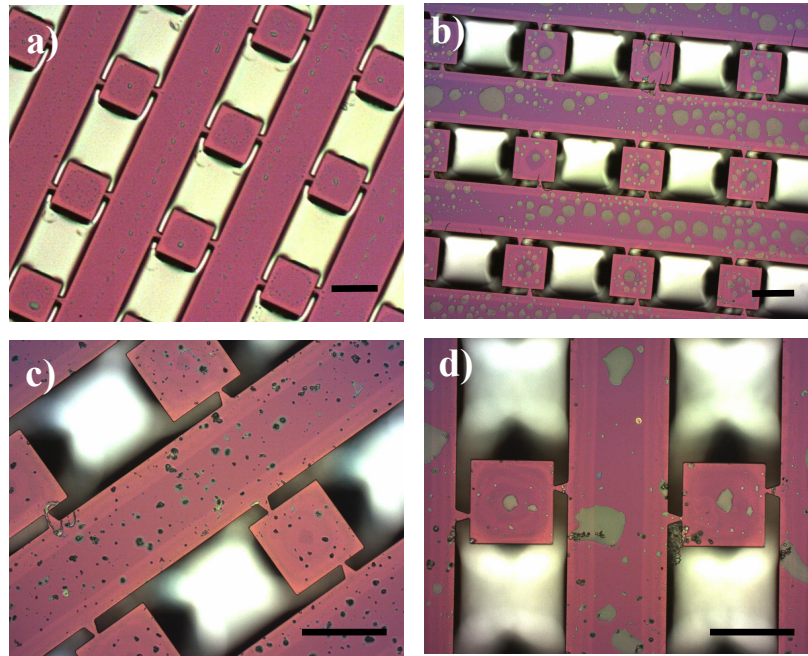


**Figure 13.** An example of the under etch progress of membranes of MR3751. The under-etch of GaAs by  $\text{H}_3\text{PO}_4:\text{H}_2\text{O}_2:\text{H}_2\text{O}$  (3:4:3) is shown at **a)** 5, **b)** 15, **c)** 22 and **d)** 25 minutes at which point the membranes are suspended. The black scale bar represents 100  $\mu\text{m}$ .

#### 4.8.2 Wet etch contaminants and removing the protective $\text{SiO}_2$ layer

Fig. 13 clearly shows that as the under-etch progresses contaminants are produced, which deposit on the membrane surface. Given that DBR-free VECSELs require extremely high membrane quality and that the typical VECSEL mode size is of the order of 70  $\mu\text{m}$  diameter, hence requiring the majority of an entire membrane surface, there is no tolerance in the process for surface contaminants on the membranes. The contaminants on the surface may be gallium oxide ( $\text{Ga}_2\text{O}_3$ ) or gallium hydroxide ( $\text{Ga}(\text{OH})_3$ ) and could be dissolved in a lower pH acid, than the  $\text{H}_3\text{PO}_4$  used in the under-etch. Reference [30] describes a reaction pathway for GaAs etched in an acid: $\text{H}_2\text{O}_2$  solution and outlines that at  $\text{pH} > 2$ ,  $\text{Ga}(\text{OH})_3$  is less soluble, which causes the formation of surface gallium oxides.  $\text{Ga}_2\text{O}_3$  is white, consistent with the colour of the contaminants in Fig. 13, and  $\text{Ga}(\text{OH})_3$  is a solid, however further investigation is required to confirm the exact composition of the contaminant [48]. It is noted that as the wet-etch progresses the amount of surface contamination does decrease.

A thorough clean of the samples, post under-etch, has shown that rinsing with acetone, methanol, isopropanol and DI water, followed by a rinse with Microposit Remover 1165, all without agitation, has resulted in the dislodging of most of the visible surface contaminants.

The suspended membranes of Fig. 13 d) should be compared to the reduced contamination of those after cleaning in Fig. 14 a) and b). It was observed that for heavily contaminated membranes this cleaning was ineffective.

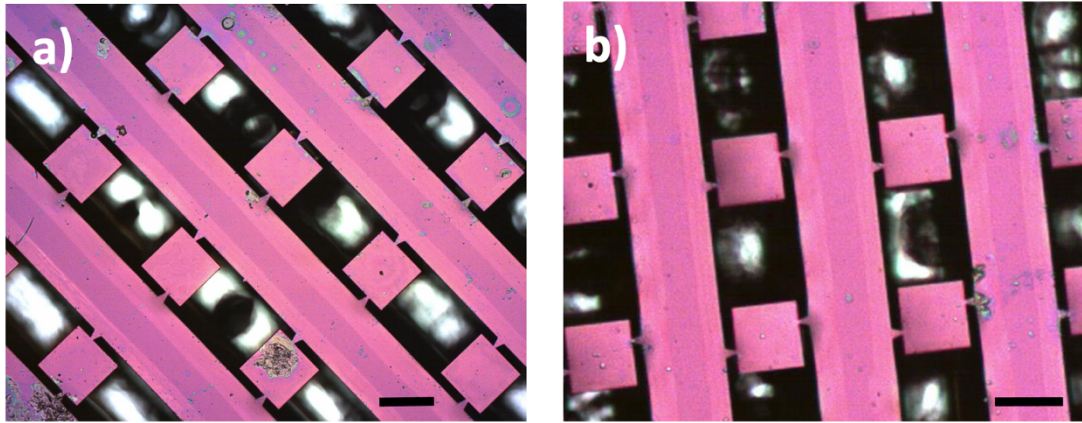


**Figure 14.** a) Suspended GaInP/AlGaInP membranes after rinsing in acetone, methanol, isopropanol and DI water. b) The membranes following a final rinse in Microposit Remover 1165. The black scale bar represents 100  $\mu\text{m}$ .

Once the GaInP/AlGaInP membranes have been under-etched and cleaned, RIE is used to remove the  $\text{SiO}_2$  protective layer to leave just the suspended membranes. The under-etch contaminants that remain are not cleanly etched by the  $\text{Ar}/\text{CHF}_3$  plasma and instead they leave a residue on the membrane surface. The RIE of a membrane without and with the under-etch contaminants are shown in Fig. 15 a) and b) respectively.

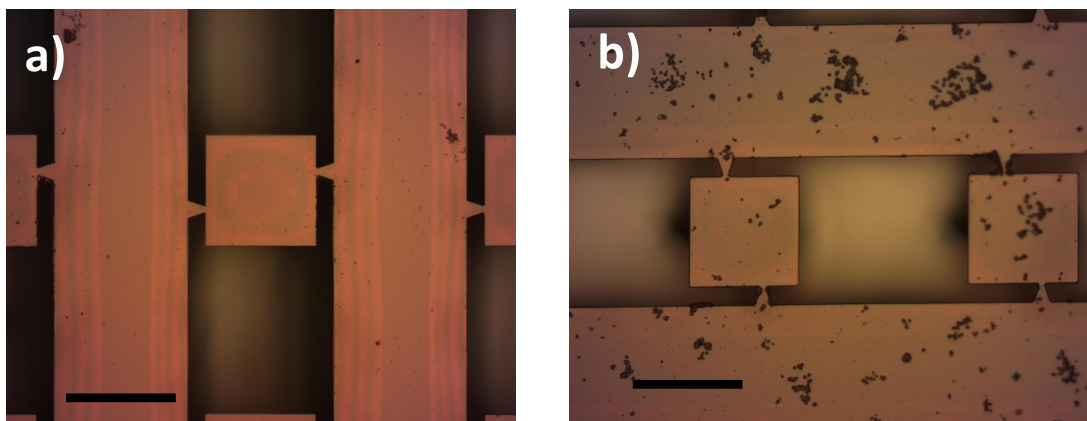


**Figure 15.** After the final RIE to completely remove the protective silica layer a) when contaminants are not present and b) when the contaminants cannot be removed.



#### 4.9 ZnCdMgSe and GaInP/AlGaInP membrane detachment via transfer printing

Transfer printing is used to detach the suspended membranes and transfer them onto a new host substrate. A desktop nanolithography platform (NanoInk NLP 2000, see Fig. 16) adapted into a home-built transfer print machine is used to transfer print suspended ZnCdMgSe or GaInP/AlGaInP membranes onto a diamond heatspreader. Diamond was chosen because of its excellent thermal transport properties, low optical loss and previous successful demonstration as a heatspreader in micro-LEDs and visible VECSELs [16,49].

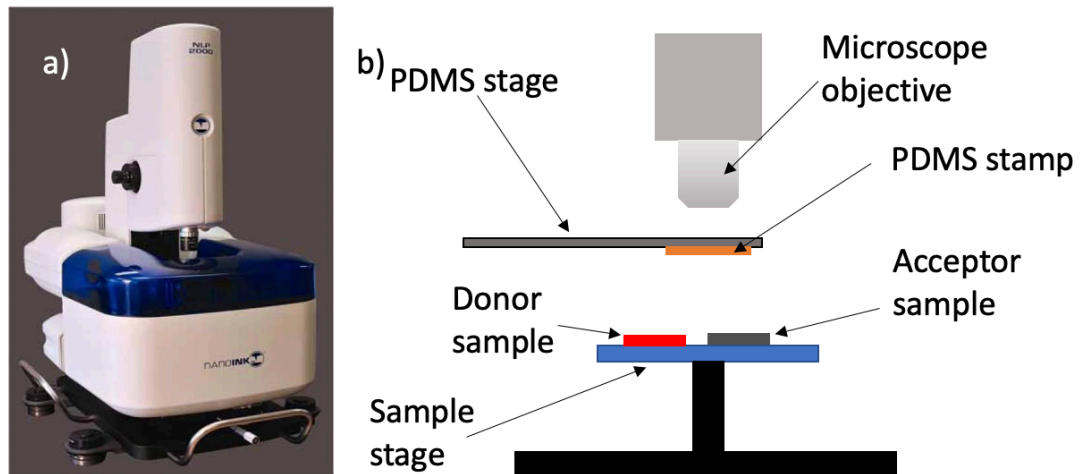


**Figure 16.** a) The NanoInk NLP 2000 system which has been converted into a transfer print machine. b) A schematic of the transfer printing system which includes a microscope for viewing the print process, a PDMS stamp and stage, donor and acceptor samples and a sample stage with tilt, rotation and translation capabilities.

Flat, 100- $\mu\text{m}$ -sided, square tip and pyramidal style PDMS stamps, used in previous investigations [1], were found to be effective for the transfer print of the membranes. The shaped stamp was pressed onto the membrane and, owing to its viscoelasticity, adhered to the membrane. The pressing breaks the anchors, freeing the membrane from the growth wafer so that it can be transferred. Fig. 17 a) shows the stamp as the pressing begins and Fig. 17 b) shows the stamp adhesion taking place. After pressing to liberate the membrane from the anchors (see Fig. 17 c)), it is free to be moved to a new acceptor substrate. The flatness and surface roughness of the diamond used as a substrate in this work does not always favour direct Van der Waals bonding and therefore a solvent wetting layer is often used to conform the membrane into a strong contact with the diamond as it evaporates [50]. A layer of isopropanol is carefully deposited onto the accepting surface of the diamond and left to evaporate so that a thin layer of the solvent remains [16]. The membrane is then pressed onto



the diamond and the PDMS stamp slowly withdrawn. A transfer-printed membrane of ZnCdMgSe on diamond is shown in Fig. 17 d). The transparent edge visible on the side of the membrane is the remains of the sidewall protection of protective silica.

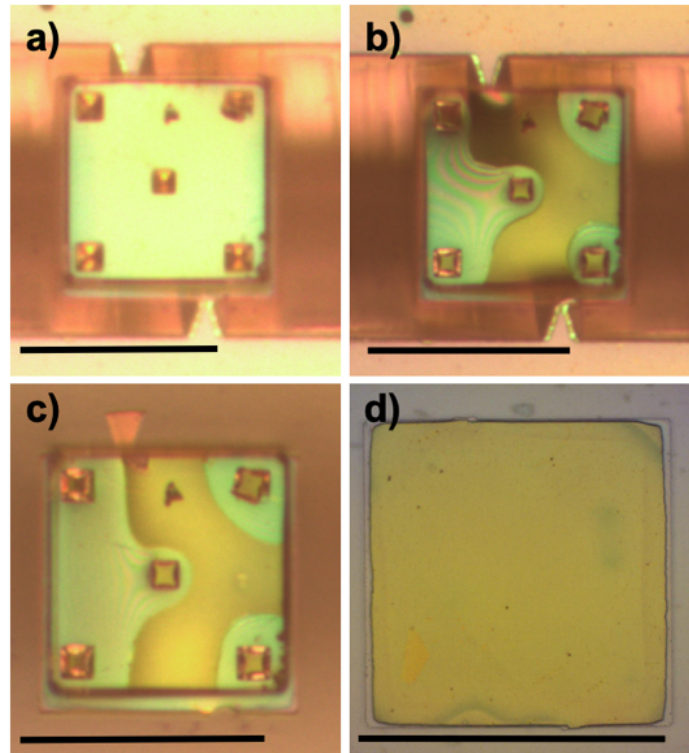


**Figure 17.** Transfer printing of a suspended ZnCdMgSe membrane onto a diamond heatspreader. The PDMS stamp is patterned with a 100- $\mu\text{m}$ -sided square tip with pyramid features [1]. a) A suspended membrane of ZnCdMgSe, imaged through the PDMS stamp before contact. b) The PDMS stamp is pressed into contact with the membrane. The brown surface seen through the stamp shows the progression of the increased stamp contact during the fast pressing. c) The membrane adheres to the stamp and the supporting anchors are broken, liberating the membrane. The ZnCdMgSe membrane is translated to a diamond heatspreader, following isopropanol wetting, and pressed into surface contact. The ZnCdMgSe membrane preferentially capillary bonds to the diamond surface. d) A 500-nm-thick ZnCdMgSe membrane transfer-printed onto a diamond. The black scale bars represent 100  $\mu\text{m}$ . Taken from [4].

For the GaInP/AlGaInP the wetting layer of isopropanol was used during some of the transfer print attempts [2], however there was no apparent improvement in the bonding quality or measurable difference in the membrane performance. Fig. 18 shows an example of a visibly high quality, contaminant free, membrane of MR3751 bonded to a diamond heatspreader. Within the membrane a dark square and a dark square border are visible and it is possible that

these are the result of internal etching, GaAs remnants on the underside of the membrane or interference fringes from membrane bowing.

In Chapter 5 the characterizations of the transfer-printed ZnCdMgSe and GaInP/AlGaInP membranes are presented and discussed.

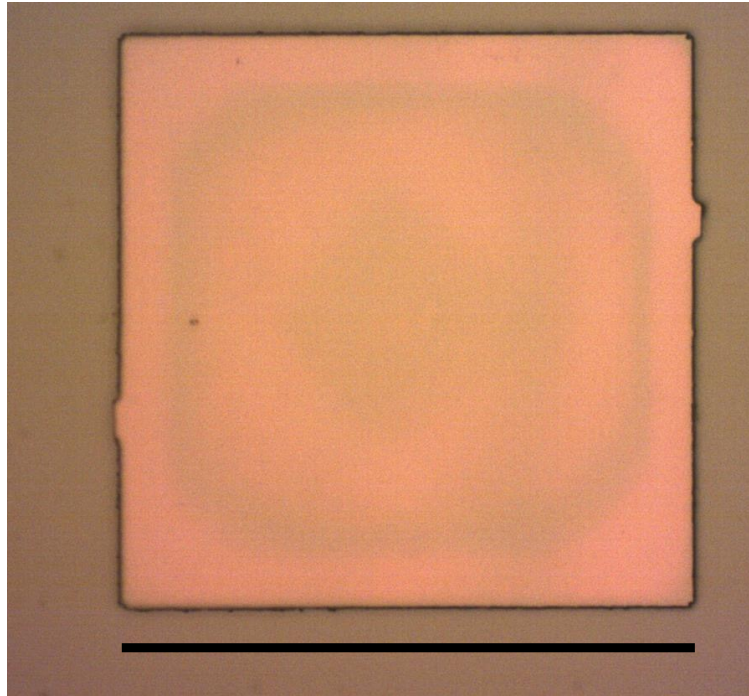


**Figure 18.** A transfer-printed 100- $\mu\text{m}$ -sided, square membrane of MR3751 on a diamond heatspreader. There is a central dark spot and dark outer ring within the membrane structure, however the membrane is clear of the under-etch contaminants. The black scale bar represents 100  $\mu\text{m}$ .

#### **4.10 Benefits of the suspension method over full substrate removal with ZnCdMgSe-on-InP**

By coating the II-VI material with  $\text{SiO}_2$ , the high-quality top surface is completely protected during the wet, under-etching steps, whereas when the samples are mounted in wax for full substrate removal, the epilayers are often subject to significant damage during the wax release due to large strain forces and the wax often contaminates the samples. An important benefit of this method is that during the removal from the substrate, the anchors maintain the strain state of the sample, preventing the cracking that is observed with larger substrate removal attempts. Once the protective  $\text{SiO}_2$  is removed, the viscoelastic PDMS stamp can then press the membrane to break the anchors, but in doing so maintains the strain state of the sample, due

to its viscoelasticity, until the membrane is deposited onto a diamond heatspreader. The yield, in terms of number of samples produced with this method, is potentially very high as hundreds of identical chips can be under-etched from a single 5 mm × 5 mm chip. This should be contrasted with the full substrate removal which yields irregularly shaped pieces of thin film or a larger, lower quality (or even fractured) film [7]. The full substrate removal results presented in Chapter 3 show poor membrane bonding, etch pits in the sample and defect introduction, which are improved upon by using the suspension method.

Previous transfer print methodologies have reported the release and transfer print of devices from InP substrates using a layer of InGaAs as a laterally-etched release layer and by exploiting the high etch selectivity between ~1 μm of doped InGaAs and InP-based device layers [51,52]. For an ELO method to be truly applicable to release any device from an InP substrate this high etch selectivity assumption cannot be made and is especially invalid with II-VI materials which have an etch selectivity from InGaAs in peroxide based etchants which is at least one or two orders of magnitude lower than InGaAs/InP [7,52]. For lateral etching of an InGaAs release layer an extremely high etch selectivity is required otherwise chemical damage will likely occur to the epitaxial layers of interest. The benefit of the suspension method is that vertical etching of an InGaAs layer requires a much shorter etch time, several seconds rather than tens of minutes, and the InGaAs is removed as a uniform front, which reduces the likelihood of etching a curvature into the epitaxial layers. Even for materials with a low etch selectivity to InGaAs, the well-known etch rate, with H<sub>3</sub>PO<sub>4</sub>:H<sub>2</sub>O<sub>2</sub> based etches, and short vertical etch time will keep the etch damage roughness to a minimum.

The demonstration of transfer printing ZnCdMgSe and GaInP/AlGaInP membranes without using an intentionally grown release layer enables the simplification of the epitaxial growth and design of a heterostructure device and, in the case of less mature semiconductor technologies such as ZnCdMgSe-on-InP, negates stacking fault and material boundary related defects which can arise during the growth of release layers. For less mature semiconductor platforms a lack of selective etchants between the epilayer and the substrate or buffer layer can pose a barrier to device formation and heterogeneous integration with more common semiconductor platforms, however this work has demonstrated that the suspension and transfer printing method can be adapted to overcome these limits to produce membranes.

#### 4.11 Future perspectives

A downside to the silica sidewall protection is that it may be damaged by the significant  $\text{PH}_3$  production during the HCl etching of InP. A thicker  $\text{SiO}_2$  or a  $\text{Si}_3\text{N}_4$  protective layer could give extra rigidity to the sidewall protection, at the expense of etch and deposition time. Improving the quality of the sidewall protection will give the opportunity to process more complicated structures, such as multi-QW ZnCdSe/ZnCdMgSe gain films, and the incorporation of these components into novel ‘green gap’ photonic devices. For device usage, the membranes may need to be larger than 100- $\mu\text{m}$ -sided. It is likely that the membrane size could be increased to a size dictated by the anchor strength without any deterioration, as long as the sidewall protection and the InGaAs buffer layer protect the ZnCdMgSe. The buffer layer thickness and growth conditions could be tuned to improve the InGaAs/InP etch selectivity whilst maintaining II-VI growth quality, for use in larger membranes.

Although somewhat outside the scope of this project, the development of selective etchants between ZnCdMgSe and InP/InGaAs could greatly simplify the suspension method. Selective etchants between InP and ZnCdMgSe would prevent damage due to under-etching of the substrate. Selective etchants between InGaAs and ZnCdMgSe with a selectivity exceeding  $10^4$  would allow for the InGaAs buffer layer to be used as a release layer, without etching a significant curvature into the underside of the ZnCdMgSe membrane. Bandgap selective etchants could enable these methods using illumination to inject holes into the smaller bandgap materials, InP and InGaAs [53].

Attempts to include release layers between InGaAs and ZnCdMgSe during this project resulted in the growth of very poor quality ZnCdMgSe material, see Chapter 3. Although the methods presented in this chapter yield high quality membranes, for full wafer-scale (rather than device scale) ELO, developing a release layer is critical. A release layer could also be used alongside the suspension and transfer printing methodology to simplify the under-etch process. The development of MgS or MgTe release layers for use in ZnCdMgSe-on-InP [9,10] would greatly facilitate heterogeneous integration of ZnCdSe/ZnCdMgSe with common semiconductor platforms. The single InGaAs buffer layer could be replaced with InGaAs/InAlAs/InGaAs, where selective etchants, such as HCl:H<sub>2</sub>O (3:1), could etch the InAlAs as the release layer and allow for the InP substrate to be recycled [23].

The suspension of ZnCdMgSe provides an opportunity to study the physical properties of this novel material in a highly controlled environment. Suspending membranes from the growth

substrate (whilst maintaining the strain state) and depositing gold contacts onto the anchors could allow for novel measurements of the thermal and electrical conductivity and the Hall Effect in II-VI or III-V materials without influence from the growth substrate [54,55]. Suspended membranes could also prove ideal for testing the mechanical strength of epitaxial layers using AFM cantilever deflection, such as measuring the Young's Modulus [44,56]. For devices which currently operate as single released membranes, such as DBR-free VECSELs or solar cells [3,57], this technique has the potential for controllable miniaturization and easy integration of these technologies.

An additional target of the work presented in this chapter was to use the GaInP/AlGaInP-on-GaAs to demonstrate that a VECSEL based on well-characterized III-V material could be constructed by transfer printing. The results of using the GaInP/AlGaInP membranes in laser tests are discussed in more detail in Chapter 5; however, laser operation has not yet been achieved via this method. In order to progress the GaInP/AlGaInP membranes towards the construction of a transfer-printed VECSEL or DBR-free VECSEL the contaminants which arise during the under-etch need to be removed. Using a different etchant such as  $\text{NH}_4\text{OH}:\text{H}_2\text{O}_2:\text{H}_2\text{O}$  (ammonium hydroxide, hydrogen peroxide mixture) or  $\text{HOC}(\text{CH}_2\text{CO}_2\text{H})_2:\text{H}_2\text{O}_2$  (citric acid, hydrogen peroxide mixture) could offer an improved etch selectivity in comparison to the  $\text{H}_3\text{PO}_4:\text{H}_2\text{O}_2:\text{H}_2\text{O}$  etch and this could enhance the membrane quality and possibly eliminate the contaminant from the etch process. Alternatively, a layer of protective PR could be applied to the GaInP/AlGaInP-on-GaAs before the under-etch, which could be rinsed off in solvents, carrying the contaminants away, afterwards.

Larger membranes would be advantageous for developing a transfer-printed VECSEL. In order to facilitate the under-etching of the larger membranes preliminary work on novel mask geometries has been completed. Octagonal membranes could offer an efficient geometry for under-etching, by allowing etching along the  $\langle 100 \rangle$  and  $\langle 110 \rangle$  directions. Fig. 19 shows ICP etched octagonal and larger 200- $\mu\text{m}$ -sided square masks in GaInP/AlGaInP-on-GaAs, before preliminary etch testing, during which they showed heavy levels of etch contamination. Further work on novel mask geometries could enable the under-etching of larger membranes and membranes which are required to have a specific shape to form a device component.

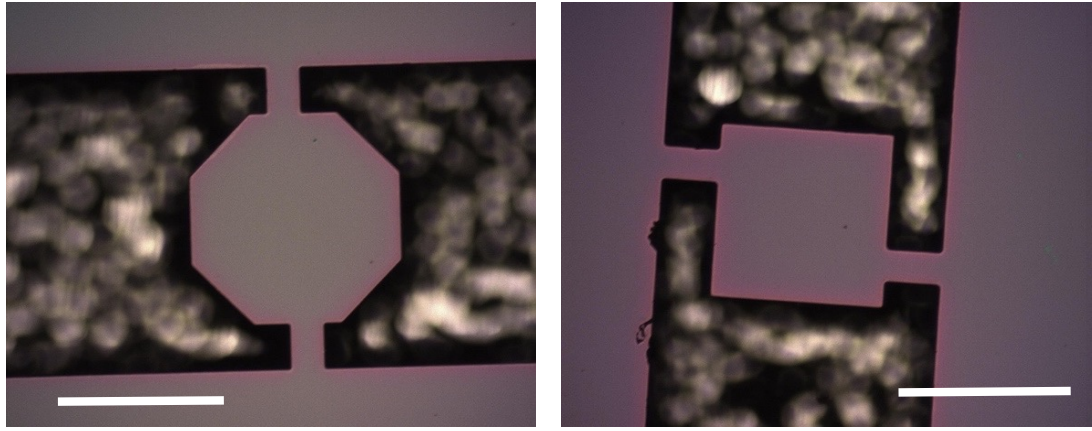


**Figure 19.** a) Octagonally shaped and b) larger 200- $\mu\text{m}$ -sided membranes ICP etched into a DBR-free VECSEL structure. The white scale bar represents 200  $\mu\text{m}$ .

#### 4.12 Conclusion

A novel method is presented for the suspension and transfer printing of ZnCdMgSe-on-InP membranes that requires no specifically engineered epitaxial release layer, no organic based sidewall protection, and is relatively independent of the etch selectivity of the III-V, InGaAs buffer layer from the II-VI, ZnCdMgSe. This suspension method can be applied to all materials grown on an InP substrate, through minor adjustments to the etch chemistry. The proof-of-principle work of this chapter represents an important step in the development of an ideal ELO system for use in the heterogeneous integration of semiconductors grown on InP. The customizable design of the membranes that are released means that this methodology offers a highly controllable and high yield method of miniaturizing wafer-scale grown devices.

Optimization of the suspension method for ZnCdMgSe-on-InP has yielded high quality ZnCdMgSe membranes, demonstrating the strain-maintained suspension of II-VI semiconductors, for the first time, and the suspension of samples from an InP substrate. The suspension method has been optimized by aligning the rails, which hold the membranes, along the  $[\bar{1}\bar{1}0]$  direction to ensure a full membrane under-etch whilst preventing the under-etch of the rails. The first transfer print of high quality II-VI membranes onto non-native substrates is demonstrated.

A 100- $\mu\text{m}$ -sided GaInP/AlGaInP, DBR-free VECSEL membrane has been under-etched and transfer-printed onto a diamond heatspreader, demonstrating the potential for the suspension and transfer printing method to construct VECSELs. In order to progress this work further, changing the wet etchant could be key to remove the contaminants generated during the wet

etch step and different mask geometries could allow for a membrane to be under-etched which has a more complimentary geometry to the substrate crystallography.

Further work on strengthening the sidewall protection is essential for further implementation of the suspension and transfer printing method to the construction of II-VI and III-V VECSELs. Once the sidewall protection consistency has been improved this methodology will enable the construction of large VECSEL arrays on-chip or on diamond as well as allowing the heterogeneous integration of novel semiconductor material systems with current semiconductor technologies.

Next, Chapter 5 will use an atomic force microscope and spectroscopic techniques to assess the quality of the membranes produced in this chapter, in order to determine their suitability as VECSEL laser samples.

## References

1. A. J. Trindade, B. Guilhabert, D. Massoubre, D. Zhu, N. Laurand, E. Gu, I. M. Watson, C. J. Humphreys, and M. D. Dawson, "Nanoscale-accuracy transfer printing of ultra-thin AlInGaN light-emitting diodes onto mechanically flexible substrates," *Appl. Phys. Lett.* **103**(25), 253302 (2013).
2. A. J. Trindade, B. Guilhabert, E. Y. Xie, R. Ferreira, J. J. D. McKendry, D. Zhu, N. Laurand, E. Gu, D. J. Wallis, I. M. Watson, C. J. Humphreys, and M. D. Dawson, "Heterogeneous integration of gallium nitride light-emitting diodes on diamond and silica by transfer printing," *Opt. Express* **23**(7), 9329 (2015).
3. H. Kahle, C. M. N. Mateo, U. Brauch, P. Tatar-Mathes, R. Bek, M. Jetter, T. Graf, and P. Michler, "Semiconductor membrane external-cavity surface-emitting laser (MECSEL)," *Optica* **3**(12), 1506 (2016).
4. G. A. Chappell, B. Guilhabert, T. Garcia, K. Zhao, I. M. Watson, M. D. Dawson, M. C. Tamargo, and J. E. Hastie, "Suspension and transfer printing of ZnCdMgSe membranes from an InP substrate," *Opt. Mater. Express* **10**(12), (2020).
5. B. E. Jones, "ZnCdMgSe and AlGaInP multi-quantum well films for colour conversion and optically-pumped visible lasers," (2015).
6. A. Rajan, R. T. Moug, and K. A. Prior, "Growth and stability of zinc blende MgS on GaAs, GaP, and InP substrates," *Appl. Phys. Lett.* **102**(3), 032102 (2013).
7. R. Moug, A. Alfaro-Martinez, L. Peng, T. Garcia, V. Deligiannakis, A. Shen, and M. Tamargo, "Selective etching of InGaAs/InP substrates from II-VI multilayer

- heterostructures," *Phys. status solidi* **9**(8–9), 1728–1731 (2012).
8. B. E. Jones, P. J. Schlosser, J. De Jesus, T. A. Garcia, M. C. Tamargo, and J. E. Hastie, "Processing and characterisation of II–VI ZnCdMgSe thin film gain structures," *Thin Solid Films* **590**, 84–89 (2015).
  9. N. M. Eldose, J. Zhu, N. Mavridi, K. Prior, and R. T. Moug, "Stacking of ZnSe/ZnCdSe Multi-Quantum Wells on GaAs (100) by Epitaxial Lift-Off," *J. Electron. Mater.* **47**(8), 4366–4369 (2018).
  10. B. Seredyński, M. Król, P. Starzyk, R. Mirek, M. Ściesiek, K. Sobczak, J. Borysiuk, D. Stephan, J.-G. Rousset, J. Szczytko, B. Piętka, and W. Pacuski, "(Cd,Zn,Mg)Te-based microcavity on MgTe sacrificial buffer: Growth, lift-off, and transmission studies of polaritons," *Phys. Rev. Mater.* **2**(4), 043406 (2018).
  11. B. Corbett, R. Loi, W. Zhou, D. Liu, and Z. Ma, "Transfer print techniques for heterogeneous integration of photonic components," *Prog. Quantum Electron.* **52**, 1–17 (2017).
  12. S. Il Park, Y. Xiong, R. H. Kim, P. Elvikis, M. Meitl, D. H. Kim, J. Wu, J. Yoon, Y. Chang-Jae, Z. Liu, Y. Huang, K. C. Hwang, P. Ferreira, L. Xiuling, K. Choquette, and J. A. Rogers, "Printed assemblies of inorganic light-emitting diodes for deformable and semitransparent displays," *Science* (80-. ). **325**(5943), 977–981 (2009).
  13. C. Op de Beeck, B. Haq, L. Elsinger, A. Gocalinska, E. Pelucchi, B. Corbett, G. Roelkens, and B. Kuyken, "Heterogeneous III-V on silicon nitride amplifiers and lasers via microtransfer printing," *Optica* **7**(5), 386 (2020).
  14. B. Corbett, R. Loi, W. Zhou, D. Liu, and Z. Ma, "Transfer print techniques for heterogeneous integration of photonic components," *Prog. Quantum Electron.* **52**, 1–17 (2017).
  15. R. Loi, J. O’Callaghan, B. Roycroft, C. Robert, A. Fecioru, A. J. Trindade, A. Gocalinska, E. Pelucchi, C. A. Bower, and B. Corbett, "Transfer Printing of AlGaInAs/InP Etched Facet Lasers to Si Substrates," *IEEE Photonics J.* **8**(6), (2016).
  16. A. J. Trindade, B. Guilhabert, E. Y. Xie, R. Ferreira, J. J. D. McKendry, D. Zhu, N. Laurand, E. Gu, D. J. Wallis, I. M. Watson, C. J. Humphreys, and M. D. Dawson, "Heterogeneous integration of gallium nitride light-emitting diodes on diamond and silica by transfer printing," *Opt. Express* **23**(7), 9329 (2015).
  17. H. Yang, D. Zhao, S. Chuwongin, J.-H. Seo, W. Yang, Y. Shuai, J. Berggren, M. Hammar, Z. Ma, and W. Zhou, "Transfer-printed stacked nanomembrane lasers on silicon," *Nat. Photonics* **6**(9), 615–620 (2012).



18. R. Loi, J. O'Callaghan, B. Roycroft, Z. Quan, K. Thomas, A. Gocalinska, E. Pelucchi, A. J. Trindade, C. A. Bower, and B. Corbett, "Thermal analysis of InP lasers transfer printed to silicon photonics substrates," *J. Light. Technol.* **36**(24), 5935–5941 (2018).
19. Z. Yang, A. R. Albrecht, J. G. Cederberg, and M. Sheik-Bahae, "Optically pumped DBR-free semiconductor disk lasers," *Opt. Express* **23**(26), 33164 (2015).
20. M. Lee, P. H. Moriya, and J. E. Hastie, "Monolithic-cavity, class-A VECSEL for quantum technology," in *SPIE PC11984, Vertical External Cavity Surface Emitting Lasers (VECSELs) XI* (2022).
21. J. McPhillimy, D. Jevtics, B. J. E. Guilhabert, C. Klitis, A. Hurtado, M. Sorel, and M. D. Dawson, "Automated nanoscale absolute accuracy alignment system for transfer printing," *ACS Appl. Nano Mater.* **3**(10), 10326–10332 (2020).
22. J. McPhillimy, B. Guilhabert, C. Klitis, M. D. Dawson, M. Sorel, and M. J. Strain, "High accuracy transfer printing of single-mode membrane silicon photonic devices," *Opt. Express* **26**(13), 16679 (2018).
23. A. R. Clawson, *Guide to References on III-V Semiconductor Chemical Etching* (n.d.).
24. P. Eliáš, I. Kosti, J. Šoltýs, and S. Hasenöhrl, "Wet-etch bulk micromachining of (100) InP substrates," *J. Micromechanics Microengineering* **14**(8), 1205–1214 (2004).
25. P. Eliáš, J. Martaus, J. Šoltýs, and I. Kostič, "Micromachining of mesa and pyramidal-shaped objects in (1 0 0) InP substrates," *J. Micromechanics Microengineering* **15**(5), 1007–1014 (2005).
26. S. Adachi, H. Kawaguchi, and G. Iwane, "InGaAsP/InP Planar-Stripe Lasers with Chemically Etched Mirrors," *J. Electrochem. Soc.* **129**(4), 883 (1982).
27. M. Kappelt and D. Bimberg, "Wet Chemical Etching of High Quality V-Grooves with {111} A Sidewalls on (001) InP," *J. Electrochem. Soc.* **143**(10), 3271 (1996).
28. A. Kodigala, Q. Gu, T. Lepetit, B. Bahari, and B. Kante, "Mechanically stable conjugate and suspended lasing membranes of bridged nano-cylinders," *Opt. Mater. Express* **7**(8), 2980 (2017).
29. I. A. Davidson, "The Growth, Processing and Characterisation of II-VI Semiconductor Structures," (2012).
30. D. H. van Dorp, S. Arnauts, M. Laitinen, T. Sajavaara, J. Meersschaut, T. Conard, and J. J. Kelly, "Nanoscale etching of III-V semiconductors in acidic hydrogen peroxide solution: GaAs and InP, a striking contrast in surface chemistry," *Appl. Surf. Sci.* **465**, 596–606 (2019).

31. G. J. Brown, S. M. Hegde, J. Hoff, C. Jelen, S. Slivken, E. Michel, O. Duchemin, E. Bigan, and M. Razeghi, "Intersubband hole absorption in GaAs-GaInP quantum wells grown by gas source molecular beam epitaxy," *Appl. Phys. Lett.* **65**(9), 1130–1132 (1994).
32. M. Shiraishi, S. Tomiya, S. Taniguchi, K. Nakano, A. Ishibashi, and M. Ikeda, "Defect studies in ZnSSe and ZnMgSSe by chemical etching and transmission electron microscopy," *Phys. Status Solidi* **152**(2), 377–383 (1995).
33. F. Semendy, N. Bambha, M. C. Tamargo, A. Cavus, and L. Zeng, *Etch Pit Studies of II-VI-Wide Bandgap Semiconductor Materials ZnSe, ZnCdSe, and ZnCdMgSe Grown on InP* (1999).
34. D. T. C. Huo, J. D. Wynn, S. G. Napholtz, F. R. Lenzo, and D. P. Wilt, "A Novel Etch Mask Process for the Etching of (011) Oriented Facet V-Grooves in InP (100) Wafers," *J. Electrochem. Soc.* **134**(11), 2850 (1987).
35. M. Hovinen, J. Ding, A. V. Nurmikko, D. C. Grillo, J. Han, L. He, and R. L. Gunshor, "Blue-green laser emission from ZnSe quantum well microresonators," *Appl. Phys. Lett.* **63**(23), 3128–3130 (1993).
36. J. Haetty, M. H. Na, H. C. Chang, H. Luo, and A. Petrou, "Fabrication of flexible monocrystalline ZnSe-based foils and membranes," *Appl. Phys. Lett.* **69**(11), 1608 (1998).
37. E. Kurtz, S. Einfeldt, J. Nürnberger, S. Zerlauth, D. Hommel, and G. Landwehr, "p-Type Doping of ZnSe. On the Properties of Nitrogen in ZnSe:N," *Phys. status solidi* **187**(2), 393–399 (1995).
38. T. J. Miller, M. A. Haase, X. Sun, B. Hao, J. Zhang, T. L. Smith, T. Ballen, J. Xie, A. S. Barnes, F. Kecman, J. Yang, J. Thielen, C. A. Leatherdale, R. Wirth, A. Biebersdorf, K. Engl, and S. Groetsch, "High efficiency green LEDs using II-VI color converters," in *Proc. SPIE 7617, Light-Emitting Diodes: Materials, Devices, and Applications for Solid State Lighting XIV*, K. P. Streubel, H. Jeon, L.-W. Tu, and N. Linder, eds. (International Society for Optics and Photonics, 2010), **7617**, p. 76171A.
39. A. J. Stoltz, J. B. Varesi, and J. D. Benson, "Comparing ICP and ECR Etching of HgCdTe, CdZnTe, and CdTe," *J. Electron. Mater.* **36**(8), 1007–1012 (2007).
40. K. Akita, R. Akimoto, B. S. Li, T. Hasama, and Y. Takanashi, "Fabrication of High-Mesa Waveguides Based on Wide-Band-Gap II–VI Semiconductors for Telecom Wavelength Applications," *Jpn. J. Appl. Phys.* **46**(1), 200–204 (2007).
41. H.-K. Kim, J. W. Bae, and T.-K. Kim, "Inductively coupled plasma reactive ion etching of ZnO using-based plasmas," *J. Vac. Sci. Technol. B Microelectron. Nanom.*

- Struct. Process. **21**, 1273 (2003).
42. J. W. Lee, E. S. Lambers, C. R. Abernathy, S. J. Pearton, R. J. Shul, F. Ren, W. S. Hobson, and C. Constantine, "Inductively coupled plasma etching of III-V semiconductors in Cl<sub>2</sub>-based chemistries," *Mater. Sci. Semicond. Process.* **1**(1), 65–73 (1998).
  43. R. J. Hoekstra, M. J. Kushner, V. Sukharev, and P. Schoenborn, "Microtrenching resulting from specular reflection during chlorine etching of silicon," *J. Vac. Sci. Technol. B Microelectron. Nanom. Struct. Process. Meas. Phenom.* **16**(2102), (1998).
  44. P. Mounaix, P. Delobelle, X. Mélique, L. Bornier, and D. Lippens, "Micromachining and mechanical properties of GaInAs/InP microcantilevers," *Mater. Sci. Eng. B* **51**(1–3), 258–262 (1998).
  45. "Crystallographic calculator – Semiconductor Spectroscopy and Devices," <http://ssd.phys.strath.ac.uk/resources/crystallography/crystallographic-direction-calculator/>.
  46. M. J. Cich, J. A. Johnson, G. M. Peake, and O. B. Spahn, "Crystallographic dependence of the lateral undercut wet etching rate of InGaP in HCl," *Appl. Phys. Lett.* **82**(4), 651–653 (2003).
  47. B. Tuck and A. J. Baker, "Chemical etching of {1 1 1} and {1 0 0} surfaces of InP," *J. Mater. Sci.* **8**(11), 1559–1566 (1973).
  48. P. Walker and W. H. Tarn, *CRC Handbook of Metal Etchants* (CRC Press, 1991).
  49. J. E. Hastie, S. Calvez, M. D. Dawson, T. Leinonen, A. Laakso, J. Lyytikäinen, and M. Pessa, "High power CW red VECSEL with linearly polarized TEM<sub>00</sub> output beam," *Opt. Express* **13**(1), 77 (2005).
  50. Z. L. Liao, "Semiconductor wafer bonding via liquid capillarity," *Appl. Phys. Lett.* **77**(5), 651–653 (2000).
  51. J. O’Callaghan, R. Loi, E. E. Mura, B. Roycroft, A. J. Trindade, K. Thomas, A. Gocalinska, E. Pelucchi, J. Zhang, G. Roelkens, C. A. Bower, and B. Corbett, "Comparison of InGaAs and InAlAs sacrificial layers for release of InP-based devices," *Opt. Mater. Express* **7**(12), 4408 (2017).
  52. R. Loi, J. O’Callaghan, B. Roycroft, C. Robert, A. Fecioru, A. J. Trindade, A. Gocalinska, E. Pelucchi, C. A. Bower, and B. Corbett, "Transfer Printing of AlGaInAs/InP Etched Facet Lasers to Si Substrates," *IEEE Photonics J.* **8**(6), (2016).
  53. S. J. Pearton, J. J. Chen, W. T. Lim, F. Ren, and D. P. Norton, "Wet Chemical Etching of Wide Bandgap Semiconductors-GaN, ZnO and SiC," *ECS Trans.* **6**(2), (2007).

54. H. Yamaguchi, R. Dreyfus, Y. Hirayama, and S. Miyashita, "Excellent electric properties of free-standing InAs membranes," *Appl. Phys. Lett.* **78**(16), 2372–2374 (2001).
55. I. Jo, M. T. Pettes, J. Kim, K. Watanabe, T. Taniguchi, Z. Yao, and L. Shi, "Thermal conductivity and phonon transport in suspended few-layer hexagonal boron nitride," *Nano Lett.* **13**(2), 550–554 (2013).
56. A. Castellanos-Gomez, M. Poot, G. A. Steele, H. S. J. van der Zant, N. Agrait, and G. Rubio-Bollinger, "Elastic Properties of Freely Suspended MoS<sub>2</sub> Nanosheets," *Adv. Mater.* **24**(6), 772–775 (2012).
57. C. M. Campbell, C.-Y. Tsai, J. Ding, and Y.-H. Zhang, "Epitaxial Lift Off of II-VI Thin Films Using Water-Soluble MgTe," *IEEE J. Photovoltaics* 1–5 (2019).

# 5. Characterizing and testing DBR-free VECSEL membranes

## Chapter overview

Following the development of the under-etching and transfer printing methods for ZnCdMgSe-on-InP and GaInP/AlGaInP-on-GaAs DBR-free VECSEL structures in Chapter 4, this chapter details a number of characterization techniques to gauge whether the membrane quality is sufficient for VECSEL operation, especially given the strict optical loss and thermal management requirements with VECSELs. Membrane surface roughness (Section 5.1) is characterized by an atomic force microscope (AFM), photoluminescence (PL) is used to investigate the radiative efficiency and thermal management (Section 5.2) and the crystalline quality and processing-induced strain relaxation is assessed using Raman spectroscopy (Section 5.4). To the best of our knowledge, here, for the first time, Raman spectroscopic mapping (Section 5.5) is explored as a novel methodology for investigating both VECSEL structures and membranes produced through the under-etching and transfer printing methods, applied in Chapter 4. Additionally, time resolved PL is used to investigate the crystalline quality of the II-VI QW gain structures, through assessment of the charge carrier lifetime (Section 5.6). Low surface roughness, high radiative efficiency and minimal processing-induced crystalline degradation in the membranes is essential for optimal device performance, forming the strongest capillary bonds and maximizing heat flow from active components.

## 5.1 Surface roughness characterization

### 5.1.1 Atomic force microscope measurements

AFM measurements of the wet etch and epitaxial surfaces of the ZnCdMgSe and GaInP/AlGaInP membranes were performed using an XE-100 Park Systems AFM to assess their surface roughness. The AFM tip used was n-type silicon with an aluminum backside coating (NSC15). The full angle of the tip was  $40^\circ$  and the resonant frequency of the tip was 325 kHz. A "true non-contact tapping mode" was used for the AFM measurements. The epitaxial side of the membrane was measured following the transfer print onto diamond, whereas the etch side was measured by detaching membranes post wet etch (pre-RIE of the topside silica) using an un-patterned piece of PDMS and then measuring the surface profile of the membrane while adhered to the PDMS.

### 5.1.2 ZnCdMgSe membrane surface roughness

The surface roughness of the epi-side membrane face was found to have a root mean square (RMS) value of  $\sim 1$  nm over a relatively large  $80 \mu\text{m}^2$  test area, and the etch side RMS roughness was  $\sim 2$  nm, over a much larger  $400 \mu\text{m}^2$  test area. The AFM profiles are shown in Fig. 1 a) and b), respectively, along with an image of the etch side surface of a detached membrane held on PDMS in Fig. 1 c). The AFM measurements of the epitaxial surface in Fig. 1 a) show that there is minimal surface roughness and that any physical sputter damage, from the RIE removal of the  $\text{SiO}_2$  protective layer, does not increase the RMS surface roughness far above 1 nm.

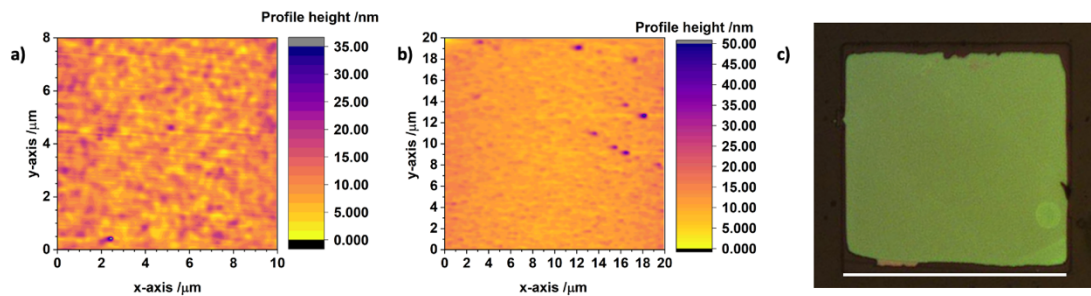


**Figure 1.** An AFM surface profile of **a)** the epitaxial growth side of a ZnCdMgSe membrane which has been transfer-printed onto diamond and **b)** the etch side of the membrane, shown etch side up in **c)**. **c)** An image of the wet etch (under-etch) surface of the ZnCdMgSe sample, which still has a protective silica layer on its epitaxial side, and has been flipped etch-side-up and is held on PDMS. The white scale bar represents  $100 \mu\text{m}$ . Adapted from [1]. The AFM scale here uses the “plasma” colour scheme. Grey and black indicate data points above and below the set scale respectively.

At present there are no previous reports of epitaxial lift-off methods for II-VI semiconductors which can produce membranes with an RMS surface roughness of  $< 2$  nm. The high surface quality of the membranes can be explained by considering the geometry used in the under-etch: ELO of smaller, as opposed to large, scale membranes. Reducing the etch time with smaller membranes decreases the likelihood of epitaxial layer etch damage due to sidewall protection breach and means that less aggressive etchants can be used within a realistic etch time window. For the successful demonstration of the under-etch method with ZnCdMgSe, the total wet etch time was around 20 minutes. Unlike previously reported II-VI ELO methodologies [2–4], the etching of InP is not on the same scale or depth, so uncontrollable etch pits do not form and cause InGaAs micromasking or expose InGaAs defect sites which compromise the etch selectivity. This means that the subsequent etch of InGaAs from ZnCdMgSe yields a very flat surface and enables the fabrication of ZnCdMgSe membranes suitable for transfer printing.

### 5.1.3 Surface roughness of the GaInP/AlGaInP

The surface roughness of the epitaxial side of a membrane of a GaInP/AlGaInP DBR-free VECSEL structure (MR3751), which was transfer-printed onto diamond, was measured using AFM and is shown in Fig. 2 a). Over a large  $400 \mu\text{m}^2$  area the RMS surface roughness of the membrane epise side was found to be 0.9 nm, which is likely limited by the epitaxial growth rather than roughening during the  $\text{SiO}_2$  deposition or removal. This very smooth surface is ideal for laser and heterogeneous integration applications. The etch-side (underside) surface roughness was measured and is shown in Fig. 2 b). Over a large  $400 \mu\text{m}^2$  area the RMS surface roughness of the membrane etch-side was found to be 4.0 nm, however over small scan regions of  $8 \mu\text{m}$  by  $8 \mu\text{m}$  the RMS roughness decreases to 1.8 nm. The variation of the RMS surface roughness with scan size indicates that there are regions of localized surface roughness and damage. Both AFM scans in Fig. 2 have artifact lines running horizontally across the surface profile and this originates from environmental noise during the long scans.

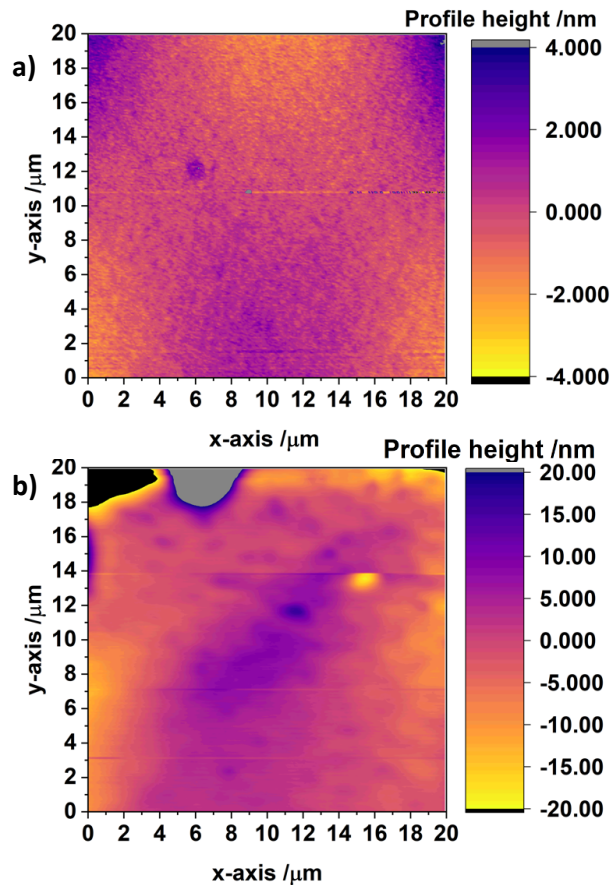


**Figure 2.** AFM surface roughness profiles of the GaInP/AlGaInP QW gain structure membrane, MR3751. The a) epise and b) etch-side are shown over a  $400 \mu\text{m}^2$  area. The AFM scale here uses the “plasma” colour scheme. Grey and black indicate data points above and below the set scale respectively.

Given the claimed high selectivity of the  $\text{H}_3\text{PO}_4:\text{H}_2\text{O}_2:\text{H}_2\text{O}$  etchants between the GaInP capping layer and the GaAs substrate, surface roughening from etch damage should be minimal. It is likely that GaAs substrate remnants heavily contribute to the etch-side surface roughness and in Fig. 2 b) there is an example of a contaminated area on the top left of the scanned area. 4.0 nm RMS surface roughness combined with localized areas of raised surface profile due to GaAs remnants can prevent the formation of a close contact between the membrane and the diamond during the transfer printing and therefore will impair heat flow between the DBR-free VECSEL membrane and the diamond. GaAs remnants also act as scatterers and absorbers on the laser surface which are likely to reduce the likelihood of laser operation. It is likely that using an alternative etchant, such as  $\text{NH}_4\text{OH}:\text{H}_2\text{O}_2$ , would improve the removal of the GaAs substrate and therefore improve the surface roughness of the GaInP/AlGaInP membranes [5].

## 5.2 Photoluminescence characterization

### 5.2.1 Photoluminescence characterization methods

Photoluminescence (PL) can be used to indirectly assess structural changes within the membranes which result from the ELO process. A strong PL signal from a direct bandgap semiconductor indicates that the material has a good radiative efficiency, resulting from a low non-radiative defect density. The PL peak position can be red-shifted due to increased sample temperature or increased biaxial tensile strain (or decreased compressive strain). The low complexity of PL measurements suits it to membrane characterization and, as seen in Chapter 2, it is a useful tool for assessing how close a grown VECSEL structure is to its intended design.

For the PL testing the samples were held within a water-cooled, brass mount which was maintained at 10 °C. Optical pumping was carried out at 447 nm using a Laserglow LRD-0447 laser-diode, focussed to a 238 x 182  $\mu\text{m}$  pump spot with up to 500 mW of output power (3.6  $\text{MWm}^{-2}$ ) for the II-VI materials and 532 nm from a Coherent Verdi V5 was used for the III-V materials. The PL signal was collected at normal incidence to the samples using a converging collection lens and focussed onto the end of a 600- $\mu\text{m}$ -core, multimode optical fibre which was connected to an Ocean Optics USB 4000 spectrometer. The PL setup is summarized for the II-VI and III-V membranes in Fig. 3.



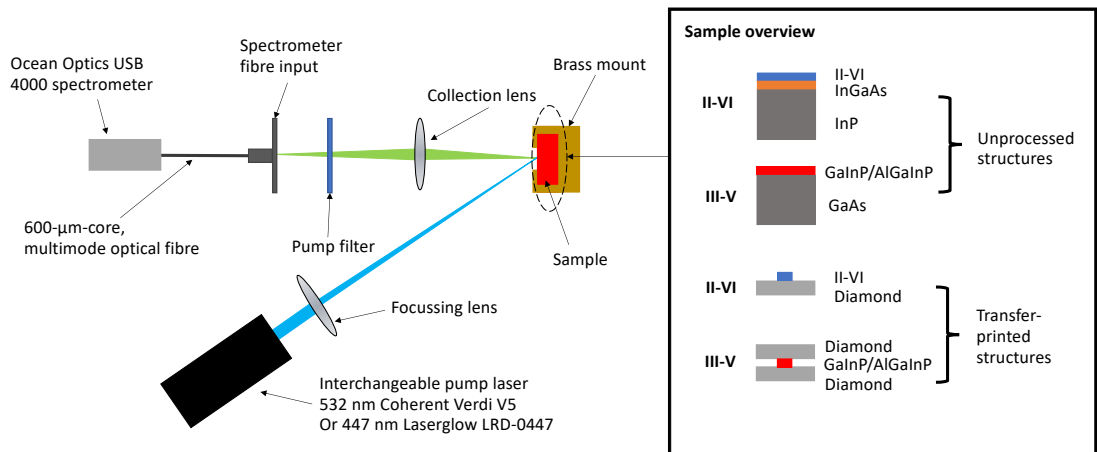


**Figure 3.** The membrane PL characterization setup. The pump laser is focussed onto the samples, which are mounted in a cooled brass holder. For the II-VI a 447 nm laser-diode is the pump source whereas for the III-V samples a 532 nm Coherent Verdi V5 is used. The PL is collected at normal incidence to the sample using a converging lens (for example a 15 mm focal length) and focussed onto a multimode fibre, which was coupled to an Ocean Optics USB 4000 spectrometer.

### 5.2.2 ZnCdMgSe membranes on diamond

PL was used to assess the effects of the suspension and transfer printing method on ZnCdMgSe and to use the optical emission quality to gauge whether defects were introduced during the ELO. An unprocessed sample was mounted in the brass mount, without a heatspreader and with indium foil on the substrate side of the wafer to ensure a good thermal contact with the mount. A ZnCdMgSe membrane, transfer-printed onto diamond, was mounted in identical conditions, with the indium foil on the opposite face of the diamond to the membrane; the membrane was only in contact with the diamond.

A quantitative comparison in peak PL signal between the unprocessed sample and the membrane on diamond, shown in Fig. 4 a), should be treated with caution due to changes in the measurement conditions, such as the absence of back reflections from the InGaAs layer in the case of the membrane PL (see the inset in Fig. 3). Nevertheless the strong PL signal after processing is indicative of the absence of significant additional non-radiative defect states being introduced during the processing. A significant red-shift in central peak position for the transferred membrane in comparison to the unprocessed wafer is observed. By measuring the intensity dependent photoluminescence (IDPL) of the unprocessed sample and membrane, shown in Fig. 4 b) and c) respectively, the redshift can be concluded to arise from greater pump-induced heating in the membrane, due to imperfect contact with the diamond. Increasing

the pump power increases the heat load on the membrane (assuming a constant quantum defect and temperature independent absorption coefficient) and the heating of the ZnCdMgSe shifts the bandgap in a Varshni relation [6,7].

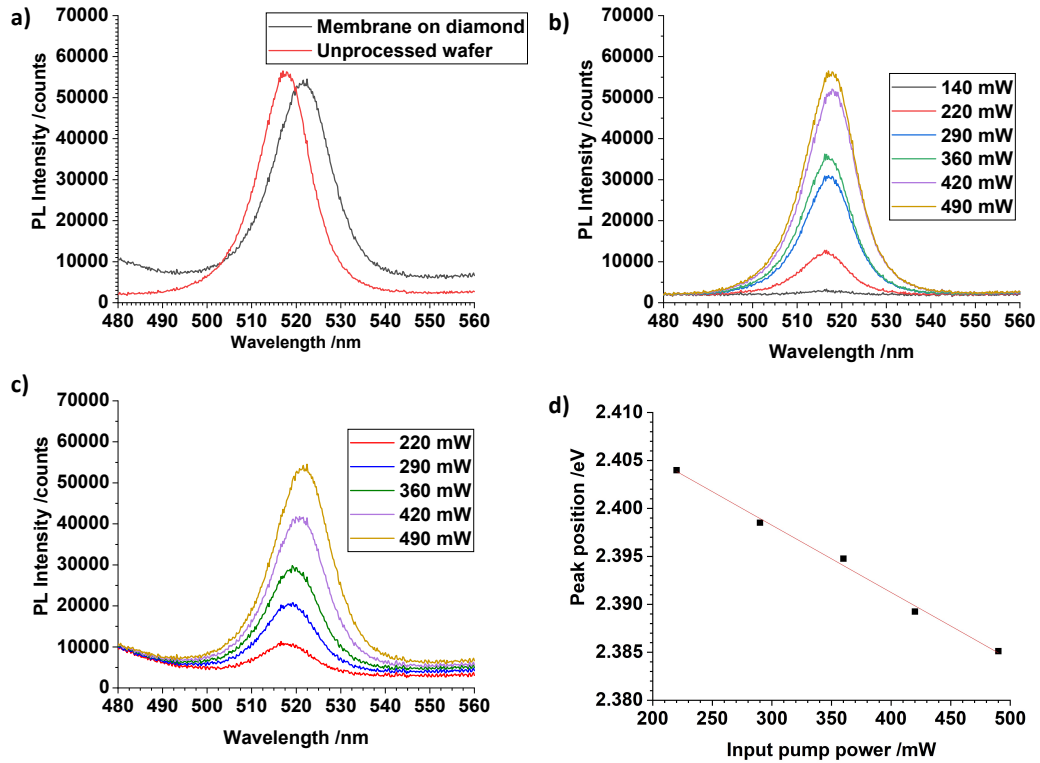


**Figure 4.** a) A comparison of the PL spectra of the as-grown wafer (red) and the membrane on diamond (black), both cooled with a heatsink temperature of 10 °C and pumped at an intensity of around  $3.6 \text{ MWm}^{-2}$ . Intensity dependent photoluminescence measurements of b) the as-grown ZnCdMgSe on InP and c) the ZnCdMgSe membrane on diamond, both cooled with a heatsink temperature of 10 °C. d) The peak position of the membrane on diamond (in eV) as a function of input pump power. b) and c) Taken from [1]. These measurements were taken with an integration time of 500 ms.

The as-grown wafer, Fig. 4 b), experienced a small  $\sim 1 \text{ nm}$  redshift for an increase in pump intensity from  $1.0 \text{ MWm}^{-2}$  to  $3.6 \text{ MWm}^{-2}$ , whereas Fig. 4 c) shows the approximately 4-nm redshift measured during an increase of the pump intensity from  $1.6 \text{ MWm}^{-2}$  to  $3.6 \text{ MWm}^{-2}$  for the membrane on diamond. For the unprocessed sample the substrate acts as a large heatsink, however, the bond between the diamond and the ZnCdMgSe membrane has an unknown thermal impedance that is a function of the bond quality. An imperfect bond would therefore limit heat transfer from the pumped region and is likely the majority source of the membrane PL redshift [8]. Previous work with GaN LEDs has shown that good thermal contact can be

achieved via transfer-printing to diamond for the same sample area as that of the membranes shown here [9]. It is possible that the transfer-printed membrane heats during optical pumping due to residue left by the evaporating solvent, which impairs heat flow. The PL peak position was found by fitting a Gaussian profile to the IDPL results of the membrane on diamond and Fig. 4 d) shows a plot of the peak position (in eV) as a function of input pump power. Using the OriginLab Origin linear fit tool, the rate of change of peak position with input pump power was found to be  $-7.01 \pm 0.29 \times 10^{-5}$  eV/mW, and by assuming that  $\frac{dE_g}{dT}$  of ZnCdMgSe is the same as ZnCdSe then the pump induced heating from increasing the input pump power from 220 mW to 490 mW is  $\sim 40$  K. This value can be compared to the 0.13 nm/K redshift of ZnCdSe QWs reported in reference [8], which would suggest that increasing the input pump power from 220 mW to 490 mW yields a  $\sim 31$  K temperature increase, with the discrepancy from the 40 K value due to material system differences.

### 5.2.3 GaInP/AlGaInP DBR-free VECSEL membranes on diamond

Fig. 5 a) shows PL spectra of the unprocessed GaInP/AlGaInP structure with a peak at 675 nm and a GaInP/AlGaInP membrane sandwiched between two diamond heatspreaders with a peak at 672 nm, showing a blue shift in the PL peak following the processing. The GaInP/AlGaInP sample has compressively-strained QWs without strain compensation layers, however a strain relaxation process in which the QWs relax to a state of reduced compression would reduce the QW bandgap causing a redshift of the PL spectrum (see Section 2.2.4.2). It is therefore likely that the strain state of the QWs in the membrane is unchanged by the suspension and transfer printing process. It is possible that the PL difference arises from 1-2 nm peak centre variation across the growth wafer surface as the transfer-printed membrane was not from the exact same site that the unprocessed PL measurements were taken from, although they were from the same sample so variation should be low [10]. The double-diamond sandwiching of the membrane offers superior thermal management due to the presence of the two, high thermal conductivity heat spreaders and the high continuity of contact enforced by compressing the membrane between two diamonds. At high levels of compression the membrane will fracture due to the stress placed upon it. The superior thermal management with the double diamond arrangement likely reduces the sample heating during the PL measurement in comparison to the unprocessed sample and results in an apparent PL blueshift when the two are compared.

IDPL measurements of the membrane in a double diamond sandwich are shown in Fig. 5 b) and show the 2 nm redshift of the membrane PL as the pump power increases from 0.1 W to 4.0 W. The origin of this redshift is likely to be entirely thermal, due to heat load from the

quantum defect of the pump. As the pump power increases interference peaks become increasingly visible and show the presence of a Fabry-Perot etalon arising from the diamond/(III-V resonant sub-cavity)/diamond cavity, an effect previously reported in InGaN-on-Si samples [11]. The refractive index contrast between AlGaInP ( $n_{\text{AlGaInP}} \approx 3.5$ ) and diamond ( $n_{\text{diamond}} \approx 2.4$ ) is sufficient to form a low finesse etalon with resolvable interference peaks, which is not the case for the II-VI materials, which are approximately index-matched with diamond. The strong PL signal and relatively small red-shift within the IDPL over the 0.2 W to 4.0 W range suggests that the double-diamond-sandwiched membrane has good thermal management and therefore could be suitable for laser operation.

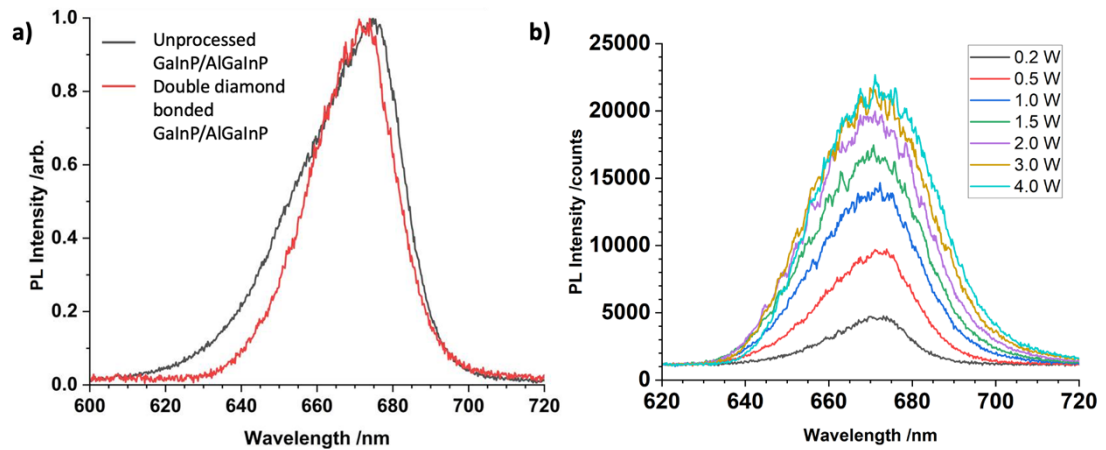


**Figure 5.** **a)** Normalized photoluminescence measurements of a 100- $\mu\text{m}$ -sided GaInP/AlGaInP membrane in a double diamond sandwich and an unprocessed GaInP/AlGaInP (MR3751) chip. **b)** Intensity dependent photoluminescence measurements of the diamond sandwiched membrane taken with 100 ms integration time over an input pump power range of 0.2 W to 4.0 W.

### 5.3 Processing induced damage and deformation

In this sub-section the ZnCdMgSe and GaInP/AlGaInP membranes are examined by visual inspection through optical microscopy. Fig.6 a), b) and c) show transfer-printed membranes of GaInP/AlGaInP and Fig. 6 d) shows a ZnCdMgSe membrane. All of the membranes shown in Fig. 6 are transfer-printed onto diamond.

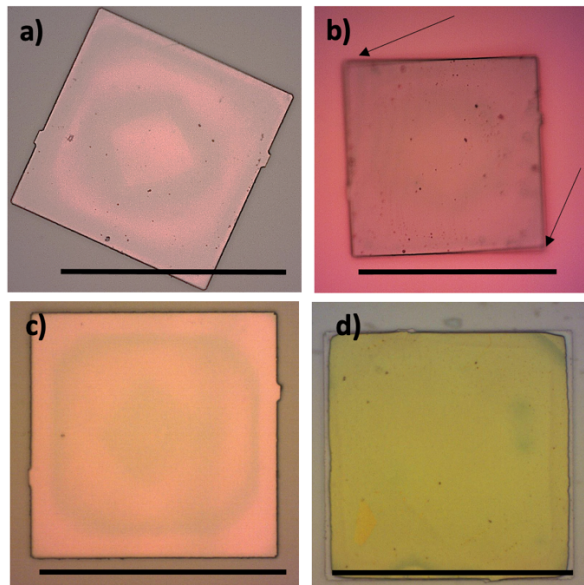


**Figure 6.** Transfer-printed GaInP/AlGaInP multi-QW membranes (MR3751) transfer-printed onto diamond showing **a)** a central square bright spot, **b)** some unfocussed membrane edges with a focussed centre at 50x magnification showing membrane curvature and black arrows to show the delamination points and **c)** a central dark spot and excellent surface quality. **d)** A ZnCdMgSe membrane on diamond, exhibiting no bright or dark spots. The black scale bar represents 100  $\mu\text{m}$ . These images have been taken under the same white light microscope.

A frequent observation within the GaInP/AlGaInP membranes, following the under-etch, was the appearance of a square, fringe-like pattern within the membranes, which does not appear with the ZnCdMgSe membranes. Fig. 6 a) shows a membrane with a central square bright spot and Fig. 6 c) shows a membrane with a central square dark spot. Typically white light interference fringes observed during transfer printing, which result from air gaps during bonding, are circular [12], and the square geometry with four-fold rotational symmetry indicates that the “fringes” observed within the GaInP/AlGaInP membranes are related to under-etch damage with the light and dark variation of the central spot resulting from etch variation. It is possible that the membrane “fringes” are actually the signs of internal etching damage, however the  $\text{H}_3\text{PO}_4:\text{H}_2\text{O}_2:\text{H}_2\text{O}$  etch should not etch the GaInP QWs or the AlGaInP barriers [13]. This has not been confirmed in this work for the 3:4:3 volumetric ratio etchant. Interestingly, the same fringe pattern is observed with mm-scale GaInP/AlGaInP membranes produced through full substrate removal [10], indicating that the membrane damage is inherent to the design and not due to the small geometry of the transfer-printed membranes or the lateral under-etch technique.

The GaInP/AlGaInP structure has no strain balancing and so it is possible that the compressively strained QWs undergo a strain relaxation process, which drives a bending moment on the released membranes. This bending is observed in Fig. 6 b), in which the bending moment is sufficient to overcome the III-V-to-diamond bonding forces and results in a curvature observable as defocussed corner regions. The impact of strain relaxation on the output power of InGaAs/GaAs-on-GaAs VECSELS, without strain compensation, has been assessed by comparing the change in lattice constant, surface quality and monomolecular recombination of samples with varied numbers of resonantly spaced, compressively-strained QWs [14]. It was shown that increasing the number of strained QWs within the structure increases the level of surface cross-hatching and increases the degree of strain relaxation, which introduces misfit dislocations, hence increasing the monomolecular recombination coefficient as the number of QWs increases [14]. From this work we can expect that the removal of the substrate would have a similar impact on the DBR-free VECSEL structures, where a strain relaxation process from the substrate removal introduces a bending moment into the membrane and in doing so introduces misfit-dislocations which may lessen, or prevent, laser performance. It should be noted from Fig. 6 a) and c) that not all of the transfer-printed GaInP/AlGaInP membranes curl and so surface contamination could be contributing to this. Curling from AlGaInP QW membranes used for DBR-free VECSELS has been observed to not prevent laser operation, even from membranes with greater curvature than those shown in Fig. 6 [15].

From Fig. 6 d) it can be seen that during the under-etch and release from the growth substrate the ZnCdMgSe membrane does not fracture or curl. During the growth of the ZnCdMgSe a very small compressive strain is inherent but, as the strain is maintained by the anchors and PDMS during the processing, there is no visible sign of deformations or cracking related to strain release. The clear border around the ZnCdMgSe membrane is likely the remnants of the SiO<sub>2</sub> sidewall protection. Given that the intended II-VI DBR-free VECSEL structure has unstrained QWs, it should be possible to expand this technique to these structures and avoid strain-related curling and fracturing.

## **5.4 Raman spectroscopy for post-epitaxial lift-off assessment**

### *5.4.1 Raman spectroscopy overview*

When photons are scattered from a sample, the majority undergo Rayleigh scattering, an elastic process in which the final energy of the scatterer and the photon are unchanged. Raman scattering is an inelastic process in which incident photons, according to a semi-classical

model, drive an induced electric dipole within a crystal structure which is modulated by the vibrational modes of the crystalline lattice. The most likely Raman process is Stokes scattering, in which the incident photons excite a vibrational mode, a phonon, within the crystalline lattice and the scattered photons have their energy reduced by  $\hbar\omega_p$  where  $\omega_p$  is the phonon frequency and  $\hbar$  is the reduced Planck constant. This scattering process can be summarized by

$$\hbar\omega_s = \hbar\omega_i \pm \hbar\omega_p \quad (1)$$

where  $\omega_i$  is the incident photon frequency and  $\omega_s$  is the scattered photon frequency. The  $\pm$  indicates anti-Stokes and Stokes scattering, with the positive and negative sign respectively, and results in the Stokes and anti-Stokes Raman shifts being symmetrical around the Rayleigh scattering case ( $\Delta\omega = 0$ ). The intensity of Raman shift modes can be plotted in a Raman shift spectrum, with an example for  $\text{Zn}_{0.75}\text{Cd}_{0.25}\text{Se}$  shown in Fig. 7 [16].

Raman shift modes can be longitudinal optical (LO) or transverse optical (TO), originating from longitudinal and transverse crystalline oscillations, respectively. A material can be described in terms of the number of pairs of LO and TO Raman active modes it has; for example a two-mode material will exhibit two LO and two TO modes, or an LO and TO mode along with an intermediate mode, I.

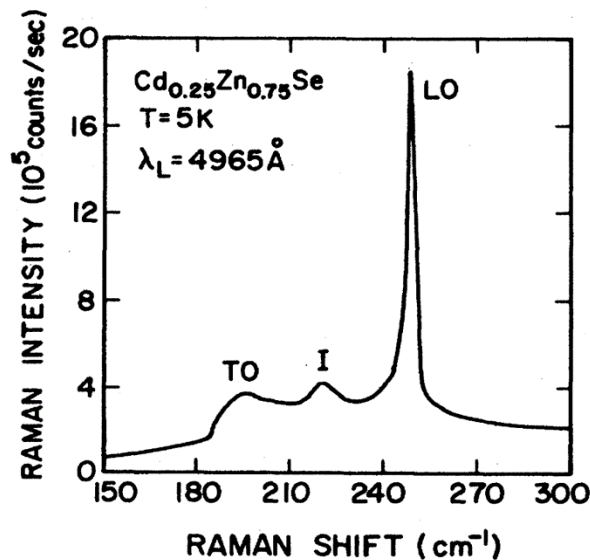


**Figure 7.** An example Raman shift spectrum for  $\text{Zn}_{0.75}\text{Cd}_{0.25}\text{Se}$  taken from reference [16]. Here, longitudinal optical (LO), transverse optical (TO) and an intermediate mode (I) are measurable.

The phonon modes within a semiconductor are influenced by the crystalline structure, material stiffness and the epitaxial strain state. The change in the volume of a semiconductor layer due to biaxial strain also changes the phonon frequencies of the layer and this is quantified by the mode Grüneisen parameter,  $\gamma_i$  [17]:

$$\gamma_i = -\frac{V}{\omega_i} \frac{d\omega_i}{dV}, \quad (2)$$

Where  $V$  is the unstrained volume of a semiconductor layer and  $\omega_i$  is the phonon frequency of a specific Raman active mode. Given that  $\omega_i = 2\pi c v_i$ , where  $v_i$  is the Raman active mode measured in wavenumbers, and that for a cubic, zincblende semiconductor  $\frac{dV}{V} = 2\varepsilon \left(1 - \frac{C_{12}}{C_{11}}\right)$ , where  $\varepsilon$  is the biaxial strain and  $C_{ij}$  are the elastic stiffness constants, a rearrangement can be made so that [18]:

$$dv_i = -2\gamma_i v_i \varepsilon \left(1 - \frac{C_{12}}{C_{11}}\right) \quad (3)$$

where  $v_i$  is the unstrained wavenumber of a Raman active mode. Using this relation it is possible to relate shifts in the Raman peak positions to changes in biaxial epitaxial strain.

In previous microfabrication work, Raman spectroscopy has been used to assess the quality of germanium membranes following epitaxial lift-off (ELO) [19], qualitatively prove strain change in InGaN/GaN multi-QWs following ELO [20,21], demonstrate the crystalline quality and qualitatively prove strain change in InGaAs membranes from ELO [22], assess residual stress in packaged electronic components [23], and quantify the uniaxial strain change of graphene on flexible polyethylene terephthalate substrates [24]. This section uses Raman spectroscopy to characterize the membrane quality and strain changes in the ZnCdMgSe and GaInP/AlGaInP membranes, similarly to references [19–22,24].

Section 5.5 builds upon this work by using novel Raman spectroscopic mapping techniques to assess how the microfabrication techniques applied in Chapter 4 impact the crystalline quality and strain state of GaInP/AlGaInP membranes as a function of spatial coordinates. To the best of our knowledge, this is the first demonstration of the application of Raman mapping to assess both VECSEL structures and membranes developed through the under-etching and transfer printing technique. The inclusion of the spatial dependence of the intensity and peak position



of Raman active modes could prove to be extremely valuable for identifying the spatial strain, defect and crystalline quality distribution around a microfabricated structure which could inform process flow design to allow for optimum device quality.

All of the Raman spectroscopy measurements taken in this chapter use a Renishaw InVia Raman microscope, operating in the back scattering geometry, with 20x magnification of the samples and a pump wavelength of 532 nm. The maximum output power of the 532 nm laser was 50 mW, with a maximum of 36 mW of this output power reaching the sample due to internal optical loss within the microscope. These measurements were taken as part of a collaboration with Dr William Tipping from the group of Professor Duncan Graham, from the Department of Pure and Applied Chemistry at the University of Strathclyde. The backscattering geometry is shown in Fig. 8, where a laser with a linear polarization along the  $y$ -axis is focused onto a test sample, the light scattered at  $180^\circ$  (back scatter) is collected and focused into a spectrometer. In Porto's notation (see [25]), the setup used can be described as  $Z(YY)\bar{Z}$  as the incident light is along the  $z$  axis and is polarized along the  $y$  axis and the scattered light propagates along the  $-z$  direction through an analyser orientated along the  $y$  axis. Only LO modes are measurable from the (100) plane of zincblende semiconductors with a backscattering Raman geometry, when the analyser and laser have the same polarization, due to the selection rules of Raman active modes [26–28], which simplifies the analysis of the Raman shift spectra.

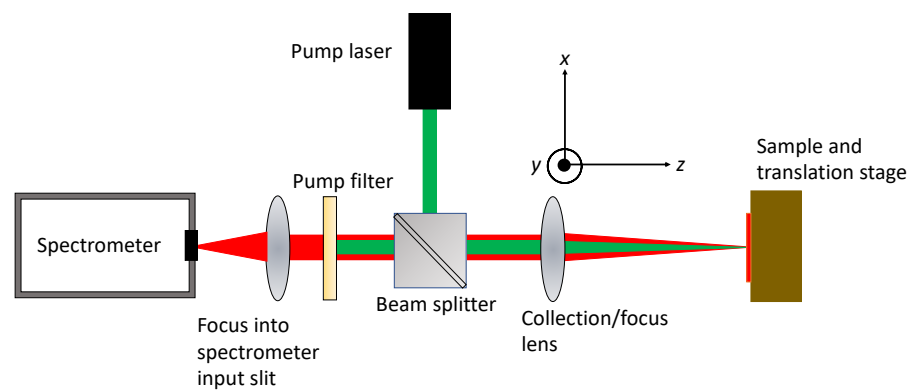


**Figure 8.** An overview of the backscattering Raman spectroscopy measurement scheme used within the Renishaw InVia Raman microscope. A pump laser is used to probe the vibrational modes of the sample and the backscattered light is examined following the removal of the pump signal. The system can be described as  $Z(YY)\bar{Z}$  in Porto's notation as the incident light is along the  $z$  axis and is polarized along the  $y$  axis and the backscattered light propagates along the  $-z$  direction through an analyser orientated along the  $y$  axis.

The spectral resolution of the spectrometer is around  $1.9 \text{ cm}^{-1}$ , however peak fitting has been reported to improve upon the resolution to which a peak centre can be determined by a factor of 20, permitting an assumed peak determining precision of around  $0.1 \text{ cm}^{-1}$  [29]. Using the GaInP/AlGaInP structure as an example, this corresponds to a minimum strain-shift resolution of 0.03 %, where we have assumed  $C_{11} = 11.91 \times 10^{11} \text{ dyn/cm}^2$  [26],  $C_{12} = 5.95 \times 10^{11} \text{ dyn/cm}^2$  [26], an unstrained InP-like mode of  $355 \text{ cm}^{-1}$  and an approximated  $\gamma_i \approx 1$  [17]. It should be noted that  $\gamma_i \approx 0.67$  could be a more realistic estimate, however data for GaInP is limited [26]. Within VECSEL structures the strain within the epitaxial layers is typically  $< \pm 0.5 \%$  and so Raman spectroscopy with peak fitting could be a useful tool for exploring the strain relaxation processes that occur in these structures during, and after, epitaxial lift-off.

#### 5.4.2 Raman spectra of transfer-printed ZnCdMgSe

Raman spectroscopy can be used to infer the quality of transfer-printed membranes, through the analysis of the strength and position of the Raman active modes. A high quality crystalline structure, with few defects, will give strong, easily resolvable peaks. DBR-free VECSEL membranes need to be transferred onto optically-transparent heatspreaders, such as diamond or silicon carbide, and Raman spectroscopy can be used to confirm membrane to heatspreader contact by measuring both membrane and heatspreader modes within the same sample area and scan. It should be noted that measuring the heatspreader modes does not verify the *quality* of the membrane-heatspreader contact, it merely confirms that at some point within the optically-pumped area the heatspreader is close to the membrane.

Due to the lack of Raman spectroscopy data on ZnCdMgSe as a function of composition it is hard to identify the origins of all of the peaks. Most quaternary II-VI materials exhibit three-mode behaviour, with ZnCdSe exhibiting intermediate one/two mode behaviour (one LO, one TO and one intermediate mode at non-binary compositions) [17,30–34]. Raman spectra were taken of  $\text{Zn}_{0.37}\text{Cd}_{0.49}\text{Mg}_{0.14}\text{Se}$  membranes, whilst held on PDMS (post detachment from the growth wafer and pre-transfer print) and following a transfer print onto a SiC heatspreader, and are shown in Fig. 9.

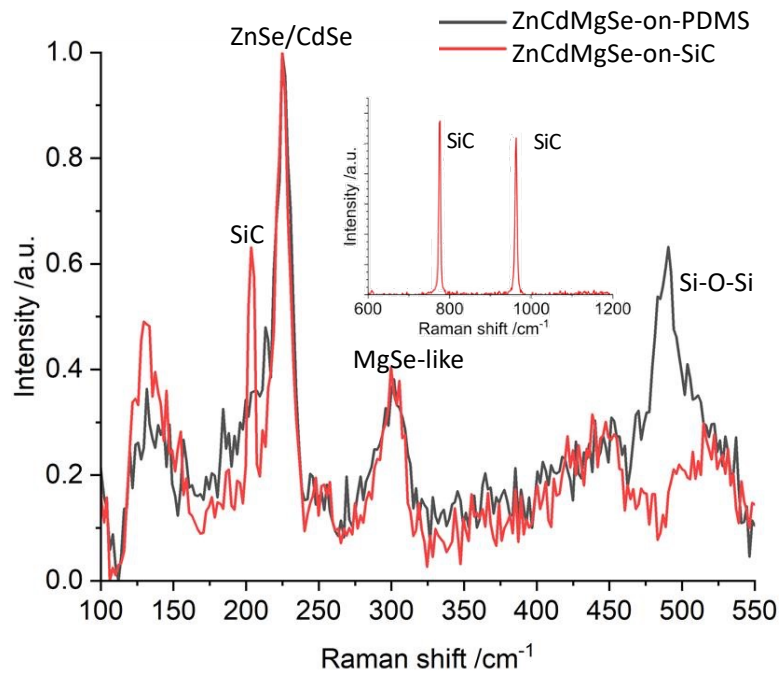


**Figure 9.** Normalized Raman shift spectra of sample CDI 340 3, a  $\text{Zn}_{0.37}\text{Cd}_{0.49}\text{Mg}_{0.14}\text{Se}$  membrane, shown for the membrane following detachment onto a PDMS stamp and on a SiC heatspreader. The inset shows the longer wavenumber component of the Raman shift spectrum, measured from the II-VI-on-SiC sample, showing extremely clear SiC-related peaks. The measurements for ZnCdMgSe-on-PDMS and ZnCdMgSe-on-SiC used 5 s and 10 s exposure times respectively.

The common peaks between the membrane held on PDMS and the membrane after transfer printing are at  $224.8\text{ cm}^{-1}$  and  $301.7\text{ cm}^{-1}$ , with the constant position of these peaks serving as preliminary evidence that both the transfer printing technique and the SiC substrate do not cause any strain-related deformation of the membranes. Given the typical three-mode behaviour of II-VI quaternaries [17], we should expect to see three LO modes within the Raman spectra of  $\text{Zn}_{0.37}\text{Cd}_{0.49}\text{Mg}_{0.14}\text{Se}$ , however given the potential for ZnCdSe to exhibit intermediate mode behaviour, where the separation of the LO and intermediate mode (at  $224.8\text{ cm}^{-1}$  [30]) is  $20 - 30\text{ cm}^{-1}$  across all  $\text{Zn}_x\text{Cd}_{1-x}\text{Se}$  compositions it is possible that these two modes are within the broad ZnSe/CdSe-labelled peak. The peak at  $301.7\text{ cm}^{-1}$  has been assigned as MgSe-like, based on reported Raman spectra of ZnMgSe [35]. If we assume that both ZnCdSe-related modes are within the ZnSe/CdSe peak then the MgSe-like LO mode presence would confirm the expected three mode behaviour expected of ZnCdMgSe. Importantly, the LO peak of InP at  $346.4\text{ cm}^{-1}$  is not observed on the membrane [17], confirming the InP removal. The LO modes of  $\text{In}_{0.53}\text{Ga}_{0.47}\text{As}$  are approximately  $230\text{ cm}^{-1}$  and  $275\text{ cm}^{-1}$  [17], and although the absence of the  $230\text{ cm}^{-1}$  peak cannot be confirmed due to the

large ZnCdSe peak, the absence of the  $275\text{ cm}^{-1}$  peak serves as confirmation of the full InGaAs removal.

The strong  $203.6\text{ cm}^{-1}$  peak of the membrane on SiC is from a Si-C vibrational mode of the 4H-SiC [36], and within the Fig. 9 inset the 4H-SiC FTO  $\frac{1}{2}$  (folded transverse optic) mode at  $775\text{ cm}^{-1}$  and the LO mode at  $963\text{ cm}^{-1}$  are clearly apparent [36], which evidences contact between the membrane and the new SiC substrate, but does not describe the quality of this contact over the whole membrane area. Within the Raman shift spectrum of the membrane on PDMS, the peak at  $490.6\text{ cm}^{-1}$  arises from the Si-O-Si stretch mode of PDMS [37], demonstrating the close contact between the ZnCdMgSe membrane and the PDMS stamp. Within the membrane on SiC, and less visibly within the membrane on PDMS, there is a peak at  $447.5\text{ cm}^{-1}$ , which appears to be unrelated to ZnSe, CdSe or MgSe longitudinal optic (LO) or transverse optic (TO) components [17], which could arise from LO-phonon replicas (a 2LO mode), which have been reported in ZnSe and ZnTe [32,38].

The presence of the strong ZnCdMgSe Raman peaks confirms the high crystalline quality of the transfer-printed membranes. For this novel material system it would be interesting to further explore the compositional dependence of the Raman spectra and to explore the changes in the shift spectrum which occur with QW samples. Additionally the Raman spectroscopy of the ZnCdSe/ZnCdMgSe could be used, alongside PL, to quickly assess the quality of epitaxially grown VECSEL structures.

#### *5.4.3 Raman spectra of transfer-printed GaInP/AlGaInP*

In order to examine any strain and quality changes in the GaInP/AlGaInP, DBR-free VECSEL samples resulting from the under-etching and transfer printing, the Raman spectra of an unprocessed wafer and a membrane transfer-printed onto diamond were taken. The Raman spectrum of the unprocessed membrane was taken under 5x magnification, with 10 % of the maximum laser power (3.6 mW) and a 10.0 s integration time. The membrane on diamond was measured under 20x magnification, with 1 % of the maximum laser power (0.36 mW) and a 1.0 s integration time. It should be noted that the processed membrane had undergone threshold testing (see Section 5.7), involving intense optical pumping, before this measurement was taken.

Within the GaInP/AlGaInP structure there are three material compositions:  $\text{Ga}_{0.44}\text{In}_{0.56}\text{P}$  QWs,  $\text{Ga}_{0.515}\text{In}_{0.485}\text{P}$  capping layers and  $(\text{Al}_{0.6}\text{Ga}_{0.4})_{0.525}\text{In}_{0.475}\text{P}$  barriers. Zincblende GaInP is reported

as being a two-mode material (InP-like and GaP-like modes observed), and  $(\text{Al}_x\text{Ga}_{1-x})_{0.52}\text{In}_{0.48}\text{P}$  has been reported as a two-mode (InP-like and AIP-like modes observed) material as long as  $x > 0.6$  [17]. Empirically-derived relations for the composition dependence of the LO and TO modes of  $(\text{Al}_x\text{Ga}_{1-x})_{0.52}\text{In}_{0.48}\text{P}$ -on-GaAs have been reported [39,40], and Table 1 summarizes the predicted LO modes for the GaInP/AlGaInP structure. The capping layer has been neglected due to its compositional similarity to the QWs and its small thickness relative to the rest of the structure.

Fig. 10 shows the Raman shift spectra for the unprocessed and transfer-printed GaInP/AlGaInP membrane respectively and show that there are two strong modes for each sample; InP-like and AIP-like. Although the predictions, in Table 1, predict four observable modes, the InP-like peaks are reported as broad, strong modes for AlGaInP [40], and so for a multi-layered GaInP/AlGaInP sample the InP-like peaks will merge into one large peak. The AIP-like peak from the barrier materials is clearly apparent, however the GaP-like peak from the QWs is likely hidden between the stronger InP-like and AIP-like peaks. The GaP-like mode is reported as weak within AlGaInP which, in combination with the fact that the thin QW layers are the only source of the GaP-like mode, results in this mode having a very low signal. As a result the GaP-like mode has been marked according to the predictions in Table 1, rather than it being a clear, resolvable peak.

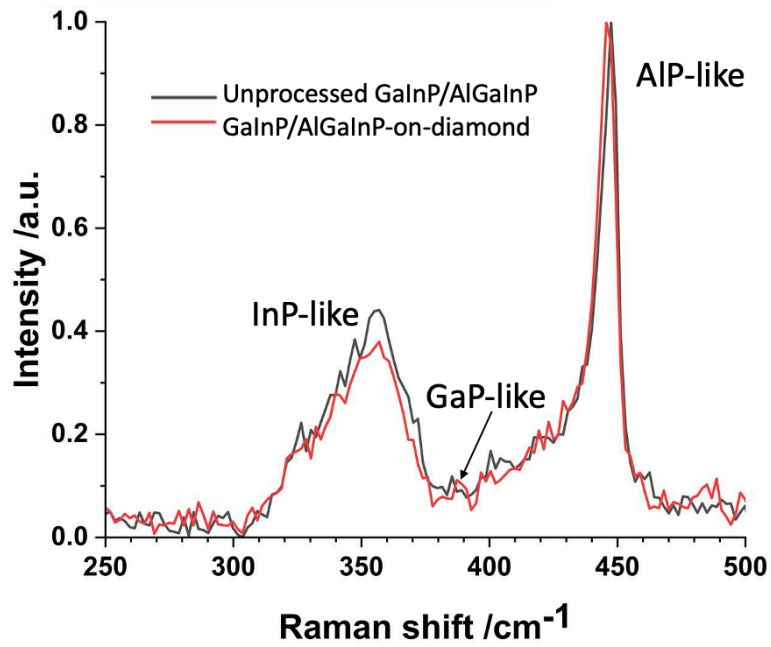


**Figure 10.** Normalized Raman spectra of the unprocessed GaInP/AlGaInP QW structure and a GaInP/AlGaInP QW gain membrane following transfer printing on diamond. The Raman spectrum of the unprocessed membrane was taken under 5x magnification, with 10 % of the maximum laser power and a 10.0 s integration time. The membrane on diamond was measured under 20x magnification, with 1 % of the maximum laser power and a 1.0 s integration time. The InP-like and AIP-like modes are labelled, along with the suspected GaP-like mode.

The under-etching and transfer printing induces a small shift in the modes, with the changes between the unprocessed InP, GaP and AIP-like modes summarized in Table 1. The peak positions have been found by performing a localized fit of a Gaussian curve in the maximum region of each peak using the Origin Quick Fit tool.

**Table 1.** Raman active modes predicted in GaInP/AlGaInP from empirically-derived laws [39,40]. Changes in the Raman active, LO modes of the GaInP/AlGaInP membrane from the under-etching and transfer printing processes.

Mode	Predicted position /cm <sup>-1</sup>	Unprocessed position /cm <sup>-1</sup>	Processed position /cm <sup>-1</sup>	Change /cm <sup>-1</sup>
InP-like	359.5 (QW) 344.7 (barrier)	356.1 ± 0.1	356.3 ± 0.1	+ 0.2 ± 0.2
GaP-like	382.1	385.6 ± 0.1	387.2 ± 0.1	+ 1.6 ± 0.2
AIP-like	447.0	447.1 ± 0.1	445.6 ± 0.1	- 1.5 ± 0.2

Given that the Grüneisen parameter can relate changes in biaxial epitaxial strain to a change in the Raman peak position, from Section 5.4.1, it can be seen that the positive changes in the peak position relate to increases in compressive strain and negative changes relate to increased tensile strain. The AlInGaP barrier material was unstrained in the GaInP/AlGaInP structure and the AIP-like mode is the only one which is solely related to the barriers. If the AIP-like mode,  $447.1 \text{ cm}^{-1}$ , is taken as the unstrained phonon frequency and for the  $\text{Al}_{0.315}\text{In}_{0.475}\text{Ga}_{0.21}\text{P}$  barrier  $C_{11} = 12.53 \times 10^{11} \text{ dyn/cm}^2$  and  $C_{12} = 6.05 \times 10^{11} \text{ dyn/cm}^2$ , then  $\varepsilon = +0.32 \%$ , an increase in tensile strain. For the GaP-like and InP-like peaks it is difficult to attribute peak position changes to strain changes due to every single layer in the structure contributing to the InP-like mode, which has a change in peak position within the experimental uncertainty, and the small signal of the GaP-like peak from the QWs. From these measurements it is possible that a strain relaxation process is taking place during the under-etching and transfer printing of the membranes, and this could be verified by repeating these Raman measurements using simpler GaInP/AlGaInP structures. These measurements suggest that the increased tensile strain of the barrier could be attributed to a release of the QW compressive strain however future work is required to verify which processing steps could contribute most to a possible strain relaxation process and whether significant defects are introduced by it.

## 5.5 Raman mapping of under-etched GaInP/AlGaInP membranes

### 5.5.1 Mapping methodologies and motivation

In this section, initial measurements of using Raman spectroscopic mapping to investigate the changes which occur to GaInP/AlGaInP samples during ELO are presented. Given the high strain sensitivity of Raman spectroscopy it could be possible to construct a strain map of a membrane, using Raman mapping. Raman mapping has been used to identify strain changes in Si/Ge nanowires [41], strain properties as a function of depth within Si/SiGe epitaxial films [42], stress changes during heating across different locations in diamond/GaN films [43] and stresses on scratched SiC surfaces [36]. Here, Raman maps of a suspended, under-etched membrane are compared to an unprocessed wafer to assess the impacts of the substrate under-etching and to see if the internal damage presented in Section 5.3 can be investigated using this technique.

The two modes of Raman mapping used in this investigation are “intensity-at-a-point”, where the intensity of a spectral position is plotted as a function of spatial coordinates, and “peak position mapping” where the spectral location of a Raman peak is plotted as a function of spatial coordinates. All of the mapping was completed at  $20 \times$  magnification. The mapping is

controlled by defining the mapped area, excitation conditions and a translation step size (automated translation stage capable of 0.1  $\mu\text{m}$  steps) in the Renishaw WiRE 4.0 software. The WiRE software was not used for the mapping analysis as it did not have the capability to locate the peaks in the presence of the background photoluminescence. Instead a series of programs (See Appendix A5.1) were written in Python using the Spyder integrated development environment [44], to complete the intensity-at-a-point and peak position maps. The intensity-at-a-point maps simply plot the intensity of a specific wavenumber as a function of spatial position on the membrane and the peak position maps use the “curve\_fit” function of the “SciPy.optimize” package to fit a Gaussian defined by

$$g(\lambda) = ae^{-\frac{(\lambda-\delta)^2}{2b^2}} + c, \quad (4)$$

where  $\lambda$  is the Raman shift value,  $\delta$  is the peak position,  $a$  and  $b$  are fitting constants defining the peak height and FWHM respectively, and  $c$  is used to account for photoluminescence related signal offset.

#### 5.5.2 Raman mapping of unprocessed and suspended GaInP/AlGaInP

Firstly a map of the unprocessed, as grown, GaInP/AlGaInP structure was taken over a 160  $\mu\text{m}$  x 160  $\mu\text{m}$  region, with 5  $\mu\text{m}$  steps. Intensity-at-a-point maps were calculated for the 355  $\text{cm}^{-1}$  (InP-like) and 446  $\text{cm}^{-1}$  (AIP-like) modes, see Fig. 11 a) and Fig. 11 b) respectively. The peak position maps for the InP-like and AIP-like modes are also plotted in Fig. 11 c) and Fig. 11 d) respectively. It should be noted that these peak positions will have small variations on the peak positions presented in Section 5.4.3 due to sample variation over the MOCVD growth wafer.



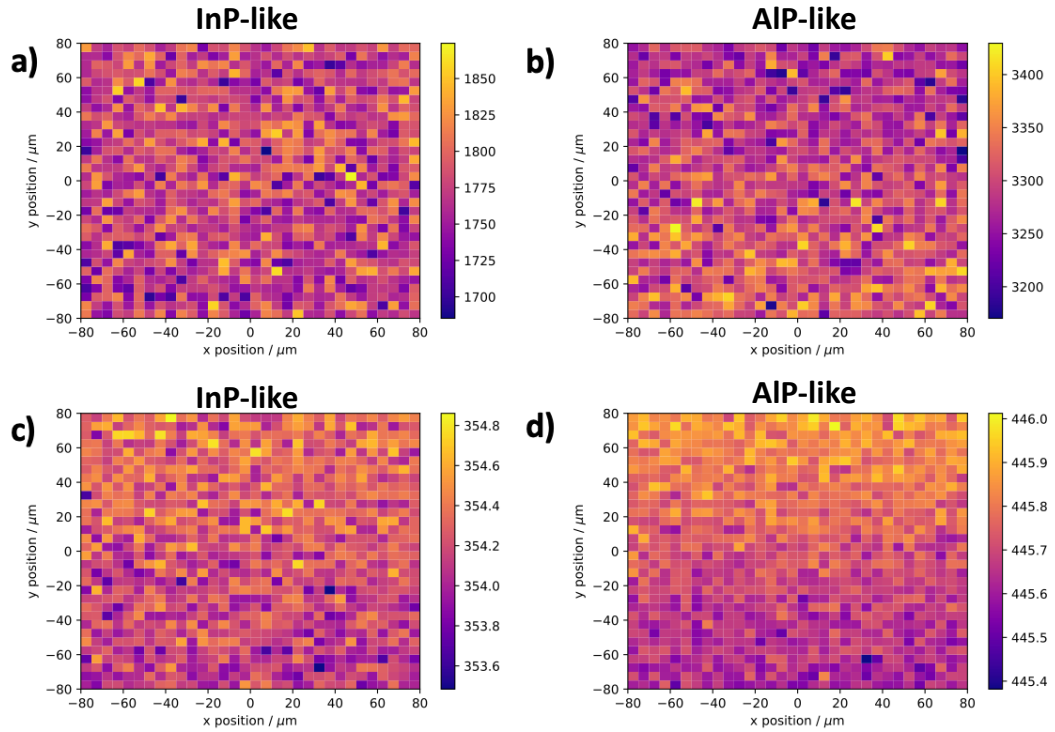


**Figure 11.** Raman maps of a  $160\ \mu\text{m} \times 160\ \mu\text{m}$  region, with  $5\ \mu\text{m}$  steps, of an unprocessed GaInP/AlGaInP chip. Intensity-at-a-point of **a)**  $355\ \text{cm}^{-1}$  (InP-like) and **b)**  $446\ \text{cm}^{-1}$  (AIP-like) modes, and peak position maps of the **c)**  $355\ \text{cm}^{-1}$  (InP-like) and **d)**  $446\ \text{cm}^{-1}$  (AIP-like) modes.

The intensity maps at  $355\ \text{cm}^{-1}$  and  $446\ \text{cm}^{-1}$ , Fig. 11 a) and b) respectively, show an intensity variation of around 10 %, which is attributed to local variations in the crystalline quality and importantly there is no obvious spatial dependence of the signal intensity. The peak position maps, Fig. 11 c) and d), show the InP-like mode varies from  $353.6\ \text{cm}^{-1}$  to  $354.8\ \text{cm}^{-1}$  and AIP-like mode varies from  $445.4\ \text{cm}^{-1}$  to  $446.0\ \text{cm}^{-1}$  with both peak position maps showing an increasing wavenumber as  $y$  position increases over the  $160\ \mu\text{m}$  scan length, which is attributed to compositional variance across the growth wafer. These Raman maps of the unprocessed wafer act as a control experiment to assess what the inherent growth variation of the sample is. The GaP-like mode was not mapped due to difficulties in resolving this peak at every spatial coordinate.

A suspended GaInP/AlGaInP membrane was mapped over the central  $80\ \mu\text{m} \times 80\ \mu\text{m}$  of a  $100\text{-}\mu\text{m}$ -sided membrane with  $2\ \mu\text{m}$  steps. Intensity-at-a-point maps were calculated for the  $354\ \text{cm}^{-1}$  (InP-like) and  $446\ \text{cm}^{-1}$  (AIP-like) modes and are shown in Fig. 12 a) and Fig. 12 b) respectively. It should be noted that  $354\ \text{cm}^{-1}$  is intensity mapped for the suspended membrane

and  $355\text{ cm}^{-1}$  is intensity mapped for the unprocessed material due to the peak position shifting. Both intensity-at-a-point plots reveal the rings observed in Section 5.3, where the maxima of the intensity indicates areas of high crystalline quality. Given that the rings do not appear within the shift maps we can conclude that the GaInP/AlGaInP is the material responsible for these peaks, where the intensity minima correspond to regions which have been damaged by the etchant. Within the intensity maps there is a small bright spot, at (30,20), and a larger dark spot, at (20,10), which likely represent defects in the membrane or surface contaminants. The dark spot at (20,10) has a large reduction in intensity signifying a significant degradation in the local crystalline quality. The bright at spot at (30,20) could be due to a defect site or pit exposing a crystalline face with a stronger Raman peak at  $354\text{ cm}^{-1}$  and  $446\text{ cm}^{-1}$  than the current membrane orientation or possibly a cosmic ray strike, a common artefact found in long exposure Raman measurements, at this point during the mapping.

Peak position maps were calculated for the InP-like and AlP-like modes of the suspended membrane and are shown in Fig. 12 c) and Fig. 12 d) respectively. There is no obvious spatial correlation in the variation of the InP-like peak, but there is a trend towards increasing wavenumber of the AlP-like peak with increasing  $y$  coordinate. With the suspended membrane the AlP-like peak has a spatial wavenumber shift of approximately  $12.5 \times 10^{-3}\text{ cm}^{-1}\mu\text{m}^{-1}$  in the  $y$  direction, in comparison to  $3.75 \times 10^{-3}\text{ cm}^{-1}\mu\text{m}^{-1}$  for the unprocessed membrane. This Raman shift gradient along a single direction could evidence a bowing of the as-grown structure, which worsens following the substrate removal. Biaxial strain should yield a concave or convex surface profile over the whole wafer surface resulting in bowing along the  $x$  and  $y$  directions, however the anchors could be limiting the bowing to one direction. The AlP-like peak position variation along the  $y$ -axis could also be related to local composition variation [45].

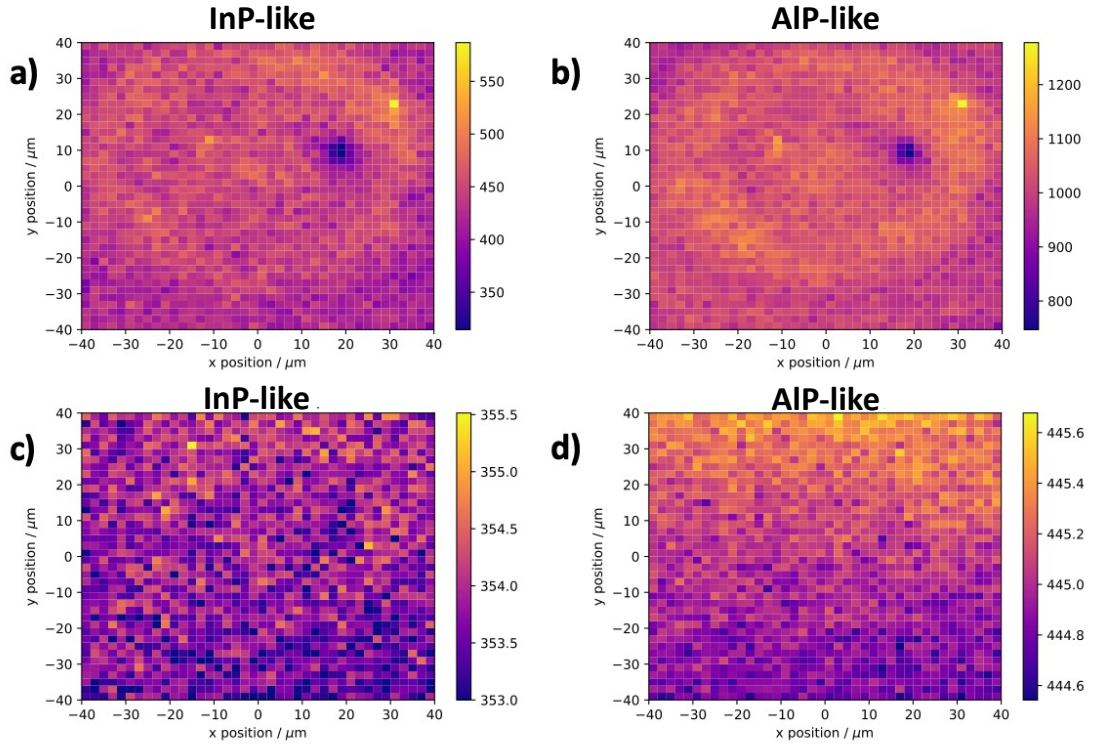


**Figure 12.** Raman maps of an  $80\ \mu\text{m} \times 80\ \mu\text{m}$  region of a suspended membrane, with  $2\ \mu\text{m}$  steps. Intensity-at-a-point of **a)**  $354\ \text{cm}^{-1}$  (InP-like) and **b)**  $446\ \text{cm}^{-1}$  (AIP-like) modes, and peak position maps of the **c)**  $354\ \text{cm}^{-1}$  (InP-like) and **d)** (AIP-like)  $446\ \text{cm}^{-1}$  modes.

## 5.6 Charge carrier lifetime in II-VI VECSEL structures

### 5.6.1 Motivation and background

Charge carrier lifetime can be used to assess the quality of a semiconductor material, as the charge carrier recombination dynamics are heavily dictated by non-radiative recombination at defect centres (Shockley-Hall-Read), radiative recombination and Auger recombination, the rates of which are represented by the material parameters  $A$ ,  $B$  and  $C$ . The “ABC model” introduced in Chapter 2 offers a simple way to relate the average charge carrier lifetime,  $\tau$ , to the recombination mechanisms by

$$\frac{1}{\tau(N)} = A + BN + CN^2 \quad (5)$$

(see Section 2.5 for more information). For low charge carrier densities,  $A$  dominates, whereas for high carrier densities  $C$  is dominant.

The charge carrier lifetime of a laser is a key parameter for reducing the laser threshold; a larger carrier lifetime yields a lower laser threshold. There is a caveat to this that an increase in the charge carrier lifetime should ideally be attributed to a decrease in  $A$  and  $C$ , and not  $B$  as this would decrease the radiative efficiency and hence decrease the output power [46]. The charge carrier lifetime properties have never been evaluated for II-VI MBE-grown VECSEL structures and this value is required as an important confirmation that achieving the laser threshold in II-VI VECSELS is actually possible, and not limited by the material quality. For VECSEL operation the minimum upper state lifetime is quoted as 1-2 ns [47], and so assuming fast electron diffusion from the barriers to the QWs this figure is taken as the goal carrier lifetime for the II-VI gain structures. To further investigate the charge carrier lifetime properties of the ZnCdSe/ZnCdMgSe QWs, some initial carrier lifetime measurements were completed in collaboration with Olivia McGleish from the group of Professor Keith Mathieson at the University of Strathclyde.

#### *5.6.2 Measurement setup and fitting*

An Edinburgh Instruments EPL-450 pulsed diode laser was used to deliver 5 ns pulses at a 20 MHz repetition frequency at 450 nm and at a quoted average power of 0.15 mW. Each pulse has a stated maximum power of 50 mW (at 10 MHz repetition frequency) and a pulse period of 500 ns, far exceeding the charge carrier lifetime. An Edinburgh Instruments Mini-tau lifetime spectrometer was used to measure the PL decay. This instrument logs the PL response within 8192 channels (TCC2 electronics module), with a temporal resolution of 305 fs/channel and uses a Hamamatsu H10720-01 high speed PMT detector, which is cooled to 0 °C and has a spectral sensitivity of 230-850 nm. The pump laser underwent beam shaping with a Keplerian telescope which comprised of 50 mm and 200 mm focal length lenses and a bandpass filter with either a 520 nm or 550 nm transmission (50 nm width) could be used in front of the detector. The setup is summarized in Fig. 13.

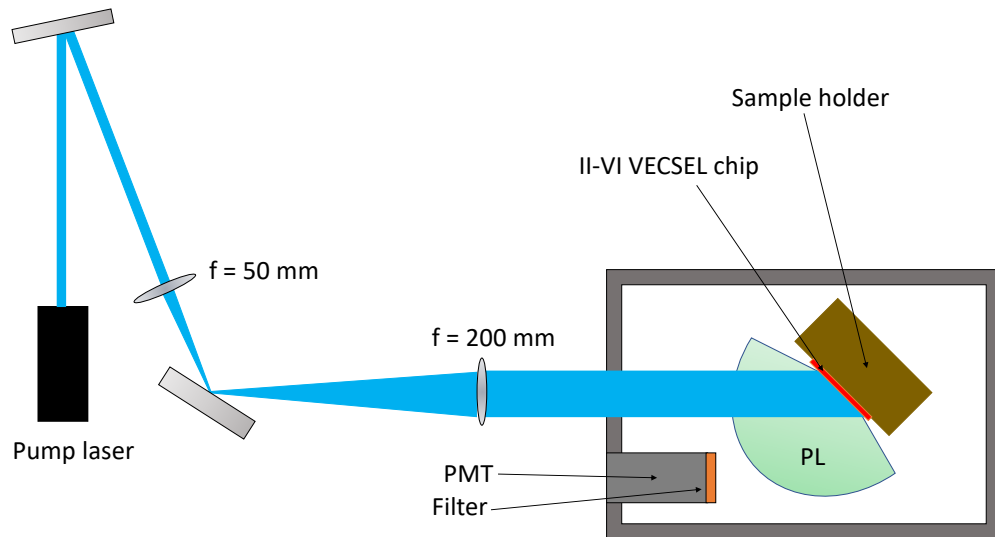


**Figure 13.** The experimental setup for the charge carrier lifetime measurements of the ZnCdSe/ZnCdMgSe QWs. The PL measurements occur within a dark container symbolized by the grey square.

Before the measurements of the II-VI samples the system was operated without a sample to assess the system response, shown in Fig. 14, which allows for a quantification of how the pump, the electronics and the reflections within the experimental housing affect the results. The samples were mounted onto glass slides, using tape for initial experiments and then nail varnish for later ones due to its smaller background signal, and held on an *xyz* stage for alignment.

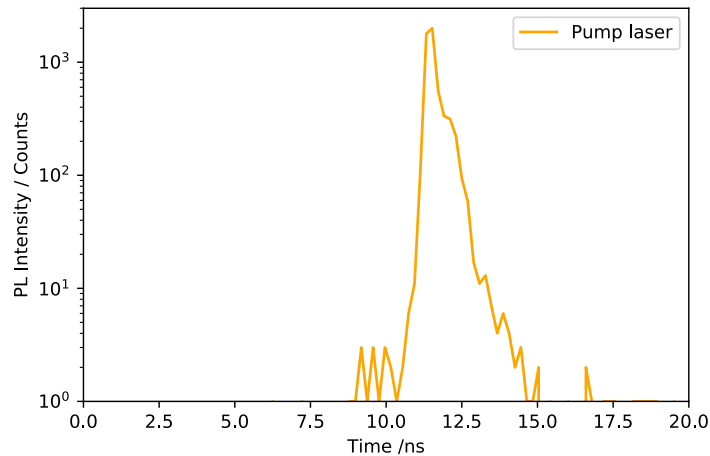


**Figure 14.** Log-linear plot of the response of the Min-tau lifetime spectrometer to the pump signal alone. This response profile is used during the analysis to infer the photoluminescence lifetime.

For the determination of the charge carrier lifetime, the instrument software (Edinburgh Instruments T900) deconvolutes the measured PL decay signal of a sample from the instrument response and uses the Levenberg- Marquardt algorithm to fit up to four exponential decay curves to the data [48]. Each exponential decay intensity,  $I_{PL}(t)$ , has the form

$$I_{PL}(t) = A_i e^{-\frac{t}{\tau_i}} \quad (6)$$

where  $t$  is time,  $A_i$  is the fitted amplitude and  $\tau_i$  is the fitted lifetime and the subscript is used to index the different decays present.

Determining the exact behaviour of the samples in terms of  $A$ ,  $B$  and  $C$  is challenging as verifying the exact injected charge carrier density is difficult and outside the scope of this work. Due to the low level of charge carrier injection a simplification is applied during the analysis that  $C$  has little influence on these measurements. The injected carrier density,  $N$ , is assumed to be the same for every sample.

### *5.6.3 Time resolved PL measurements of CDI 447*

CDI 447 (see Chapter 3 for sample details) demonstrated the highest PL brightness of any sample from the first and second growth campaigns. The PL decay of CDI 447 was measured with Filter 4 (550 nm with 50 nm width) and Filter 5 (520 nm with 50 nm width). The filter was varied to ensure that all parts of the CDI 447 PL spectrum were assessed between the two measurements. The measurements with Filter 4 yielded decay components of 0.75 ns and 4.10 ns, with a Chi-squared of 1.160 (the best fit obtained during these measurements (see Fig. 15), and Filter 5 yielded decay components of 0.43 ns and 4.09 ns, with a Chi-squared of 1.378 (see Fig. 16).

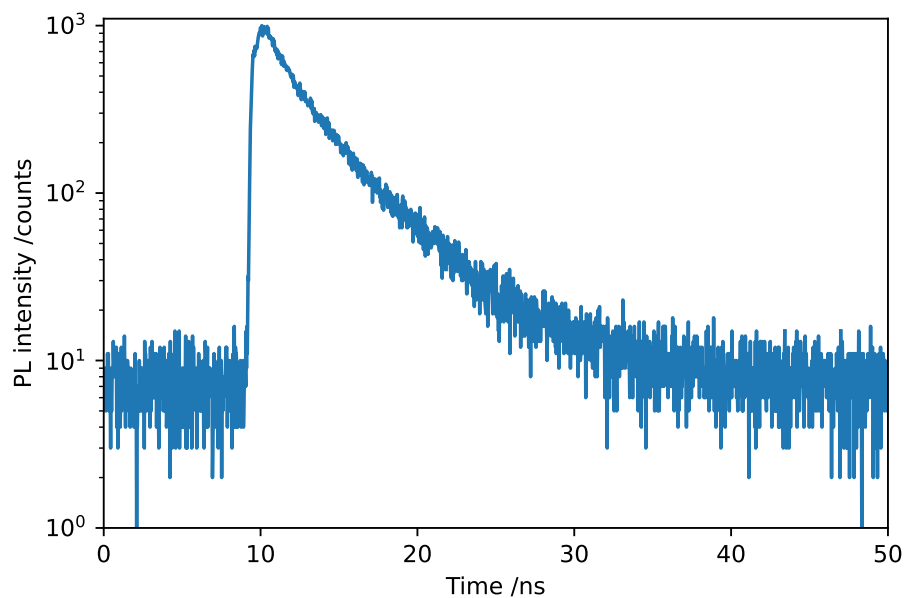


**Figure 15.** Log-linear plot of the PL decay curve of CDI 447 at 550 nm (filter 4). The exponential decay components are 0.75 ns and 4.10 ns.

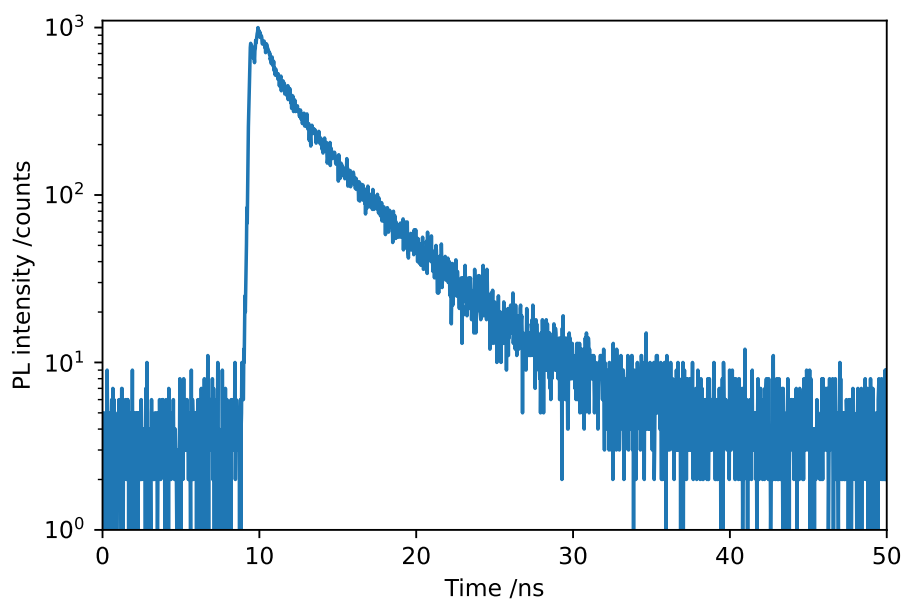


**Figure 16.** Log-linear plot of the PL decay curve of CDI 447 at 520 nm (filter 5). The exponential decay components are 0.43 ns and 4.09 ns.

The Chi-squared values for the CDI 447 measurements indicate a high quality and 10 ns after the pump peak (at around 20 ns into the scan) CDI 447 has an order of magnitude greater PL intensity than CDI 356 and CDI 358 showing that excellent material quality is possible with optimized ZnCdSe/ZnCdMgSe growth conditions.

#### *5.6.4 Impacts of the measured lifetimes on laser threshold*

From the measurements taken it is difficult to make precise conclusions about the variation of  $A$  and  $B$  within these structures. The variation in the decay rates between different samples is a strong indication that the growth process is introducing a highly variable defect density, which requires further work to optimize. The 4 ns decay component measured within CDI 447 demonstrates that with optimized growth conditions, high radiative quality ZnCdSe/ZnCdMgSe-based VECSEL structures can be grown. The 4 ns component of the PL decay exceeds 1 ns, which is typical for QWs used within VECSEL structures [49], and gives initial encouragement that the material quality may be sufficient for the laser threshold. Further work could include varying the excitation density, to obtain more information on the values of  $A$  and  $B$ , and using a monochromator and a streak camera to obtain wavelength dependence data. The wavelength dependence data is important for analysing the charge carrier lifetime in VECSELs due to the sub-cavity resonance effects which could increase the PL lifetime of resonant wavelengths and because the resonant periodic gain arrangement influences the PL intensity. Measuring the PL lifetime from the cleaved edge of a ZnCdSe/ZnCdMgSe-based VECSEL structure would allow for assessment of the charge carrier lifetime without subcavity resonance effects.

#### **5.7 DBR-free VECSEL tests with transfer-printed membranes**

The transfer-printed GaInP/AlGaInP membranes were tested for laser oscillation in an attempt to prove that the transfer-printed, 100- $\mu\text{m}$ -sided, DBR-free VECSEL membranes could handle the high heat load associated with optical pumping. The membranes were tested in a symmetrical, concentric laser cavity formed by two 100 mm radius of curvature, high reflectivity (>99.9 %) external mirrors. A Coherent Verdi V5 was used to optically-pump the sample at 532 nm with a focussed pump spot of approximately 80  $\mu\text{m}$  diameter. The samples were tested in water-cooled brass mounts of various designs to improve the heatsinking. The testing setup is shown in Fig. 17.



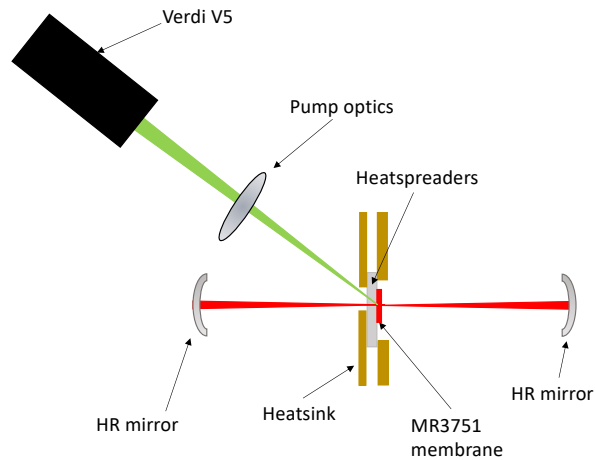


**Figure 17.** The test resonator for the transfer-printed membranes. A concentric resonator formed by a pair of 100 mm radius of curvature high reflectivity mirrors, optically pumped at 532 nm with an 80  $\mu\text{m}$  diameter pump spot.

During tests with membranes transfer-printed onto single diamonds, no membrane was able to reach threshold and most samples had a low brightness and damage threshold. Given the strict thermal requirements of VECSELs, where the optical pump intensity is around 500  $\text{MWm}^{-2}$ , double-diamond bonding was attempted to improve the heat flow from the membranes [50,51]. Double-diamond bonding has only previously been reported with larger membranes, greater than 400  $\mu\text{m}$  x 600  $\mu\text{m}$  surface area, and for the 100- $\mu\text{m}$ -sided, transfer-printed, square membranes this resulted in the membranes being crushed between the two diamonds (see Fig. 18 a). During the double-diamond bonding the smaller, transfer-printed, membranes are under a higher mechanical pressure and have a “bonding torque” exerted on them as the diamonds rotate during the pressing to form the bond. Numerous attempts at the double-diamond bonding were made, one attempt was sufficient for PL and IDPL measurements (Section 5.2.3), however during threshold testing the sample shattered. A potential solution could be to build a photoresist “cushion”, of similar thickness to the membrane, around the membrane that will reduce the “bonding torque” and the pressure on the membrane during bonding.

The colour variation over the membranes in Fig. 18 a) and b) shows the variation of bond quality. The transfer-printed membrane in Fig. 18 b) has been imaged through the underside of the diamond heatspreader so that the bonding surface can be examined. Numerous cracks and contaminants are present which cause localized regions of debonding, resulting in hot spots during optical pumping which lead to further debonding and damage. The cracks and contaminants also scatter light from the membrane surface which contribute to the resonator

losses and further reduce the likelihood of the transfer-printed lasers reaching threshold. It is noted that following laser alignment attempts a colourful residue could be observed around the membranes, which could be the result of the solvent remnants and organic contaminants within the solvents, both of which will impair heat flow from the membrane.

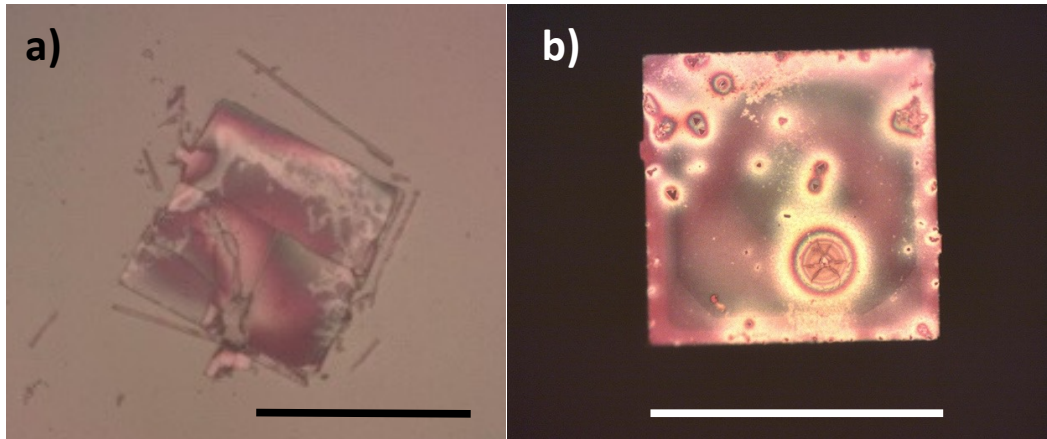


**Figure 18.** Difficulties with testing the transfer-printed membranes. **a)** A transfer-printed GaInP/AlGaInP membrane which has been crushed between two diamonds during a double-sided bond formation. **b)** the underside of a membrane viewed through the heatspreader with cracks and contaminants causing bond degradation and increasing the resonator losses due to scatter. The black and white scale bars represent 100  $\mu\text{m}$ .

Alongside the processing-related barriers to operation the membrane geometry itself may contribute due to surface recombination of charge carriers at the membrane perimeter and in-plane amplified spontaneous emission (ASE). The GaInP capping layer in the GaInP/AlGaInP structure prevents oxidation, however it has a lower bandgap than the AlGaInP barrier material which could lead to surface recombination of the pump injected charge carriers. Given that the laser mode and pump spot size are approximately equal to the lateral dimensions of the membrane it is also possible that charge carriers may recombine on the perimeter surface [52]. The low finesse resonator formed by the parallel edges of the square membranes could lead to in-plane ASE which leads to competition with the DBR-free VECSEL modes in the vertical direction [53]. Parasitic ASE could be reduced by roughening the sidewalls of the membrane by adjusting the ICP etch recipe, or intentionally damaging the sidewalls with a wet etchant. For GaInSb/AlGaAsSb VECSELs it has been found that if the pump spot diameter to sample size ratio is  $< 0.5$  then lateral laser operation can be avoided [53], and if this relation holds for GaInP/AlGaInP VECSELs then the transfer-printed VECSEL membranes also need to have lateral dimensions exceeding 200  $\mu\text{m}$ .

In order to progress the transfer-printed VECSEL, future work needs to focus on improving the diamond-to-membrane bonding in terms of the continuity of contact and reducing contaminant presence, which will improve the heat flow from the active region and reduce the resonator losses. It is possible that switching the under etchant to  $\text{NH}_4\text{OH}:\text{H}_2\text{O}_2$  for the GaInP/AlGaInP structure will improve the bonding results as AlGaInP-based micro-LEDs with 0.2 nm RMS etch side roughness have been reported following GaAs under-etching with this etchant [5,54].

### **5.8 Conclusions and future perspectives**

500-nm-thick,  $100 \times 100 \mu\text{m}^2$  square membranes of ZnCdMgSe were transfer-printed onto transparent diamond heatspreaders, achieving optical contact with no observable flexing or fractures occurring during transfer. Photoluminescence measurements revealed an intense peak at  $\sim 520$  nm under optical pumping at 447 nm, with a 4 nm redshift induced over  $3.6 \text{ MWm}^{-2}$  incident pump intensity. The high quality membranes show the potential for this method to be a powerful tool for miniaturizing and carefully positioning membranes of any device grown on InP with an InGaAs buffer layer. In the case of the II-VI-on-InP material system the suspension and transfer printing methods demonstrated here give an opportunity for this wide bandgap material system to be heterogeneously integrated with other material systems to construct on-chip optical components.

$100 \times 100 \mu\text{m}^2$  square membranes of the GaInP/AlGaInP, DBR-free VECSEL structure, which has been shown to produce working lasers using the full substrate removal method [10], have also been transfer-printed onto diamond heatspreaders. The IDPL showed that double-diamond-sandwiched membranes have a strong thermal contact, however obtaining high quality bonds between the GaInP/AlGaInP membranes is difficult due to damage and contaminants from the under-etch process.

Given the ns-scale charge carrier lifetime measured from the ZnCdSe/ZnCdMgSe QWs, if a high quality membrane of the II-VI VECSEL structure can be transferred onto diamond then the II-VI DBR-free VECSEL should be able to reach threshold. The transfer-printed GaInP/AlGaInP DBR-free VECSELs were unable to reach threshold due to local areas of poor bonding quality, etch damage and their small lateral dimensions which could encourage parasitic amplified spontaneous emission. With these difficulties in mind, a transfer-printed DBR-free VECSEL membranes likely need to be larger than  $200 \mu\text{m} \times 200 \mu\text{m}$ , accurately strain-balanced or lattice-matched and free of contaminants.

Following the under-etching and transfer printing both the ZnCdMgSe and GaInP/AlGaInP membranes exhibited  $\sim 1$  nm RMS surface roughness on the epise, which was superior to the etch side in both cases. If the membrane could be flipped during the transfer printing process by printing the membranes onto another stamp then the bonding surface would be the epise of the membrane instead of the etch side. Using the epise as the bonding surface with the diamond (or SiC) heatspreader should allow for an improved bond quality due to the superior surface roughness. Additionally the bonding between the membranes and the heatspreaders could be improved by thermal annealing processes.

In this work Raman spectroscopic mapping has been used, for the first time, as a useful diagnostic tool for assisting in under-etching microfabrication methodology development. The intensity and position of a Raman peak can be used to infer changes in crystalline quality and strain during the ELO steps. Raman spectroscopy has been used to identify ZnCdSe-like and MgSe-like LO modes for ZnCdMgSe and has verified that the membranes have a good crystalline quality following the under-etching and transfer printing. The presence of the SiC Raman shift peaks confirm contact (but not the quality of the contact) between the ZnCdMgSe membrane and the heatspreader, following transfer-printing. Within the GaInP/AlGaInP structures clear InP-like and AlP-like LO modes were observed with a weak GaP-like mode, and the shifts in the peak position of the AlP-like mode indicates a strain relaxation process occurs during the under-etching.

The unprocessed GaInP/AlGaInP structure and GaInP/AlGaInP membranes have undergone Raman mapping, however due to the complexity of this structure it is difficult to attribute shifts in peak position solely to strain changes. Future work should focus on repeating the mapping of the membranes during the different stages of under-etching and transfer printing method but using a single QW unit so that peak position variations are more likely due to processing induced strain changes. From the peak position map it should then be possible to produce a strain map, as long as the Raman shift of the unstrained QW constituents is also measured. Improvements in the peak fit resolution and accuracy could be achieved using non-Gaussian or Gaussian combination fits [29]. In order to compliment the IDPL and Raman spectroscopy measurements, some further x-ray diffraction measurements would allow for direct measurement of the strain change during the under-etching and transfer printing process and, in the case of the GaInP/AlGaInP samples, could give additional insight into the strain relaxation processes which were identified with the Raman spectroscopy. With advancements

in the speed of Raman mapping technology, the technique of III-V membrane quality assessment demonstrated in this chapter could prove to be a useful technique for high throughput quality assessment of semiconductor integrated devices that are produced on an industrial scale.

The next chapter, the conclusion, finalizes the thesis by summarizing the modelling and material processing results presented in this work, and outlining a future plan for the development of the II-VI VECSEL.

## References

1. G. A. Chappell, B. Guilhabert, T. Garcia, K. Zhao, I. M. Watson, M. D. Dawson, M. C. Tamargo, and J. E. Hastie, "Suspension and transfer printing of ZnCdMgSe membranes from an InP substrate," *Opt. Mater. Express* **10**(12), (2020).
2. J. M. M. Santos, B. E. Jones, P. J. Schlosser, S. Watson, J. Herrnsdorf, B. Guilhabert, J. J. D. McKendry, J. De Jesus, T. A. Garcia, M. C. Tamargo, A. E. Kelly, J. E. Hastie, N. Laurand, and M. D. Dawson, "Hybrid GaN LED with capillary-bonded II-VI MQW color-converting membrane for visible light communications," *Semicond. Sci. Technol.* **30**(3), 035012 (2015).
3. R. Moug, A. Alfaro-Martinez, L. Peng, T. Garcia, V. Deligiannakis, A. Shen, and M. Tamargo, "Selective etching of InGaAs/InP substrates from II-VI multilayer heterostructures," *Phys. status solidi* **9**(8–9), 1728–1731 (2012).
4. T. J. Miller, M. A. Haase, X. Sun, B. Hao, J. Zhang, T. L. Smith, T. Ballen, J. Xie, A. S. Barnes, F. Kecman, J. Yang, J. Thielen, C. A. Leatherdale, R. Wirth, A. Biebersdorf, K. Engl, and S. Groetsch, "High efficiency green LEDs using II-VI color converters," in *Proc. SPIE 7617, Light-Emitting Diodes: Materials, Devices, and Applications for Solid State Lighting XIV*, K. P. Streubel, H. Jeon, L.-W. Tu, and N. Linder, eds. (International Society for Optics and Photonics, 2010), **7617**, p. 76171A.
5. M.-C. Tseng, C.-L. Chen, N.-K. Lai, S.-I. Chen, T.-C. Hsu, Y.-R. Peng, R.-H. Horng, S. C. Hsu, D. S. Wu, C. Y. Lee, J. Y. Su, R. H. Horng, S. H. Huang, C. Y. Chiu, B. R. Wu, C. F. Weng, P. Ravadgar, T. M. Wu, S. P. Wang, J. H. He, T. H. Yang, Y. M. Chen, T. C. Hsu, A. S. Liu, D. Liu, Q. Yu, Z. Feng, and X. Xu, "P-side-up thin-film AlGaInP-based light emitting diodes with direct ohmic contact of an ITO layer with a GaP window layer," *Opt. Express*, Vol. 22, Issue S7, pp. A1862-A1867 **22**(107), A1862–A1867 (2014).
6. Y. P. Varshni, "Temperature dependence of the elastic constants," *Phys. Rev. B*

- 2(10), 3952–3958 (1970).
7. L. Malikova, W. Krystek, F. H. Pollak, N. Dai, A. Cavus, and M. C. Tamargo, "Temperature dependence of the direct gaps of ZnSe and Zn<sub>0.56</sub>Cd<sub>0.44</sub>Se," *Phys. Rev. B* **54**, 54 (1996).
  8. B. E. Jones, P. J. Schlosser, J. De Jesus, T. A. Garcia, M. C. Tamargo, and J. E. Hastie, "Processing and characterisation of II–VI ZnCdMgSe thin film gain structures," *Thin Solid Films* **590**, 84–89 (2015).
  9. A. J. Trindade, B. Guilhabert, E. Y. Xie, R. Ferreira, J. J. D. McKendry, D. Zhu, N. Laurand, E. Gu, D. J. Wallis, I. M. Watson, C. J. Humphreys, and M. D. Dawson, "Heterogeneous integration of gallium nitride light-emitting diodes on diamond and silica by transfer printing," *Opt. Express* **23**(7), 9329 (2015).
  10. B. E. Jones, "ZnCdMgSe and AlGaInP multi-quantum well films for colour conversion and optically-pumped visible lasers," (2015).
  11. C. Hums, T. Finger, T. Hempel, J. Christen, A. Dadgar, A. Hoffmann, and A. Krost, "Fabry-Perot effects in InGa<sub>N</sub>GaN heterostructures on Si-substrate," *J. Appl. Phys.* **101**(3), 033113 (2007).
  12. B. F. Spiridon, M. Toon, A. Hinz, S. Ghosh, S. M. Fairclough, B. J. E. Guilhabert, M. J. Strain, I. M. Watson, M. D. Dawson, D. J. Wallis, and R. A. Oliver, "Method for inferring the mechanical strain of GaN-on-Si epitaxial layers using optical profilometry and finite element analysis," *Opt. Mater. Express* **11**(6), 1643 (2021).
  13. A. R. Clawson, *Guide to References on III-V Semiconductor Chemical Etching* (n.d.).
  14. A. Jasik, A. K. Sokół, A. Broda, I. Sankowska, A. Wójcik-Jedlińska, M. Wasiak, A. Trajnerowicz, J. Kubacka-Traczyk, and J. Muszalski, "Impact of strain on periodic gain structures in vertical external cavity surface-emitting lasers," *Appl. Phys. B* **122**(10), 258 (2016).
  15. H. Kahle, "Personal communication," (n.d.).
  16. R. G. Alonso, E.-K. Suh, A. K. Ramdas, N. Samarth, H. Luo, and J. K. Furdyna, "Raman spectroscopy of two novel semiconductors and related superlattices: Cubic CdMnSe and CdZnSe," *Phys. Rev. B* **40**(6), 15–1989 (1989).
  17. S. Adachi, *Properties of Semiconductor Alloys : Group-IV, III-V and II-VI Semiconductors* (Wiley, 2009).
  18. R. J. Angel, M. Murri, B. Mihailova, and M. Alvaro, "Stress, strain and Raman shifts," *Zeitschrift für Krist. - Cryst. Mater.* **234**(2), 129–140 (2019).
  19. E. Mieda, T. Maeda, N. Miyata, T. Yasuda, Y. Kurashima, A. Maeda, H. Takagi, T. Aoki, T. Yamamoto, O. Ichikawa, T. Osada, M. Hata, A. Ogawa, T. Kikuchi, and Y.

- Kunii, "Wafer-scale layer transfer of GaAs and Ge onto Si wafers using patterned epitaxial lift-off," *Jpn. J. Appl. Phys.* **54**(3), 036505 (2015).
20. Y. Kobayashi, K. Kumakura, T. Akasaka, and T. Makimoto, "Layered boron nitride as a release layer for mechanical transfer of GaN-based devices," *Nature* **484**(7393), 223–227 (2012).
  21. M.-S. Lin, C.-F. Lin, W.-C. Huang, G.-M. Wang, B.-C. Shieh, J.-J. Dai, S.-Y. Chang, D. S. Wu, P.-L. Liu, and R.-H. Horng, "Chemical–Mechanical Lift-Off Process for InGaN Epitaxial Layers," *Appl. Phys. Express* **4**(6), 062101 (2011).
  22. S. K. Kim, J. Shim, D.-M. Geum, C. Z. Kim, H.-S. Kim, Y.-S. Kim, H.-K. Kang, J. D. Song, S.-J. Choi, D. H. Kim, W. J. Choi, H. Kim, D. M. Kim, and S. H. Kim, "Cost-effective Fabrication of In<sub>0.53</sub>Ga<sub>0.47</sub>As-on-Insulator on Si for Monolithic 3D via Novel Epitaxial Lift-Off (ELO) and Donor Wafer Re-use," in *2016 IEEE International Electron Devices Meeting (IEDM)* (IEEE, 2016), pp. 25.4.1-25.4.4.
  23. L. Ma, W. Qiu, and X. Fan, "Stress/strain characterization in electronic packaging by micro-Raman spectroscopy: A review," *Microelectron. Reliab.* **118**, (2021).
  24. Z. H. Ni, T. Yu, Y. H. Lu, Y. Y. Wang, Y. P. Feng, and Z. X. Shen, "Uniaxial Strain on Graphene: Raman Spectroscopy Study and Band-Gap Opening," *ACS Nano* **2**(11), 2301–2305 (2008).
  25. S. P. S. Porto and J. F. Scott, "Raman Spectra of CaWO<sub>4</sub>, SrWO<sub>4</sub>, CaMoO<sub>4</sub> and SrMoO<sub>4</sub>," *Phys. Rev.* **157**(3), 716 (1967).
  26. T. Kato, T. Matsumoto, M. Hosoki, and T. Ishida, "Strain-induced shift of optical phonon frequency in InGaP layers grown on GaAs substrates," *Jpn. J. Appl. Phys.* **26**(10 A), L1597–L1600 (1987).
  27. Y. Kanemitsu, A. Yamamoto, H. Matsue, Y. Masumoto, S. Yamaga, and A. Yoshikawa, "Raman study of disorder and strain in epitaxial Zn<sub>Sx</sub>Se<sub>1-x</sub> films on a GaAs substrate," *Appl. Phys. Lett* **60**(1330), (1992).
  28. J. A. Steele, P. Puech, and R. A. Lewis, "Polarized Raman backscattering selection rules for (hhl)-oriented diamond- and zincblende-type crystals," *J. Appl. Phys.* **120**(5), 055701 (2016).
  29. R. A. Mayanovic and X. Yuan, "An Empirical Study on Raman Peak Fitting and Its Application to Raman Quantitative Research," *Appl. Spectrosc.* **71**(10), (2017).
  30. R. G. Alonso, E. K. Suh, A. K. Ramdas, N. Samarth, H. Luo, and J. K. Furdyna, "Raman spectroscopy of two novel semiconductors and related superlattices: Cubic Cd<sub>1-x</sub>Mn<sub>x</sub>Se and Cd<sub>1-x</sub>Zn<sub>x</sub>Se," *Phys. Rev. B* **40**(6), 3720–3728 (1989).
  31. D. Wang, D. Huang, and C. Jin, "Raman spectra of Zn<sub>1-x</sub>Mg<sub>x</sub>SySe<sub>1-y</sub>

- quaternary alloys," *J. Appl. Phys.* **80**, 1248 (1996).
32. R. Vogelgesang, A. J. Mayur, M. Dean Sciacca, Eunsoon Oh, I. Miotkowski, A. K. Ramdas, S. Rodriguez, and G. Bauer, "Raman and Infrared Spectroscopy of Optical Phonons in II–VI Alloys, Epilayers and Superlattices," *J. Raman Spectrosc.* **27**(3–4), 239–247 (1996).
  33. J. Polit, E. M. Sheregii, V. I. Ivanov-Omskii, E. Sciesińska, J. Sciesińska, and W. Gębicki, "Raman Scattering and Far Infrared Reflection–Absorption Spectra of the Four-Component Solid Solution  $Zn_xCd_yHg_{1-x-y}Te$ ," *Phys. status solidi* **208**(1), (1999).
  34. V. M. Burlakov, A. P. Litvinchuk, V. N. Pyrkov, G. G. Tarasov, and N. I. Vitrikhovskii, "Optical Properties of the Quaternary II–VI Mixed Crystals in the Far Infrared Region," *Phys. status solidi* **128**(2), 389–400 (1985).
  35. D. Huang, C. Jin, D. Wang, X. Liu, J. Wang, and X. Wang, "Crystal structure and Raman scattering in  $Zn_{1-x}Mg_xSe$  alloys," *Appl. Phys. Lett.* **67**(24), 3611 (1995).
  36. Shin-ichi Nakashima, Takeshi Mitani, Masaru Tomobe, Tomohisa Kato, and Hajime Okumura, "Raman characterization of damaged layers of 4H-SiC induced by scratching," *AIP Adv.* **6**(015207), (2016).
  37. D. Cai, A. Neyer, R. Kuckuk, and H. M. Heise, "Raman, mid-infrared, near-infrared and ultraviolet-visible spectroscopy of PDMS silicone rubber for characterization of polymer optical waveguide materials," *J. Mol. Struct.* **976**(1–3), 274–281 (2010).
  38. D. Nesheva, M. J. Šćepanović, S. Šćepanović, S. Aškrabić, Z. Levi, I. Bineva, and Z. V. Popović, "Raman Scattering from ZnSe Nanolayers," *ACTA Phys. Pol. A* **116**, (2009).
  39. M. Kondow, S. Minagawa, and S. Satoh, "Raman scattering from AlGaInP," *Appl. Phys. Lett.* **51**(24), 2001–2003 (1987).
  40. T. Hofmann, G. Leibiger, V. Gottschalch, I. Pietzonka, and M. Schubert, "Infrared dielectric function and phonon modes of highly disordered  $(Al_xGa_{1-x})_{0.52}In_{0.48}P$ ," *Phys. Rev. B* **64**(155206), (2001).
  41. M. I. Alonso, E. Bailo, M. Garriga, A. Molero, P. O. Vaccaro, A. R. Goñi, A. Ruiz, and M. Alonso, "Composition and Strain Imaging of Epitaxial In-Plane SiGe Alloy Nanowires by Micro-Raman Spectroscopy," *J. Phys. Chem. C* **119**(38), 22154–22163 (2015).
  42. W. Qiu, C. L. Cheng, R. R. Liang, C. W. Zhao, Z. K. Lei, Y. C. Zhao, L. L. Ma, J. Xu, H. J. Fang, and Y. L. Kang, "Measurement of residual stress in a multi-layer semiconductor heterostructure by micro-Raman spectroscopy," *Acta Mech. Sin.*



- Xuebao **32**(5), 805–812 (2016).
43. J. A. Cuenca, M. D. Smith, D. E. Field, F. C-P. Massabuau, S. Mandal, J. Pomeroy, D. J. Wallis, R. A. Oliver, I. Thayne, M. Kuball, and O. A. Williams, "Thermal stress modelling of diamond on GaN/III-Nitride membranes," *Carbon N. Y.* **174**, 647–661 (2021).
  44. "Home — Spyder IDE," <https://www.spyder-ide.org/>.
  45. L. . B. Freund and S. Suresh, *Thin Film Materials: Stress, Defect Formation and Surface Evolution* (Cambridge University Press, 2003).
  46. M. Kuznetsov, F. Hakimi, R. Sprague, and A. Mooradian, "Design and characteristics of high-power (>0.5-W CW) diode-pumped vertical-external-cavity surface-emitting semiconductor lasers with circular TEM<sub>00</sub> beams," *IEEE J. Sel. Top. Quantum Electron.* **5**(3), 561–573 (1999).
  47. M. Guina, A. Rantamäki, and A. Härkönen, "Optically pumped VECSELs: review of technology and progress," *J. Phys. D. Appl. Phys.* **50**(38), 383001 (2017).
  48. "Levenberg-Marquardt Method -- from Wolfram MathWorld," <https://mathworld.wolfram.com/Levenberg-MarquardtMethod.html>.
  49. S. Calvez, J. E. Hastie, M. Guina, O. G. Okhotnikov, and M. D. Dawson, "Semiconductor disk lasers for the generation of visible and ultraviolet radiation," *Laser Photonics Rev.* **3**(5), 407–434 (2009).
  50. H. Kahle, C. M. N. Mateo, U. Brauch, P. Tatar-Mathes, R. Bek, M. Jetter, T. Graf, and P. Michler, "Semiconductor membrane external-cavity surface-emitting laser (MECSEL)," *Optica* **3**(12), 1506 (2016).
  51. A. Broda, B. Jeżewski, I. Sankowska, M. Szymański, P. Hoser, and J. Muszalski, "Growth and characterization of InP-based 1750 nm emitting membrane external-cavity surface-emitting laser," *Appl. Phys. B Lasers Opt.* **126**(12), 192 (2020).
  52. L. A. Coldren, S. W. Corzine, and M. L. Masanovic, *Diode Lasers and Photonic Integrated Circuits* (Wiley, 2012).
  53. T. Töpfer, M. Rattunde, and S. Kaspar, "High-power 2.0  $\mu\text{m}$  semiconductor disk laser - Influence of lateral lasing," *Appl. Phys. Lett* **100**, 192107 (2012).
  54. J. F. C. Carreira, E. Xie, R. Bian, J. Herrnsdorf, H. Haas, E. Gu, M. J. Strain, and M. D. Dawson, "Gigabit per second visible light communication based on AlGaInP red micro-LED micro-transfer printed onto diamond and glass," *Opt. Express*, Vol. 28, Issue 8, pp. 12149-12156 **28**(8), 12149–12156 (2020).

## 6. Conclusion

The intention of the work presented in this thesis is to advance the capabilities of VECSEL technology through two ways: by demonstrating DBR-free VECSEL operation at “green gap” wavelengths using the novel ZnCdSe/ZnCdMgSe-on-InP, II-VI semiconductor material system; and by developing the heterogeneous integration techniques to enable III-V and II-VI VECSELs to be constructed by transfer printing. The ZnCdSe/ZnCdMgSe-on-InP platform will enable the expansion of DBR-free VECSELs from red and infra-red wavelengths to the rest of the visible spectrum, expanding the application scope of this laser class [1–3]. The suspension and transfer printing method can yield high quality GaN/AlInGaN-based devices [4,5], and in this work the goal of adapting these techniques aims to construct DBR-free VECSELs with high spatial accuracy, minimal defect introduction and high quality thermal contact with an intracavity heatspreader.

Across the four work chapters, numerous results were presented, including: a) a numerical model for designing II-VI DBR-free VECSEL structures, b) the growth of II-VI VECSEL structures and epitaxial lift-off via full substrate removal, c) the development of the suspension method for the ZnCdMgSe-on-InP and GaInP/AlGaInP-on-GaAs material systems, d) the characterization of transfer-printed ZnCdMgSe and GaInP/AlGaInP membranes, e) the development of a blue-InGaN-diode-pumping scheme, and f) the application of this pump scheme to an AlInGaP-based VECSEL. In this concluding chapter, a summary of outcomes will be presented alongside a consideration of the future visions for the work of this thesis.

### 6.1 II-VI gain structure design and membrane characterization

Chapter 2 presents numerical modelling that enables the design of DBR-free VECSEL gain structures, starting from fundamental material parameters. Referenced values and Vegard’s law are used to determine the set of material parameters for ZnCdSe and ZnCdMgSe lattice-matched to InP. The background theory behind quantum confinement is explained and the effects of biaxial strain and temperature on the material parameters are discussed. The Kuznetsov VECSEL performance model is introduced as a tool for designing VECSEL gain structures and is applied to gain structure design, along with the RPG principle [6,7]. The optical material gain spectrum of a 4 nm  $\text{Zn}_{0.48}\text{Cd}_{0.52}\text{Se}/\text{Zn}_{0.3}\text{Cd}_{0.28}\text{Mg}_{0.42}\text{Se}$  QW is calculated for the transverse electric polarization, for the  $n = 1$  and  $n = 2$  sub-bands, with Lorentzian linewidth broadening of the sub-band energy levels and accounting for only electron and heavy hole recombination [8], which showed a peak gain of  $\sim 5000 \text{ cm}^{-1}$  at a charge carrier density

of  $10^{25} \text{ m}^{-3}$ . The material gain calculations were used to calculate the material gain parameter and the transparency carrier densities used in the Kuznetsov analysis, to allow for a more accurate II-VI DBR-free VECSEL performance model. From this improved model, the ideal gain structure design was determined to have eight QWs, resonantly distributed within four electric field antinodes.

Chapter 5 details the characterization of the ZnCdMgSe and GaInP/AlGaInP membranes, which were under-etched and transfer printed in Chapter 4, in terms of surface roughness, PL brightness, crystalline quality and bonding quality with diamond or SiC. AFM measurements showed nm-scale surface roughness on the ZnCdMgSe transfer printed membranes, but showed heavy levels of etch damage and contamination on the GaInP/AlGaInP membranes. PL measurements confirmed high levels of optical quality of the transfer printed membranes and temperature-induced red-shifting of the PL spectra was used to assess the membrane-to-heatspreader bonding quality. Measurements of the PL lifetime of unprocessed II-VI, DBR-free VECSEL structures were completed. The highest quality sample, CDI 447, showed a  $\sim 4$  ns charge carrier lifetime, which is within the  $\sim$  ns timescale of semiconductors successfully used in III-V VECSEL structures [9]. Raman spectroscopy measurements showed evidence that the under-etch and transfer printing does not affect the II-VI membrane crystal quality, however for GaInP/AlGaInP membranes there is some evidence of a strain relaxation process.

Novel Raman spectroscopic maps were created for an unprocessed GaInP/AlGaInP sample and a suspended GaInP/AlGaInP membrane. The InP-like and AlP-like LO modes were plotted as intensity at a point and peak position maps. Intensity at a point maps showed ring shapes within the membrane structure following under-etching, corresponding to regions of poor crystalline quality due to internal, etch-related damage. This work shows promise for future development as a diagnostic tool for assessing strain changes, as well as material and bonding quality in transfer printed devices.

## **6.2 Material processing and VECSEL development**

Chapter 3 reports the progress towards a working II-VI, DBR-free VECSEL. The construction of a blue-InGaN-diode-pumped, AlInGaP VECSEL was used as an exercise to develop the 447 nm pump optics for the barrier pumping of the II-VI, DBR-free VECSEL. The optimum method for InP substrate removal utilises glycol phthalate or S1800-series photoresist (PR) for sample mounting, which then undergo full substrate removal using a single wet etch with HCl:H<sub>2</sub>O (3:1). The InGaAs buffer layer is removed with H<sub>3</sub>PO<sub>4</sub>:H<sub>2</sub>O<sub>2</sub>:H<sub>2</sub>O (1:1:6). The

resulting II-VI membrane is released from the mounting wax or PR using acetone. Full substrate removal could be improved by first bonding the epise of the II-VI, DBR-free VECSEL to diamond using room-temperature plasma assisted bonding [10] to give the membrane structural rigidity and to enforce a high quality II-VI-to-diamond bond.

Varying the InGaAs buffer layer thickness showed that, if the InGaAs layer is too thin, the HCl-based etchants damage the membranes during the substrate removal. However, if this layer is too thick, stacking faults form, causing defects within the II-VI layers. 360 nm InGaAs, as in CDI 447, appears to offer a good compromise between the 500 nm InGaAs of CDI 517 (which yielded low quality membranes) and the 30-40 nm InGaAs of CDI 637-640 (which are susceptible to etch damage but have superior surface quality and PL brightness). Further work is required to test the InGaAs thicknesses from 40 nm to 360 nm to find the optimum value. Including a  $2\lambda$  ZnCdMgSe buffer layer into the gain structure design improved II-VI material quality, due to the physical distancing between the QWs and the II-VI/III-V interface. Once a reliable processing methodology is developed, the II-VI gain structure design could include compressively strained QWs, within a strain balanced heterostructure, to enhance TE gain.

Chapter 4 focusses on the adaptation and development of suspension and transfer printing methods for application to II-VI and III-V DBR-free VECSEL structures, enabling their heterogeneous integration with diamond/SiC heatspreaders and other materials. Wet and dry etching methods for the two material systems are reviewed and inductively coupled plasma (ICP) etching of ZnCdMgSe-on-InP is demonstrated using Ar/Cl<sub>2</sub> and Ar/BCl<sub>3</sub> etch recipes. A literature review is conducted to find a wet etchant that selectively etches InP over ZnCdMgSe, however, to best of the author's knowledge, no such etchant has been reported.

A hardmask comprised of an array of 100- $\mu$ m-sided square membranes, held to rails by anchors, was patterned into ZnCdMgSe-on-InP and a GaInP/AlGaInP-on-GaAs, DBR-free VECSEL structure, and ICP was used to etch the device pattern through the epilayers and into the substrate. Sidewall protection formation is discussed and examples of formation methodologies are shown, however, the ideal method for consistently forming reliable sidewall protection requires further investigation. HCl-based etchants were used to under-etch the ZnCdMgSe membranes from the InP substrate, and a short etch of H<sub>3</sub>PO<sub>4</sub>:H<sub>2</sub>O<sub>2</sub>:H<sub>2</sub>O (1:1:6) was used to remove the InGaAs buffer layer. The effects of the InP wet-etch anisotropy on the under-etch were investigated and aligning the rails along  $[\bar{1} \bar{1} 0]$  gives the most efficient under-etch. GaInP/AlGaInP membranes were under-etched from GaAs with H<sub>3</sub>PO<sub>4</sub>:H<sub>2</sub>O<sub>2</sub>:H<sub>2</sub>O

(3:4:3), generating a large volume of contaminants which coated the membranes. Cleaning the membranes with solvents reduced the contamination, however, etching with  $\text{NH}_4\text{OH}:\text{H}_2\text{O}_2:\text{H}_2\text{O}$  or  $\text{HOC}(\text{CH}_2\text{CO}_2\text{H})_2:\text{H}_2\text{O}_2$  could improve this. A 500-nm-thick ZnCdMgSe membrane and a GaInP/AlGaInP-on-GaAs, DBR-free VECSEL membrane were successfully transfer printed onto diamond using a thin isopropanol wetting layer to assist in strong bond formation. Transfer-printed GaInP/AlGaInP, DBR-free VECSEL structures on diamond were optically-pumped at 532 nm within a concentric resonator, however, they did not reach laser threshold due to surface contaminants on the membranes and localized regions of poor bonding quality.

The suspension method presented in Chapter 4 requires no specifically engineered released layer or organic-based sidewall protection and, in the II-VI case, is independent of the etch selectivity of InGaAs with the ZnCdMgSe. Small process adjustments could allow this method to be applied to all semiconductor devices grown on InP. Through optimization of the sidewall protection (or developing selective etchants between ZnCdMgSe and InP), extremely high quality II-VI and III-V membranes could be realised for use in novel photonic devices.

### **6.3 Physical limitations in II-VI DBR-free VECSEL development**

Assuming that the MBE-grown II-VI DBR-free VECSEL structures have the assumed ABC coefficients used in Chapter 2, then the II-VI VECSEL should reach laser threshold under standard VECSEL operating conditions (no cryogenic requirements, standard optical pumping). If the defect density of the structures is too high, either after growth or processing, or if the individual layer thicknesses are inaccurate, then the threshold of the laser will increase or laser action may be impossible due to excessive optical loss.

It is likely that the full substrate removal and the process of transferring a membrane onto diamond introduces misfit dislocation defects into the II-VI membranes. The  $C_{11}$  and  $C_{12}$  stiffness constants of ZnCdSe and ZnCdMgSe are smaller than other common III-V materials such as GaP, InP, AlP or GaAs [11], and so for a given stress, ZnCdMgSe (which comprises the bulk of the gain structure) will experience a greater epitaxial strain than the typical materials used in demonstrated DBR-free VECSELs. The full-substrate removal ELO process likely results in localized regions of high strain, which introduces significant defects into the II-VI material, altering the ABC coefficients. Alternatively, the low stiffness of the II-VI materials means that they should easily conform to the surface topography of a host substrate and therefore strongly bond to surfaces, assuming a nm-scale membrane surface roughness.

The development of selective etchants between ZnCdMgSe and InP would be extremely advantageous for the processing of the II-VI VECSEL membranes. Membrane damage during the full substrate removal with the HCl-based etchants frequently occurs, even with the InGaAs etch stop layer. This results in a high etch pit density within the membrane, which is sufficient to prevent the laser threshold being reached. VECSELs have a low single-pass gain, so very little loss can be tolerated within the laser oscillator, meaning etch-related damage to the membrane needs to be eliminated to give the best results.

#### **6.4 Future vision**

The accuracy of the material gain modelling completed in this work could be improved by including multiband and many-body effects. Although the calculated and measured PL spectra are in good agreement, experimental verification of the material gain spectrum using pump-probe experiments, similar to that reported in [12], is recommended for future work.

Future progress on transfer-printed VECSELs should focus on transfer printing larger membranes, to prevent lateral parasitic laser oscillation. Membrane bonding could be improved by flipping them after substrate release, allowing the low roughness episeide to be transfer-printed onto the diamond heatspreader. There is much interest in removing substrates from VECSELs, to improve thermal management through thin device operation, and VECSEL-to-diamond heterogeneous integration [13,14]. The suspension and transfer printing method could offer this without complicated bonded techniques and with nm-scale placement precision for future on-chip VECSEL devices and VECSEL arrays [15]. The recent development of continuous roller transfer printing, capable of constructing device arrays exceeding 75,000 units [16], opens the possibility of industrially-scalable VECSEL arrays, which could be used for optical communication and projection.

Full VECSELs contain a greater variety of materials within their epitaxial structure compared with simpler DBR-free VECSELs. Within a typical GaInP/AlInGaP VECSEL there are InGaP QWs and capping layers, AlInGaP barriers (multiple compositions for strain management), AlAs and AlGaAs from the DBR and a GaAs substrate. Each of these materials has a significantly different etch chemistry. An under-etching of a full GaInP/AlGaInP VECSEL structure was completed in this work (Fig. 1) by applying sidewall protection, as described in Chapter 4, to prevent the  $\text{H}_3\text{PO}_4:\text{H}_2\text{O}_2$ -based etchants from etching the DBR. Transfer printing the membranes revealed underside DBR etch damage. Through development of the sidewall protection and careful under-etchant selection, transfer printed VECSELs can be realised.

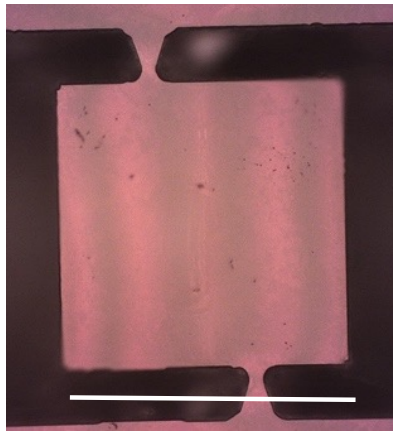


**Figure 1.** A suspended full VECSEL membrane at 20 × magnification. The white scale bar represents 100 μm.

Novel materials, heterogeneous integration and transfer printing are the key themes of this project, with the work presented in this thesis enabling an interesting future vision of VECSELs to be envisaged. Epitaxial growth could be used to provide wafers with single component layers, rather than growing devices on an entire wafer, ensuring that successive stacked layers are grown to a high quality. Suspension and transfer printing could be used to transfer print layers of the desired materials into a VECSEL heterostructure which may be impossible to grow epitaxially. For example, nm-thick ZnCdSe layers could be sandwiched between InGaN barriers (Fig. 2), to take advantage of the excellent mechanical and thermal properties of GaN-based materials, whilst allowing barrier pumping at 447 nm (or 532 nm), but with the red-green-blue emission range of the II-VI materials. Furthermore, other II-VI and III-V semiconductors could be incorporated into the same VECSEL.

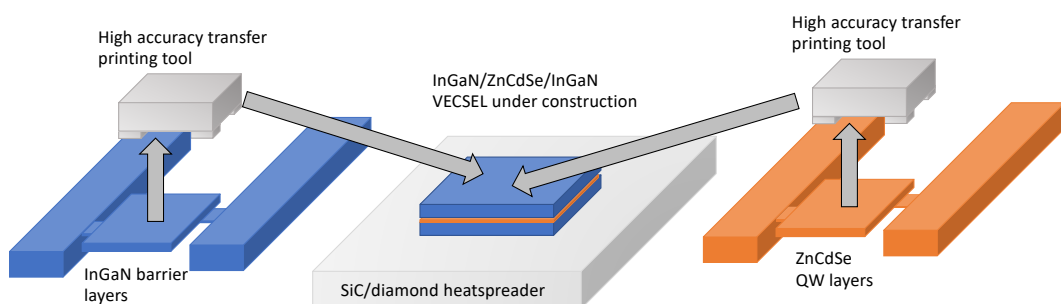


**Figure 2.** Transfer printing could be used to construct VECSEL gain structures which could not be epitaxially grown. Here, an example of ZnCdSe QWs within InGaN barriers is given.

The ability to control the orientation of the semiconductor materials whilst they are stacked could also lead to interesting new device physics, as the layers are strained by the angle of their orientation. The wide bandgap II-VI material system could also afford the opportunity for interesting polariton-based lasers in the VECSEL geometry [17].

There is fast progress in longer, visible wavelength GaN-based lasers. In particular, the photoelectro-chemical etching of GaN can be used to produce nanopores within GaN, which reduce its refractive index due to the presence of air within the epitaxial structure, enabling a greater refractive index contrast within GaN-based DBRs and an enhanced reflectivity [18]. Additionally, nanopores decrease the GaN elastic modulus and hardness, and enable its usage as a mechanical release layer for the heterogeneous integration of GaN-based devices [20]. The structure of nanopores can be engineered to give birefringence to nanoporous DBRs which, along with ~100% reflectivity at blue wavelengths, can be applied to control the polarization of GaN-based VCSELs [19]. Nanoporous GaN-based DBRs show promise for expanding the wavelength coverage of GaN-based laser sources, and are going to be included within the next generation of industrially developed 515 nm and 525 nm GaN-based VCSELs [21]. The heterogeneous integration of II-VI QWs with high refractive index contrast, nanoporous GaN DBRs could offer another route to “green-gap” VECSELs.

In order to develop a working II-VI VECSEL, improving the material processing to obtain higher membrane quality and bonding to diamond/SiC is essential. The development of selective etchants and release layers could greatly enable this. Once a high quality ZnCdSe/ZnCdMgSe membrane on diamond has been constructed and the II-VI VECSEL has reached threshold, there are two other key results that could be obtainable. Firstly, it would be possible to frequency double the green output of the II-VI VECSEL to the UV, to demonstrate UV emission with a single frequency doubling step, which improves efficiency and reduces system complexity. Secondly, it would be possible to build upon the work on white and RGB II-VI lasers [3,22] to develop a white VECSEL. The white VECSEL gain structure would be designed to have an extremely broad gain bandwidth, by using a large number of QWs with varied thickness throughout the structure and arranged with a weak RPG, to encourage the maximum modal gain bandwidth. The shorter wavelength QWs would likely be needed in a higher number density as their output can pump the longer wavelength QWs. Ultimately, the II-VI VECSEL would be a compact, efficient and high-quality visible laser which would find numerous uses in medicine, dentistry, projection, quantum technologies and spectroscopy.



## References

1. H. Kahle, C. M. N. Mateo, U. Brauch, P. Tatar-Mathes, R. Bek, M. Jetter, T. Graf, and P. Michler, "Semiconductor membrane external-cavity surface-emitting laser (MECSEL)," *Optica* **3**(12), 1506 (2016).
2. Z. Yang, A. R. Albrecht, J. G. Cederberg, and M. Sheik-Bahae, "80 nm tunable DBR-free semiconductor disk laser," *Appl. Phys. Lett.* **109**(2), 022101 (2016).
3. L. Zeng, B. X. Yang, A. Cavus, W. Lin, Y. Y. Luo, M. C. Tamargo, Y. Guo, and Y. C. Chen, "Red–green–blue photopumped lasing from ZnCdMgSe/ZnCdSe quantum well laser structures grown on InP," *Appl. Phys. Lett.* **72**(24), 3136 (1998).
4. A. J. Trindade, B. Guilhabert, E. Y. Xie, R. Ferreira, J. J. D. McKendry, D. Zhu, N. Laurand, E. Gu, D. J. Wallis, I. M. Watson, C. J. Humphreys, and M. D. Dawson, "Heterogeneous integration of gallium nitride light-emitting diodes on diamond and silica by transfer printing," *Opt. Express* **23**(7), 9329 (2015).
5. A. J. Trindade, B. Guilhabert, D. Massoubre, D. Zhu, N. Laurand, E. Gu, I. M. Watson, C. J. Humphreys, and M. D. Dawson, "Nanoscale-accuracy transfer printing of ultra-thin AlInGaN light-emitting diodes onto mechanically flexible substrates," *Appl. Phys. Lett.* **103**(25), 253302 (2013).
6. S. W. Corzine, R. S. Geels, J. W. Scott, R. H. Yan, and L. A. Coldren, "Design of Fabry-Perot Surface-Emitting Lasers with a Periodic Gain Structure," *IEEE J. Quantum Electron.* **25**(6), 1513–1524 (1989).
7. M. Kuznetsov, F. Hakimi, R. Sprague, and A. Mooradian, "Design and characteristics of high-power (>0.5-W CW) diode-pumped vertical-external-cavity surface-emitting semiconductor lasers with circular TEM<sub>00</sub> beams," *IEEE J. Sel. Top. Quantum Electron.* **5**(3), 561–573 (1999).
8. S. L. Chuang, *Physics of Photonic Devices*, 2nd ed. (Wiley, 2009).
9. M. Guina, A. Rantamäki, and A. Härkönen, "Optically pumped VECSELs: review of technology and progress," *J. Phys. D. Appl. Phys.* **50**(38), 383001 (2017).
10. Z. Yang, D. Follman, A. R. Albrecht, P. Heu, N. Giannini, G. D. Cole, and M. Sheik-Bahae, "16 W DBR-free membrane semiconductor disk laser with dual-SiC heatspreader," *Electron. Lett.* **54**(7), 430–432 (2018).
11. S. Adachi, *Properties of Semiconductor Alloys : Group-IV, III-V and II-VI Semiconductors* (Wiley, 2009).
12. M. Mangold, V. J. Wittwer, O. D. Sieber, M. Hoffmann, I. L. Krestnikov, D. A. Livshits, M. Golling, T. Südmeier, and U. Keller, "VECSEL gain characterization," *Opt. Express* **20**(4), 4136 (2012).

13. B. Heinen, T.-L. Wang, M. Sparenberg, A. Weber, B. Kunert, J. Hader, S. W. Koch, J. V. Moloney, M. Koch, and W. Stolz, "106 W continuous-wave output power from vertical-external-cavity surface-emitting laser," *Electron. Lett.* **48**(9), 516 (2012).
14. R. Sheikhi, Y. Huo, F. G. Shi, and C. C. Lee, "Low Temperature VECSEL-to-Diamond Heterogeneous Integration with Ag-In Spinodal Nanostructured Layer," *Scr. Mater.* **194**, 113628 (2021).
15. J. McPhillimy, B. Guilhabert, C. Klitis, M. D. Dawson, M. Sorel, and M. J. Strain, "High accuracy transfer printing of single-mode membrane silicon photonic devices," *Opt. Express* **26**(13), 16679 (2018).
16. E. Margariti, G. Quinn, D. Jevtics, B. Guilhabert, M. D. Dawson, and M. J. Strain, "Continuous roller transfer-printing and automated metrology of > 75,000 micro-LED," (n.d.).
17. B. Seredyński, M. Król, P. Starzyk, R. Mirek, M. Ściesiek, K. Sobczak, J. Borysiuk, D. Stephan, J.-G. Rousset, J. Szczytko, B. Piętka, and W. Pacuski, "(Cd,Zn,Mg)Te-based microcavity on MgTe sacrificial buffer: Growth, lift-off, and transmission studies of polaritons," *Phys. Rev. Mater.* **2**(4), 043406 (2018).
18. K.-P. Huang, K.-C. Wu, F.-H. Fan, W.-P. Tseng, B.-C. Shieh, S.-H. Chen, and C.-F. Lin, "InGaN Light-Emitting Diodes with Multiple-Porous GaN Structures Fabricated through a Photoelectrochemical Etching Process," *ECS J. Solid State Sci. Technol.* **3**(10), R185–R188 (2014).
19. R. T. Elafandy, J.-H. Kang, C. Mi, T. K. Kim, J. S. Kwak, and J. Han, "Study and Application of Birefringent Nanoporous GaN in the Polarization Control of Blue Vertical-Cavity Surface-Emitting Lasers," *ACS Photonics* **8**, 1041–1047 (2021).
20. S. Huang, Y. Zhang, B. Leung, G. Yuan, G. Wang, H. Jiang, Y. Fan, Q. Sun, J. Wang, K. Xu, and J. Han, "Mechanical properties of nanoporous GaN and its application for separation and transfer of GaN thin films," *ACS Appl. Mater. Interfaces* **5**(21), 11074–11079 (2013).
21. S. Wills, "Optics & Photonics News - Partnership Targets Green VCSELs," [https://www.optica-opn.org/home/industry/2022/december/partnership\\_targets\\_green\\_vcseles/](https://www.optica-opn.org/home/industry/2022/december/partnership_targets_green_vcseles/).
22. F. Fan, S. Turkdogan, Z. Liu, D. Shelhammer, and C. Z. Ning, "A monolithic white laser," *Nat. Nanotechnol.* **10**(9), 796–803 (2015).

# Research output

## Journal papers

P. H. Moriya, R. Casula, **G. A. Chappell**, D. C. Parrotta, S. Ranta, H. Kahle, M. Guina and J. E. Hastie, “InGaN-diode-pumped AlGaInP VECSEL with sub-kHz linewidth at 689 nm”, *Optics Express*, **29**, 3, 3258-3268 (2021)

**G. A. Chappell**, B. Guilhabert, T. Garcia, K. Zhao, I. M. Watson, M. D. Dawson, M. C. Tamargo, and J. E. Hastie, “Suspension and transfer printing of ZnCdMgSe membranes from an InP substrate”, *Optical Materials Express*, **10**, 12, pp. 3328-3341 (2020)

## Editor’s pick

## Conference papers

P. H. Moriya, R. Casula, D. C. Parrotta, **G. A. Chappell**, S. Ranta, H. Kahle, M. Guina and J. E. Hastie, “InGaN-diode-pumped AlGaInP VECSEL with sub-kHz linewidth at 689 nm”, *FiO + LS 2020*

**G. A. Chappell**, B. Guilhabert, I. M. Watson, M. D. Dawson, M. C. Tamargo and J. E. Hastie, “Progress towards transfer printing of II-VI and III-V DBR-free VECSELS”, *SPIE Photonics West 2020 Vertical External Cavity Surface Emitting Lasers (VECSELS) X*

**G. A. Chappell**, B. Jones, T. Garcia, M. C. Tamargo, and J. E. Hastie, “Narrow Linewidth Semiconductor Disk Lasers and Progress Towards ZnCdMgSe Vertical Gain Structures”, *MRS Spring Meeting 2019*

R. Casula, P. H. Moriya, **G. A. Chappell**, D. C. Parrotta, S. Ranta, H. Kahle, M. Guina, and J. E. Hastie “GaN-diode-pumped AlGaInP VECSEL for strontium optical clocks”, *SPIE Photonics West 2019 Vertical External Cavity Surface Emitting Lasers (VECSELS) IX*

# Appendix

## A2.1 Angle of propagation of light in a repeating unit heterostructure

Consider Snell's law applied to light entering from a medium,  $n_0$ , into a heterostructure of two materials of refractive indices  $n_1$  and  $n_2$  respectively with two repeating units and then exiting back into the medium,  $n_0$ . The light enters at angle  $\theta_{In}$ , has an angle of  $\theta_N$  through each layer where  $N$  is the layer number and then exits at  $\theta_{Out}$ . The Snell's law equations governing this are coupled and given by

$$n_0 \sin(\theta_{In}) = n_1 \sin(\theta_1) \quad (46a)$$

$$n_1 \sin(\theta_1) = n_2 \sin(\theta_2) \quad (46b)$$

$$n_2 \sin(\theta_2) = n_1 \sin(\theta_3) \quad (46c)$$

$$n_1 \sin(\theta_3) = n_2 \sin(\theta_4) \quad (46d)$$

$$n_2 \sin(\theta_4) = n_0 \sin(\theta_{Out}) \quad (46e)$$

where  $n_0$  is the refractive index of air. Already from comparison of (46b) and (46c) it can be seen that  $\theta_1 = \theta_3$  and from comparison of (46c) and (46d) we can see that  $\theta_2 = \theta_4$  and we can extrapolate that for all odd numbered layers  $\theta_N$  is equal for each one and for all even numbered layers  $\theta_N$  is equal for each one. From this reasoning we can use (46e) to show that

$$\theta_{Out} = \sin^{-1}\left(\frac{n_2}{n_0} \sin(\theta_2)\right), \quad (47)$$

and from (46a) and (46b) we can see that

$$\theta_2 = \sin^{-1}\left(\frac{n_0}{n_2} \sin(\theta_{In})\right). \quad (48)$$

From substitution of (48) into (47) we see that

$$\theta_{out} = \sin^{-1} \left( \frac{n_2}{n_0} \sin \left( \sin^{-1} \left( \frac{n_0}{n_2} \sin(\theta_{in}) \right) \right) \right), \quad (49)$$

which simplifies by cancellation of sin functions to

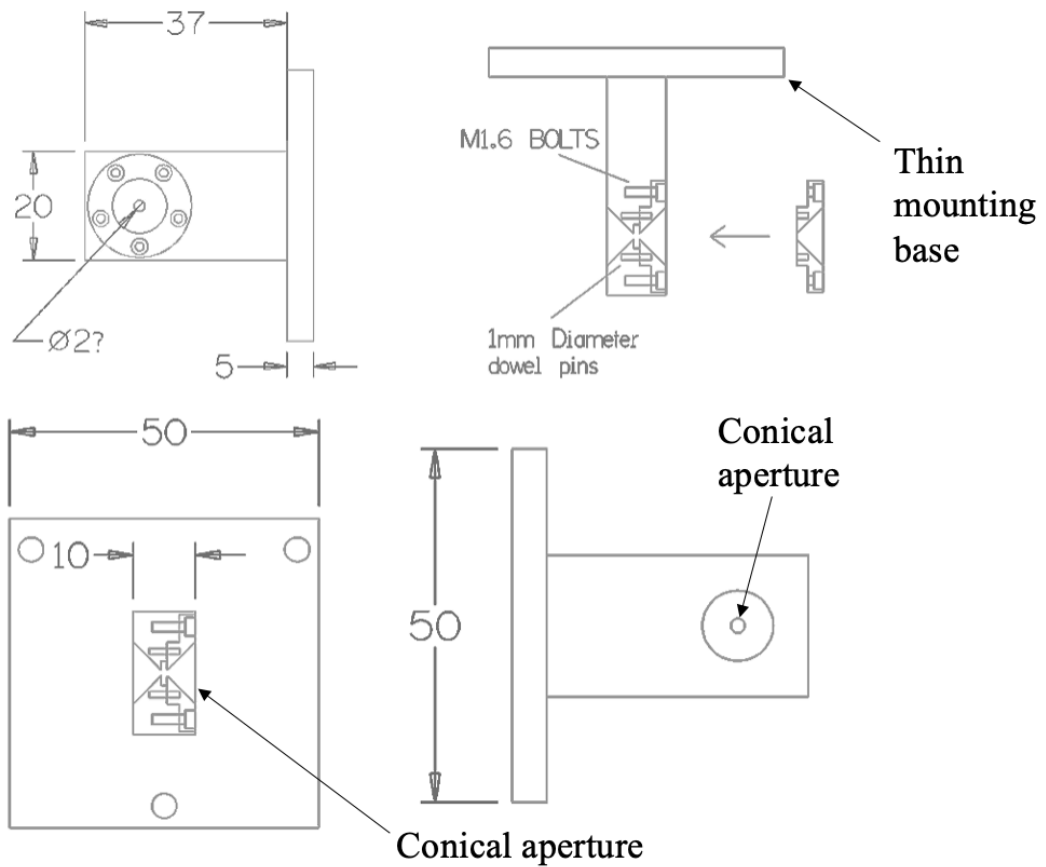
$$\theta_{out} = \sin^{-1} \left( \frac{n_2 n_0}{n_0 n_2} \sin(\theta_{in}) \right) = \sin^{-1}(\sin(\theta_{in})) = \theta_{in}. \quad (50)$$

This can be used to simplify the modelling of the DBR-free structures.

### A3.1 DBR-free VECSEL mount

These technical drawings were completed by Lewis Hannah, to a given specification.

Distances are in mm and brass was used as the construction material.



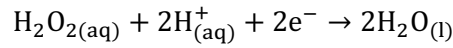
#### **A4.1 Varying the wet etchants**

Given the difficulties with forming a stable silica sidewall protection, selective etchants, sidewall passivating etches, multi-step etches and varied etch concentrations were assessed to determine whether the optimization of the under-etching chemistry could yield improved membrane quality. These experiments are summarized in Table 6 and from these it was concluded that although the sidewall protection hold time still limits the membrane quality. A two-step etch process of HCl:H<sub>3</sub>PO<sub>4</sub> (3:1) followed by HCl shows the most promise for InP under-etching.

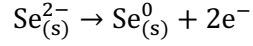
**Table A1.** Wet-etchant summary for the ZnCdMgSe membrane under-etch.

<b>Etchant</b>	<b>Proposed purpose</b>	<b>Comments</b>	<b>Results</b>
NaOH:H <sub>2</sub> O <sub>2</sub>	Selectively etch InGaAs from ZnCdMgSe.	Etchant mixed as per [1,2] Used to under-etch unprotected membranes.	No etching observed after 70 minutes.
Br <sub>2</sub> :CH <sub>3</sub> OH	Selectively etch InP from ZnCdMgSe.	Dangerous etchant, failed to meet safety standards.	N/A
H <sub>2</sub> SO <sub>4</sub> :H <sub>2</sub> O <sub>2</sub> : H <sub>2</sub> O (1:10:1)	Form a passivation layer of Se by reducing the Se* in the ZnCdMgSe surface [3]. Se is insoluble in HCl.	Unprocessed ZnCdMgSe etched for 60 s in the test etchant. This sample and a control sample were etched for 2 minutes in HCl.	Control sample had fewer etch pits than the tested sample, suggesting that passivation had not been achieved.
HCl:H <sub>3</sub> PO <sub>4</sub> (1:1)	Less aggressive under-etching.	Used to under-etch. Higher proportion of H <sub>3</sub> PO <sub>4</sub> reduces the aggression.	Slow under-etch rate. Sidewall protection compromised after 30 minutes
HCl:H <sub>3</sub> PO <sub>4</sub> (3:1)	Under-etching.	Used to under-etch.	Faster etching than HCl:H <sub>3</sub> PO <sub>4</sub> (1:1). Sidewall protection compromised. Slow-etch plane formation slows under-etch rate
HCl:H <sub>3</sub> PO <sub>4</sub> (3:1) followed by HCl	Under-etching.	First etch of HCl:H <sub>3</sub> PO <sub>4</sub> (3:1) to complete the majority of the under-etch and then completion with more aggressive undiluted HCl etchant.	Successfully under-etched membranes. Undiluted HCl can etch the slow-etch faces which arise during the initial HCl:H <sub>3</sub> PO <sub>4</sub> (3:1) etch. Sidewall protection still compromised.

\*Etching ZnSe with H<sub>2</sub>SO<sub>4</sub>:H<sub>2</sub>O<sub>2</sub>:H<sub>2</sub>O (1:10:1) has been shown to initiate the reaction

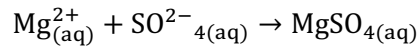
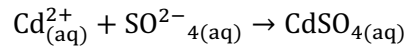
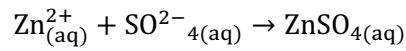


and



which results in the ZnSe surface becoming elemental selenium, Se<sub>(s)</sub><sup>0</sup> [3].

The group II elements undergo these etching reactions in the Se surface treatment :



#### A4.2 Under-etch trials

Fig. A2 shows a membrane following an initial under-etch attempt with a 10 minute etch with 3HCl:H<sub>3</sub>PO<sub>4</sub>. The etch damage caused by the etchant can be seen as the recession of the II-VI material (the brown layer). The interference fringes show the under-etched areas which are now bowing following the substrate removal. Underneath the membrane a ~45° tilted dark rectangle is the InP pillar that remains under the membrane following the 10 minute under-etch.



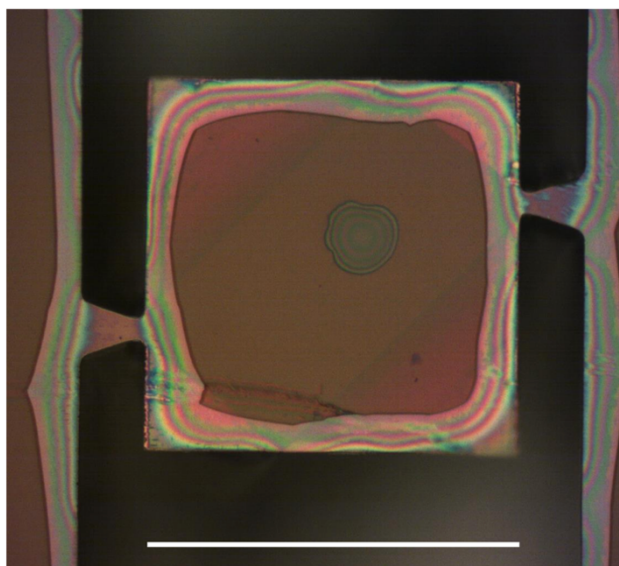


**Fig. A2** A 100- $\mu\text{m}$ -sided ZnCdMgSe membrane, following an initial 10 minute trial under-etch with  $3\text{HCl}:\text{H}_3\text{PO}_4$ .

### **A5.1 Raman mapping Python programs**

#### *A5.1.1 Intensity-at-a-point mapping program*

```
#Import necessary libraries
import numpy as np
import matplotlib.pyplot as plt
import math
from scipy.optimize import curve_fit
#State spectral properties
High_wavenumber=1376.97656
Low_wavenumber=-512.08203
Spectrum_range=High_wavenumber-Low_wavenumber
Number_of_entries=1012
Spectral_resolution=Spectrum_range/Number_of_entries
Target_wavenumber_lower=400.0
Target_wavenumber_upper=500.0
#Scan properties
x_scan_size=33
x_step=1
y_scan_size=33
y_step=1
Number_of_points=x_scan_size*y_scan_size
```

```

Spectrum_size=1012
#Spectral extraction points
Lower_extraction=560
Upper_extraction=600
#Lower_extraction=500
#Upper_extraction=560
#For the through diamond results
#445 peak
#Lower_extraction=540
#Upper_extraction=600
#360 peak
#Lower_extraction=600
#Upper_extraction=630
#Diamond peak
#Lower_extraction=65
#Upper_extraction=75
#Lower_extraction=650
#Upper_extraction=700
"""
#Extract spectrum from file
Low_extraction_coordinate=int((High_wavenumber-
Target_wavenumber_upper)/Spectral_resolution)
High_extraction_coordinate=int((High_wavenumber-
Target_wavenumber_lower)/Spectral_resolution)
"""
#MAP 45 deg rotated membrane 20x 532 nm 1pc 5s 36 by 36 70mu x 70 mu 2mu step_Copy
#MAP 20x 1pc 5s 532 nm 80 by 80 2mu step 41 by 41_Copy
#17_6_2021/MAP 20x 1pc 5s 532 nm 80 by 80 2mu step 41 by 41_Copy.txt
#22_6_2021/MAP 532nm_5s_1pc_20x 41 by 41 2 mu step 80 mu by 80 mu_Copy_Copy.txt
#Extract a Raman spectrum
with open('Unprocessed MR3751/MR3751 unprocessed MAP
20x_10pc_1s_X33_Y33_160mu_by_160mu_532nm_Copy.txt', 'r') as f:
    lines = f.readlines()[1:]
    x = [float(line.split()[0]) for line in lines]
    y = [float(line.split()[1]) for line in lines]

```

```

Raman_shift=[float(line.split()[2]) for line in lines]
Intensity=[float(line.split()[3]) for line in lines]
#Extract the data of interest and build into a matrix
#Matrix format = [position number, Raman shift, intensity]
#Position numbers work left to right
Raman_peaks=[]
Peak_intensity=[]
Position=[]
for n in range(0,Number_of_points):
    Position.append(n)
    for i in range(Lower_extraction,Upper_extraction):
        Raman_data_point=Raman_shift[i+(Spectrum_size*(n))]
        Intensity_data_point=Intensity[i+(Spectrum_size*(n))]
        Raman_peaks.append(Raman_data_point)
        Peak_intensity.append(Intensity_data_point)
#Fit a Gaussian to each peak. Define the Gaussian and vectorize it
def Gaussian(z,a,b,position,offset):
    return (a*math.exp(-(z-position)**2)/(2*(b**2)))+offset
g=np.vectorize(Gaussian)
#Sort through the lines of Raman spectra and fit a Gaussian to each peak
#Peak position is stored in a variable which lines up with the "Position" variable
Intensity_at_point=[]
Point_value=[]
Point_of_interest=17
#577 and 578 for 354 cm-1
for n in range(0,Number_of_points):
    Intensity_at_point.append(Peak_intensity[Point_of_interest+(n*(Upper_extraction-
Lower_extraction))])
    Point_value.append(Raman_peaks[Point_of_interest+(n*(Upper_extraction-
Lower_extraction))])

#This section plots the map
x= np.arange(-80, 85, 5)
y= np.arange(-80,85, 5)
X, Y = np.meshgrid(x, y)

```

```

#Split "Raman_peak_positions" into a matrix
Raman_peak_position_components=np.array_split(Intensity_at_point,x_scan_size)
#Now build up the Raman map matrix
Raman_map_matrix=[]
for u in range(0,x_scan_size):
    Raman_map_matrix.append(Raman_peak_position_components[x_scan_size-1-u])
#gist_rainbow
#Plotting details
cmap = plt.get_cmap('plasma')
fig, (ax0) = plt.subplots()
plt.xlabel('x position /  $\mu\text{m}$ ')
plt.ylabel('y position /  $\mu\text{m}$ ')
im = ax0.pcolormesh(X, Y, Raman_map_matrix, cmap=cmap)
fig.colorbar(im, ax=ax0)
ax0.set_title('Intensity at 355 cm $^{-1}$ ')
#plt.xlim(0,10)
#plt.ylim(0,10)
#plt.savefig('Unprocessed MR3751/MR3751 unprocessed MAP 355 peak.pdf')

```

#### *A5.1.2 Peak position mapping program*

```

#Import necessary libraries
import numpy as np
import matplotlib.pyplot as plt
import math
from scipy.optimize import curve_fit
#State spectral properties
High_wavenumber=1376.97656
Low_wavenumber=-512.08203
Spectrum_range=High_wavenumber-Low_wavenumber
Number_of_entries=1012
Spectral_resolution=Spectrum_range/Number_of_entries
Target_wavenumber_lower=400.0
Target_wavenumber_upper=500.0
#Scan properties
x_scan_size=33

```

```

x_step=1
y_scan_size=33
y_step=1
Number_of_points=x_scan_size*y_scan_size
Spectrum_size=1012
#Spectral extraction points
Lower_extraction=560
Upper_extraction=600
#Lower_extraction=525
#Upper_extraction=535
#For the through diamond results
#445 peak
#Lower_extraction=540
#Upper_extraction=600
#360 peak
#Lower_extraction=600
#Upper_extraction=630
#Diamond peak
#Lower_extraction=65
#Upper_extraction=75
#Lower_extraction=700
#Upper_extraction=750
""""
#Extract spectrum from file
Low_extraction_coordinate=int((High_wavenumber-
Target_wavenumber_upper)/Spectral_resolution)
High_extraction_coordinate=int((High_wavenumber-
Target_wavenumber_lower)/Spectral_resolution)
""""
#MAP_532nm_1pc_10s_X17_Y17_5mu_step_80by80.txt
#On_PDMS_MAP 10s_1pc_20x_532nm_X11_Y11_8mu_step_Copy
#MR3751 unprocessed MAP 20x_10pc_1s_X33_Y33_160mu_by_160mu_532nm_Copy
#MAP 45 deg rotated membrane 20x 532 nm 1pc 5s 36 by 36 70mu x 70 mu 2mu step_Copy
#MAP 20x 1pc 5s 532 nm 80 by 80 2mu step 41 by 41_Copy
#Extract a Raman spectrum

```

```

#17_6_2021/MAP 20x 1pc 5s 532 nm 80 by 80 2mu step 41 by 41_Copy.txt
#22_6_2021/MAP 532nm_5s_1pc_20x 41 by 41 2 mu step 80 mu by 80 mu_Copy_Copy.txt
#Through diamond MAP 532 nm 20x 5s 1pc 46 by 46 2 mu step 90 mu by 90 mu_Copy
with open('Unprocessed MR3751/MR3751 unprocessed MAP
20x_10pc_1s_X33_Y33_160mu_by_160mu_532nm_Copy.txt', 'r') as f:
    lines = f.readlines()[1:]
    x = [float(line.split()[0]) for line in lines]
    y = [float(line.split()[1]) for line in lines]
    Raman_shift=[float(line.split()[2]) for line in lines]
    Intensity=[float(line.split()[3]) for line in lines]
#Extract the data of interest and build into a matrix
#Matrix format = [position number, Raman shift, intensity]
#Position numbers work left to right
Raman_peaks=[]
Peak_intensity=[]
Position=[]
for n in range(0,Number_of_points):
    Position.append(n)
    for i in range(Lower_extraction,Upper_extraction):
        Raman_data_point=Raman_shift[i+(Spectrum_size*(n))]
        Intensity_data_point=Intensity[i+(Spectrum_size*(n))]
        Raman_peaks.append(Raman_data_point)
        Peak_intensity.append(Intensity_data_point)
#Fit a Gaussian to each peak. Define the Gaussian and vectorize it
def Gaussian(z,a,b,position,offset):
    return (a*math.exp(-((z-position)**2)/(2*(b**2))))+offset
g=np.vectorize(Gaussian)
#Sort through the lines of Raman spectra and fit a Gaussian to each peak
#Peak position is stored in a variable which lines up with the "Position" variable
Raman_peak_positions=[]
for n in range(0,Number_of_points):
    x_data=[]
    for z in range (0,(Upper_extraction-Lower_extraction)):
        x_data.append(Raman_peaks[z+(n*(Upper_extraction-Lower_extraction))])
    y_data=[]

```

```

for t in range(0,(Upper_extraction-Lower_extraction)):
    y_data.append(Peak_intensity[t+(n*(Upper_extraction-Lower_extraction))])
popt, pcov = curve_fit(g, x_data, y_data,p0=[800,1,355,1])
Peak_Position=popt[2]
Raman_peak_positions.append(Peak_Position)
plt.plot(x_data,g(x_data,popt[0],popt[1],popt[2],popt[3]),color='red')
plt.plot(x_data,y_data,color='blue')
plt.savefig('445_fitting.pdf')
#This section plots the map
x1= np.arange(-80, 85, 5)
y1= np.arange(-80,85, 5)
X, Y = np.meshgrid(x1, y1)
#Split "Raman_peak_positions" into a matrix
Raman_peak_position_components=np.array_split(Raman_peak_positions,x_scan_size)
#Now build up the Raman map matrix
Raman_map_matrix=[]
for u in range(0,x_scan_size):
    Raman_map_matrix.append(Raman_peak_position_components[x_scan_size-1-u])
#Gist rainbow
#Plotting details
cmap = plt.get_cmap('plasma')
fig, (ax0) = plt.subplots()
im = ax0.pcolormesh(X, Y, Raman_map_matrix, cmap=cmap)
plt.xlabel('x position /  $\mu\text{m}$ ')
plt.ylabel('y position /  $\mu\text{m}$ ')
fig.colorbar(im, ax=ax0)
ax0.set_title('Raman shift map')
#plt.xlim(0,10)
#plt.ylim(0,10)
plt.savefig('Unprocessed MR3751/unprocessed 354 MAP.pdf')
"""

```

## Appendix references

1. J. Haetty, M. H. Na, H. C. Chang, H. Luo, and A. Petrou, "Fabrication of flexible monocrystalline ZnSe-based foils and membranes," *Appl. Phys. Lett.* **69**(11), 1608 (1998).
2. E. Kurtz, S. Einfeldt, J. Nürnberger, S. Zerlauth, D. Hommel, and G. Landwehr, "p-Type Doping of ZnSe. On the Properties of Nitrogen in ZnSe:N," *Phys. status solidi* **187**(2), 393–399 (1995).
3. A. Osinsky, Y. Qiu, J. Mahan, H. Temkin, S. A. Gurevich, S. I. Nesterov, E. M. Tanklevskaia, V. Tretyakov, O. A. Lavrova, and V. I. Skopina, "Novel wet chemical etch for nanostructures based on II-VI compounds," *Appl. Phys. Lett.* **71**(4), 509–511 (1997).